The role of grain boundaries for the deformation and grain growth of olivine at upper mantle conditions

DISSERTATION

zur Erlangung des akademischen Grades eines Doktors

der Naturwissenschaften (Dr. rer. nat.)

in der Bayreuther Graduiertenschule für Mathematik und

Naturwissenschaften (BayNAT)

der Universität Bayreuth

vorgelegt von

Filippe Ferreira

aus *Belo Horizonte (Brasilien)*

Bayreuth, 2021

The role of grain boundaries for the deformation and grain growth of olivine at upper mantle conditions

DISSERTATION

zur Erlangung des akademischen Grades eines Doktors

der Naturwissenschaften (Dr. rer. nat.)

in der Bayreuther Graduiertenschule für Mathematik und

Naturwissenschaften (BayNAT)

der Universität Bayreuth

vorgelegt von

Filippe Ferreira

aus *Belo Horizonte (Brasilien)*

Bayreuth, 2021

Die vorliegende Arbeit wurde in der Zeit von Februar 2017 bis September 2020 in Bayreuth am Bayerischen Geoinstitut unter Betreuung von Dr. rer. nat. habil. Katharina Marquardt angefertigt.

Vollständiger Abdruck der von der Bayreuther Graduiertenschule für Mathematik und Naturwissenschaften (BayNAT) der Universität Bayreuth genehmigten Dissertation zur Erlangung des akademischen Grades eines Doktors der Naturwissenschaften (Dr. rer. nat.).

Dissertation eingereicht am: 05.10.2020

Zulassung durch das Leitungsgremium: 08.10.2020

Wissenschaftliches Kolloquium: 21.01.2021

Amtierender Direktor: Prof. Dr. Markus Lippitz

Prüfungsausschuss:

Dr. Katharina Marquardt (Gutachterin)

Prof. Dr. Daniel Frost (Gutachter)

PD Dr. Catherine McCammon (Vorsitz)

Prof. Dr. Gregor Golabek

The role of grain boundaries for the deformation and grain growth of olivine at upper mantle conditions

Filippe Ferreira

To Maria Bernadete and Wilson Ferreira

Summary

Crystal defects such as vacancies, dislocations and grain boundaries are central in controlling the rheology of the Earth's upper mantle. Their presence influences element diffusion, plastic deformation and grain growth, which are the main microphysical processes controlling mass transfer in the Earth's lithosphere and asthenosphere. Although substantial information exists on these processes, there is a general lack of data on how these defects interact at conditions found in the Earth's interior. A better understanding of processes occurring at the grain scale is necessary for increased confidence in extrapolating from laboratory length and time scales to those of the Earth. This would improve our knowledge of large-scale geodynamic processes and interpretations of geophysical observations such as electrical conductivity and seismic anisotropy.

In this work, I examined the evolution of olivine grain boundaries during experimental deformation and their impact on deformation in the dislocation-accommodated grain-boundary sliding (disGBS) regime. Previous studies suggest that disGBS may be the main deformation mechanism for olivine in most of Earth's upper mantle. I used electron backscattered diffraction and transmission electron microscopy data to investigate the micromechanics involved in disGBS, with a focus on the interactions between dislocations and grain boundaries. These interactions are to date only poorly understood and not yet quantitatively investigated in olivine. The results presented here suggest that grain boundaries play a major role in moderating deformation in the disGBS regime. I present observational evidence that the rate of deformation is controlled by assimilation of dislocations into grain boundaries. I also demonstrate that the ability for dislocations to transmit across olivine grain boundaries evolves with increasing deformation. Finally, I show that dynamic recrystallization of olivine creates specific grain boundaries, which are modified as deformation progresses.

The effective contribution of grain-boundary processes on the rheology of the upper mantle is correlated to the amount of grain boundaries in upper mantle rocks, that is,

their grain-size distribution and evolution. The grain-size distribution in the Earth's mantle is controlled by the balance between damage (recrystallization under a stress field) and healing (grain growth) processes. However, grain growth, one of the main processes controlling grain size, is still poorly constrained for olivine at conditions of the upper mantle. Experimental data on grain growth kinetics of olivine is to date restricted to pressures of up to 1.2 GPa. To evaluate the effects of pressure on grain growth of olivine, I performed grain growth experiments at pressures ranging from 1 to 12 GPa using piston-cylinder and multi-anvil apparatuses. I found that the olivine grain-growth rate is reduced as pressure increases. The results presented here suggest that grain-boundary diffusion is the main process of grain growth at high pressure. Based on the experimental results, I present an equation which includes the effect of an activation volume on the grain growth of olivine. The results indicate that at deep upper mantle conditions (depths of 200 to 410 km), the effect of pressure on inhibiting grain growth counteracts the effect of increasing temperature. I present estimations of viscosity as a function of depth considering the grain-size evolution predicted here. They indicate that the viscosity is approximately constant at the deep upper mantle conditions.

Zusammenfassung

Kristalldefekte wie Leerstellen, Versetzungen und Korngrenzen beeinflussen die rheologischen Eigenschaften des oberen Erdmantels entscheidend. Sie bestimmen die Diffusion von Elementen in Mineralen, deren plastische Verformung und deren Kornwachstum, welche die wichtigsten mikrophysikalischen Prozesse des Massentransfers in der Lithosphäre und Asthenosphäre der Erde darstellen. Obwohl es umfangreiche Informationen zu diesen Prozessen gibt, sind die Wechselwirkungen zwischen den verschiedenen Kristalldefekten bei Bedingungen des Erdinneren weitgehend unbekannt. Ein besseres Verständnis der auf Korn-Maßstab ablaufenden Prozesse ist erforderlich, um die im Labor untersuchten Parameter und Prozesse mit größerer Sicherheit auf die Erde zu extrapolieren. So verbessert sich auch das Verständnis geodynamischer Prozesse auf großem Maßstab sowie die Interpretation

geophysikalischer Beobachtungen, wie zum Beispiel elektrische Leitfähigkeit und seismische Anisotropie.

In dieser Arbeit habe ich die Entwicklung der Olivinkorngrenzen während der experimentellen Deformation und ihre Rolle bei der Deformation im disGBS-Regime (dislocation-accommodated grain-boundary sliding, versetzungsbedingtes Korngrenzgleiten) untersucht. Frühere Studien legen nahe, dass disGBS der Hauptverformungsmechanismus für Olivin im überwiegenden Teil des oberen Erdmantels sein könnte. Um die Mikromechanik von disGBS zu untersuchen, habe ich Elektronenrückstreubeugung und Transmissionselektronenmikroskopie verwendet. Der Schwerpunkt lag dabei auf den Wechselwirkungen zwischen Versetzungen und Korngrenzen. Diese Wechselwirkungen sind bisher nur wenig verstanden und in Olivin noch nicht quantitativ untersucht worden. Die hier vorgestellten Ergebnisse deuten darauf hin, dass Korngrenzen eine wichtige Rolle bei der Deformation im disGBS-Regime spielen. Ich präsentiere den ersten Beobachtungsnachweis, dass die Verformungsrate durch Assimilation von Versetzungen in Korngrenzen gesteuert wird. Ich präsentiere auch zum ersten Mal, dass sich die Fähigkeit von Versetzungen sich über Olivinkorngrenzen hinweg fortzusetzen mit zunehmender Verformung weiterentwickelt. Schließlich zeige ich, dass die dynamische Rekristallisation von Olivin spezifische Korngrenzen erzeugt, die sich mit fortschreitender Deformation verändern.

Der effektive Beitrag der Korngrenzen zur Rheologie des oberen Mantels korreliert mit ihrem Anteil in den Gesteinen des oberen Mantels. Dieser Anteil wird durch die Korngrößenverteilung bestimmt. Die Korngrößenverteilung im Erdmantel wird durch das Gleichgewicht zwischen Verkleinerungsprozessen (Rekristallisation in einem Spannungsfeld) und Ausheilungsprozessen (Kornwachstum) gesteuert. Das Kornwachstum ist jedoch für Olivin unter Bedingungen des oberen Mantels immer noch wenig erforscht. Experimentelle Daten zur Kinetik von Olivin-Kornwachstum sind bisher auf Drücke von bis zu 1.2 GPa beschränkt. Um die Auswirkungen des Drucks auf das Kornwachstum von Olivin zu bewerten, habe ich Experimente bei Drücken im Bereich von 1 bis 12 GPa unter Verwendung von Stempel-Zylinder-Pressen und Vielstempel-Pressen durchgeführt. Die Ergebnisse zeigen, dass die Wachstumsrate von Olivinkristallen mit zunehmendem Druck abnimmt. Außerdem weisen die Ergebnisse darauf hin, dass die Korngrenzendiffusion der Hauptprozess für Kornwachstum bei hohem Druck ist. Basierend auf den experimentellen Ergebnissen

präsentiere ich eine Gleichung, die die Auswirkung eines Aktivierungsvolumens auf das Kornwachstum von Olivin berücksichtigt. Die Ergebnisse zeigen, dass unter Bedingungen des tiefen oberen Mantels (Tiefen von 200 bis 400 km) die Auswirkung des Drucks auf die Hemmung des Kornwachstums der Auswirkung einer Temperaturerhöhung mit zunehmender Tiefe entgegenwirkt. In dieser Arbeit zeige ich Abschätzungen der Viskosität als Funktion der Tiefe unter Berücksichtigung der hier vorhergesagten Korngrößenentwicklung. Die Abschätzungen zeigen an, dass die Viskosität unter den Bedingungen des tiefen oberen Mantels ungefähr konstant ist.

Acknowledgments

I would like to thank Dr. Katharina Marquardt and Dr. Marcel Thielmann for their valuable guidance, support and encouragement during this project. I would like to also extend my gratitude to Dr. Caroline Bollinger, Dr. Robert Farla, Dr. Lars Hansen and Dr. Florian Heidelbach for sharing with me their knowledge and experience on rock deformation and high-pressure techniques. I appreciate all the help students, researchers and professors from BGI gave me during these years. Especially, I would like to thank Prof. Dr. Hans Keppler for the help with the synthesis of olivine, Prof. Dr. Tomoo Katsura and his research group for assistance with the fabrication of assembly parts, Dr. Nobuyoshi Miyajima for assistance with the TEM and Sumith Abeykoon for help with the multianvil experiments. I am thankful to Prof. Dr. Daniel Frost, Prof. Dr. Gregor Golabek and PD Dr. Catherine McCammon for their participation in the PhD Defence Committee and for the valuable insights they provided. I am grateful to the technical staff of BGI, in special to the skilful work of Heinz Fischer and Stefan Übelhack in the preparation of assembly parts, and of Raphael Njul and Alexander Rother in the preparation of samples. I am also thankful to the support of Detlef Kraußе, Sven Lindhart, Ulrike Trenz and Dorothea Wiesner. I am grateful to the friends I made in Bayreuth for the great time we shared. I am also thankful to all the support and understanding my family always offered me. Finally, I would like to express my gratitude to Joana Polednia for the translations and for her unlimited support and care.

CONTENTS

FIGURES

TABLES

ABBREVIATIONS

BF: Bright field

CSL : Coincidence site lattice

DF: Dark field

EBSD: Electron backscattered diffraction

EBSP: Electron backscattered pattern

EDS: Energy dispersive spectroscopy

EMP: Electron microprobe

En: Enstatite

FIB: Focused ion beam

Fo: Forsterite

FTIR: Fourier-transform infrared

GB: Grain boundary

GBS: Grain-boundary sliding

DifGBS: Diffusion-accommodated grain-boundary sliding

DisGBS: Dislocation-accommodated grain-boundary sliding

GBCD: Grain boundary character distribution

GBPD: Grain boundary plane distribution

HAGB: High-angle grain boundary

KAM: Kernel average misorientation

LAGB: Low-angle grain boundary

MA: Multianvil

Mis2mean: Misorientation to mean orientation

MUD: Multiples of uniform distribution

Ol: Olivine

Px: Pyroxene

SADP: Selected area diffraction pattern

SEM: Scanning electron microscope

TEM: Transmission electron microscope

WDS: Wavelength dispersive spectroscopy

Chapter 1: Introduction

The Earth's interior produces a great amount of heat, mainly due to the energy accumulated during the accretionary process (accretionary heat) and due to the decay of radioactive elements such as thorium, uranium and potassium (e.g., Jaupart et al., 2007). For this reason, temperatures inside the Earth approach 7000 K. In contrast, the temperature in outer space is close to 0 K. This temperature difference creates a heat flux within the Earth which is associated with a convective flow of matter, one of the main processes behind tectonics (Bercovici, 2003; Condie, 1997). Tectonic plates are formed by the Earth's crust and the uppermost mantle (Figure 1.1). These layers form a mechanically distinct portion of the Earth: the lithosphere. The lithosphere, cold and rigid, superposes the asthenosphere, a weaker and warmer portion of the Earth. As the asthenosphere convects, the negatively buoyant plates above it are consumed at subduction zones, whereas oceanic crust is created at spreading centres. The knowledge of these ongoing dynamic processes that drive plate tectonics is based on multiple sources of information. Geophysical observables such as global seismicity, magnetotellurics, and geodesy provide insight into the Earth's structure and its electromagnetic and gravity field, respectively, while geochemistry and mineral physics provide constraints on the interpretation of remote data.

Plate tectonics have a major role on how Earth and its biosphere evolved throughout its 4.54 Ga of history. For instance, volcanism is associated with the creation and maintenance of Earth's atmosphere and climate, which allowed the thriving of life in our planet (Nisbet and Sleep, 2001). Furthermore, as supercontinents were formed and broken apart, mountains and basins evolved and contributed to diversify life as we know it today (e.g., Raven and Axelrod, 1972). Plate tectonics is also the main cause of natural hazards such as earthquakes and volcanic eruptions, which triggered mass extinctions during Earths' history (e.g. Wignall et al., 2009).

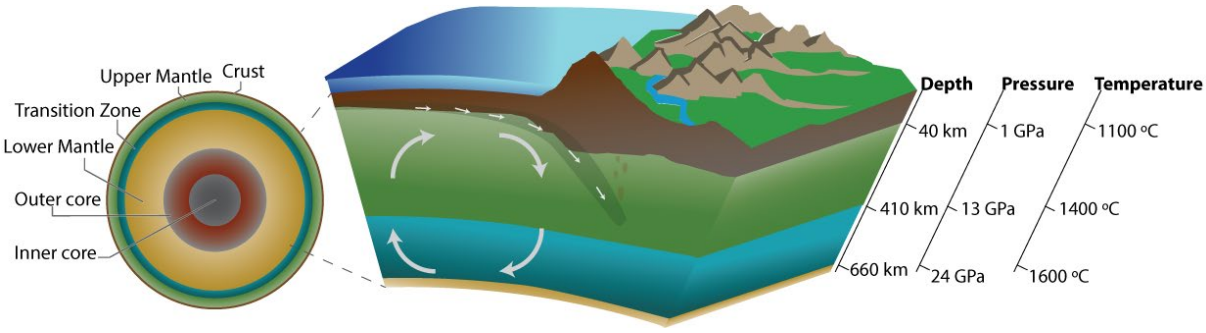

Figure 1.1: Earth's structure and mantle convection (indicated by arrows). Modified from USGS (1999).

One key ingredient of plate tectonics is rheology, the study of how matter deforms in response to stresses. Viscosity, a measure of the resistance of a material to deformation, is a fundamental parameter controlling several processes occurring in the Earth's interior and surface, such as rock exhumation, ocean spreading, magma ascent, etc. The estimation of the viscosity in the Earth's interior relies on the analyses of seismic-wave attenuation, post-glacial rebound, and gravity anomaly data (Karato, 2012). These results are interpreted in the light of experimental measurements and modelling of time-dependent deformation of rocks. On this basis, microphysical processes operating at the grain to atomic scale during rock deformation must be first understood and quantified for a sensible extrapolation of lab data to natural conditions.

Rocks are polycrystalline, which means that they are composed of crystallites joined together by grain boundaries. Studies focusing on grain-boundary effects on rock viscosity are still scarce, although different studies indicate that grain boundaries greatly affect deformation (e.g., Hansen et al., 2019, 2011; Hirth and Kohlstedt, 2003). Particularly for the upper mantle, the strength of olivine single crystals (e.g., Bai et al., 1991) differs significantly from the strength of polycrystalline aggregates of olivine with deformation accommodated by dislocation creep (Raterron et al., 2019; Tielke et al., 2016). Since dislocation creep is argued to be one of the main deformation mechanisms in the Earth's upper mantle (Karato and Wu, 1993), this difference suggests that grain boundaries play a critical role in moderating the macroscopic mechanical properties of this region. For instance, grain boundaries affect deformation by allowing grain-boundary sliding to occur (e.g., Lim and Raj, 1985). Dislocation-accommodated grain-boundary sliding (DisGBS), is predicted to be a major creep mechanism in the upper mantle (Hansen et al., 2011; Kohlstedt and Hansen, 2015; Ohuchi et al., 2015). Nevertheless, only scarce data on the microphysical process

behind disGBS in olivine is available. In particular, there is a lack of information on how grain boundaries moderate deformation in this regime. For example, disGBS requires the interaction of crystal defects, such as dislocations and vacancies, with grain boundaries (Langdon, 2006, 1994, 1970). However, these interactions during olivine deformation are not yet understood. In Chapter 4, I investigate how olivine grain boundaries evolve during deformation in the disGBS regime and how the interactions between grain boundaries and dislocations affect deformation of olivine.

The effective contribution of grain-boundary processes in the Earth's interior ultimately depends on the amount of grain boundaries, that is, on grain size. The grain-size evolution in the Earth's mantle plays an important role in the Earth's heat flux and its thermal evolution (Hall and Parmentier, 2003; Rozel, 2012; Solomatov, 2001), it moderates chemical mixing and the formation of chemical heterogeneities in the Earth's mantle (Solomatov and Reese, 2008), controls the dynamics of subducting slabs and plumes (Dannberg et al., 2017) and the localization of deformation in shear zones (Mulyukova and Bercovici, 2019; Thielmann, 2018; Thielmann et al., 2015). Grain size also affects our interpretation of geophysical observations such as seismic attenuation (Dannberg et al., 2017; Jackson et al., 2002; Tan et al., 2001) and electrical conductivity (Pommier et al., 2018; ten Grotenhuis et al., 2004). Grain size evolution in the Earth's deep interior is controlled by grain size reduction (damage) and grain growth (healing) processes (e.g., Bercovici and Ricard, 2012; Dannberg et al., 2017; Solomatov and Reese, 2008). Grain size reduction occurs when deformed grains reduce their total elastic energy introduced by dislocations by recovering into new (smaller) grains, free of dislocations (e.g., Urai et al., 1986). The new grain size is dependent on the density of dislocations being produced, which in turn is dependent on the applied shear stress (e.g., Kohlstedt and Weathers, 1980; Takeuchi and Argon, 1976). In contrast, grain growth occurs in order to minimize the excess free energy associated with grain boundaries (e.g., Evans et al., 2001) or dislocations (e.g., Gottstein and Shvindlerman, 2009). At deeper portions of the upper mantle, seismological observations indicate that shear stresses are significantly reduced (Kohlstedt and Hansen, 2015). Thus, grain growth has a major role on defining grain sizes in this region. Although grain growth of olivine has been experimentally investigated by several authors, no studies have investigated the effect of pressure on grain growth. Therefore, additional experimental data is needed to improve estimations of grain-size evolution in the upper mantle. In Chapter 5, I therefore, investigate how

pressure affects grain growth of olivine at pressure and temperature conditions of the Earth's upper mantle.

Pressure influences the operating deformation mechanisms in minerals. Increasing pressure leads to changes in olivine's unit cell dimensions (e.g., Yagi et al., 1975), which might affect its creep strength (e.g., Shun-ichiro Karato, 1989), and change the activity of its slip systems (Couvy et al., 2004; Li et al., 2003; Mainprice et al., 2005; Raterron et al., 2007). Pressure also has a major role in vacancy formation, which by its turn affects element diffusion and climb of dislocations (e.g., Karato, 2012), which are essential processes in high-temperature deformation. Furthermore, recent experimental data shows that increase of pressure favours deformation of olivine in the disGBS regime, which has been argued to be its dominant deformation mechanism at middle upper mantle conditions and below (Ohuchi et al., 2015). We recently demonstrated through direct observation of microstructural development that intra- and intergranular mechanisms operate simultaneously during deformation in the disGBS regime at pressures between 3.5 and 5 GPa (Bollinger et al., 2019). Furthermore, we observed that grain-boundary processes increase their relevance at high temperatures (T>1100 ºC), which indicates a link between thermally-activated processes (such as element diffusion) and grain-boundary sliding. However, there is a lack of experimental data investigating the microphysical process behind disGBS during deformation at higher pressures. In Chapter 6, I thus present technical developments towards the investigation of grain-size sensitive deformation of olivine under deep upper mantle conditions (P = 7-10 GPa, T =1400 ºC) using a cubic 6-ram press.

The structure of grain boundaries is one of the main factors controlling grain boundary properties such as its energy and mobility (e.g., Watanabe, 1988). In order to quantify relations between grain boundary structure and its properties, the characterization of the grain boundary crystallography is necessary. A three-dimensional representation of a grain boundary plane requires the crystal orientation of the neighbouring grains and the orientation of the grain boundary plane. The grain boundary plane and character distribution technique allows the statistical characterization of grain boundary planes based on electron backscatter diffraction data (Rohrer et al., 2004; Saylor and Rohrer, 2002). Hitherto, the use of this technique was only possible in proprietary software and required the use of a command-line interpreter, which is unfamiliar for many (possible) users. In Chapter 7, I present a *MATLAB*® toolbox for

the automation of grain boundary plane and character distribution tasks and for data visualization.

In summary, this study aims to:

1. Investigate the role of grain boundaries during deformation of olivine in the disGBS regime, with focus on their interaction with dislocations;
2. Explore the effect of pressure on the grain growth of olivine and its implications for the viscosity of the upper mantle;
3. Introduce new designs of high-pressure deformation assembly and anvils for experimental studies at deep upper mantle conditions;
4. Present a new *MATLAB*® toolbox for the analysis of grain boundaries from EBSD data.

1.1. Olivine: Structural data, deformation mechanisms and influence on the rheology of the upper mantle

Olivine is a nesosilicate mineral presenting a solid solution between forsterite (Mg_2SiO_4) and fayalite (Fe_2SiO_4) end-members (Figure 1.2). It crystallizes in the orthorhombic symmetry (a= 4.762, b= 10.225, c= 5.994 and α=β=γ=90º) and space group Pbnm (Birle et al., 1968).

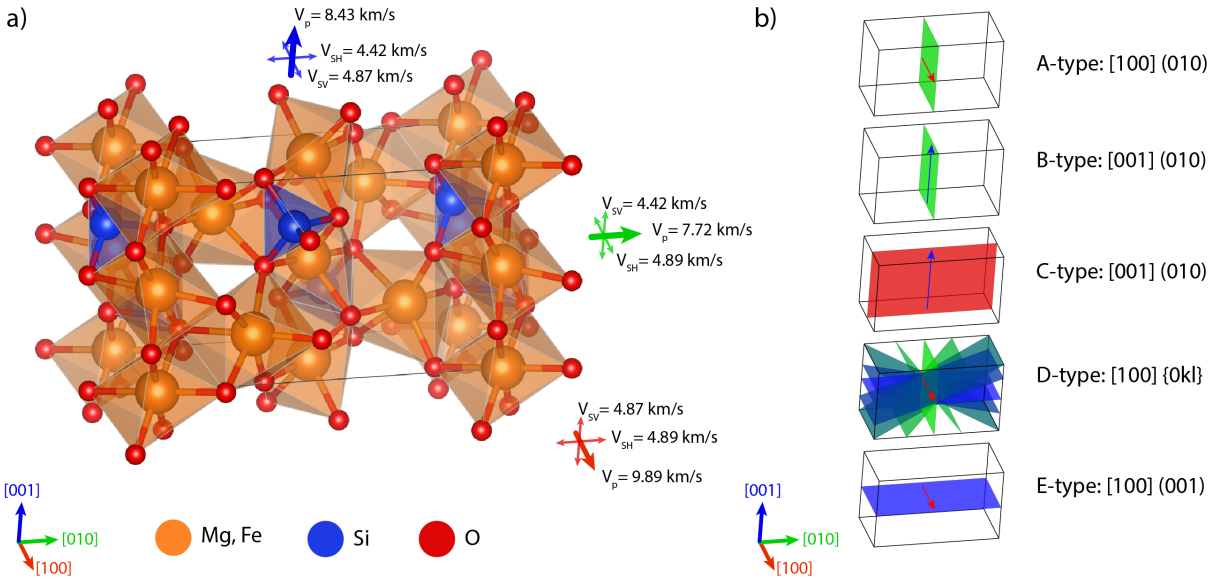

Figure 1.2: Olivine crystal structure and deformation mechanisms: a) Olivine crystal structure and sound velocities through [100], [010], [001] axes. b) Olivine slip systems.

Natural olivine is commonly found in xenoliths within volcanic rocks or in exhumed peridotite rocks. Olivine is formed at upper mantle conditions, at depths ranging from a few km down to approximately 410 km, where a mechanical discontinuity marks the upper limit of the transition zone. Under these conditions, olivine is stable for temperatures spanning from 1100 ºC to 1400 ºC and pressures up to 13 GPa (Cordier, 2002). Olivine is the main phase in the Earth's upper mantle comprising around 60% of its weight (Ringwood, 1975). This knowledge is based on direct observation of natural outcrops of mantle rocks and xenoliths, and by coupling large-scale geophysical observations to lab measurements of the physical properties of minerals, such as elasticity. Olivine is an elastically anisotropic mineral. P-wave velocities in olivine single crystals are faster along the [010] direction and slower in the [100] direction (Figure 1.2a). Since olivine is the most abundant mineral of the upper mantle, the development of lattice preferred orientation (LPO), usually attributed to dislocation creep (see Section 1.2.1), leads to large-scale seismic anisotropy in this region (e.g., Christensen and Crosson, 1968; Karato et al., 2008; Ribe, 1989). LPO, together with seismic anisotropy data, can thus be employed to analyse the dynamical behaviour of the deep Earth. For instance, in a large extent of the upper mantle, the flow direction is characterized by high velocities of compressional and Rayleigh waves and by faster velocities of horizontally than vertically-polarized shear waves (Karato and Wu, 1993; Ribe, 1989). Thus, the LPO development of olivine is of great interest. Several studies were performed in order to characterize LPO development of olivine in natural environments, through experiments or modelling (e.g., Ave'lallemant and Carter, 1970; Karato and Wu, 1993; Tommasi et al., 2000; Turner, 1942; Wenk, 1985). These studies demonstrate that in the shallow portion of the upper mantle ($\lessapprox$ 210 km), dislocation creep is the major mechanism to influence LPO development. The highly elastic anisotropic character of olivine is followed by viscoplastic anisotropy. Only a few slip systems are found to become active during deformation: [100] (010), [001] (010) and [100] (001) (Figure 1.2b). Furthermore, analyses of samples from distinct geodynamic environments reveal that the vast majority of natural LPO patterns can be explained by the activity of the (010)[100] slip system alone (Ismaïl and Mainprice, 1998). Nonetheless, since olivine lacks five independent slip systems, plastic flow cannot be fully accommodated by dislocation creep, according to the Von Mises Criterion (Mises, 1928). This criterion can be relaxed if other deformation mechanisms are also active. For instance, Cordier et al. (2014) proposed the motion of disclinations, i.e. rotational

defects, as an additional mechanism allowing for plastic flow. Alternatively, grain-boundary sliding accommodated by dislocation creep (disGBS; see Section 1.2.3) has been proposed as a deformation mechanism for olivine in the upper mantle (Hansen et al., 2011; Hirth and Kohlstedt, 1995; Ohuchi et al., 2015). In addition, other studies (Maruyama and Hiraga, 2017; Miyazaki et al., 2013) have suggested that deformation by grain-boundary sliding accommodated by diffusion creep (difGBS) would also result in olivine crystal alignment and, consequently, contribute to seismic anisotropy. At deep portions of the upper mantle (~210 km), the rapid decrease of seismic anisotropy is believed to mark a transition from dislocation to diffusion creep or superplasticity (see Section 1.2.2) as the dominant deformation mechanism (Boullier and Nicolas, 1975; Karato, 1992; Karato and Wu, 1993). This would reduce the LPO strength of olivine aggregates creating a near isotropic visco-elasto-plastic medium. Alternatively, Mainprice et al. (2005) and Raterron et al. (2007) argue that the increase of pressure enhances the activity of the [001](*hk*0) slip system. As multiple slip systems become active, the bulk LPO strength is reduced. This resulting low seismic anisotropy of aggregates would, therefore, explain the seismological observations.

1.2. Grain boundaries and their role on deformation and grain growth

A grain boundary is commonly defined as an interface between grains of the same phase with a misfit between their lattice orientations (misorientation), caused by a planar defect (Gottstein and Shvindlerman, 2009; Lejcek, 2010; Sutton and Balluffi, 1995). A boundary separating different phases is defined as an interphase boundary. A grain boundary differs from the crystal interior for having a less ordered structure and a stress field associated to it, which confers to grain boundaries different properties to those of the crystal lattice. Grain boundaries have been more recently recognized as interfaces presenting thermodynamically-stable states (Cantwell et al., 2014; Dillon and Harmer, 2007). These interface-stabilized “phases” known as complexions, present different composition and structure from the bulk material.

A first step to correlate the grain boundary structure to its properties is to classify them. Grain boundaries can be broadly separated into two groups in respect to their misorientation angles: Low and high-angle boundaries. Low-angle boundaries are accommodated by an array of dislocations (Read and Shockley, 1950). These

dislocations can be of two main types: Edge dislocations, forming tilt boundaries, and screw dislocations, forming twist boundaries (Burgers, 1940). Tilt boundaries might be further classified into symmetric or asymmetric tilt boundaries whether or not the grain boundary planes of the neighbouring grains have the same indices. High-angle boundaries are usually named general or random boundaries, mainly because no specific physical property is linked to them. Particularly, however, some high-angle boundaries can be further classified into Coincident Site Lattice (CSL) boundaries, which are interfaces between grains that share a lattice site (Randle, 1996). They are commonly represented by the Σn notation, where n refers to the reciprocal density of coincident sites. For instance, a Σ3 boundary is a twin relationship in a bicrystal where, for each 3 atoms, 1 is shared between the adjoining lattices. CSL boundaries are often called special boundaries because their presence, especially those with low Σ, might increase the performance of materials by improving bulk material properties such as strength and corrosion resistance (e.g., Davies and Randle, 2001; Gleiter, 1985; Randle, 2006, 1996; Randle and Ralph, 1988; Watanabe, 1984, 1988, 2011). This is attributed to the lower energy of these grain boundaries in comparison to general boundaries. Nonetheless, the CSL classification does not provide direct information on the crystallography of the grain boundaries and, therefore, a correlation between grain boundaries and properties is not unambiguously defined (Randle, 1996; Rollett et al., 2007a). The macroscopic geometrical relationship between two neighbouring grains can, however, be uniquely defined by five independent parameters, thus five macroscopic degrees of freedom are available: The misorientation between two adjacent crystals is described using three Eulerian angles given with respect to the crystal lattice of one crystal, conventionally: $\varphi_1, \Phi, \varphi_2$ (Wenk, 1985). The two remaining degrees of freedom describe the grain boundary plane orientation using two radial angles: ϕ and θ (Randle, 1993; Rhines, 1970). This description provides the basis of the grain boundary plane distribution technique, which is further discussed in Chapter 4.

Grain boundaries influence rheology by various ways. In the following sections, the effect of grain boundaries in specific deformation mechanisms and on grain growth is discussed.

1.2.1 **Dislocation creep**

Dislocation creep involves shearing of a crystal through the motion of linear defects called dislocations. As the dislocations progresses, atomic bonds are broken and reconnected. The motion of dislocations occur in a defined crystallographic plane (slip plane) along a crystal direction (slip direction), which define a slip system (Figure 1.3). In a polycrystalline material, as the dislocations reach the grain boundaries, different types of interactions might occur depending on the structure of the dislocations and of the grain boundaries as well as the environmental properties (e.g., temperature, shear stress, strain rate, etc.). During deformation at low temperature, grain boundaries may introduce obstacles for the motion of dislocations. Stress concentration and magnification due to dislocation pile-up in the vicinity of the grain boundaries leads to bulk mechanical hardening (Hirth, 1972). With decreasing grain size, the density of grain boundaries and thus obstacles increases, rendering the material harder. This relation is known as the Hall-Petch effect (Hall, 1951; Petch, 1953).

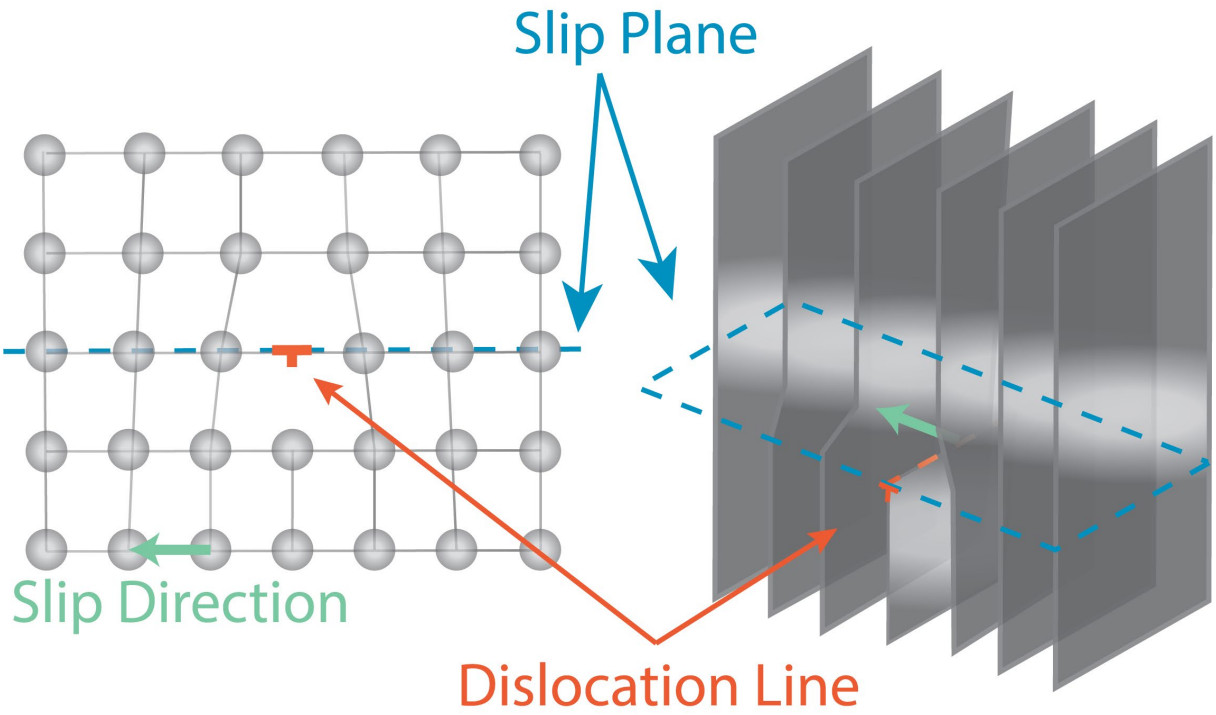

Figure 1.3: Deformation through dislocation creep. Dislocation creep involves the movement of dislocations on a specific plane (slip plane) along a certain direction (slip direction). Modified from Noels and Cdang (2020).

Another possible interaction between grain boundaries and dislocations is the transfer of dislocations across individual grain boundaries (slip transfer/ transmission), a central

process by which grain boundaries moderate macroscopic deformation at high temperatures. The geometrical configuration of the grain boundaries may influence slip transmission in different ways. Although a continuum of possibilities exist, three cases are exemplified (Bieler et al., 2014; Priester, 2013; Shen et al., 1988):

1. slip transfer occurs through the grain boundary in a (near) direct transmission of dislocations (Figure 1.4a);
2. slip progress to the next grain with only partial continuity, leaving residual grain-boundary dislocations (Figure 1.4b);
3. or the grain boundary is impenetrable and the dislocation is assimilated or dissociated into the grain boundary. Indirect transmission might occur when local stresses activate dislocations sources on the neighbouring grain (Figure 1.4c).

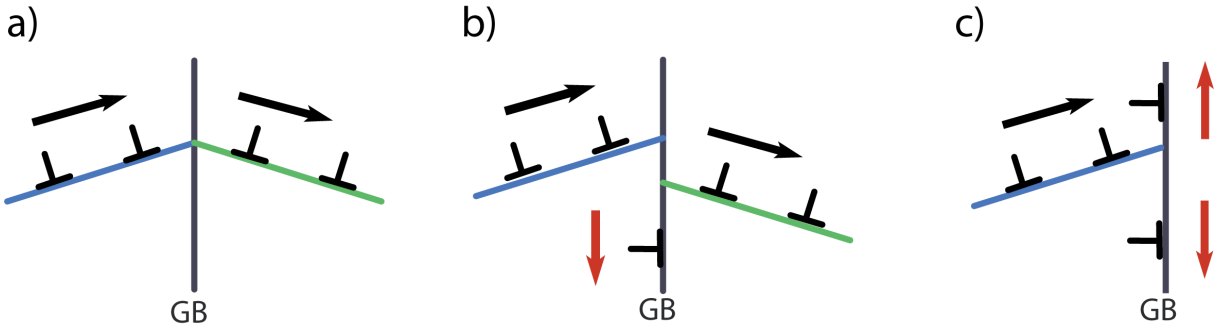

Figure 1.4: Slip transfer across grain boundaries: a) Direct transmission of slip across the grain boundary (GB). b) Indirect transmission of slip: Incoming and outcoming slip systems have a different Burgers Vector (black arrows). Residual boundary dislocations (red arrows) are originated. c) No transmission occurs: The grain boundary acts as a barrier for slip transfer. Dislocation pile-up leading to heterogeneous stress distribution near the grain boundaries. Modified from Sutton and Balluffi (1995).

This interaction has been discussed extensively for metals, alloys and ceramics (e.g., Dingley and Pond, 1979; Head, 1953; Kacher et al., 2014; Shen et al., 1988). Experiments (Kacher et al., 2011; Kondo et al., 2016; Lee et al., 1990, 1989; Oh et al., 2009; Shirokoff et al., 1993) and modelling (de Koning et al., 2003; Sangid et al., 2011; Spearot and Sangid, 2014; Zeng et al., 2008; Zheng et al., 2018) of these interactions provided useful information about the mechanisms involved. The transmission, annihilation or reaction of dislocations with interfaces depends on many characteristics of the interface including the composition, structure, energy and free volume, the applied and local stresses, the dislocation types and the dislocations mutual interactions (e.g. Bayerschen et al., 2016; Kacher et al., 2014). Additionally, the

geometric relationships between the grain boundary and dislocations are shown to have a great effect on slip transfer in metals and alloys (see reviews of Bayerschen et al., 2016; Hunter et al., 2018). Thus, the distribution of geometrical configurations of grain boundaries is critical for predicting the macroscopic influence of grain boundaries on deformation in the dislocation-creep regime.

1.2.2 **Diffusion creep**

Diffusion creep involves the flux of atoms in polycrystalline materials. The driving force for this diffusional process is the change in equilibrium (concentration) of vacancies or interstitial atoms due to an imposed shear stress (Herring, 1950). Deformation is thus achieved by the shape modification of individual crystals due to mass transfer (Figure 1.5). Two main mechanisms for diffusion creep can be distinguished: Nabarro-Herring creep (Figure 1.5a), which involves defect diffusion within a crystal lattice (Herring, 1950; Nabarro, 1948), and Coble creep (Figure 1.5b), which involves defect diffusion along the grain boundaries (Coble, 1963). As grain boundaries possess a less ordered structure than the lattice, the grain-boundary diffusion rate is usually faster than the lattice diffusion rate. This is related to a larger amount of defects in grain boundaries in comparison to the lattice, rather than an increase in their mobility (Uberuaga et al., 2015). Independent of the diffusion path, grain boundaries act as sources or sinks for vacancies. This explains the grain-size sensitivity of diffusion creep and the major control of grain boundaries on the deformation rate in this deformation regime. Furthermore, in order to maintain material continuity, diffusion creep must always occur together with grain-boundary sliding (Stevens, 1971), another deformation process involving grain boundaries.

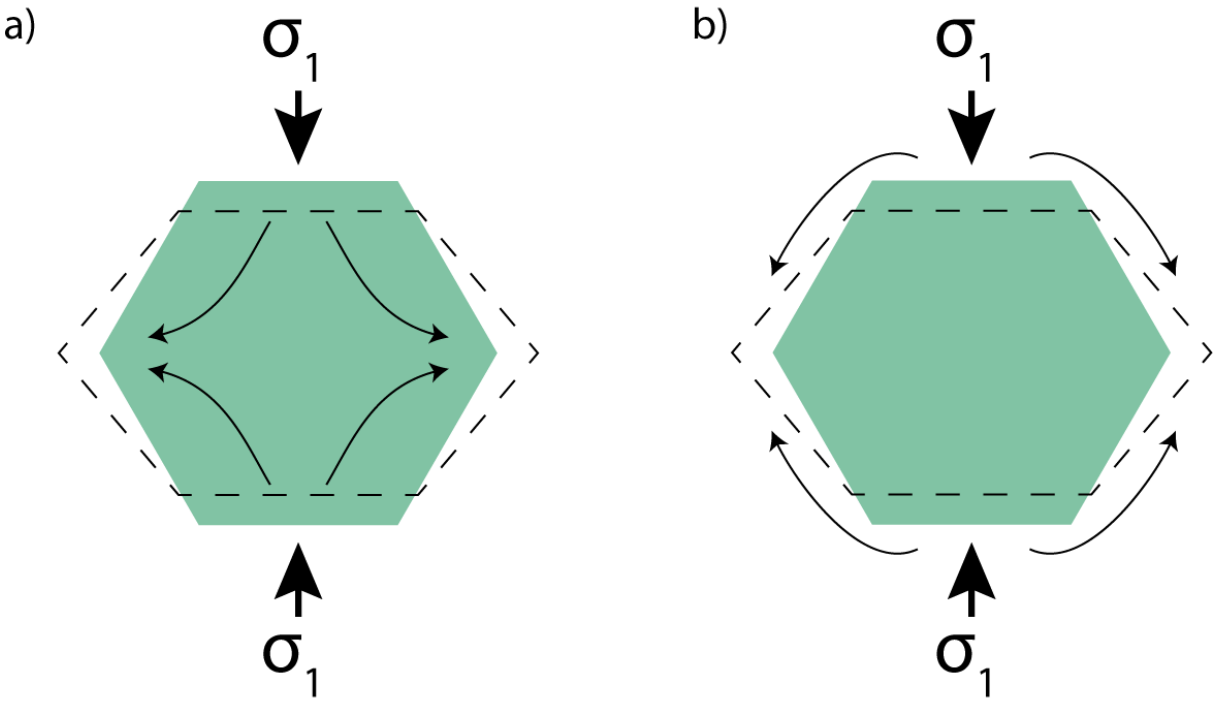

Figure 1.5: Deformation through diffusion creep: a) Nabarro-Herring creep (bulk diffusion) b) Coble creep (grain boundary diffusion). Dashed polygon indicates the change in the shape of a grain due to transfer of matter from compression to tension regions. Arrows indicate the flow of matter (atomic diffusion). Motion of vacancies occurs in the opposite sense of the arrows.

1.2.3 **Grain-boundary sliding**

Deformation by grain-boundary sliding involves the relative motion between grains parallel to their grain boundaries (Figure 1.6). The main mechanism for grain-boundary sliding was proposed to be the motion of grain-boundary dislocations (Ishida and Brown, 1967; Lim and Raj, 1985; McLean, 1971; Pond et al., 1978a; Pshenichnyuk et al., 1998). In this model, grain-boundary sliding occurs as a result of a mixture of climbing and gliding of dislocations in the grain boundary, causing relative motion and/or rotation of the grains (Ishida and Brown, 1967). Dislocation glide in the grain-boundary plane requires the Burgers vectors of those dislocations to be parallel to the grain-boundary plane, and thus dissociation of the dislocations is usually necessary as dislocations enter the grain boundaries. If the Burgers vector of a dislocation is not parallel to the grain boundary, the movement of the dislocation requires climb and thus absorption and/or emission of vacancies. This process is diffusion-controlled and therefore thermally activated. Langdon (1994) proposed two distinct types of grain-boundary sliding: Rachinger sliding, in which grain-boundary sliding (GBS) is

accommodated by intragranular movement of dislocations (disGBS; Figure 1.6a), and Lifshitz sliding, in which GBS is accommodated by the diffusion of vacancies (difGBS; Figure 1.6b). For Rachinger sliding, Langdon (1994) proposed that the rate of sliding is dictated by the climbing rate of lattice dislocations at obstacles such as grain boundaries or subgrain boundaries. Therefore, the overall strain rate and the macroscopic response would depend on the total number of dislocation-boundary interactions (Langdon, 2006, 1994, 1970). For Lifshitz sliding, Raj and Ashby (1971) proposed that the stresses developed due to sliding in a non-perfectly planar boundary create a concentration gradient of vacancies in a boundary. This results in a diffusional process which might be the rate-controlling mechanism during deformation. As highlighted by Raj and Ashby (1971), the generation of local stresses, being the driving force for difGBS, is highly dependent on the grain-boundary geometry.

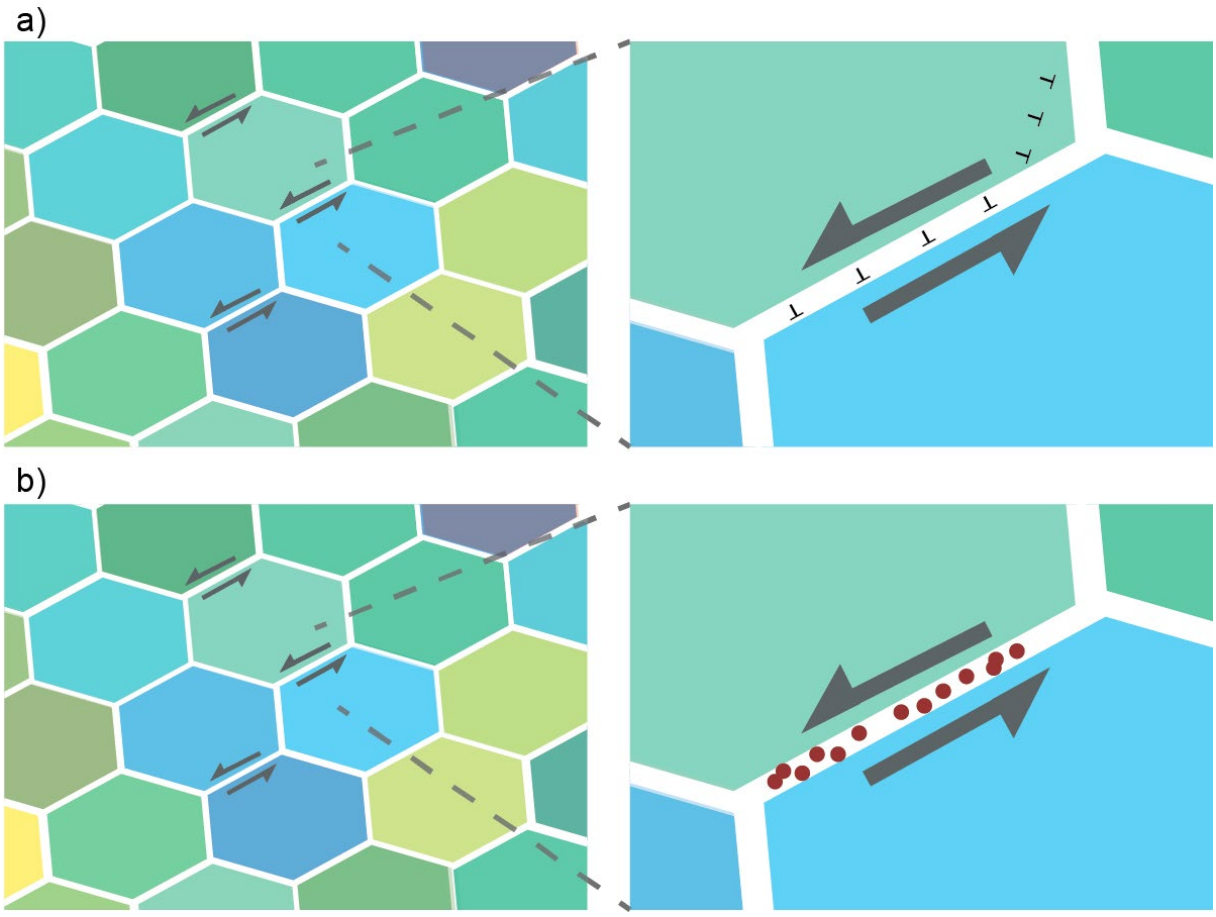

Figure 1.6: Deformation through grain-boundary sliding: a) Dislocation-accommodated grain-boundary sliding (disGBS) b) Diffusion-accommodated grain-boundary sliding (difGBS). Arrows indicate relative motion between grains.

1.2.4 **Grain-boundary migration and grain growth**

Grain growth is an important part of the sintering and densification processes in crystalline materials. Grain growth in polycrystalline materials occurs by the migration of grain boundaries (Atkinson, 1988; Burke and Turnbull, 1952; Evans et al., 2001). Grain growth occurs by the growing of larger grains at the expense of smaller ones, leading to a modification of the overall grain-size distribution towards larger grain sizes. Driving forces for grain growth include gradient in dislocations (strain-driven grain-boundary migration), grain-boundary curvature (static grain growth) and magnetic fields. Normal (static) grain growth occurs by the minimization of the excess Gibbs-free energy associated with grain boundaries in comparison to a crystal lattice. In other words, grain growth towards a single-crystal material is energetically favourable over maintaining a polycrystal. In reality, however, grain growth is limited by several factors, such as:

1. The bulk energy reduction of the system lessens with increasing average grain size;
2. Impurities impeding grain growth, i.e., solute drag (e.g., Liu and Kirchheim, 2004);
3. Grain-boundary smoothing (e.g., Holm and Foiles, 2010).

Grain-boundary migration rates are not only a function of the driving force but also its mobility. The grain-boundary mobility, in turn, is highly dependent on the structure and the composition of the grain boundaries (Gottstein and Shvindlerman, 2009).

When a second phase exists, grain growth of the primary phase is hindered by a drag force caused by the second phase. This effect is known as Zener drag or Zener pinning (e.g., Nes et al., 1985). When grain growth of the second phase also occurs, the grain growth processes is called coalescence (Hillert, 1965). The presence of a second-phase particle might lead to abnormal grain growth, where certain grains grow abnormally larger than the average grain size. Another motivation for abnormal grain growth is the presence of grain boundaries with different (anisotropic) mobilities (e.g., Rollett and Mullins, 1997).

1.3. Olivine grain boundaries: structure and composition

Processes occurring at the grain boundaries such as the motion of dislocations and vacancies are highly dependent on the structure and composition of the grain boundaries (Sutton and Balluffi, 1995). The structure and composition of olivine-dominated rocks have been subject of several studies, as reviewed by Marquardt and Faul (2018). The thickness of grain boundaries is an important aspect of the structure of grain boundaries, as it controls grain-boundary segregation and diffusion (Carter and Sass, 1981). Olivine grain boundaries typically show a structural width (distance between two neighbouring lattices) on the order of 0.5 - 1 nm (Ricoult and Kohlstedt, 1983).

Another important aspect controlling processes at the grain boundaries is the crystallography of grain boundary planes (e.g., Atkinson, 1985; Watanabe, 1988). Previous studies show that specific grain boundaries of olivine are preferentially developed during static grain growth (Marquardt et al., 2015; Marquardt and Faul, 2018). Marquardt et al. (2015) found that the distribution of grain boundary planes in forsterite with a small amount of Al are dominated by (100), (010) and (001) grain boundary planes, while Marquardt and Faul (2018) found that highly pure forsterite aggregates show a dominance of (001) GB planes. These results suggest that grain boundaries with low energy, such as (100), (010) and (010) in olivine (Adjaoud et al., 2012), are preferentially developed. This inverse correlation between grain-boundary energy and population was previously demonstrated in ceramic materials such as MgO (e.g., Rohrer, 2011; Saylor et al., 2002).

The presence of preferential grain boundaries of olivine might have a great effect on the rheology of the upper mantle and its interpretation from geophysical measurements. For example, Miyazaki et al. (2013) suggest that grain-boundary sliding occurs preferentially along low-energy grain boundaries (e.g. (001) and (010) planes). The authors suggest that the development of these grain boundaries would influence the development of CPO in olivine, leading to the observed seismic anisotropy in the Earth's upper mantle. Different grain boundaries might have different grain-boundary diffusivities, which by its turn affects diffusion creep and grain growth. For instance, molecular-dynamic simulations demonstrate that Si, O and Mg ions in a melt with composition close to $MgSiO_3$ have higher self-diffusion coefficients in the

vicinity of (010) grain boundaries of Forsterite when compared to (100) and (001) grain boundaries (Gurmani et al., 2011). Grain boundaries presenting higher diffusivities are also more electrically conductive, if the mechanism controlling the transport of charges is the diffusion of vacancies or interstitials at the grain boundaries (Misener, 1973; ten Grotenhuis et al., 2004). In fact, Pommier et al. (2018) demonstrated that the alignment of olivine grain boundaries increases electrical conductivity in experimentally-deformed samples. The authors suggested that, during deformation in the dislocation creep regime, specific grain boundaries presenting higher conductivity were created, greatly increasing bulk conductivity when compared to undeformed aggregates. Thus, the study of processes that lead to the development of olivine grain boundaries is essential for an improved interpretation of geophysical measurements of electrical conductivity of the Earth's upper mantle.

Grain boundaries in upper mantle rocks are also subject to study due to its capacity to store and mobilize chemical elements which are incompatible in the lattice structure. This has motivated several studies on the composition of grain boundaries, which were mostly focused on the characterization of non-stoichiometric impurities (including volatiles) at grain boundaries such as C, Ca, Al, Sr, and H_2O (e.g., De Hoog et al., 2010; Demouchy, 2010; Hayden and Watson, 2008; Hiraga et al., 2002, 2003, 2004; Bachhav et al., 2015). The effect of H_2O (as H^+ or OH^-) in olivine either at grain boundaries or within the lattice is a subject of great discussion (e.g., Bai and Kohlstedt, 1992; Berry et al., 2005; Bolfan-Casanova, 2005; Demouchy, 2010; Demouchy and Bolfan-Casanova, 2016; Gardés et al., 2012; Hirth and Kohlstedt, 1996; Karato and Jung, 1998; Karato, 2003; Karato et al., 1986; Kohlstedt et al., 2012, 1996; Mackwell and Kohlstedt, 1990; Nicholls and Ringwood, 1973; Ohtani, 2005; Wang et al., 2006). The presence of water reduces the melting temperature (solidus) of mantle rocks (Hirth and Kohlstedt, 1996), controls phase transformations (e.g., Frost and Dolejš, 2007), and is argued to lower the creep strength while increasing chemical diffusivity in olivine-dominated rocks (Jung, 2001; Jung et al., 2006; Karato et al., 1986; Mackwell et al., 1985; S Mei and Kohlstedt, 2000; S. Mei and Kohlstedt, 2000). However, more recent studies suggest that water has little or no effect on the upper mantle rheology, assuming that creep is rate-limited by dislocation climb (Fei et al., 2014, 2013). All the same, grain boundaries are argued to be an important deposit of incompatible elements, such as potassium, thorium and uranium, that are transported and concentrated at shallower portions of the Earth during melt percolation (Hiraga et al.,

2004). According to these authors, chemical segregation has a large impact on grain-boundary processes such as grain-boundary diffusion, sliding, fracture and migration. For instance, Yabe et al., (2020) found that the segregation of Ca and Al at the grain boundaries of olivine enhances the rates of interface-controlled creep and diffusion creep. This leads to contrasting physical properties between these aggregates and pure olivine, thus changing our understanding of the physical properties of the Earth's mantle.

Chapter 2: Methods

2.1. Sample preparation

Polycrystalline aggregates composed of olivine with small amounts of orthopyroxene (corresponding to dunite and lherzolite) were produced by two different methods: Grinding olivine crystals and by synthesizing through the solution-gelation method. The first method involves selecting single crystals of olivine which are optically free of inclusions. The crystals were then ground in an agate mortar and hot pressed using the piston cylinder for 12 hours at 1200 °C and 0.7 GPa. As this method involves natural samples, a greater control on the purity of the sample cannot be ensured. On the other hand, the solution-gelation (sol-gel) method is an effective technique to create chemically pure and homogeneous solids (Hench and West, 1990). The sol-gel method involves the formation of a colloidal solution from inorganic and/or organic reactants, the gelation of the solution and the removal of the solvent (Brinker and Scherer, 2013). The sol-gel method can be employed for the preparation of starting materials of different compositions, including ceramic materials such as SiO_2, Al_2O_3, K_20, NaO, CaO, MgO and FeO, which are constituents of most of the rock-forming minerals present in the Earth's crust and mantle. When compared to other methods of fabrication of starting material such as glass fabrication, mixing of oxide powder and mineral/rock grinding, the sol-gel method produces materials with very small grain sizes in a narrower grain-size distribution. Because of these characteristics, the sol-gel method was employed in this study. The preparation technique used here is based on the method B of Edgar (1973, p. 57) and the olivine sol-gel preparation described by Tan et al. (2001), Jackson et al.(2004) and Faul & Scott (2006). The precursors used as source of SiO_2, MgO and FeO were respectively tetraethyl orthosilicate (TEOS, $Si(OC_2H_5)_4$, Sigma-Aldrich, purity ≥ 99.0%), magnesium nitrate hexahydrate ($Mg(NO_3)_2 \cdot 6H_2O$, Roth, purity ≥ 99.999%) and Iron (III) nitrate nonahydrate (Fe(NO3)3 · 9H2O, Sigma-Aldrich, purity ≥ 98%). The yielding of each reactant was first analysed. The yield of SiO_2 and MgO reactants were estimated by gravimetric analyses and the yield of FeO by titration. The amount of source material was then

calculated to obtain olivine with a Mg/Fe mole ratio of 9:1, that is, of Fo_{90} composition. An excess of ~5 wt.% SiO_2 was included to buffer Si activity, creating a small percentage of orthopyroxene with similar Mg/Fe mole ratio of olivine, that is of En_{90} composition. For an increasing amount of pyroxene, smaller average grain sizes of olivine and pyroxene are produced (e.g., Nakakoji and Hiraga, 2018; see also Chapter 5). In this study, two batches of aggregates were created containing 6 vol.% (FSG4 batch) and 13 vol.% of pyroxene (FSG5 batch). The average grain size of olivine after sintering was 2.6 μm and 3.1 μm for the batches FSG4 and FSG, respectively (see Section 5.3.1).

The synthesis process was started by weighing the required Fe and Mg nitrates. The nitrates were mixed in a beaker with a solution of 1:1 distilled water/ HNO_3, just enough that the nitrates were completely dissolved and no supernatant product is visible. Any excess of HNO_3 should be evaporated before adding TEOS/ ethanol, as the reaction with ethanol is highly exothermic. The required TEOS was weighed and mixed with ethanol with a volume twice of that of TEOS. The TEOS/ethanol is added into the beaker and the solution was constantly stirred until a homogeneous solution is obtained. Ammonia (NH_4OH) was then added drop-wise to the solution while stirring until a stiff gel was obtained. The solution was then left for 12 hours at room temperature to ensure a complete gelation process. The gel was heated slowly in a hot plate under a fume hood up to 70 °C, and left until it was dry (Figure 2.1a). The gel was then grounded and placed in a platinum crucible. The gel was subsequently heated for 24 hours at 110 °C in a furnace under a fume hood. The temperature was then increased at a rate not higher than 60 °C/hour up to 400 °C. The gel was dried at this temperature for one more day or until all the fumes of N-oxides disappear. The resulting powder was left to cool down and then grounded in an agate mortar with ethanol for at least 15 minutes. The fine powder was then dried under infrared light for approximately 10-30 minutes. The powder was later cold pressed into pellets in a stainless-steel die together with a few drops of ethanol at a confining pressure of approximately 150 MPa, for 3 minutes. The pellets were removed from the pressure vessel and left to dry: first at room temperature and then for at least 1 hour at 125 °C. The pellets were then placed in a Pt cage for sintering at controlled oxygen fugacity in a gas-mixing furnace. The oxygen fugacity (fO_2) in the gas-mixing furnace is controlled by mixing CO and CO_2 gases, which react according to the following equation:

$CO + 0.5O_2 \leftrightarrows CO_2$. (2.1)

At chemical equilibrium, the oxygen fugacity is given by (Fegley Jr, 2012):

$$fO_2 = {K_P}^{-2} \left[\frac{X_{CO_2}}{X_{CO}}\right]^2_{eq} \quad (2.2)$$

where K_P is the temperature-dependent equilibrium constant and X_n the mole fraction of the reacting gases. The temperature in the gas mixing furnace, monitored by a thermocouple, was increased from 700 °C to 1400 °C at a rate not higher than 300 °C/hour. As the temperature increases, the gas mixing ratio was adjusted to keep olivine in its oxygen fugacity stability field (Nitsan, 1974).

The final calcination temperature and gas mixing ratio was kept for 12 hours to ensure complete reaction. The furnace power was then turned off. As the temperature decreases, the gas-mixing ratio was continuously adjusted to keep the sintered olivine in its oxygen-fugacity stability field. When the temperature reached 700 °C, the supply of CO gas was turned off and the pellets were removed from the furnace, while being flushed by CO_2 gas. The pellets were left to cool down, their surface slightly ground with a paper filter to remove the oxidation layer and/or carbon deposition at the surface, re-ground in an agate mortar and kept in an oven at ~ 125 °C or in a desiccator until use. Olivine was sintered in a piston-cylinder apparatus at a confining pressure of 0.7 GPa and temperature of 1200 °C for 2 hours. The samples were then cored in dimensions to be used for the static (multianvil) and deformation experiments (Figure 2.1b). To ensure that the samples were dry, the cores were fired in the gas mixing furnace for 1 hour at 1000 °C in a controlled atmosphere before encapsulating.

a) b)

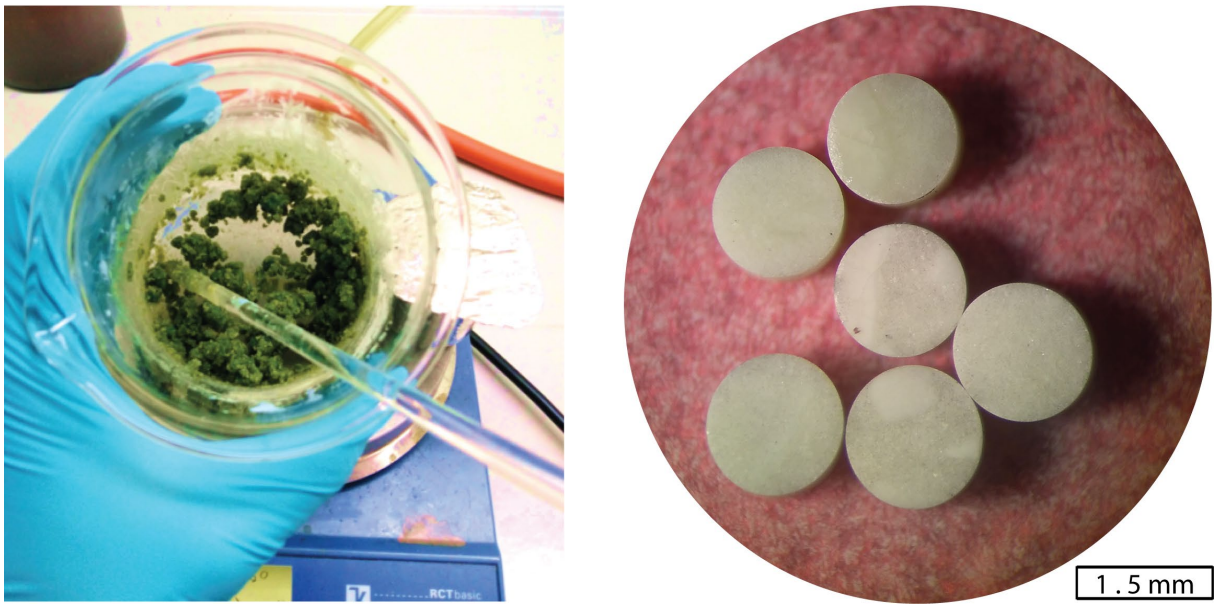

Figure 2.1: Olivine sol-gel preparation: a) Gel obtained after the drying of the solvents in a hot plate. b) Resulting cores of olivine aggregates prepared for deformation experiments.

2.2. High-pressure techniques

Experiments at the pressure and temperature conditions of the Earth's interior can nowadays be routinely achieved with the aid of high pressure and temperature apparatuses. In these devices, high pressure is created by applying large forces to small areas. In this work, we used different apparatuses to synthesize starting materials and to conduct static and deformation experiments. Each apparatus used here has specific characteristics such as the temperature and pressure range (Figure 2.2) that make it suitable for a given application. For the deformation experiments, the possible geometries of deformation, the maximum amount of strain and the possibility to measure differential stresses are also of interest. The main features of each apparatus, and how the experiments were carried out in each of them, are described in the following sections.

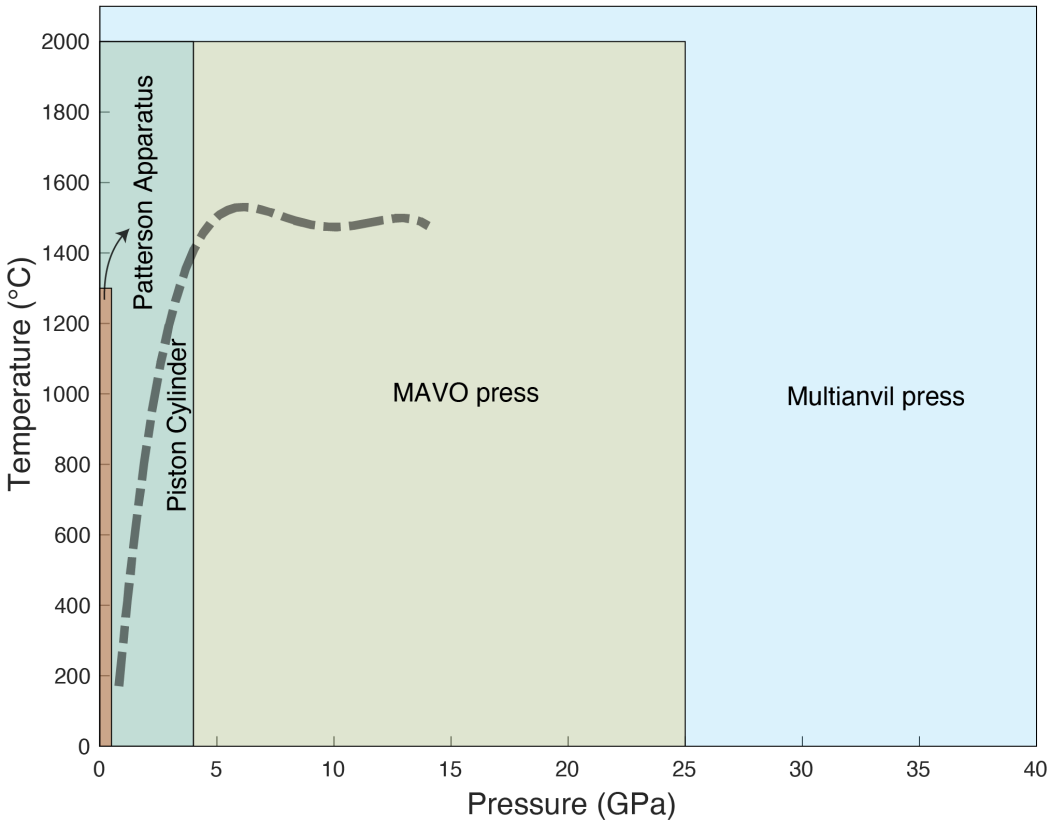

Figure 2.2: Pressure and temperature range of the techniques used in this study. The dashed line shows the upper mantle geotherm. Pressure and temperature as a function of depth is obtained from Dziewonski & Anderson (1981) and Anderson (1980), respectively.

2.2.1 **Piston Cylinder**

The piston-cylinder apparatus consists of a tungsten carbide/ steel pressure vessel (Boyd and England, 1960). Pressure is achieved by uniaxially compressing the assembly between a tungsten carbide piston surrounded by steel (master ram) at the bottom, and a steel ram (end load) at the top. Hydrostatic pressure is reached due to the low-strength materials used as pressure media, such as salt or glass. The nominal pressure inside the assembly is calculated by measuring the oil pressure applied by the hydraulic pump and knowing the cross-sectional area of the piston. A correction is applied to account for friction and shear within the assembly and the pressure vessel. This correction value is smaller than 5% of the nominal pressure in high-temperature experiments (Edmond and Paterson, 1971; McDade et al., 2002). Heating is done by supplying electrical power through the pressure vessel to a resistance furnace inside

the assembly. The temperature is monitored by a thermocouple with its measuring (hot) junction close to the sample.

In this study, the piston-cylinder apparatus was used for static experiments and to prepare the starting material for deformation and static experiments. The piston-cylinder experiments were conducted using a 19 mm talc/*Pyrex*® assembly (Figure 2.3). The starting material powder was hammered into a $Ni_{80}Fe_{20}$ capsule. The $Ni_{80}Fe_{20}$ capsule is used to buffer the oxygen fugacity within the Ni-NiO buffer. The small amount of iron in the capsule prevents diffusional exchange between Ni from the capsule and Fe from the sample (e.g., Faul et al., 2018). The capsule is welded shut and the excess weld tips are grinded. The capsule is tightly fitted into a porous (machinable) Al_2O_3 sleeve, which is surrounded at the top and bottom by tapered pistons of porous Al_2O_3, and radially outwards by a graphite furnace, borosilicate glass (*Pyrex*®) and the talc pressure media, respectively. Temperature was monitored during the experiments with an S-type (90%Pt/10%Rh–Pt) thermocouple. The experiments were performed by adjusting pressure to the target pressure, heating the sample to the target temperature at a 100 ºC/minute rate and maintaining these conditions for the duration of the experiment. The samples were quenched by reducing the current in the sample heater to achieve a temperature reduction of 300 °C per minute. This step reduces thermal shock in the sample and subsequent fracturing of grains. The pressure was subsequently reduced over 8 hours. In the experiments performed here, uncertainties in pressure for the 19 mm piston-cylinder assembly are on the order of 0.02 GPa and thermal gradients are around 25ºC within the sample (Watson et al., 2002).

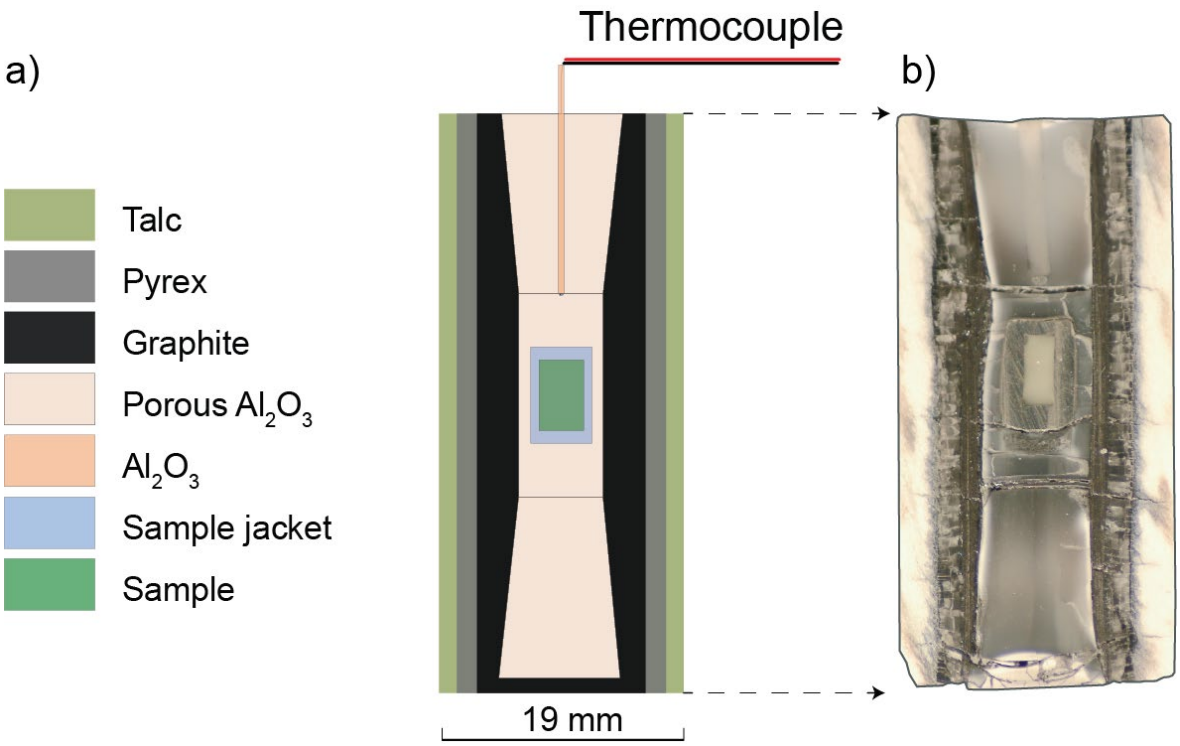

Figure 2.3: Piston-cylinder assembly: a) Cross section of the 19 mm piston cylinder assembly. b) Recovered sample after the experiment.

2.2.2 **Multianvil press**

The attainable pressure in the piston-cylinder apparatus is limited due to the compressive strength of the pressure vessel materials (e.g., steel). Although multianvil presses also rely on uniaxial presses to reach high pressures, the presence of anvils provides lateral support to the assembly. This allows multianvil presses to reach pressures much higher than the compressive strength of its anvils (Ito, 2007; Liebermann, 2011). In this study, I used a 6-8 Kawai-type multianvil, which is capable of a load of 5000 ton (Frost et al., 2004).

The multianvil experiments were performed using second-stage WC anvils of 11 mm truncated edge length, acting on a Cr_2O_3-doped MgO octahedra (Figure 2.4) with an edge length of 18 mm. The experiments in the multianvil were performed in analogy to the piston-cylinder experiments, except that a longer decompression duration of at least 12 hours was necessary. The temperature in the multianvil experiments was monitored using a D-type (97%W/3%Re–75%W/25%Re) thermocouple. Uncertainties in pressure determination for the 18/11 multianvil assembly for the experiments shown here are around 0.5 GPa and thermal gradients in the order of 40 ºC within the sample

(Walter et al., 1995). No correction was applied for the pressure effect on the electromotive force (emf) of the thermocouple.

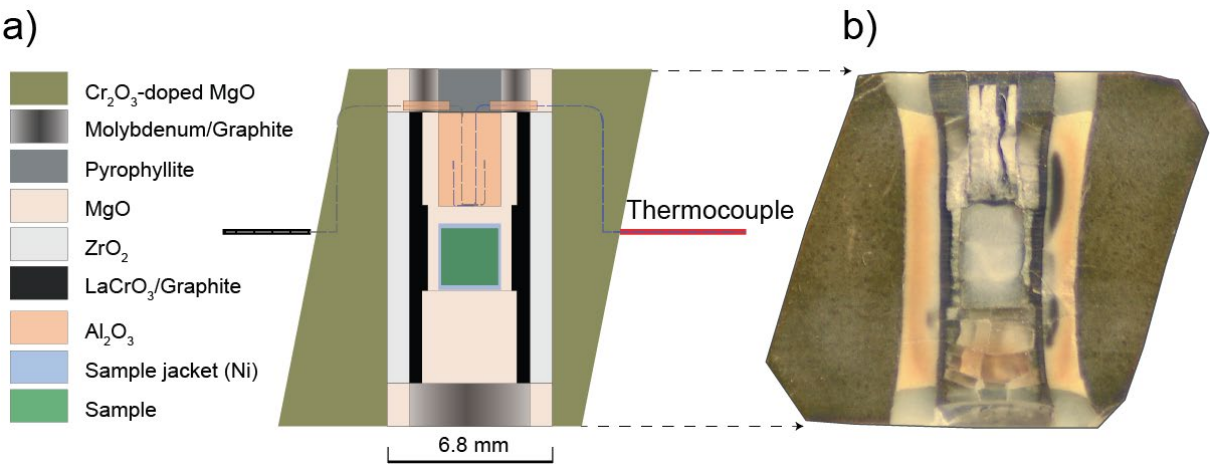

Figure 2.4: Multianvil assembly: a) Cross section of the 18 mm octahedra . b) Recovered sample after the experiment.

2.2.3 **6-ram MAVO press**

The *MAVO LPQ6-2400-100* press (*Voggenreiter Verlag GmbH*) is a large-volume multianvil system composed of six independent hydraulic rams (Bollinger et al., 2019; Laumonier et al., 2017; Manthilake et al., 2012; Soustelle and Manthilake, 2017; Walte et al., 2020). This press is capable of reaching forces up to 8 MN at a maximum oil pressure of 630 bar (Manthilake et al., 2012). The six mutually orthogonal rams (Figure 2.5a) act on second stage anvils made of cylindrical cores of tungsten carbide fitted into hardened steel rings, which are surrounded by brass (Figure 2.5b). In the 5/8 design, the second stage anvils present a 5 mm edge length that acts on a cube with an edge length of 8 mm with a square truncation area of 25 mm^2 (Figure 2.5b and Figure 2.5c). The sample is placed in a Ni capsule filled with NiO at the top and bottom, thus limiting the oxygen fugacity of olivine by the Ni-NiO buffer. Alumina pistons are placed at the bottom and top of the sample. Porous alumina is used at the bottom to minimize deviatoric stresses before the target pressure is reached. The upper alumina piston has 4 holes designed to fit a thermocouple with the hot junction sitting on the top of the sample. The sample and the pistons are fitted into a pre-sintered MgO confining sleeve, surrounded by a graphite furnace. Molybdenum electrodes transmit the electrical current from the anvils to the furnace. A ZrO_2 sleeve is used for thermal

insulation of the assembly. The pressure medium is composed of pre-fired pyrophyllite ($Al_2Si_4O_{10}(OH)_2$). Pyrophyllite gaskets of 2.1 mm thickness are placed between the anvils to ensure that hydrostatic pressure is achieved while minimizing friction between the anvils. Balsa wood spacers are used for support and alignment of the anvils. A type-D thermocouple (97%W/3%Re–75%W/25%Re) was used to measure the experimental temperature. The second-stage anvils and assembly are placed in an aluminium cage and centred with the first-stage anvils.

The deformation experiments are carried out by first reaching the target pressure. During this initial compression stage, the hydrostatic pressure is increased linearly over a duration of 30 to 60 minutes. This is achieved by the advancement of the master ram (e.g. ram 1) following the assigned pressure profile, while the remaining rams advance towards the deformation assembly, maintaining the cubic geometry of the assembly. The position of the anvils is measured by displacement sensors with an accuracy of 0.001 mm. This procedure minimizes deviatoric stress and deformation of the assembly during the initial compression. Subsequently, the sample is heated to the target temperature at a rate of 100 ºC/minute. The sample is kept at the target pressure and temperature for 20 minutes. This procedure allows for microstructural recovery before the deformation experiment is started.

The deformation experiment is conducted during an experimental duration, *t*, which is the time needed to reach a total (engineering) strain ε, at a given strain rate, $\dot{\varepsilon}$, given by:

$$t = \frac{\varepsilon}{\dot{\varepsilon}} \tag{2.3}$$

The deformation of the assembly in a pure-shear geometry is done by simultaneously pushing two opposing anvils towards the sample along the compression axis (e.g., rams 3 and 4) and retracting two other opposing anvils (e.g., rams 5 and 6) away from the deformation assembly, while the last pair (e.g., rams 1 and 2) maintains the confining pressure. The position of the anvils is computer-controlled to maintain a constant anvil-displacement rate (i.e., constant strain rate). The displacement rate ($\dot{h}$) is calculated using the following relation:

$$\dot{h} = \frac{\Delta l}{t} \tag{2.4}$$

where Δl is the shortening length given by:

$$\Delta l = \varepsilon \times l_0 \quad (2.5)$$

where l_0 is the initial sample dimension along the compression axis.

The experiment is finished by stopping the deformation, quenching the experiment and decompressing. During decompression, further deformation of the sample is minimized by reducing the load applied by the master ram (e.g. ram 1) over a period of at least 8 hours. The remaining rams retract at the same rate as the master ram, keeping the final geometry of deformation.

Because the different parts of the assembly partially accommodate the total deformation, the actual strain rate, $\dot{\varepsilon}$, experienced by the sample is equal or smaller than the anvil displacement rate, $\dot{h}$. The total shortening length is calculated by measuring the sample before the experiment using a calliper and after the experiment via SEM images. The measurement uncertainty of the calliper is of 0.005 mm, which places the uncertainty in the shortening length determination of 0.7% for a typical l_0 of 0.7 mm. The applied (steady-state) stress might be estimated through empirical calibrations. For instance, the differential stress ($\boldsymbol{\sigma}$) is related to the density of dislocations (ρ), through the following relation (Takeuchi and Argon, 1976):

$$\boldsymbol{\sigma} = \alpha \mu b \rho^{1/2} \quad (2.6)$$

where α is a material's constant, μ is the shear modulus and $\boldsymbol{b}$ is the Burgers vector, which for olivine equals to 3, 60 GPa and 0.5 nm, respectively (Durham et al., 1977; Kohlstedt and Weathers, 1980). The density of dislocations in olivine can be assessed by various methods such as TEM imaging (e.g. Goetze and Kohlstedt, 1973), EBSD (e.g., Wallis et al., 2016), and by optical or scanning electron microscopy after oxidation decoration of Fe-bearing olivine (e.g., Kohlstedt et al., 1976). Other paleostress scales for olivine include recrystallized grain and subgrain sizes (e.g. Jung and Karato, 2001; Twiss, 1977; Van der Wal et al., 1993).

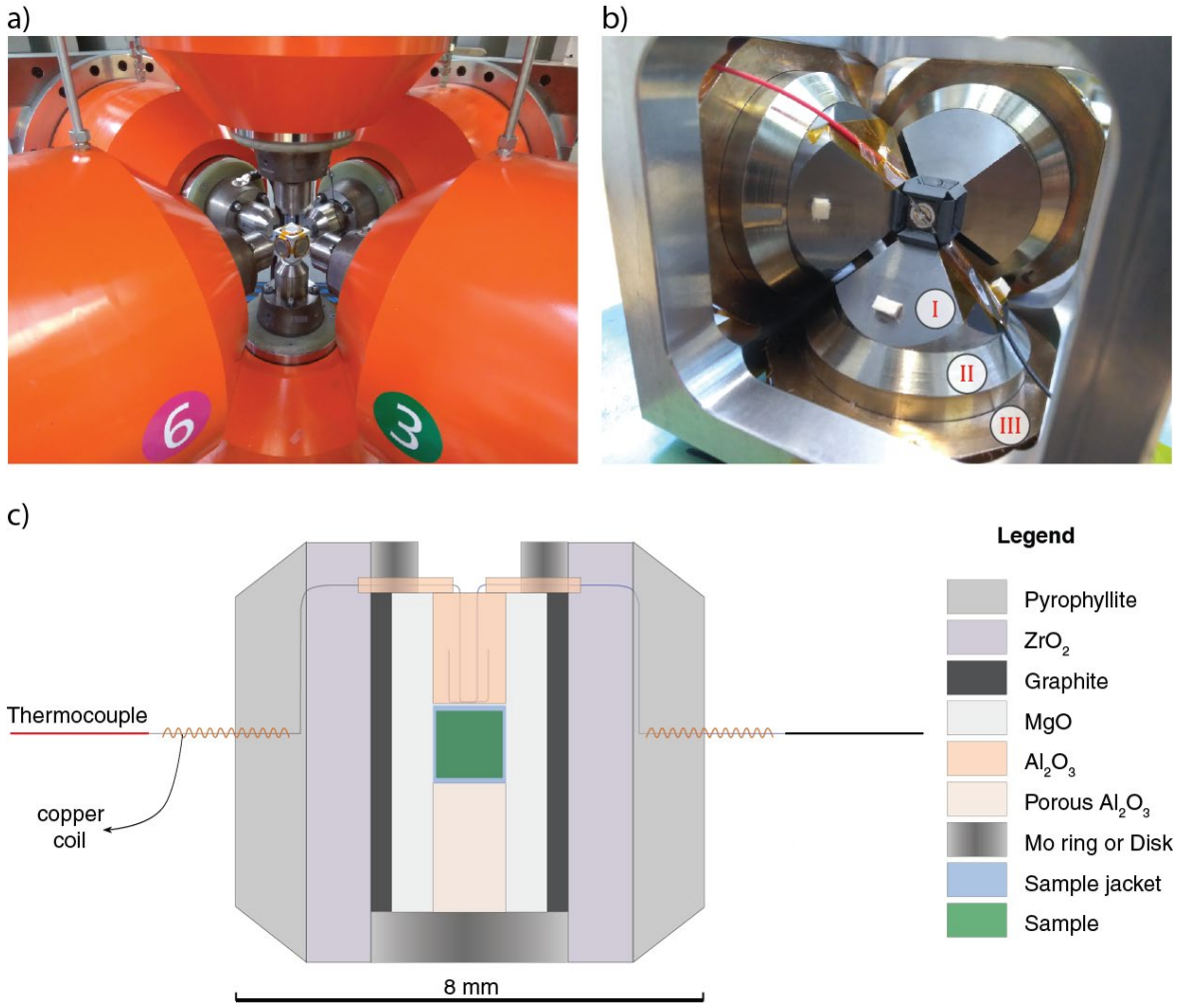

Figure 2.5: Deformation experiments using a MAVO press: a) Cubic arrangement of rams with the deformation assembly at the centre. b) Deformation assembly surrounded by the second-stage anvils. The second stage-anvils are consist of a tungsten carbide core (I) surrounded by hardened steel (II) and brass (III). c) Schematic drawing of the deformation assembly used for pure shear experiments at the MAVO press.

2.2.4 **Paterson apparatus**

Although experimental deformation using solid pressure media (as in section 2.2.3) has the advantage of providing large hydrostatic pressures, retrieving rheological information might not be straightforward. For example, estimations of shear stress requires either ex-situ analyses of resulting microstructure (e.g., Kohlstedt et al., 1976) or the use of synchrotron light (e.g., Li et al., 2004). The Paterson apparatus (Paterson, 1970; Paterson and Olgaard, 2000) involves the pressurization of a sample in an inert gas medium (such as Argon). As friction is reduced between the gas-solid interface, shear stresses can be directly calculated from the applied load (uniaxial compression) or torque (torsion). The Paterson apparatus consists of a pressure vessel oriented

vertically, where the torque and axial forces are transmitted to the sample via external actuators (Figure 2.6). Experiments in torsion geometry, as reported in Chapter 4, can be performed under displacement control (constant strain rate) or torque control (constant stress). This is done by using a servo-motor to control the twist rate and the torque applied to a cylindrical sample. The strain, γ, increases linearly from the torsion axis centre towards the outside surface of the sample. At a given radius, r, the strain is given by:

$$\gamma = \frac{r\,\theta}{l} \tag{2.7}$$

where θ is the angular displacement (twist amount) and l is the sample's length (Figure 2.6). The displacement or twist rate, $\dot{\theta}$, is related to the maximum strain rate, $\dot{\gamma}_{max}$, experienced by a sample through:

$$\dot{\theta} = \left(\frac{2l}{d}\right)\dot{\gamma}_{max} \tag{2.8}$$

where d is the sample's diameter. The torque, *M*, by its turn, is related to the shear stress, τ, by the following relation for a solid cylinder during power-law creep with a stress exponent *n*:

$$M = \frac{\pi\, d^3\, \tau}{4(3+1/n)} \tag{2.9}$$

The samples analysed in Chapter 4 were obtained from the experiments PT0535 (starting material) and PT0499 (deformed sample) performed by Hansen et al. (2012a, 2012b) at the University of Minnesota, USA. The starting material for these experiments, Fo_{50} ($MgFeSiO_4$), was prepared by hot-pressing mixtures of synthetic Fayalite (Fe_2SiO_4) and San-Carlos olivine ($Mg_{1.82}Fe_{0.18}SiO_4$) at 1250 ºC and 0.3 GPa for 8 h. The PT0499 sample was deformed at 1200 ºC, confining pressure of 0.3 GPa, under constant stress of 97 MPa, and maximum strain of 10.9. Uncertainties in temperature, pressure, and shear stress determination are of 2ºC, 1 MPa and 3 MPa, respectively.

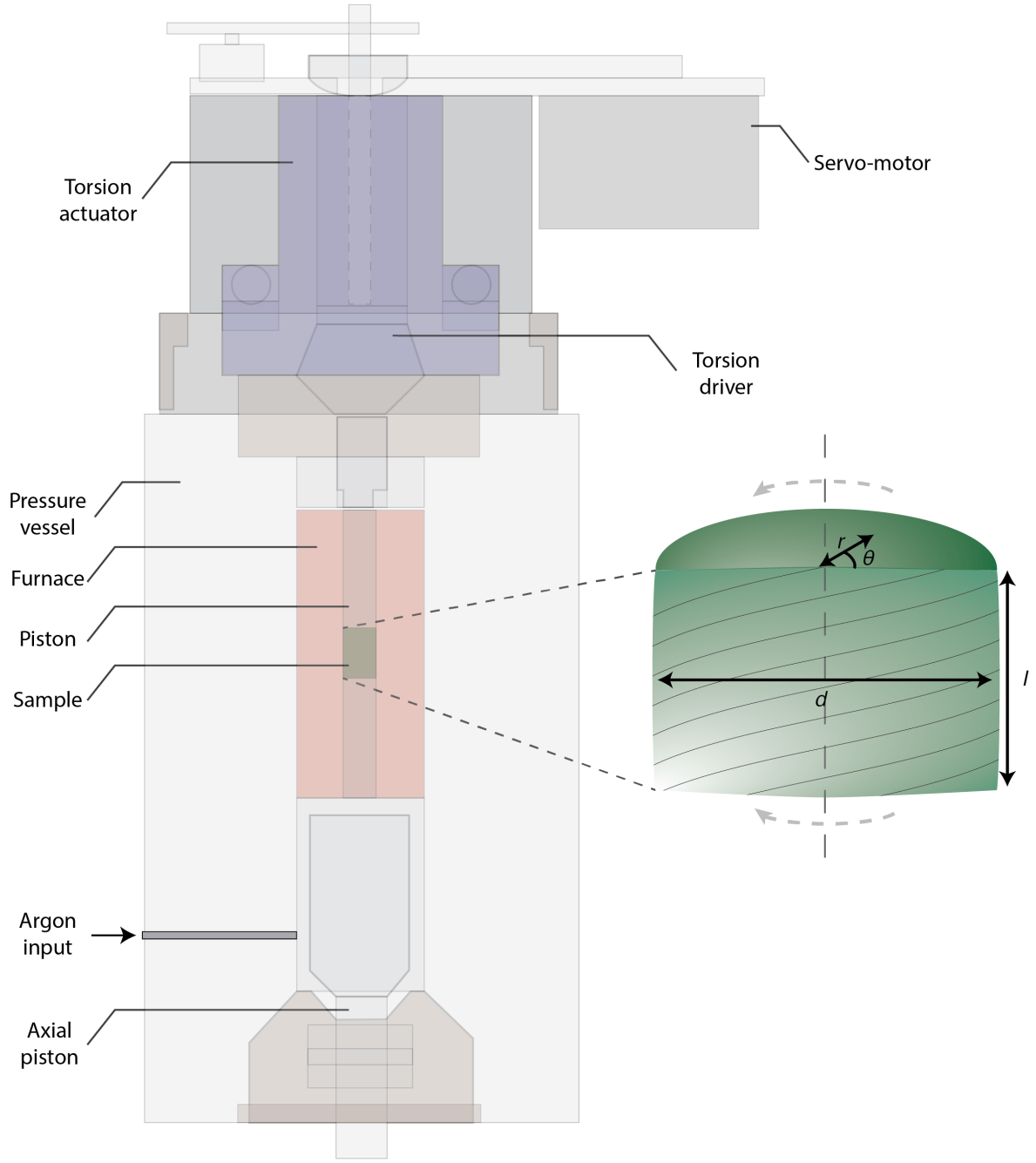

Figure 2.6: Schematics of the Paterson apparatus and geometric parameters of a sample deformed in torsion. Modified from Paterson & Olgaard (2000)

2.3. Analytical techniques

Rheology is a complex function of the ambient conditions during deformation (e.g., temperature, pressure, stress, strain rate) and the structure and composition of a material. For example, the composition (including the presence of fluids), and

arrangement of minerals (i.e., microstructure) dictates the processes and rates of rock deformation in the Earth's crust and mantle (e.g., Bürgmann and Dresen, 2008; Hirth and Kohlstedt, 2003). Hence, various analytical techniques are employed to characterize samples and to evaluate the effect of different variables on rock deformation. Here we use electron microscopy and spectroscopy techniques to investigate microstructures down to a nanometre scale, as well as the water content and chemical composition of the samples. In the next sections, I describe the analytical techniques employed in this work and how the analyses were performed.

2.3.1 **Electron-backscatter diffraction**

Electron-backscatter diffraction (EBSD) is a scanning electron microscopy (SEM)-based technique that allows the analyses of crystal orientations of a single crystal or polycrystalline materials. In a SEM, an electron beam is accelerated towards a sample and multiple interactions between the electron beam and the sample's atoms might occur (Goldstein et al., 2018; Prior et al., 1999). Electrons interact with the sample and deviate from their initial trajectory (scatter) elastically or inelastically. During elastic scattering, the energy of the electron beam is mostly maintained, while it is significantly reduced during inelastic scattering. Elastic scattering occurs due to the interaction of the incident electrons with the nucleus (Rutherford scattering) and with the electron cloud of the target atom. Due to the attracting forces between opposing charges (Coulombic attraction), electrons that travel close to the nucleus of the target atom are scattered at a higher angle than the ones farther away. The electrons that interact with a lattice plane and scatter at an angle θ will form three-dimensional cones of high-intensity electrons named Kossel cones (Figure 2.7) that satisfy Braggs' law:

$$n\lambda = 2\,d\,sin(\theta) \tag{2.10}$$

where *n* is the diffraction order, λ is the wavelength of the electron beam and *d* the interplanar spacing. The Kossel cones intercept a phosphor screen positioned near the sample, forming so-called Kikuchi bands. As the electron beam interacts with different lattice planes within a depth of approximately 50-100 nm, several bands are formed, giving rise to the electron backscatter pattern (EBSP).

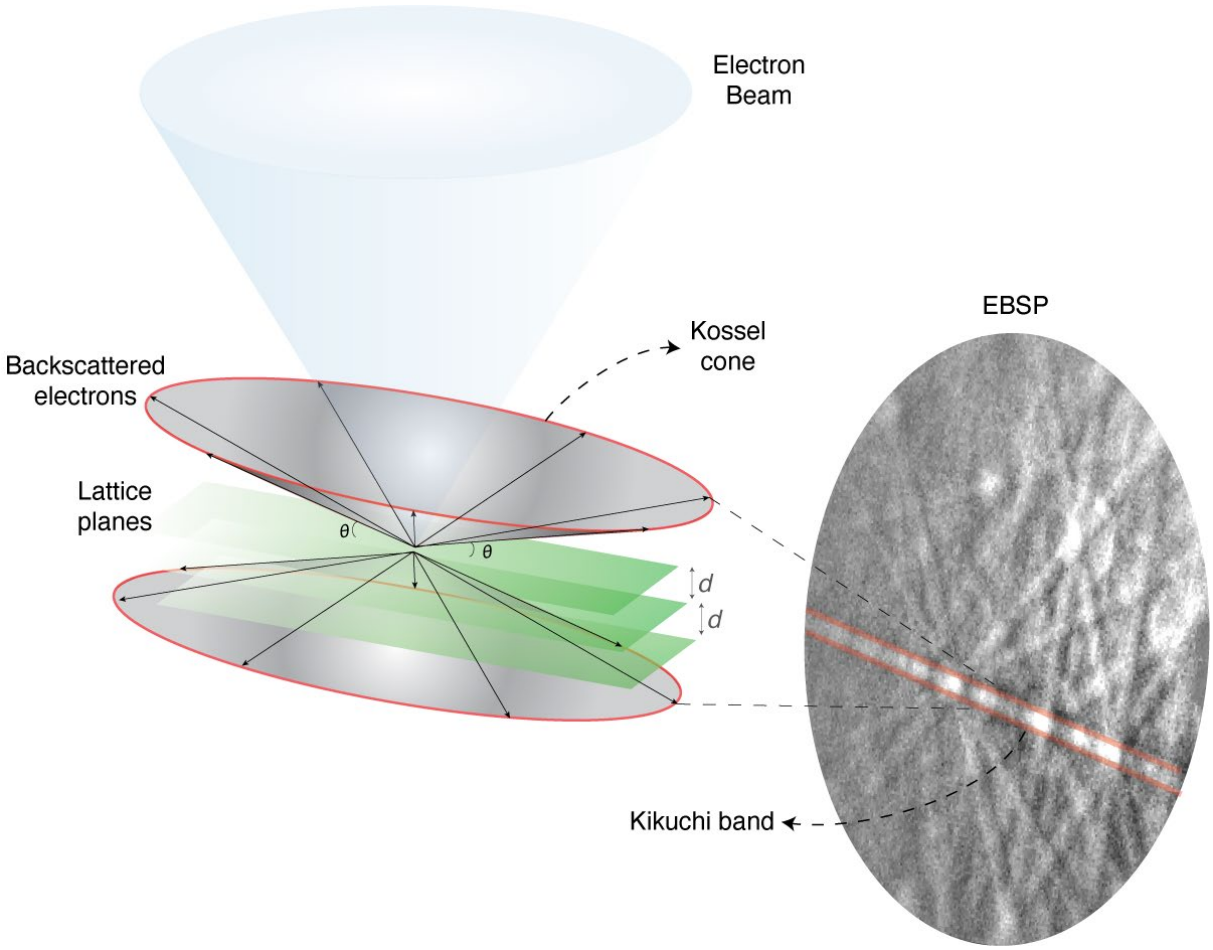

Figure 2.7: Formation of an electron backscatter pattern (EBSP): The electron beam hits a sample and different interactions occur, (e.g., electron scattering). The backscattered electrons that satisfy the Bragg equation forms cones with an opening angle θ. A phosphor screen, positioned near the sample, captures these cones as lines named Kikuchi bands. The interaction of the beam with different lattice planes create an EBSP.

Each Kikuchi band is a gnomonic projection of a crystallographic plane and thus the crystal orientation can be assigned by knowing the orientation of different crystallographic planes with respect to each other. This is done by first capturing the EBSP with a camera and converting the pattern to a digital image (Figure 2.8a). The resulting image is corrected to remove the background noise and increase the contrast of the bands. The position and intensities of an EBSP (i.e., the pixel coordinates and their grayscale levels) are then transformed from a Cartesian to a Hough space, which has polar coordinates that indicate the angle (θ) and distance (ρ) of the bands to the EBSP centre (Figure 2.8b). Pixels of high intensity in the EBSP (e.g., zone axes) will interfere constructively in the Hough space and appear as bright spots, while low-intensity pixels or noise will appear darker (Figure 2.8c). The positions of the bands

are identified (Figure 2.8d) and interplanar angles between several (commonly 5-15) Kikuchi bands calculated. The interplanar angles between the Kikuchi bands are subsequently compared with those calculated between the most intense reflectors (i.e., those with a higher structure factor). The set of crystallographic planes which best fit the experimental pattern is assigned to the bands (Figure 2.8e). Finally, a crystal orientation is given by the rotation that brings the crystal-reference frame (e.g., [a], [b] and [c] axes) to an external-reference frame (e.g. X, Y and Z axes of a sample; Figure 2.8f). The movement of the microscope stage and/or deflection of the electron beam by magnetic scan coils allows for the acquisition of crystal orientations over an area range.

The resulting EBSD data includes the spatial coordinates and crystal orientations given by a triplet of Euler angles: $\varphi_1, \Phi, \varphi_2$ (Wenk, 1985). This allows the representation of the data in different forms. Maps of crystallographic orientation allow the spatial visualization of crystal orientations. The presence of preferential crystallographic orientations (e.g., those formed by deformation in the dislocation creep regime) can be visualized through pole figures (PFs) or inverse pole figures (IPFs). PFs are stereographic projections of a defined crystallographic plane or direction in relation to an external reference frame. IPFs, in contrast, are projections of the different crystallographic planes or directions parallel to a defined external direction.

The relation between different crystallographic orientations is also of interest. The rotation to bring into coincidence one orientation into another is called misorientation, which is defined by a rotation axis and a rotation angle. The misorientation analysis allows the investigation of operative deformation mechanisms. For example, the analysis of intragranular misorientation, such as the kernel average misorientation (*KAM*) and misorientation to the grain mean orientation (*mis2mean*), allows the correlation between lattice distortion (e.g. those caused by dislocation structures) with crystal directions. The *KAM* is given pixel-wise by the average misorientation of a kernel defined by its n-order neighbours. The *mis2mean* is given by the misorientation between a pixel contained in a grain and the grain's average orientation.

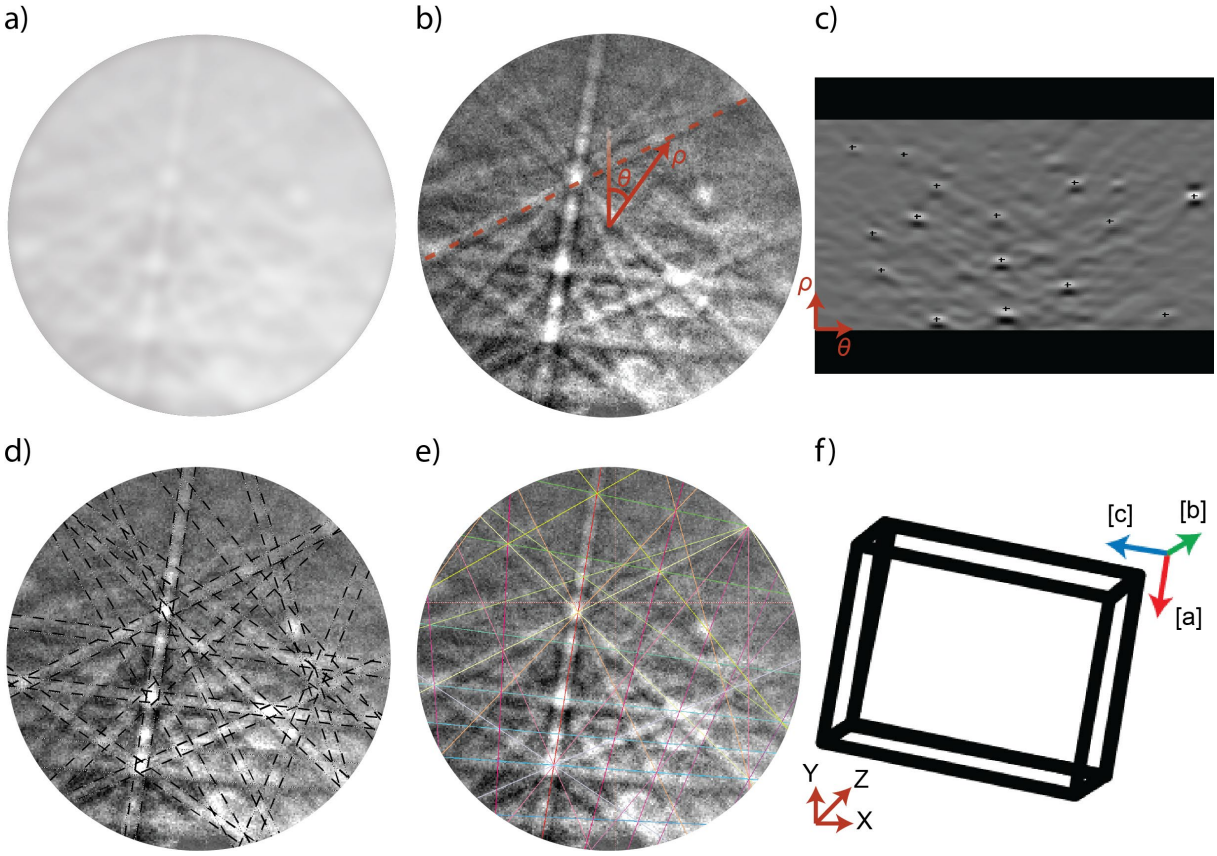

Figure 2.8: Indexing of an EBSP: a) A raw EBSP is captured and different image processes are applied to remove background noise. b-c) Feature recognition of the EBSP's Hough transform allows the determination of the Kikuchi bands. d) Interplanar angles are calculated for different combinations of bands and compared with a lookup table with theoretically calculated values. e) Error minimization routines are used to calculate the best-fit crystal orientation. f) A crystal orientation is assigned to the EBSP.

In this study, the samples were prepared by polishing the surface of interest with diamond particles down to 0.25 µm and finally with colloidal silica. The samples were cleaned in ultrasonic bath, dried and coated with a carbon layer of 3-4 nm to ensure electron conduction in the SEM. EBSD data were acquired using an *FEI Scios Dual-Beam* SEM, coupled with an *EDAX DigiView 5* EBSD detector. Operating conditions of the SEM are acceleration voltage of 20-30 keV and a beam current of 3.2- 6.4 nA. Raw EBSD data were processed using *EDAX OIM Analysis*™ software. Processed EBSD data were further analysed with the *MTEX* toolbox for texture analyses in *MATLAB*® (Hielscher and Schaeben, 2008).

2.3.2 **Energy and wavelength-dispersive spectroscopy**

In contrast to elastically scattered electrons, the electrons from the beam that scatter inelastically after interacting with a sample, transfer their energy to the atoms of the sample. This results in the generation of different signals that can be used to probe the compositional information of a specimen, for example by the emission of characteristic X-rays (Goldstein et al., 2018). Characteristic X-rays are formed when the electron beam interact with an inner shell of an incident atom. If an electron in this shell is sufficiently excited by the electron beam, it is ejected from the atom, leaving the atom in an energized state (ionization). An electron of an outer shell (with higher energy) fills the electron gap left, returning the atom to its ground state (de-excitation). The excess energy of this electron is then emitted as X-ray photons. This excess energy is characteristic for each element. The X-ray photons are captured by a detector (spectrometer), which measures its intensity (as counts per time per amp) as a function of their energy. This characteristic energy can then be used to identify elements present in a sample through energy-dispersive spectroscopy (EDS) or their specific wavelength through wavelength-dispersive spectroscopy (WDS). Quantitative elemental analysis of specimens from measured X-ray energy intensity is based on the assumption that the ratio of concentration of the element i between a specimen and a standard (C_i and $C_{(i)}$, respectively) is equal to the ratio of X-ray intensity from the unknown specimen (I_i) and the standard $(I_{(i)})$, that is (Castaing, 1951; Goldstein et al., 2018):

$$\frac{C_i}{C_{(i)}} = \frac{I_i}{I_{(i)}}. \tag{2.11}$$

The scattering of the electron beam differs for each element present in a sample. Thus, a change of intensity due to a combination of elements occurs, which is known collectively as matrix effects. Matrix effects include the contribution of the electron scattering and retardation due to the different atomic numbers (Z_i), X-ray absorption (A_i) and X-ray fluorescence (F_i) of each element *i*. Thus, the equation 2.11 can be rewritten as:

$$\frac{C_i}{C_{(i)}} = [ZAF]_i \frac{I_i}{I_{(i)}}. \tag{2.12}$$

Therefore, matrix corrections (e.g., *ZAF* or $\phi(\rho z)$ corrections), must be applied in order to correlate X-ray intensities to element concentration.

The sample preparation for the EDS and WDS analyses was similar to the one for EBSD, although a thicker carbon coating of 10 nm was applied. EDS data were acquired using an *FEI Scios Dual-Beam* SEM, coupled with an *EDAX Octane Super* detector. The SEM was operated with an acceleration voltage of 20-30 keV and beam current of 1.6 - 6.4 nA. The WDS analyses were performed in an *JEOL JXA-8200* electron microprobe. The data was collected with an electron beam voltage and current of 15 keV and 15 nA, respectively. Counting time was of 20 seconds per element peak acquisition and 10 seconds for background collection.

2.3.3 **Transmission electron microscopy**

The transmission electron microscope consists fundamentally of an electron source and a series of electromagnetic lenses along a column, from top to bottom: condenser, objective, intermediate and projector lenses (Figure 2.9). The condenser lenses focus the electron beam originated from the electron gun into the object sample. The objective lens is used to focus and magnify the image, while further magnification is provided by the intermediate and projector lenses. The resulting magnified object (or diffraction pattern) is finally projected on a phosphor screen positioned at the end of the column. Two operating modes are possible in a TEM: imaging and diffraction mode. In the imaging mode, two types of analyses are possible (Williams and Carter, 2009): bright field (BF) and dark field (DF) imaging. In the BF mode, the transmitted (direct) beam is chosen in a selected area diffraction pattern (SADP) by inserting an aperture in the image plane. In contrast, in the DF mode, the transmitted beam is blocked and a diffracted beam (scattered electrons) is used for imaging. In the diffraction mode, a selected area aperture is used for the collection of a diffraction pattern at a previously selected area in the imaging mode.

In this study, the samples used in TEM analyses were prepared from doubly-polished thin sections with a thickness of 30 µm. The samples were glued on a Cu mesh grid using *Araldite*® resin. Samples were further thinned to obtain electron-transparent areas using a *Gatan precision ion-polishing system* (*PIPS*) model 691. The samples were carbon-coated before TEM analyses to ensure electron conduction. Additional samples of specific grain boundaries were prepared using an *FEI Scios* focused ion beam (FIB) system. TEM lamellae of approximately 20, 15, and 0.1 µm in width, height,

and thickness, respectively, were prepared using a Ga^+ beam in the FIB. TEM analyses were performed with an *FEI Titan* with a field emission source operating at 200 keV. Indexing of SADP were performed using the interface *diffractGUI* of the *Crystbox* software (Klinger and Jäger, 2015). Contrast-limited adaptive histogram equalization (Zuiderveld, 1994) was applied to TEM images using a Rayleigh distribution.

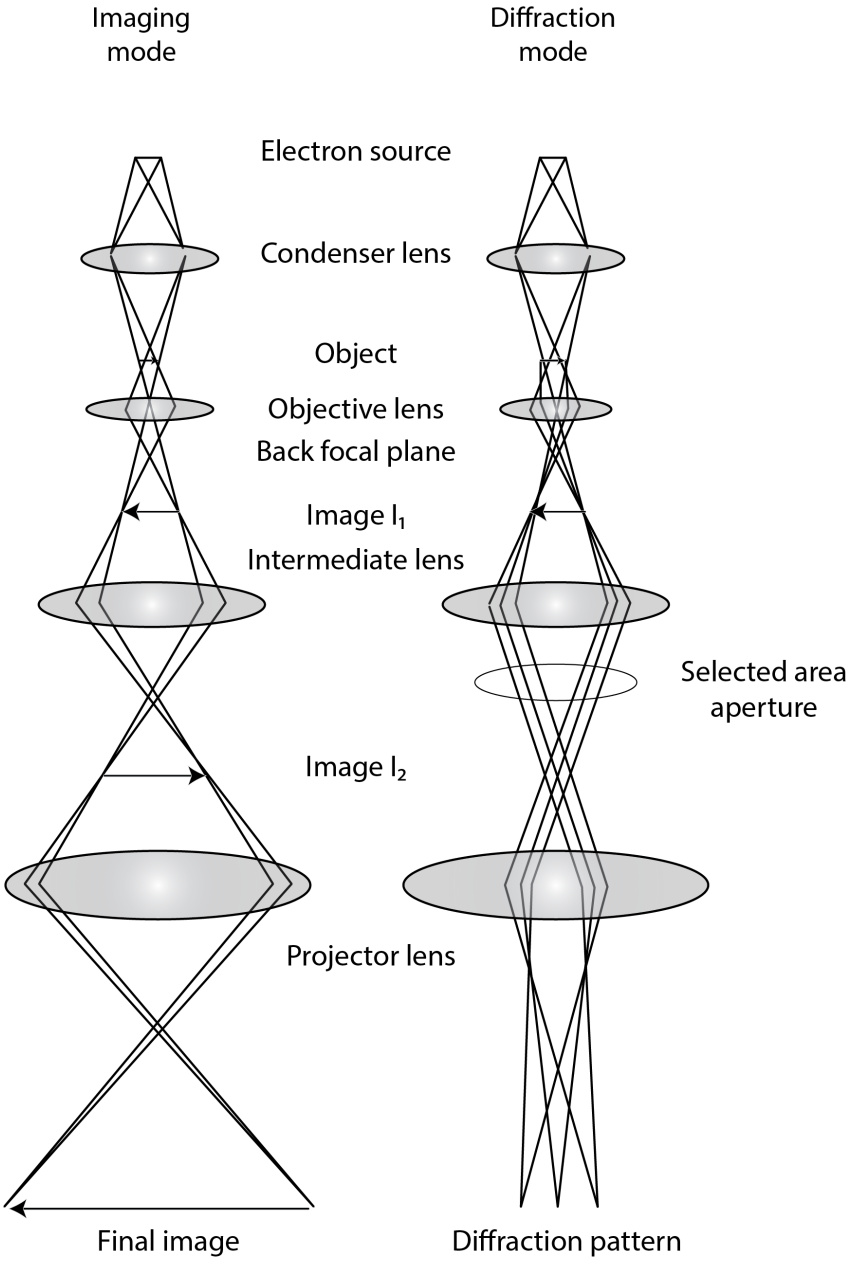

Figure 2.9: Schematic model of image (left) and diffraction pattern (right) formation in a TEM. Modified from McLaren (2005).

2.3.4 **Fourier-transform infrared spectroscopy**

Infrared spectroscopy is an analytical technique of identification and quantification of molecules, based on their characteristic vibrational frequency, that is, the stretching and bending of interatomic bonds (Stuart, 2004). Infrared radiation is absorbed by a molecule in the wavelength range which corresponds to the frequency of its vibration. This range is commonly defined as infrared absorption bands. Typical instrumentation for infrared spectroscopy includes an infrared source, an interferometer, a detector, a signal amplifier and a converter. For Fourier-transform infrared (FTIR) spectroscopy, a Michelson interferometer (Figure 2.10) is commonly used. The Michelson interferometer consists fundamentally of a pair of mirrors (one stationary and one mobile), a beamsplitter and a photodetector. The process of acquiring a FTIR spectrum involves the emission of radiation in the infrared range that passes through a semi-reflective surface (beamsplitter). Half of the incident radiation is redirected towards the static mirror while the other half is transmitted through the beamsplitter to the mobile mirror. The beam reflection from the two mirrors will create two distinct beams. As the mirror moves, the beam reflected by the mobile mirror moves at a different distance from the second beam. This distance is known as optical-path difference (OPD). As a result of the OPD, a difference in wavelength is created between the two beams. When the two beams return to the beamsplitter they will interfere and give rise to an interference pattern (interferogram). This signal is subsequently amplified and converted to a digital form. A Fourier transform is then applied, which converts from an intensity as a function of the OPD space (interferogram) to an intensity as a function of wavenumber space (FTIR spectrum).

The quantification of FTIR spectra is based on the Beer-Lambert law, which correlates light absorbance (A) to concentration of a substance (c) by:

$$A = \varepsilon c l \tag{2.13}$$

where l is the pathlength of the sample and ε is a constant of proportionality known as molar absorptivity. Considering A as the logarithm of the ratio between the light intensity when entering the sample, I_0, and after being transmitted through the sample I, and transmittance, T, as the ratio between I and I_0, the equation 2.13 can be rewritten as:

$$\log\left(\frac{I_0}{I}\right) = -\log T = \varepsilon c l \tag{2.14}$$

Different calibrations based on the Beer-Lambert law exist for the quantification of the water content in olivine (e.g., Bell et al., 2003; Paterson, 1982; Withers, 2013). In this work we performed unpolarized FTIR of doubly polished polycrystalline samples of 200 µm thickness. The spectra were acquired under atmospheric conditions, using an aperture of 100 µm and a resolution of 2 cm^{-1}. The water contents from FTIR absorbance spectra were calculated using the calibration of Paterson (1982). The spectrum baseline was fitted to a spline curve estimated using the function *msbackadj* from *MATLAB*®. The numerical integration of the spectrum area over the baseline in the range of 2950 cm^{-1} to 3780 cm^{-1} was done via the trapezoidal method (using the function *trapz*) using *MATLAB*®.

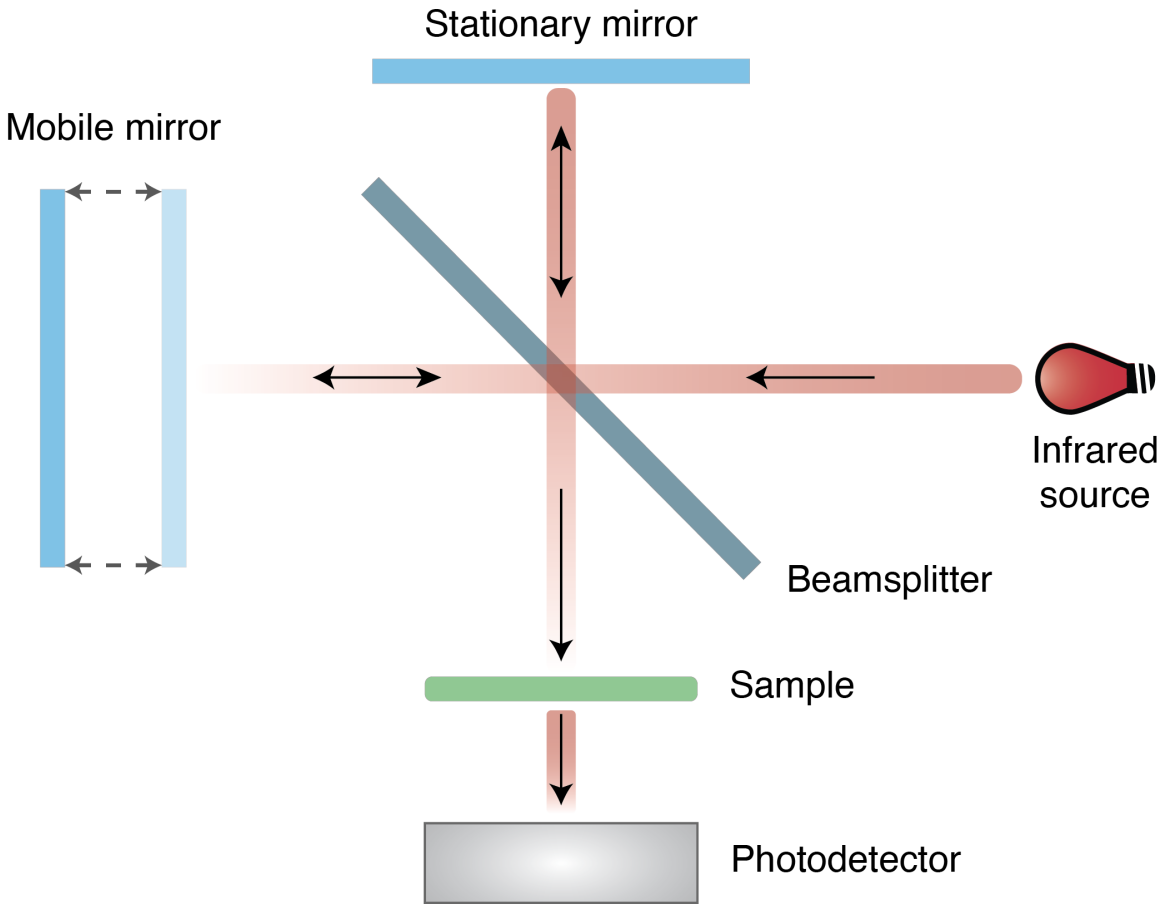

Figure 2.10: Simplified model of an interferometer used in FTIR spectroscopy. Modified from Stuart (2004)

Chapter 3: Synopsis

This chapter summarizes the main findings of this study which aimed to answer the questions presented in Chapter 1. The Chapter 4, published as Ferreira et al. (2021), is focused on the evolution of grain boundaries during deformation of olivine and the interactions of grain boundaries with dislocations. The Chapter 5, submitted to the *Journal of Geophysical Research: Solid Earth*, discusses the effect of pressure on the grain growth of olivine. The Chapter 6, which has been prepared for submission, presents a new high-pressure deformation assembly and discusses the effect of grain boundaries during deformation of olivine at high pressure and temperature. The Chapter 7, which has also been prepared for submission, presents a new toolbox for the analyses of grain boundaries using EBSD data. The contribution of co-authors to this study is presented at the end of this chapter. The computer scripts used in this Thesis are available at: https://doi.org/10.5281/zenodo.5344419.

3.1. The effect of grain boundaries on plastic deformation of olivine

Previous studies (e.g., Hansen et al., 2011; Kohlstedt and Hansen, 2015; Ohuchi et al., 2015) demonstrate that dislocation-accommodated grain-boundary sliding (disGBS) is likely the main deformation mechanism for olivine in most of Earth's upper mantle. In Chapter 4, we used electron backscattered diffraction (EBSD) and transmission electron microscopy (TEM) data to investigate the micromechanics involved in the deformation of olivine deformed experimentally in the disGBS regime. We evaluated the evolution of grain boundaries using the grain-boundary plane distribution (GBPD) technique. The interaction between dislocations and grain boundaries were investigated using misorientation data and through the evaluation of potential slip transfer through the *m'* factor (e.g., Luster and Morris, 1995).

The results shown in Figure 3.1 illustrate the evolution of grain boundaries as a function of strain. We demonstrated that the grain boundary planes evolve from an uniform distribution, for the starting material, to (hk0) planes at deformed samples. At the highest strain interval investigated, $\gamma \approx 10$, the (010) and (010) planes are the most abundant. We propose a model where the grain boundaries are formed as a result of dislocation creep predominantly along the (010) [100] slip system (Figure 3.2).

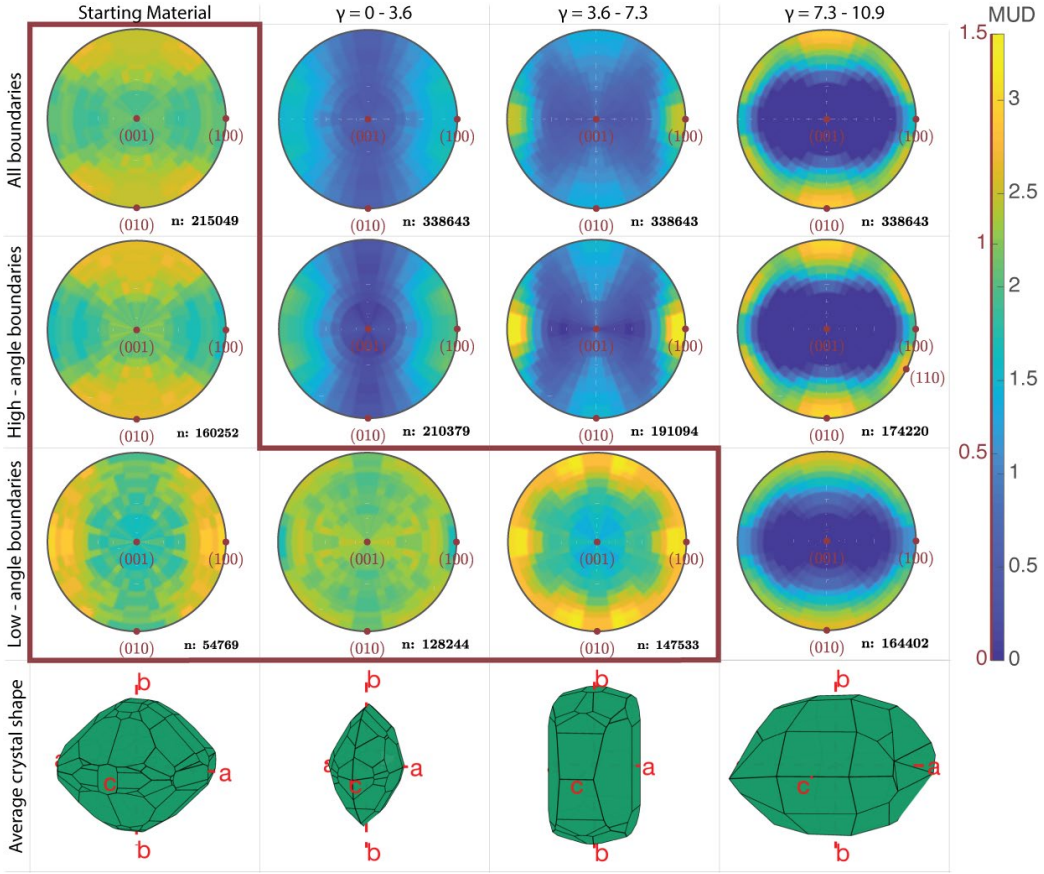

Figure 3.1: GBPDs of olivine for all, high-angle (misorientation angle higher than 20º) and low-angle grain boundaries (misorientation angle between 2º and 20º) for the starting material and for increasing strain. The pole figures within the red bounding area are scaled to have a maximum MUD of 1.5 (left side of the color scale) while the remaining pole figures are scaled to have a maximum MUD of 3.4 (right side of the color scale). The number of boundary segments (n) is given below each plot. Pole figures are upper hemisphere projections. The bottom row illustrates the average crystal shape estimated from the grain-boundary plane distribution of all boundaries.

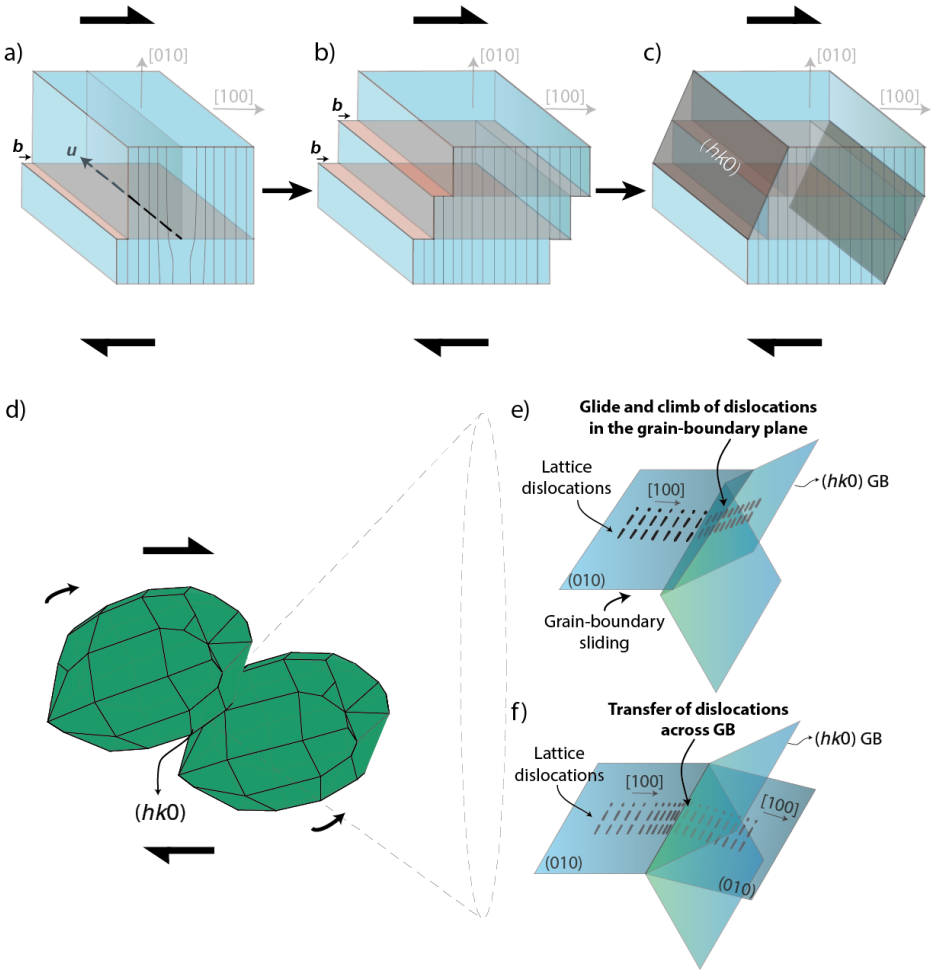

Figure 3.2: Schematic model of the proposed grain-boundary formation mechanism and its influence on grain boundary sliding. a) A dislocation with line direction ***u*** glides through the crystal on the [100](010) slip system, shearing the crystal by one Burgers vector, ***b***. b) Progressive deformation leads to continuous shearing of the crystal. c) As a result of the general shape change of the crystal, the grain boundaries become parallel to approximately (140). The continuous absorption of dislocations into the grain boundaries leads to relative rotation between grains d) and e), which progresses until the neighboring grains are oriented in such a manner that f) dislocations are easily transferred to the neighboring crystal. This transfer occurs when the burgers vectors of the active dislocations in neighboring lattices are close to parallelism.

Pommier et al. (2018) suggested that certain grain boundaries with higher electrical conductivity could be responsible for creating electrical anisotropy in the Earth's mantle. Our results suggest that the activation of different slip systems would result in the development of different grain-boundary populations. This would lead to varied geophysical responses throughout the upper mantle, as multiple slip systems of olivine are likely activated in this region (e.g., Jung et al., 2006).

Misorientation data and the slip transfer analyses indicate that the grain boundaries are not strong barriers for the motion of dislocations, and no widespread pile-up of

dislocations occur near the grain boundaries . Our results suggest that the dislocations are either transmitted through the grain boundaries or assimilated as grain-boundary dislocations. The motion of grain-boundary dislocations modifies the grain-boundary structure and allow grain-boundary sliding to occur. This process would ultimately control the strain rate of olivine deformed in the disGBS regime, and thus be an important processes controlling mass and heat flow in the Earth's upper mantle.

3.2. Pressure dependence of olivine grain growth at upper mantle conditions

The grain size evolution in the mantle influences the predominant deformation mechanism and thus has a great effect on the viscosity in this region. Grain sizes in the upper mantle are controlled by grain-size reduction, trough static or dynamic recrystallization, and grain growth. Grain growth of olivine, the major phase of the upper mantle, has been extensively studied (e.g., Faul and Scott, 2006; S. Karato, 1989; Nakakoji and Hiraga, 2018; Nichols and Mackwell, 1991), although no studies investigated how does pressure conditions at the middle and at the deep upper mantle affect the grain growth of olivine. In Chapter 5, we investigated the grain growth of olivine through experiments performed using piston cylinder and multianvil apparatus at pressures ranging from 1 to 12 GPa and temperatures ranging from 1323 K 1793 K. The resulting grain sizes after each experiment were measured using EBSD and are shown in Figure 3.3 as log-normal distributions fitted to the grain-size data.

Our results demonstrate that the grain-growth rate of olivine decreases as pressure increases. Grain-boundary diffusion was proposed to control grain growth and diffusion creep of olivine (Nakakoji and Hiraga, 2018). Fei et al., (2016) demonstrated that the grain-boundary diffusion coefficient of Silicon, the slowest diffusing species in olivine (Farver and Yund, 2000), decreases for increasing pressure. We suggest therefore that the decrease in the grain-growth rate of olivine might be explained by the decrease in the rates of Si grain-boundary diffusion for increasing pressures.

Non-linear least-squares fitting of our grain size data at 1673 K and 13 vol.% Px to a normal grain growth equation gives k_0 = 2.11 x 10^{-7} ($m^{3.88}s^{-1}$), n = 3.88, V^* = 4.30 x 10^{-6} (m^3/mol) and E^* = 607 (kJ/mol). Extrapolation of these results to geological durations (e.g. 1-100 Ma), considering existing olivine flow laws (Goetze et al., 1978; Hansen et

al., 2011; Hirth and Kohlstedt, 2003) and assuming that shear stresses are on the order of 0.1-1 MPa at a depth of ~210 km (P ≈ 7 GPa) (Kohlstedt and Hansen, 2015), olivine is expected to deform in a grain-size sensitive rheology at these conditions. Thus, our results indicate that a change to a Newtonian rheology at deeper parts of the upper mantle (e.g. Karato and Wu, 1993) may be influenced by the slower grain growth rate of olivine, preserving smaller grain sizes than previously expected for the middle to deep upper mantle (e.g., S. Karato, 1989).

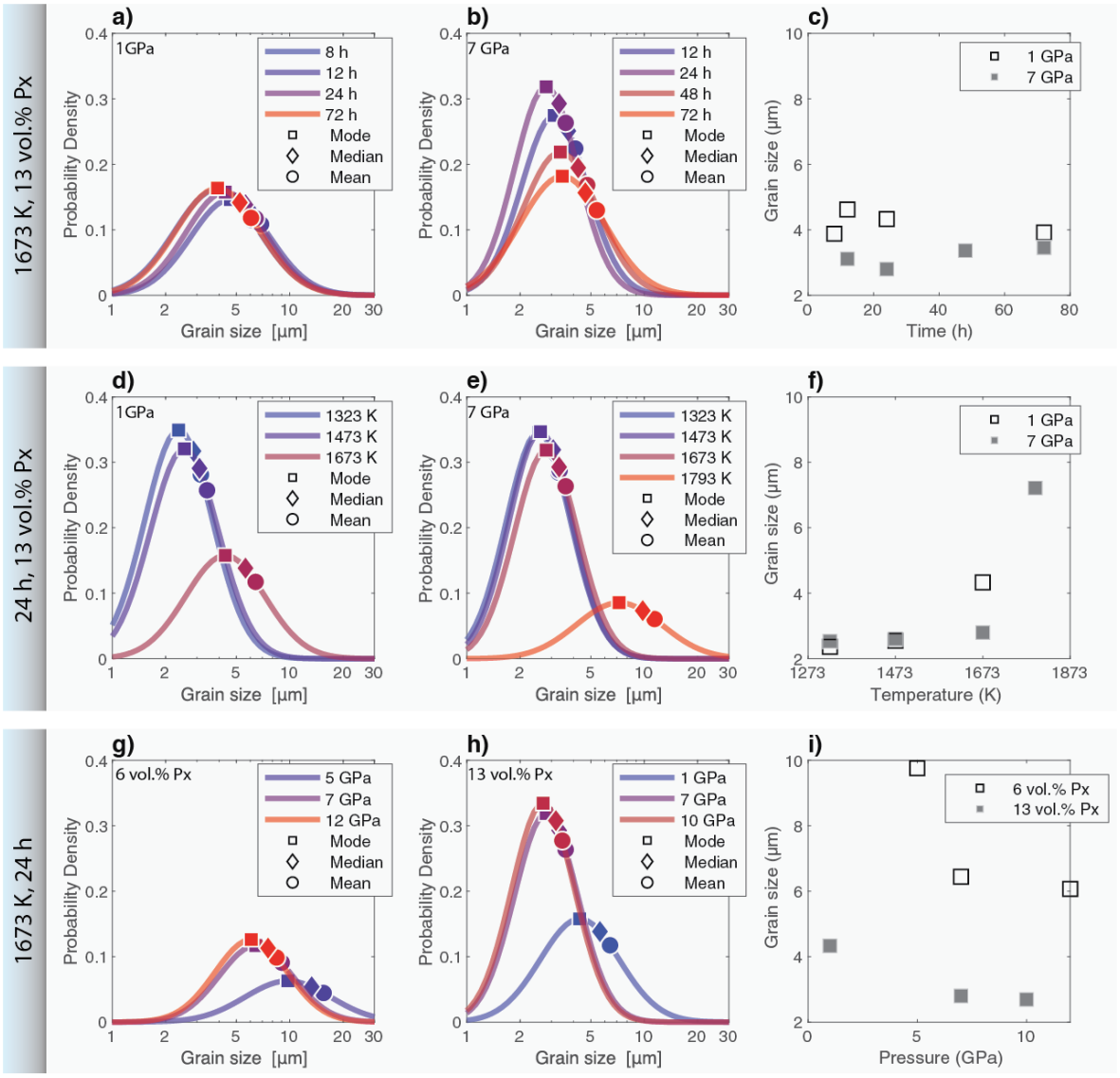

Figure 3.3: Lognormal fit to the grain-size distributions: The upper row (a-c) shows a time series of experiments performed at 1673 K and pressures of a) 1 GPa and b) 7GPa. c) Mode of the of the fit to the grain-size distribution as a function of time. The middle row (d-f) shows the temperature series of experiments performed for 24 hours at pressures of d) 1 GPa and e) 7GPa. f) Mode of the of the fit to the grain-size distribution as a function of temperature. The bottom row (g-i) shows the pressure series of experiments performed at 1673 K for 24 hours for samples containing g) 6 vol.% and h) 13 vol.% of pyroxene. i) Mode of the fit to the grain-size distribution as a function of pressure for samples with a Pyroxene content of 6 vol.% and 13 vol.%.

The impact of an activation volume for grain growth on the deep upper-mantle viscosity is illustrated in Figure 3.4. The expected viscosities when considering an activation volume of 4.3 x 10^{-6} m^3/mol are approximately one order of magnitude lower than when no activation volume (0 m^3/mol) is considered. These results suggest that, with increasing depths in the Earth's upper mantle, the reduction of grain-growth rates of olivine due to increasing pressure may offset the temperature effect. Based on these observations, we suggest that upper mantle viscosities may be lower at increasing pressures than previously expected.

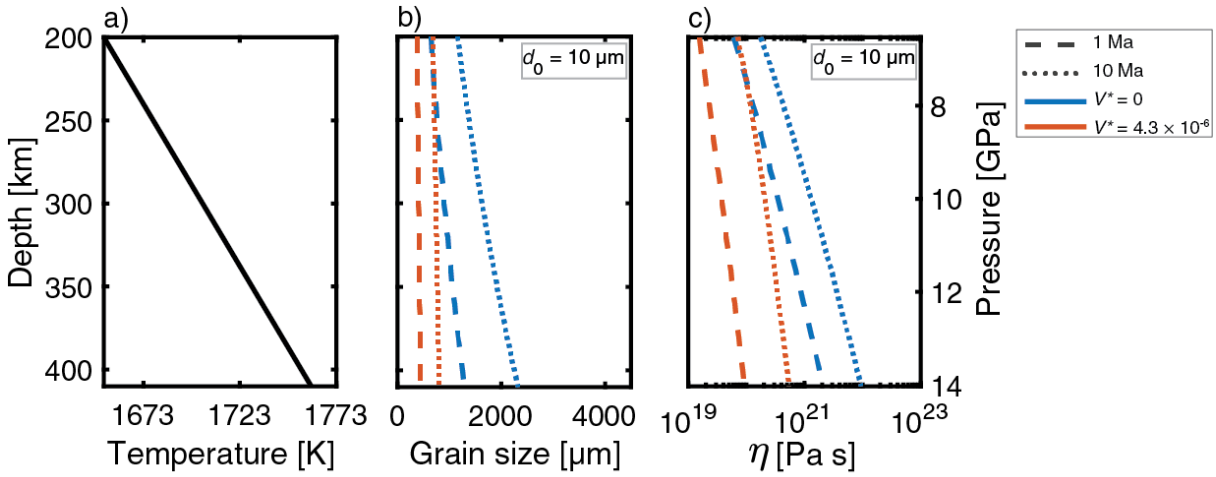

Figure 3.4: Viscosity estimation at deep upper mantle conditions: a) Average temperature profile of the deep upper mantle (Katsura et al., 2004). b) Expected grain sizes at 1 Ma (dashed lines) and 10 Ma (dotted lines) at the conditions of the geotherm shown in figure a, considering an initial grain size d_0= 10 µm, an activation volume of V* = 0 m3/mol (blue lines) and V* = 4.3 x 10-6 m3/mol (orange lines). Resulting viscosity profile of the deep upper mantle considering the grain size evolution shown in b, for a constant shear stress of 1 MPa and strain rates from experimental flow laws of diffusion creep (Hansen et al., 2011; Hirth and Kohlstedt, 2003), disGBS (Hansen et al., 2011), and dislocation creep (Hirth and Kohlstedt, 2003).

3.3. Towards the investigation of the grain-boundary effects in the plastic deformation of olivine at high pressures

Information on the natural deformation of olivine under the conditions Earth's deep upper mantle (depths>200 km) is limited. Thus, the microphysical processes operating at depths are mostly inferred from geophysical observations coupled with experimental data. However, experimental data on deformation of olivine at high pressures is limited and great uncertainty still exists about the deformation mechanisms operating at large

depths. Here, we investigate the effect of grain boundaries on the strength of olivine-dominated aggregates at deep upper mantle conditions (7-10 GPa, 1623 K). We present a new set of deformation anvils and assembly (8-5) used to investigate the simultaneous deformation of coarse (reconstituted San Carlos olivine) and fine-grained (sol-gel) olivine aggregates. The experiments were performed in pure-shear geometry using a MAVO-6 press (*Max Voggenreiter GmbH*). Recovered samples after the deformation experiments were analyzed using EBSD.

Figure 3.5 shows secondary-electron images of the recovered samples from experiments performed at 7 GPa. The fine-grained olivine aggregates deformed almost an order of magnitude faster than the coarse-grained aggregates. Figure 3.6 illustrates intragranular misorientations found in the fine-grained samples after deformation. The presence of sub-grain structures even in the smallest grain-size fraction indicate that dislocation creep was operative. These results suggest that deformation by dislocation creep in fine-grained olivine is faster than for coarse-grained olivine in our experiments. Our results differ to those observed for low-temperature deformation of olivine, where an increase in grain boundaries correlate to a decrease in strain rates (e.g., Hansen et al., 2019; Kumamoto et al., 2017). During low-temperature deformation, grain boundaries act as barriers for dislocation motion, leading to strain hardening (Hall, 1951; Petch, 1953). At high-temperature deformation, however, diffusive processes take place, allowing dislocations to climb obstacles such as grain boundaries (Weertman, 1957), or to be assimilated within the grain boundary (see Chapter 4). The motion of grain-boundary dislocations is one of the main mechanisms controlling grain-boundary sliding (e.g., Ishida and Brown, 1967; Langdon, 1970). Consequently, an increase in the amount of grain boundaries would allow more incorporation of dislocations and subsequent sliding. Therefore, smaller average grain sizes lead to faster strain rates, that is, strain weakening.

Experiments performed at pressures of 10 GPa (see Figure 6.7) show widespread fracturing and faulting, when plastic deformation was expected. At large confining pressures, fracturing should be inhibited (e.g., Byerlee, 1968; Lockner and Beeler, 2002) and its occurrence is unclear. Possible explanations include failure due to localized heating, phase transitions, thermal contraction, and release of elastic energy from the anvils or assembly parts (i.e. blow out). The use of acoustic-emission

measurements during the experiments (e.g., Ohuchi et al., 2017; Wang et al., 2017) could provide important information of the mechanisms involved in this process.

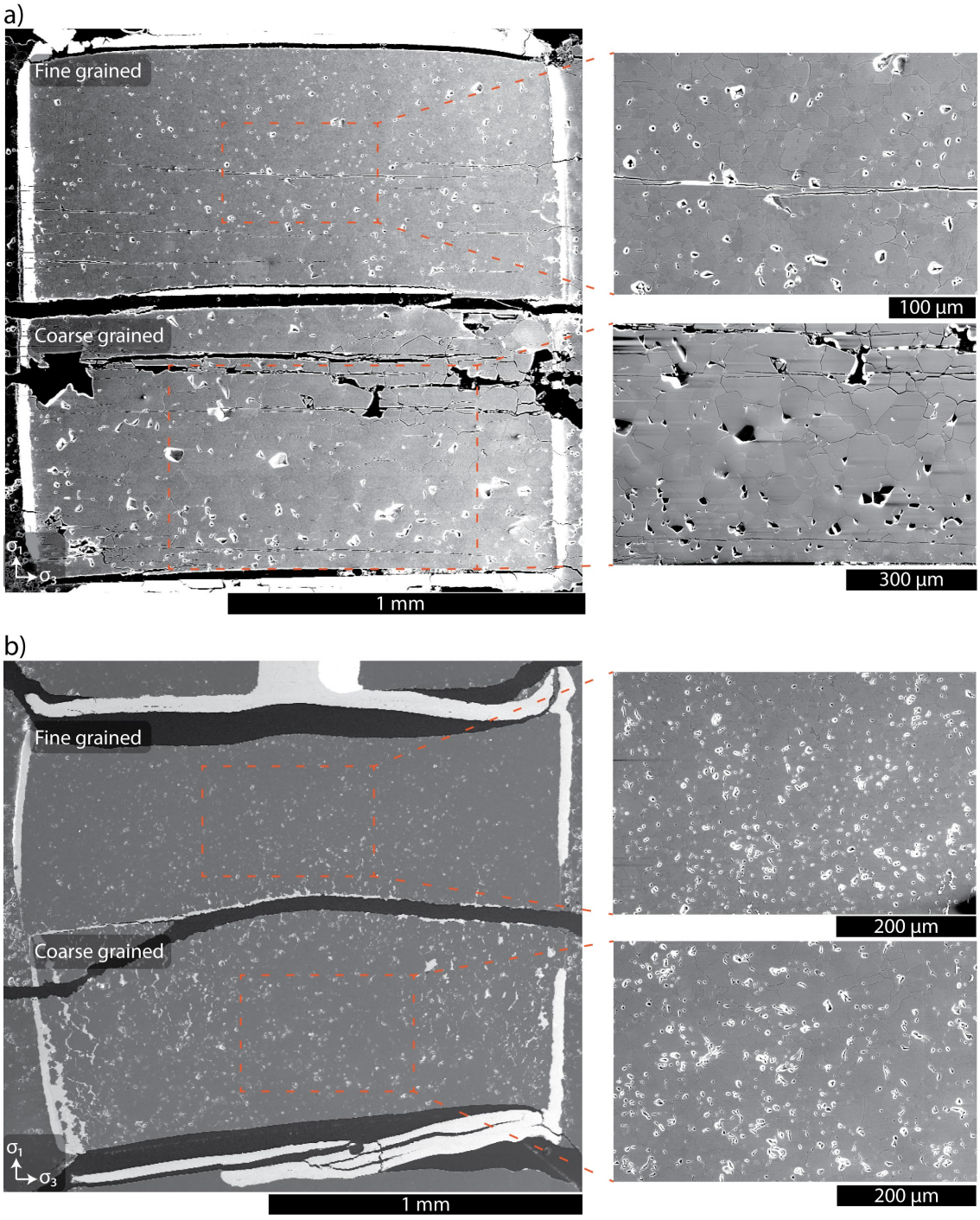

Figure 3.5. Secondary electron images of recovered samples after deformation at a confining pressure of 7 GPa: a) Experiment HH221. b) Experiment HH222. The direction of maximal compression, σ_1, is vertical and the direction of minimal compression, σ_3, horizontal.

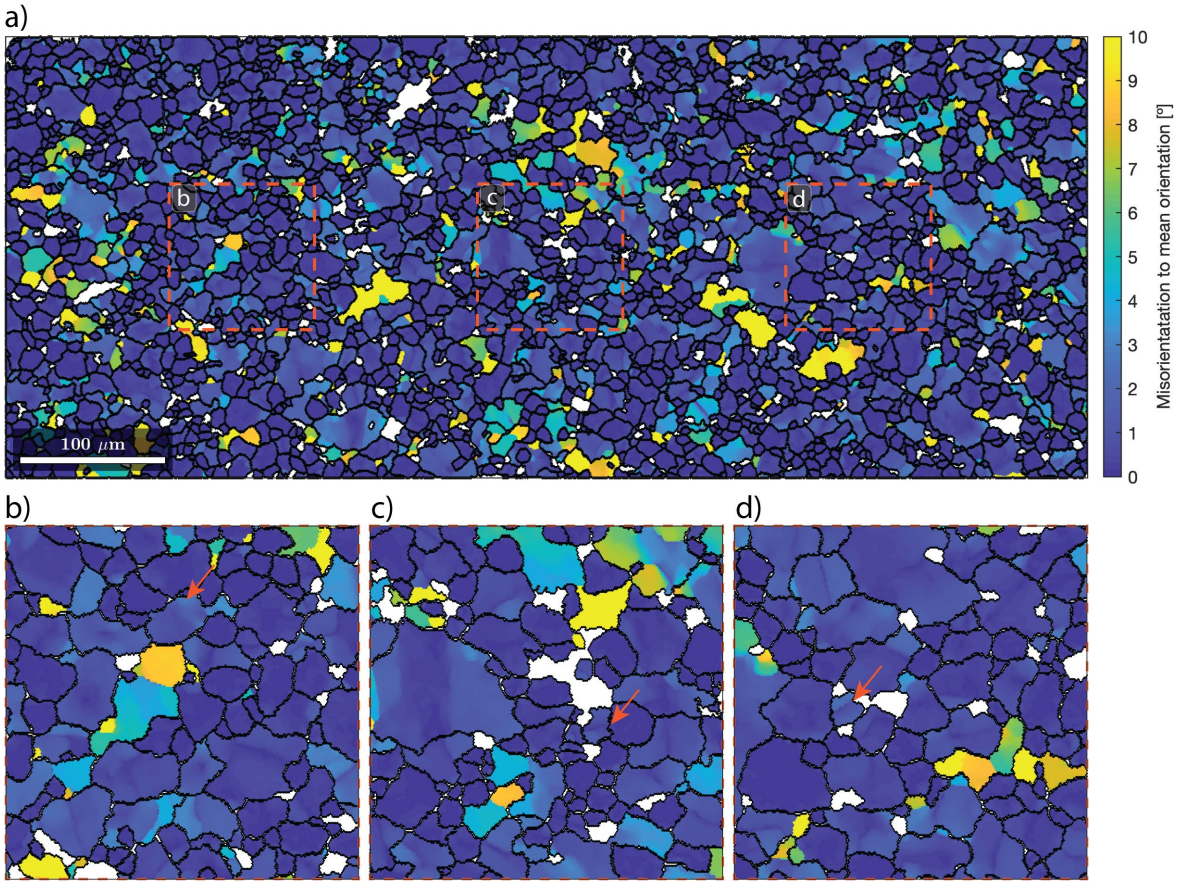

Figure 3.6: Intergranular misorientation of fine-grained olivine in experiment HH222. EBSD data are colour-coded by the angular misorientation to the mean orientation of the grains, from 0º (dark blue) to 10º (light yellow). Arrows in b-d) indicate sharp misorientation bands in very small grains (<10 µm). Insets dimensions are 100 µm x 100 µm.

3.4. A MATLAB®/MTEX toolbox for grain boundary plane and character distribution

Many properties of polycrystalline materials are directly correlated with the structure of grain boundaries (Sutton and Balluffi, 1995). Therefore, the characterization of grain boundaries is needed in order to understand macroscopic processes such as plastic deformation, fracture, corrosion, segregation and diffusion in materials (Watanabe, 2011). The grain boundary plane and character distribution (GBPD and GBCD) calculated from 2-D EBSD data are cost-effective and fast techniques to obtain a macroscopic description of grain boundaries. Computer programs written in *FORTRAN* language by Rohrer and collaborators (Saylor et al., 2002; Saylor and Rohrer, 2002) allow the calculation of the GBPD and GBCD from EBSD data. Nonetheless, tools for

importing, visualizing, treating and exporting EBSD-related data in proprietary software packages are still limited. In Chapter 7, we provide a toolbox written in *MATLAB*® to extract grain-boundary information from EBSD data, execute the GBPD and GBCD programs and plot the results. We also compare the output data from our toolbox with commercially available alternatives such as the EDAX OIM™ software.

The toolbox that we provide can be easily combined with the *MTEX* toolbox for *MATLAB*® (Hielscher and Schaeben, 2008). *MTEX* is an open-source toolbox that allows EBSD data from several vendors or any generic spatial/crystal orientation data to be imported and analysed. *MTEX* provide functions to access and classify grain boundaries according to their properties, or any other user-defined criteria. This allows for better control on the exported grain-boundary segments and improved understanding of grain-boundary types and populations.

Furthermore, our toolbox provide important advantages when compared to existing proprietary software such as *EDAX OIM*™. The OIM™ software create segments by connecting triple junctions following the calculated grain boundaries. Using the grain-boundary segmentation and smoothing methods provided by MTEX, we are able to better define complex grain geometries and avoid segmentation artifacts such as stair-casing (Figure 3.7).

In contrast to *EDAX OIM*™, our toolbox also allows the analyses of grains within other grains. This distinction is of great importance for the analyses of geological samples, as inclusions, overgrowth and twinning microstructures are common features in rocks (e.g., Vernon, 2004). Lastly, the provided toolbox is open source, which allows for continuous improvement and increasing number of functions.

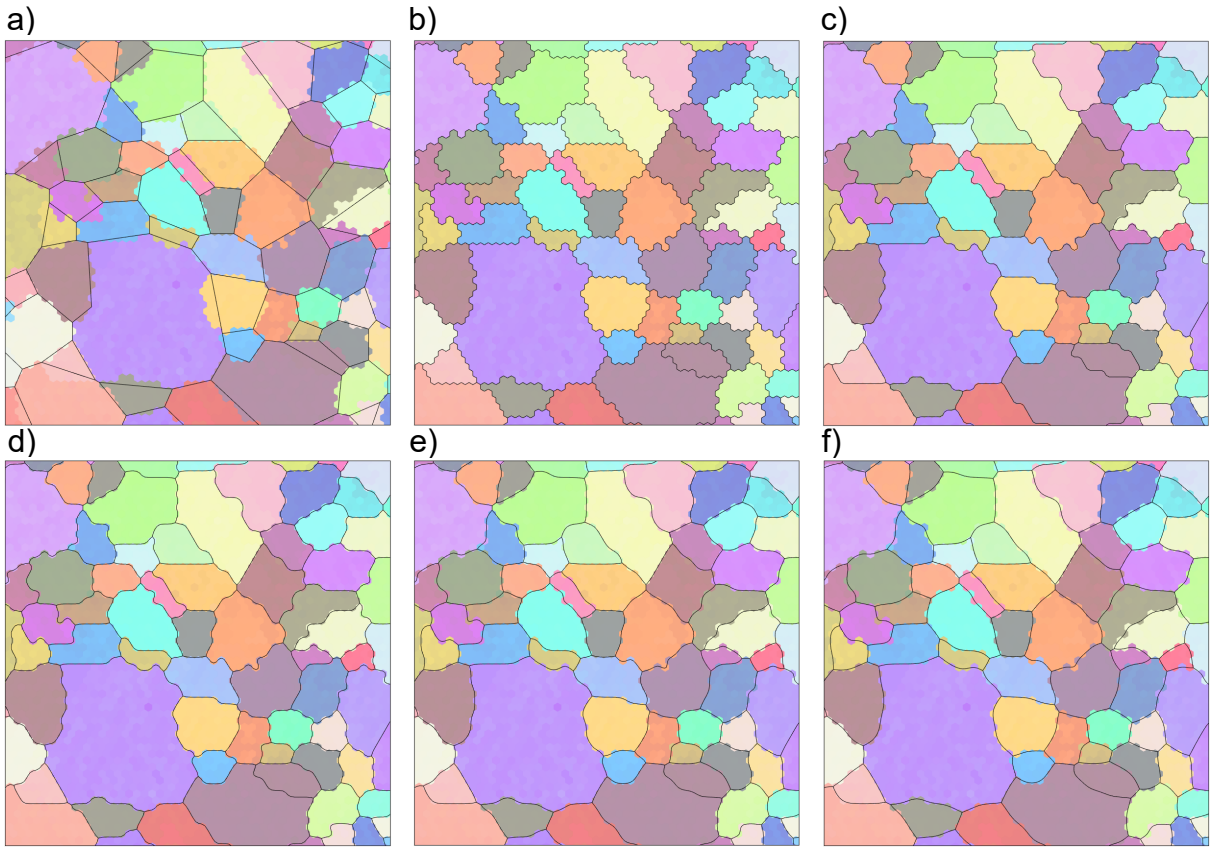

Figure 3.7: Comparison of segments (black lines) exported from a) *EDAX OIM*™ and *MTEX* for b) no smoothing and increasing number of smoothing iterations of c) 1, d) 2, e) 5 and f) 10 iterations.

List of manuscripts and statements of author contributions

- The effect of grain boundaries on plastic deformation of olivine. **Ferreira, F.**, Hansen, L., Marquardt, K. *Journal of Geophysical Research: Solid Earth 126,* no. 7 (2021): e2020JB020273. https://doi.org/10.1029/2020JB020273.

  F. Ferreira collected and analysed the data and wrote the first draft of the manuscript. L. Hansen provided the samples. K. Marquardt designed the study. All authors discussed the data analyses and results and contributed to the manuscript writing.

- Pressure dependence of olivine grain growth at upper mantle conditions. **Ferreira, F.**, Thielmann, M., Farla, R., Koizumi, S., Marquardt, K. *Journal of Geophysical Research – Solid Earth*. Under review.

  F. Ferreira performed the experiments, collected and analysed the data and wrote the first draft of the manuscript. M. Thielmann and K. Marquardt contributed to data analysis and manuscript writing. R. Farla assisted with the multianvil experiments and contributed to manuscript writing. S. Koizumi provided vacuum-sintered olivine aggregates. K. Marquardt designed the study.

- Towards the investigation of the grain-boundary effects in the plastic deformation of olivine at high pressures. **Ferreira, F.**, Farla, R., Thielmann, M., Marquardt, K. In preparation for submission.

  F. Ferreira performed the experiments, collected and analysed the data and wrote the manuscript. R. Farla performed the experiments and commented on the manuscript. M. Thielmann and K. Marquardt assisted with data analysis and contributed to manuscript writing. K. Marquardt designed the study.

- A *MATLAB*®/MTEX toolbox for grain boundary plane and character distribution. **Ferreira, F.**, Rohrer G., Thielmann, M., Marquardt, K. In preparation for submission.

  F. Ferreira wrote the *MATLAB*® toolbox, analysed the data and wrote the manuscript. G. Rohrer wrote the original programs on which the toolbox is based, provided test data and assisted with code writing. M. Thielmann and K. Marquardt assisted with code writing and the manuscript writing.

Chapter 4: The effect of grain boundaries on plastic deformation of olivine

Filippe Ferreira[1], Lars Hansen[2], and Katharina Marquardt[1*]

[1] Bayerisches Geoinstitut, Universität Bayreuth, Bayreuth, Germany

[2] Department of Earth and Environmental Sciences. University of Minnesota, Minneapolis, USA.

[*]Now at Faculty of Engineering, Department of Materials. Imperial College London, London, UK

This chapter has been published as:

Ferreira, F., Hansen, L., & Marquardt, K. The effect of grain boundaries on plastic deformation of olivine. Journal of Geophysical Research: Solid Earth, e2020JB020273.

Author Contributions:

F. Ferreira collected and analysed the data and wrote the first draft of the manuscript. L. Hansen provided the samples. K. Marquardt designed the study. All authors discussed the data analyses and results and contributed to the manuscript writing.

Abstract

The plastic deformation of olivine has been studied for decades. However, the precise role of grain boundaries during deformation in, for example, the dislocation-accommodated grain-boundary sliding regime, remains poorly understood. Specifically, we lack knowledge regarding the manner in which grain boundaries interact with other defects, such as dislocations, during deformation. To investigate the interaction of dislocations and grain boundaries, we analyzed the structure and distribution of grain boundaries in a polycrystalline aggregate of Fo_{50} deformed in torsion (Hansen et al., 2012a). We characterized the microstructure of the aggregate using electron-backscatter diffraction and transmission electron microscopy in three perpendicular directions. An increase in plastic strain is associated with the development of a strong crystallographic preferred orientation and a grain-boundary plane distribution that evolves from a uniform distribution to one dominated by (010)-type planes. We use the *m'* factor, to evaluate the potential for transmission of dislocations across grain boundaries based on the relative orientations of slip systems between neighboring grains. With progressive deformation, our analysis indicates an increase in abundance of apparently slip-transparent boundaries until moderate strains (γ=4) are reached. Based on these observations, we propose that specific types of grain boundaries are created by dislocation activity and that the input of dislocations into grain boundaries facilitates grain-boundary sliding. Our results provide insight into the microphysics of olivine deformation and highlight the importance of the coupled study of inter- and intragranular mechanisms during rock deformation.

4.1. Introduction

The mechanical properties of Earth's upper mantle affect large-scale geophysical phenomena such as long-term flow of the asthenosphere and intermediate- to short-term deformation of the lithosphere. Viscous deformation of the mantle is central to mantle convection (e.g., Hess, 1964), vertical motion of the lithosphere in response to changes in surface loads (e.g., Christensen, 1987), the evolution of stresses at the base of major seismogenic faults (e.g., Freed, 2004), and the localization of deformation to form new plate boundaries (e.g., Bercovici, 2003; Tackley, 2000). Unfortunately, constitutive models for the viscous deformation of olivine, the primary mineral in the upper mantle, are in part empirical and require calibration through experiments. Thus, extrapolation of those models to geological conditions relies heavily on the quality of the calibration. In general, confidence in extrapolation increases if models are based on the microphysical processes facilitating deformation. Consequently, we aim to elucidate a key process in deforming rocks, the interaction of dislocations and grain boundaries, with a specific focus on the evolution of grain boundaries during deformation.

Previous studies demonstrate that grain boundaries can influence the deformation of Earth's mantle through the activation of grain-boundary sliding, and this sliding appears intimately associated with the generation and motion of lattice dislocations. In dislocation-accommodated grain-boundary sliding (disGBS), stress concentrations produced by grains sliding past their neighbors are relaxed by dislocation motion. This process is predicted to be a major creep mechanism in the upper mantle (e.g., Bollinger et al., 2019; Hansen et al., 2011; Kohlstedt and Hansen, 2015; Ohuchi et al., 2015). Alternatively, in diffusion-accommodated grain-boundary sliding, stress concentrations are relaxed by diffusion of point defects, which may also be highly relevant in the upper mantle (e.g., Maruyama and Hiraga, 2017; Miyazaki et al., 2013).

In addition, disGBS likely relies on the motion of grain-boundary dislocations. The role of grain-boundary dislocations in facilitating the actual sliding process has been discussed previously in numerous studies (e.g., Ishida and Brown, 1967; Lim and Raj, 1985; Pond et al., 1978b; Pshenichnyuk et al., 1998). Ishida and Brown (1967) proposed that grain-boundary sliding occurs as a result of a mixture of climbing and

gliding of dislocations in the grain boundary, causing relative motion and/or rotation of the grains. Dislocation glide in the grain-boundary plane can only occur if the Burgers vectors of these dislocations is parallel to the grain-boundary plane. Consequently, most types of dislocations must dissociate to glide within the boundary. If the Burgers vector of a dislocation is not parallel to the grain boundary, the movement of the dislocation requires climb and thus absorption and/or emission of vacancies. Therefore, the ease of grain-boundary sliding likely depends on the availability of grain-boundary dislocations and the structure of the grain boundary itself.

One source of grain-boundary dislocations is lattice dislocations that interact with the grain boundary. A popular model for the role of disGBS in moderating rheological behavior comes from Langdon (1994), who proposed that the overall macroscopic strain rate depends on the rate at which lattice dislocations climb and are incorporated into grain boundaries. It is those newly incorporated dislocations that then give rise to grain-boundary sliding. Therefore, the overall rheological behavior hypothetically depends on interaction among the incorporation of lattice dislocations into boundaries, the structure of the grain boundaries, and the motion of the grain-boundary dislocations that lead to sliding. Because this interaction should involve a link between grain-boundary structure and dislocation-boundary interaction, we aim to elucidate the microphysics of disGBS in olivine by studying the evolution of the grain-boundary plane population and the influence of specific types of grain boundaries on dislocation motion. To this end, we employed electron-backscatter diffraction and statistical analyses on more than one million grain boundaries.

4.2. Methods

4.2.1 **Sample**

Here we analyze microstructural features in an olivine (Fo_{50}) aggregate deformed in torsion at constant torque in a Paterson apparatus at the University of Minnesota (sample PT-0499; Hansen et al., 2012a). Fo_{50} was implemented in this deformation experiment because it is significantly weaker than olivine with lower Fe contents (e.g., Fo_{90}). Although this material has a much higher Fe content than olivine in Earth's upper mantle, previous studies reveal that similar deformation mechanisms (Hansen et al.,

2012a, 2012b; Zhao et al., 2009) and microstructural evolution (Hansen et al., 2014) occur in Fo_{90} and Fo_{50} olivine, despite the difference in the homologous temperature of the experiments (e.g., at the experimental conditions of PT-0499, T = 1473 K and P = 300 MPa, T/T_m = 0.67 for Fo_{90} and T/T_m = 0.83 for Fo_{50} (Wang, 2016)). As described in Hansen et al., (2012a), the starting material was obtained by first calcining mixtures of San Carlos olivine (Fo_{91}) and Fe_2SiO_4 to produce Fo_{50}. Fo_{50} powders were then hot-pressed in a Paterson apparatus at 1523 K (T/T_m = 0.86) and 300 MPa. The starting material has an average grain size of ~40 μm. The microstructure and crystallographic preferred orientation (CPO) of the starting material (sample PT-0535) are presented in Figure A.3.1. The sample was deformed at a shear stress, τ, of 168 MPa, temperature, T, of 1473 K, and shear strain rate, $\dot{\gamma}$, of 5×10^{-4} s^{-1}. Deformation was carried out to a maximum shear strain at the outer radius of the sample, $\gamma_{\max}$, of 10.9. Further description of sample preparation and deformation conditions and the mechanical results are presented in Hansen et al. (2012a). Along a radial section (Figure 4.1), the finite shear strain, γ, increases linearly with the sample radius, r, from the center towards the outer edge, $r_{\max}$, according to (Paterson and Olgaard, 2000)

$$\gamma = \frac{r\gamma_{\max}}{r_{\max}}. \quad (1)$$

Analysis of the radial section therefore allows the microstructure to be characterized over a range in shear strain.

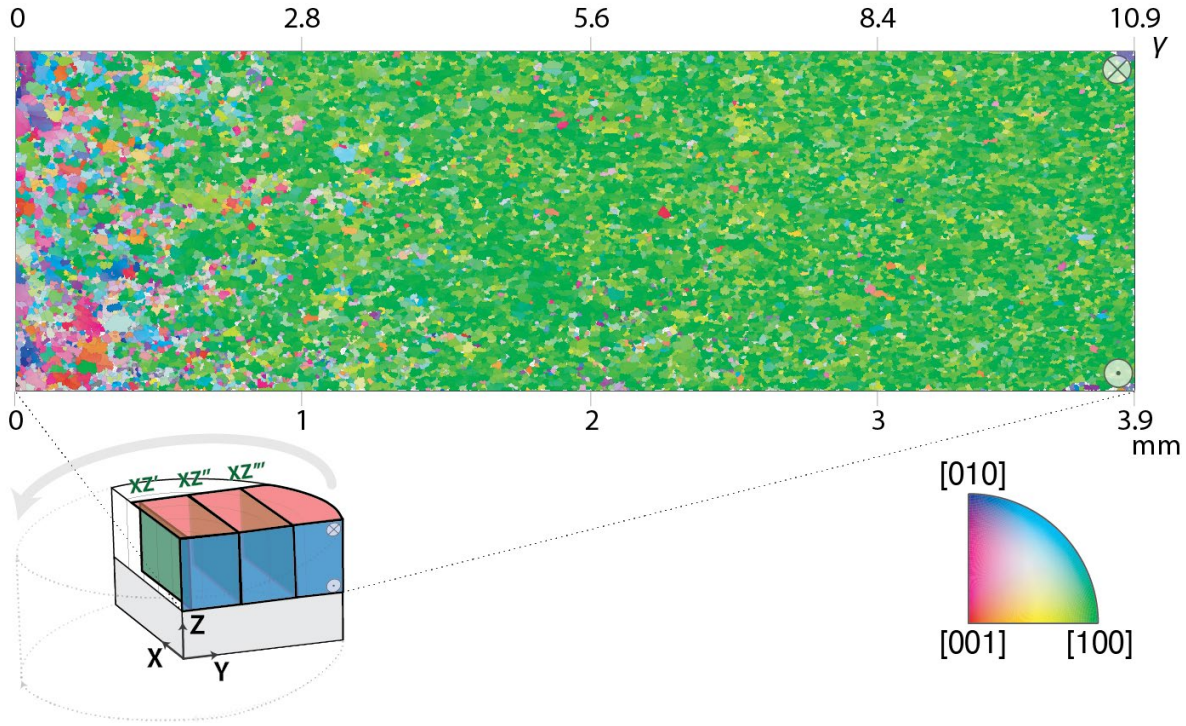

Figure 4.1: Geometry of deformation and orientation map of a radial section of the sample. Orientations are colored with respect to the X direction as indicated in the inverse pole figure. The bottom axis of the map indicates the sample radius, and the upper axis indicates the accumulated shear strain. Shear sense is top into the page, as indicated by the arrow on the bottom left diagram and at the right side of the orientation map. The torsion axis is parallel to Z and the mapped section is parallel to the YZ plane and colored blue on the bottom left diagram. EBSD maps were also acquired on the red and green sections in the bottom left diagram. The green sections are normal to the YZ plane and parallel to the Z axis, although they do not contain the Z axis. We refer to these sections as XZ', XZ'' and XZ'''. The red section is normal to the Z axis, which we refer to as the XY plane. TEM data were acquired in planes XZ', XZ'' and XZ'''.

4.2.2 **EBSD data acquisition and treatment**

Electron backscatter diffraction (EBSD) data were acquired using an FEI Scios Dual-Beam Scanning electron microscope with a 20 keV beam energy and 3.2 nA beam current, coupled with an EDAX DigiView 5 EBSD detector. EBSD data were acquired from three mutually orthogonal surfaces according to the deformation geometry (Figure 4.1). These sections consist of a radial section parallel to and containing the torsion axis (YZ plane), a transverse section normal to the torsion axis (XY plane), and a tangential section parallel to the torsion axis but not containing it (XZ', XZ'', or XZ''' plane). Mapping was conducted at a step size of 1 μm using a hexagonal grid. The chosen step size is at least 20 times smaller than the average grain size. Raw EBSD data were processed using EDAX OIM Analysis™ software. We refrained from computationally expensive routines such as dictionary indexing (Callahan and De

Graef, 2013; Marquardt et al., 2017; Roşca and Graef, 2013; Singh and Graef, 2016) or Neighbor Pattern Averaging and Re-indexing (Wright et al., 2015), as the standard cleaning routines outlined in the following proved to be sufficient. Indexed points were each assigned a confidence index, which is the difference in the number of votes received by the highest and second highest ranking possible solutions divided by the number of total possible votes. Thus, a confidence index of 1 indicates that a unique solution was found for all indexed Kikuchi bands. A confidence index close to 0 indicates that many possible solutions were found, and thus the indexing has a large uncertainty. For each EBSD map, 75 to 95% of the data had a confidence index higher than 0.1. Pixels with lower confidence indices are mainly associated with decompression cracks. Data with a confidence index smaller than 0.1 were deleted. Not-indexed or deleted pixels were not further considered. Grain boundaries were defined by misorientation angles higher than 20º bounding continuous regions of similar orientation that include more than 20 indexed pixels. Larger regions of not-indexed pixels associated with decompression cracks were excluded from the EBSD data based on the ratio between the number of pixels in the region and its boundary length. Regions of not-indexed pixels with a ratio smaller than 0.8 were removed. Low-angle grain boundaries were defined by misorientation angles ranging from 2 to 20º. The cutoff at 20° was chosen based on the observations of Heinemann et al. (2005) of low-angle grain boundaries in forsterite. Misorientation angles smaller than 2º are not considered here. The grain-boundary traces were reconstructed by connecting triple points using the EDAX OIM Analysis™ software ensuring the best-fit trace did not deviate from the mapped grain boundary by more than twice the step size (Wright and Larsen, 2002). EBSD data were further analyzed with the MTEX toolbox for texture analyses in MATLAB® (Hielscher and Schaeben, 2008). Orientation distribution functions were calculated from orientation data using a half width of 8º for all analyses. Orthopyroxene, which buffers SiO_2 activity, is present in ~1% of the sampled area, however, we only present data for olivine and olivine grain boundaries.

4.2.3 **Transmission Electron Microscopy**

Three areas were selected for transmission electron microscopy (TEM). The areas of interest were selected from low, intermediate, and high-strain regions of the sample in the XZ', XZ'' and XZ''' planes (Figure 4.1), respectively. Doubly polished thin sections

mounted in resin were prepared with a thickness of 30 µm. The samples were glued on a copper mesh grid using Araldite® resin. Samples were further thinned to obtain electron-transparent areas using a Gatan precision ion polishing system model 691. Samples were carbon coated before TEM analyses to ensure electron conduction. Additional samples of specific grain boundaries were prepared using an FEI Scios focused ion beam system. TEM lamellae of approximately 20, 15, and 0.1 µm in width, height, and thickness, respectively, were prepared using a Ga^+ beam. TEM analyses on all samples were performed in an FEI Titan operating at 200 keV. Contrast-limited adaptive histogram equalization was applied to TEM images using a Rayleigh distribution.

4.2.4 **The grain-boundary character distribution**

A 'five parameter' description of grain boundaries has been in use for several decades to describe the character of grain boundaries in polycrystalline materials (e.g., Read and Shockley, 1950; Rhines, 1970; Watanabe, 2011). The five parameters fully characterize a grain boundary. The grain-boundary character and grain-boundary plane distributions can be determined stereologically based on the work of Saylor and Rohrer (2002) and Rohrer et al. (2004). Two parameters define the axis and one the angle of misorientation (Figure A.3.2a). The description of the plane normal requires two spherical angles, the radial angle, α, and the azimuthal angle in relation to the section surface, β (Figure A.3.2b).

However, acquiring enough measurements of these parameters has traditionally been unfeasible. Progress in the automated indexing of electron channeling patterns and electron backscatter patterns (EBSP) made the determination of the grain-boundary character distribution technically feasible (Watanabe, 1984). This process has been further simplified through automated EBSP collection, i.e., EBSD (Wright and Adams, 1992). Geometrical aspects of grains, and therefore grain boundaries, can then be derived. Three types of analyses of the grain-boundary character distribution can be performed: 2-D, pseudo-3-D, or 3-D. 3-D analyses require serial sectioning of the sample by automated ion milling (e.g., Kelly et al., 2016) or by serial polishing (e.g., Khorashadizadeh et al., 2011). Pseudo-3-D analyses require two orthogonal surfaces intersecting at a sharp edge, at which the full orientation of individual boundaries can be analyzed (e.g., Randle and Dingley, 1989). 2-D analyses require only a single

surface and have the main advantage of sampling a larger number of boundary segments in less time with simpler sample preparation. 2-D analyses use the determined crystal orientations and the grain-boundary segment orientation, which is rotated into the crystal reference frame (Figure A.3.2c). Although the actual grain-boundary plane is unknown, it must be contained in a set of planes whose poles are orthogonal to the grain-boundary segment. This set of possible planes can be represented in a stereographic projection by a great circle normal to the line segment and weighted by the probability of intersecting with the planar surface. Planes that are parallel to the section are less likely to be sampled than the ones perpendicular to the section (Figure A.3.2d). If enough boundaries are observed, the intersection of the great circles gives rise to the position of the most common grain boundaries. Since non-habit planes will be sampled with a lower probability, their statistical relevance will be considerably smaller (Saylor and Rohrer, 2002).

The grain-boundary plane distributions (GBPDs) presented here are calculated from EBSD data acquired in three mutually orthogonal surfaces (Figures 4.1 and 4.2), considering the same minimum number of boundary segments for all surfaces. Orthogonal surfaces are frequently used for the stereological analyses of textured samples (Howard & Reed, 2004). The validity of using orthogonal surfaces to reconstruct 3-D microstructures from textured samples has been demonstrated by several theoretical and experimental studies (e.g., Larsen and Adams, 2004; Rollett et al., 2007b; Saylor et al., 2004). The GBPD was calculated with an angular resolution of 10º (9x9 binning). Crystal shapes were constructed considering that the GBPD provides an estimate of the average area of the grain-boundary plane for each type of boundary. We extracted the multiples of uniform distribution from the GBPD using a grid of 288 potential habit plane orientations (15º angular resolution of the GBPD). The software WinXMorph (Kaminsky, 2005) was used to reconstruct the apparent crystal shapes. The shapes were built considering that multiples of uniform distribution obtained from the GBPD are directly related to the relative area of grain-boundary planes and that the area of a given habit plane is the inverse of its distance to the center (origin) of the crystal (see Rheinheimer et al., 2015; Saylor and Rohrer, 2002). The crystal shapes allow for comparison with average crystal shapes obtained from numerical models and allows for correlation with interface properties such as grain boundary energy (e.g., Salama et al., 2020).

To date, only the GBPD resulting from surface-energy minimization via grain growth has been analyzed in olivine (Marquardt et al., 2015; Marquardt and Faul, 2018). However, the GBPD can also be influenced by dynamic processes such as deformation. Here we examine the GBPD of deformed olivine to investigate the interaction of dislocations with grain boundaries and the relationship of that interaction to the evolution of the GBPD.

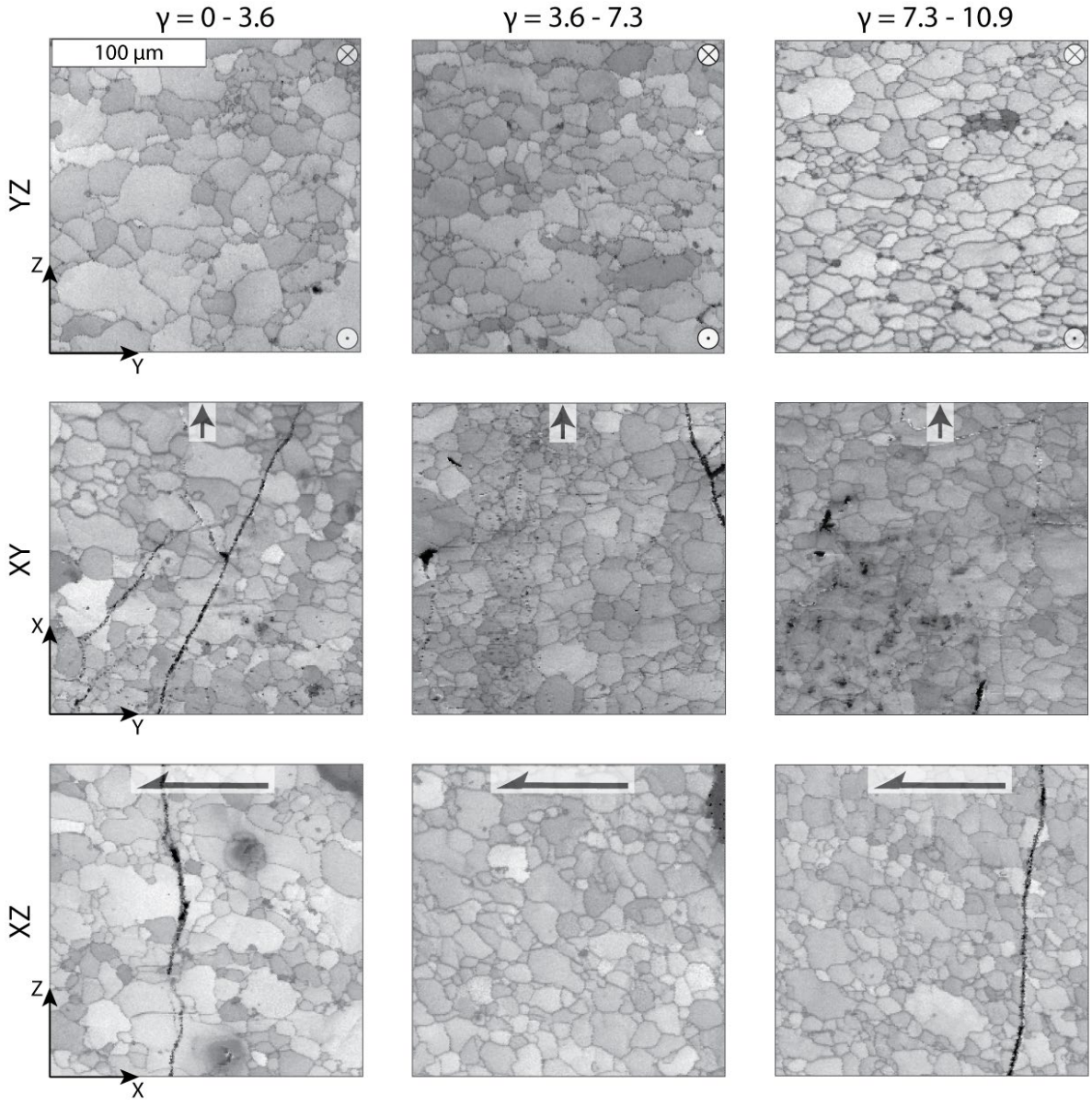

Figure 4.2: Example of microstructures observed in the torsionally deformed sample: EBSD image quality maps for different mapped surfaces and strain intervals. Lighter pixels indicate diffraction patterns with higher contrast. Maps are 200 x 200 µm. The shear sense is indicated by the arrows.

4.2.5 **Slip-transfer analyses**

The potential transfer of dislocations across individual grain boundaries (slip transfer/ transmission) is a significant process by which grain boundaries moderate macroscopic deformation (e.g., Dingley and Pond, 1979). Slip-transfer analyses are based on the hypothesis that transfer of dislocations from one grain to an adjacent grain requires geometric compatibility between their slip systems. Transmissibility is increased for smaller angles between the slip plane normals, ψ, and for smaller angles between the slip directions, κ, of the incoming (I) and outgoing (II) slip systems (Figure 4.3). This relation is described by the *m'* factor (Equation 4.2), which ranges from 0 for a boundary that is unfavorable for dislocation transfer, to 1, for a boundary that is favorable for dislocation transfer (Luster and Morris, 1995).

$$m' = (n_{\mathrm{A}} \cdot n_{\mathrm{B}})(b_{\mathrm{A}} \cdot b_{\mathrm{B}}) = cos\,(\psi) \cdot cos\,(\kappa) \tag{4.2}$$

The orientation of the slip plane normal, n, and slip direction, b, in the crystal reference frame are defined as

$$n_{\mathrm{A,B}} = g_{\mathrm{A,B}}.\, n_{\mathrm{I,II}} \tag{4.3}$$

$$b_{\mathrm{A,B}} = g_{\mathrm{A,B}}.\, b_{\mathrm{I,II}}, \tag{4.4}$$

where g is the mean orientation of the neighboring grains (A, B).

Note that equations 4.2-4.4 do not include any parameter describing the geometry of grain boundaries, for example grain boundary orientation, as in other models for slip transmission (e.g., Bayerschen et al., 2016). Thus, the *m'* factor is independent of the smoothing of grain boundaries and the EBSD step size.

For slip transfer to occur, the resolved shear stress acting on the slip systems in each grain should be maximized (Lee et al., 1989; Luster and Morris, 1995). The slip system considered to be best aligned for creep within each grain is the one with the highest resolved shear stress, τ_r, given by

$$\tau_{\mathrm{r}} = M_{ij} \otimes \sigma_{ij}, \tag{4.5}$$

where $\sigma_{ij}$is the applied stress, and M_{ij} is the Schmid tensor,

$$M_{ij} = n_i \otimes b_j. \tag{4.6}$$

For a tangential section of a sample deformed in torsion with a top-to-the-left sense of shear on the YZ plane, and assuming a simple-shear geometry, the stress tensor is given by

$$\sigma_{ij} = \begin{pmatrix} P & 0 & 0 \\ 0 & P & \tau \\ 0 & \tau & P \end{pmatrix}, \tag{4.7}$$

where P is the confining pressure and τ is the shear stress. For simplicity, we consider the local stress state at each point in the microstructure to be equal to this macroscopic stress state, although we recognize that local variations in stress can be significant (e.g., Wallis et al., 2019).

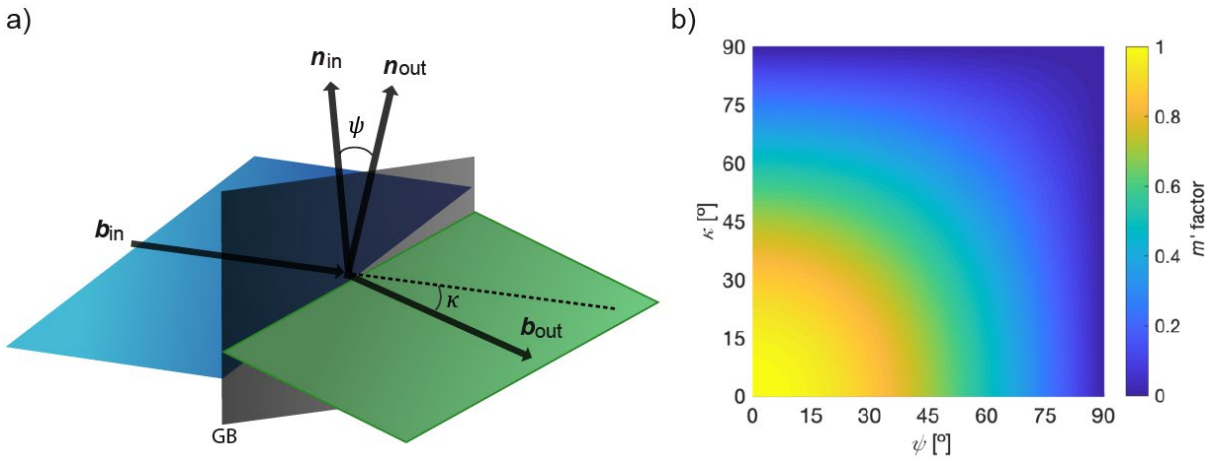

Figure 4.3: a) Schematic of slip transfer across a grain boundary. ***b*** is the slip direction (Burgers vector), ***n*** is the slip plane normal, and κ and ψ are the angles between the slip direction and slip plane normal of the neighboring crystals, respectively. b) Slip transfer is predicted to occur when both κ and ψ are small, which corresponds to an *m'* factor close to 1.

For our analysis of slip transfer in olivine, we consider the set of slip systems listed in Table 4.1. As reviewed by Tommasi et al. (2000), these slip systems represent the most often identified slip systems in olivine over a wide range of conditions. We also included slip systems identified in olivine deformed at low-temperature and high-stress conditions (Mussi et al., 2014, 2015).

Table 4.1: Olivine slip systems

Slip plane (***n***)	Slip direction (***b***)
(0 1 0)	[1 0 0]
(0 1 0)	[0 0 1]
(1 0 0)	[0 0 1]
(0 0 1)	[1 0 0]
{0 1 1}	[1 0 0]
(1 1 0)	[0 0 1]
(1 3 0)	[0 0 1]

4.3. Results

The CPO evolution in our sample is presented as a function of increasing strain in Figure 4.4. As previously demonstrated for this sample and other similar samples (Hansen et al., 2014), the [100] axes progressively align with the shear direction. The distribution of [010] axes gradually changes from a girdle to a cluster normal to the shear plane. Similarly, after moderate strains ($\gamma \approx 5$), the distribution of [001] axes changes from a girdle to a cluster perpendicular to the shear direction and within the shear plane.

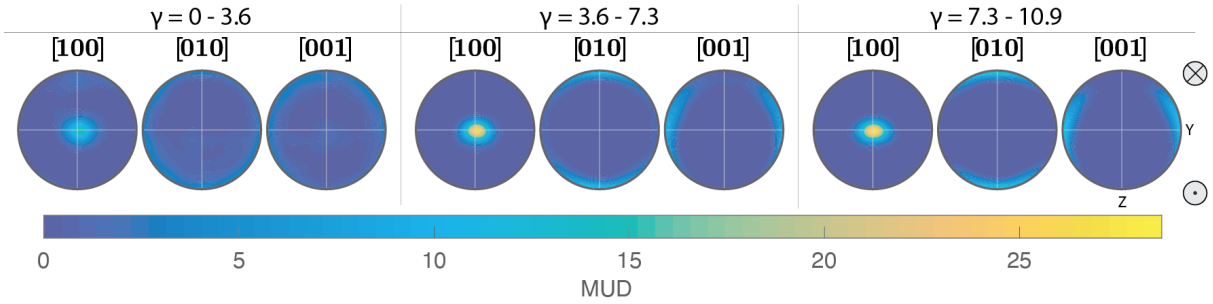

Figure 4.4: Crystallographic preferred orientations illustrated with pole figures contoured for multiples of uniform distribution (MUD). The stereographic projections are plotted in the lower hemisphere. Shear sense is top into the page, as indicated at the right side of the image. Three sets of pole figures are presented for three different ranges of shear strain.

To obtain a first approximation of the evolution of the 2-D shape of grains, we fit an ellipse to each grain and calculated the angle, θ, between the major axis and the shear direction (Figure 4.5). Figure 4.5a and 4.5b present grains colored by the angle θ at

strains of γ ≈ 5.6 and γ ≈ 9, respectively. Figure 4.5c and 4.5d present the θ distribution (rose diagram) of both samples. Figure 4.5.e presents the average shape of the fitting ellipses at strains of γ ≈ 5.6 (yellow) and γ ≈ 9 (red). The average θ for γ ≈ 5.6 is θ = 23º and for γ ≈ 9 is θ = 31º.

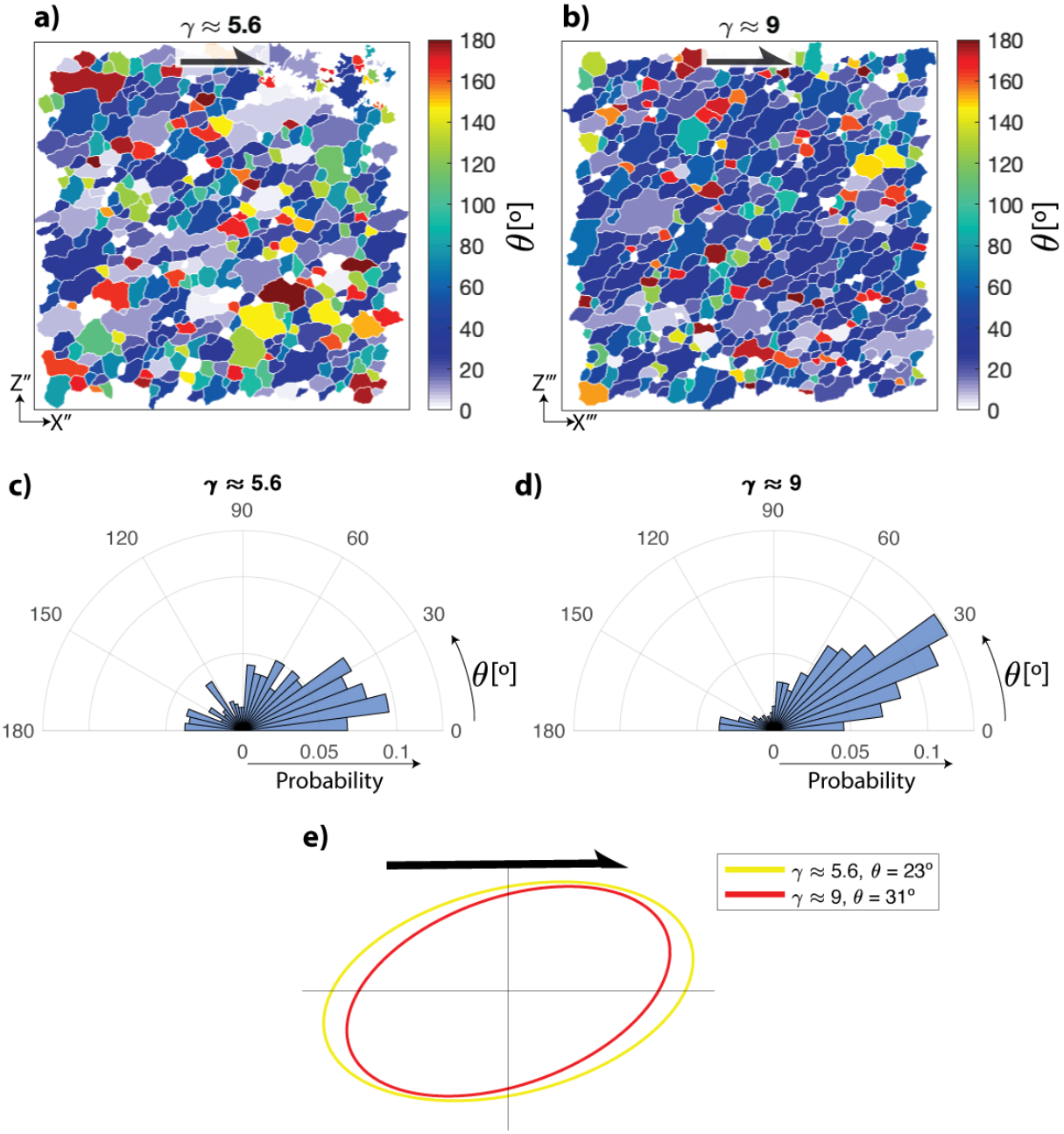

Figure 4.5: Fit of ellipses to a subset of grains on the XZ'' (γ ≈ 5.6) and XZ''' (γ ≈ 9) sections. Grains are colored by the angle, θ, between the major axis of the best-fitting ellipse and the shear direction at a) γ ≈ 5.6 and b) γ ≈ 9. Shear sense is top to the right. Polar histograms indicate the angle distribution at c) γ ≈ 5.6 and d) γ ≈ 9. e) Average shape of grains at γ ≈ 5.6 (yellow) and γ ≈ 9 (red).

To investigate the evolution in the abundance of different types of grain boundary, the grain-boundary plane distribution (GBPD) was calculated. The GBPD is presented in Figure 4.6 as a function of increasing strain. The GBPDs are divided into distributions of either high-angle or low-angle grain boundaries. Additionally, the GBPD of the starting, undeformed material is displayed in the left column. Figure A.3.3 presents a more complete representation of the crystal planes. The bottom row of Figure 4.6 illustrates the average crystal shapes estimated from the grain-boundary plane distribution, considering both high- and low-angle boundaries, although the distributions are dominated by the high-angle boundaries.

The starting material exhibits a relatively uniform distribution of grain boundaries with multiples of uniform distribution (MUD) in the range of 1 to 1.3. In other words, the data indicate no clear preference of grain boundaries for any specific crystal plane. High-angle grain boundaries (HAGBs) comprise most (75%) of the total grain boundary area and thus exhibit a similar distribution to the GBPD of all grain boundaries. Distributions of low-angle grain boundaries (LAGBs) exhibit isolated clustering of plane normals. This latter result, however, is likely due to an insufficient number of boundary segments in the analyzed maps (Figure A.3.4 and Rohrer et al. (2004)).

The first strain interval (γ = 0 - 3.6) results in a GBPD with weak clusters (1 to 2.1 MUD) of {*hk*0} type interfaces. This clustering is primarily due to HAGBs, which represent 62% of all segments. The distribution of LAGBs is essentially uniform.

The second strain interval (γ = 3.6 - 7.3) results in a stronger clustering of (100) with MUD up to 3.4. The LAGB population increases for this strain interval, comprising 43% of the total. LAGBs reveal a weak girdle distribution close to {*hk*0}.

The highest strain interval (γ = 7.3 - 10.9) results in a clustering (MUD up to 3.1) of planes close to (*hk*0), especially near (010) and (110). The same distribution is observed for HAGBs. From low to high strain, the relative amount of LAGBs continuously increases, accounting for approximately 50% of all grain boundaries in the range of strains from 7.3 to 10.9 (see also Figure 4.7). LAGBs exhibit a clustering around (010)-type boundaries with MUD values up to 2.7. Planes close to (001) are essentially absent for this strain interval.

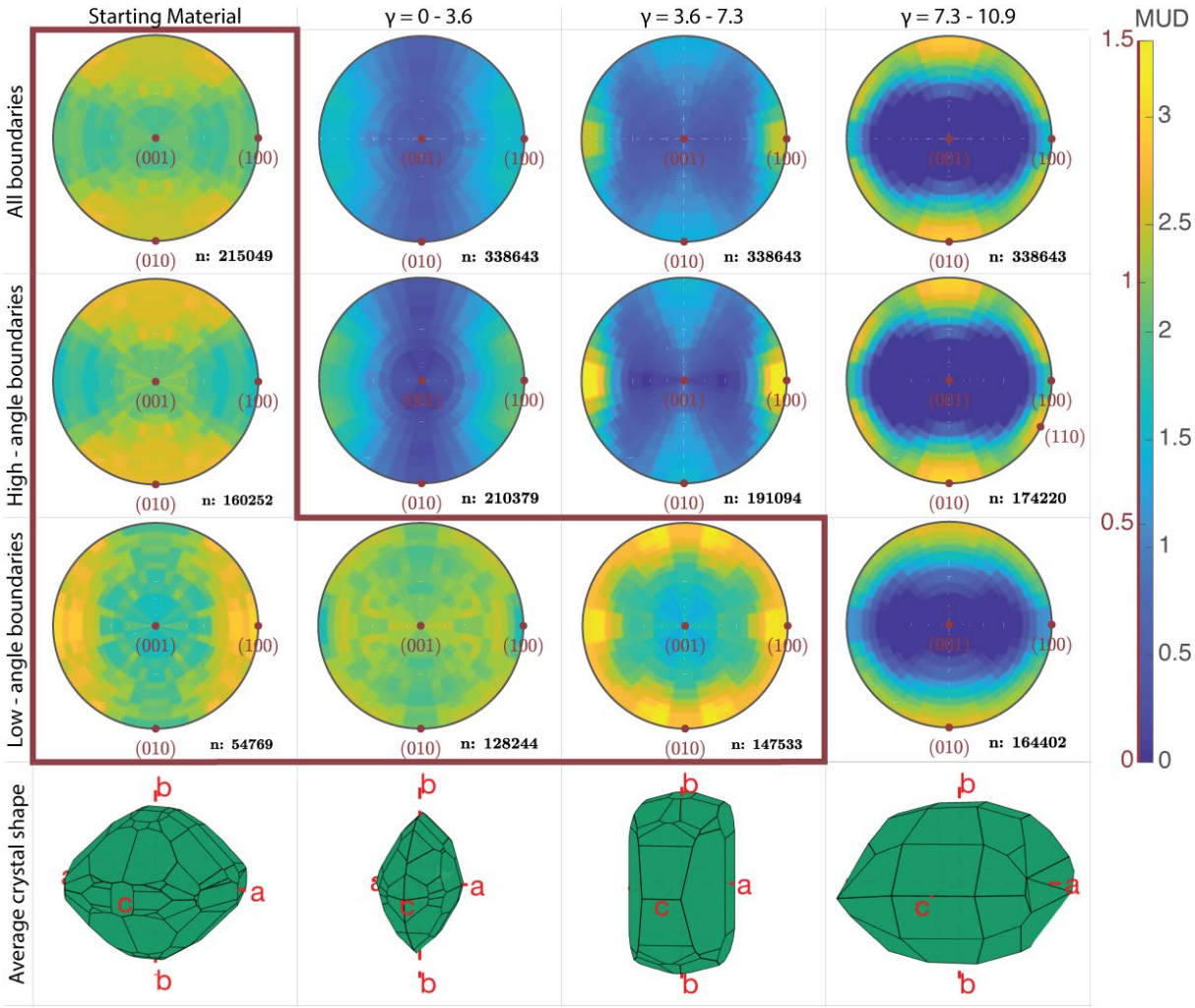

Figure 4.6: GBPDs of olivine for all, high-angle (misorientation angle higher than 20º) and low-angle grain boundaries (misorientation angle between 2º and 20º) for the starting material and for increasing strain. The pole figures within the red bounding area are scaled to have a maximum MUD of 1.5 (left side of the color scale), while the remaining pole figures are scaled to have a maximum MUD of 3.4 (right side of the color scale). The number of boundary segments (n) is given below each plot. Pole figures are upper hemisphere projections. The bottom row illustrates the average crystal shape estimated from the grain-boundary plane distribution of all boundaries.

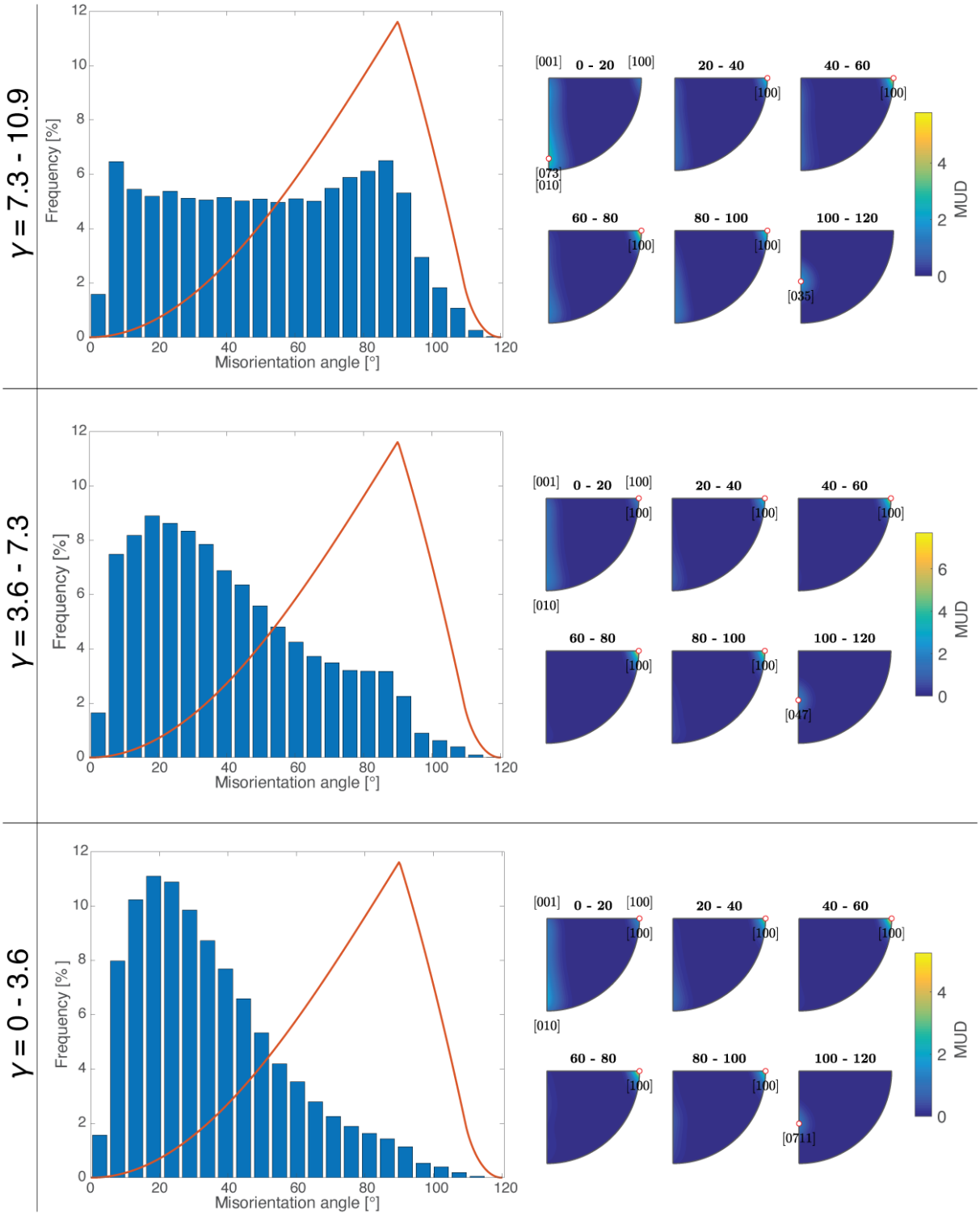

Figure 4.7: Misorientation distributions from the YZ plane of sample PT-0499 as a function of strain. (left column) Misorientation-angle distributions. Bars represent the distribution of misorientations between neighboring grains, and the red line provides the uniform misorientation-angle distribution for reference. (right column) Misorientation-axis distributions: Misorientation axes are presented in the crystal reference frame in intervals of 20 degrees from 0 to 120º. The location of maximum density of misorientation axes is indicated with a red circle, and annotations denote the corresponding axes.

In association with the evolution of grain-boundary types, the calculated values of the *m'* factor (Figure 4.9) indicate that the fraction of grain boundaries connecting grains with similarly oriented slip systems increases as deformation increases. Figure 4.9 presents the spatial distribution of grain boundaries in the YZ plane colored for the *m'* factor, which ranges from 0 to 1 as slip systems of adjacent grains are better aligned. The potential ease of slip transmission, as estimated by the *m'* factor, is predicted to increase until an accumulated shear strain of γ=4 and remain approximately constant at higher strains. The rapid initial increase of the *m'* factor is correlated with an increase in the number of grains oriented to favor activation of the [100] (010) slip system (Figure 4.10), assuming a homogeneous stress state. The [100] {011} slip system is predicted to be highly active, although the apparent resolved shear stress on this system is highest at lower strains and significantly reduced at γ>3.

To supplement information on the potential transfer of dislocations through grain boundaries and other possible dislocation-boundary interactions in greater detail, we performed TEM analyses (Figure A.3.5). The TEM analyses were performed in the XZ', XZ'', and XZ''' sections (see Figure 4.1), which allow observation of dislocations of the most likely slip system [100](010) due to the strong texture in the sample. In these sections, most grains have [001] pointing out of the plane, and thus parallel to the incident electron beam. For individual grains, the orientation was confirmed by indexing TEM diffraction patterns. Figure A.3.5 illustrates the contrasting behavior of different olivine grain boundaries. On the one hand, low-angle grain boundaries (i.e., dislocation walls) are intersected by dislocation arrays, apparently without acting as significant barriers to dislocation motion (Figure A.3.5a, b, c). On the other hand, grain boundaries with a higher misorientation truncate dislocation arrays, apparently acting as barriers for dislocation propagation (Figure A.3.5d, e, f).

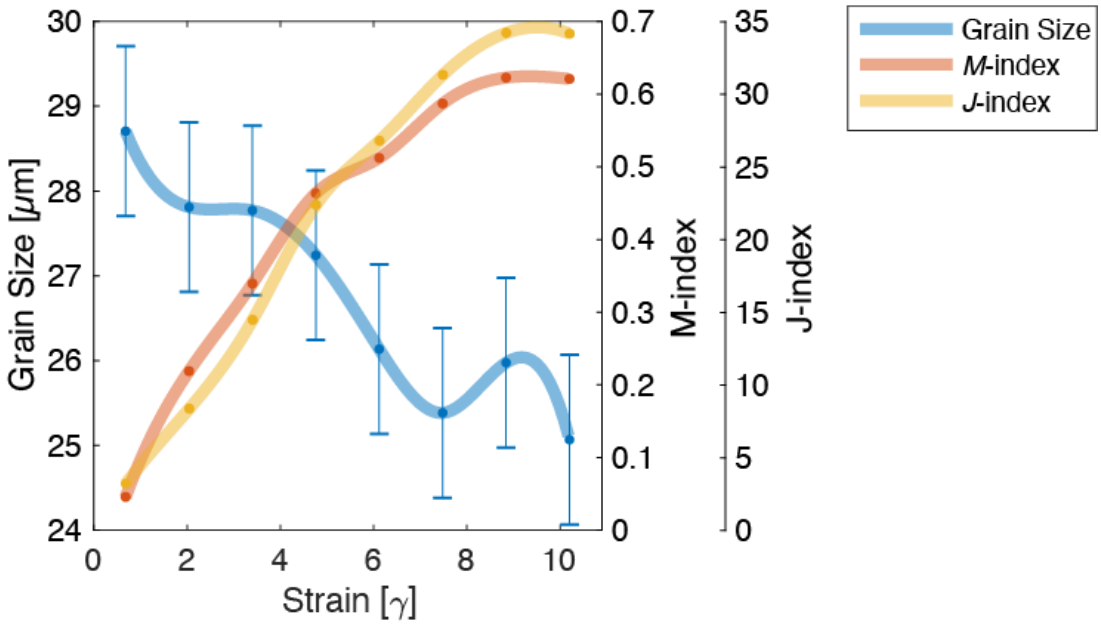

Figure 4.8: Grain size and texture strength evolution as a function of strain. Grain size is given by the longest distance between any two vertices of the grains. Texture strength is given by the *M*-index, which ranges from 0 (random fabric) to 1 (single-crystal orientation), and by the *J*-index which ranges from 1 (random fabric) to infinity (single-crystal orientation).

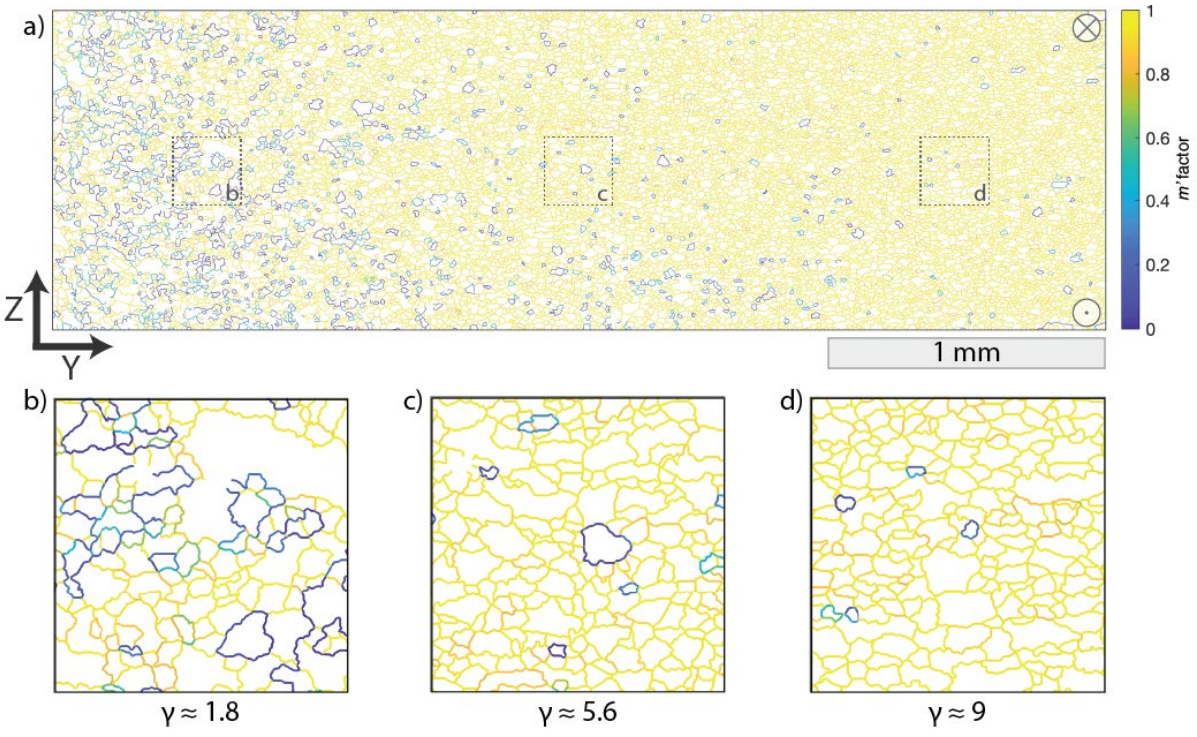

Figure 4.9: a) Grain-boundary map in the YZ plane colored according to the *m'* factor. The magnitude of the shear strain increases from left to right. Slip transfer is predicted to be easier as grains align with increasing strain. Insets 1, 2, and 3 are magnified in b ($\gamma \approx 1.8$), c ($\gamma \approx 5.6$) and d ($\gamma \approx 9$), respectively. Insets are 250 x 250 μm. Shear sense is top into the plane of the figure. The *m'* factor ranges from 0 for an impenetrable boundary (dark blue), to 1 for a transparent boundary (pale yellow).

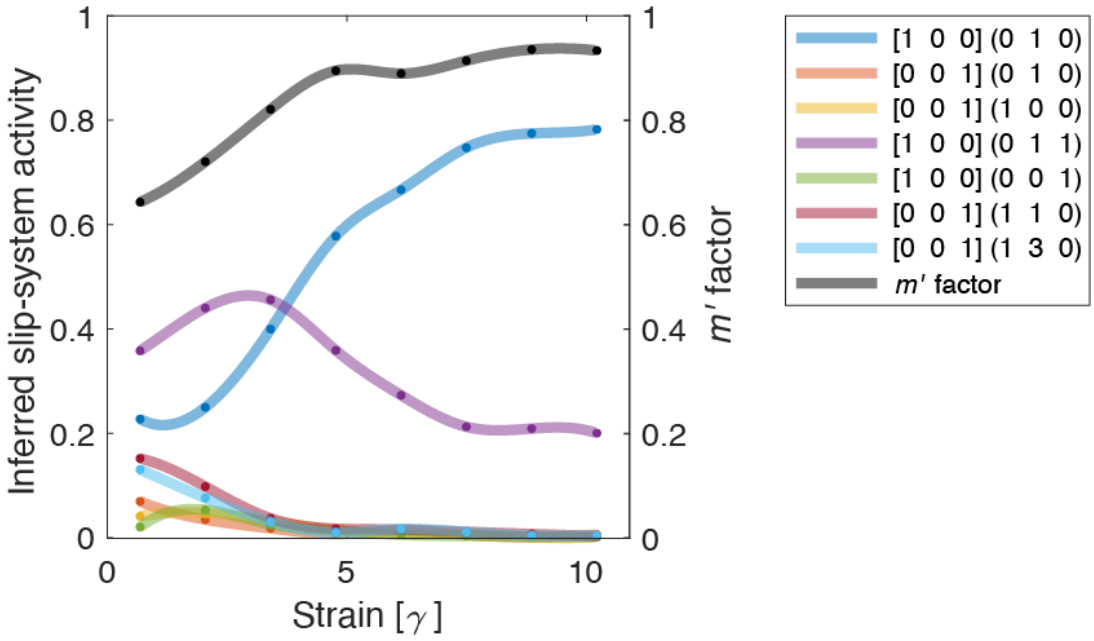

Figure 4.10: Slip-system activity and *m'* factor evolution for increasing strain. The data are presented for 8 sections of equal area along the YZ surface (see Figure 4.1). The apparent slip-system activity is given by the ratio between the number of grains in a favorable orientation for activation of a given slip system (that is, with the highest Schmid factor) and the total number of grains. The given *m'* factor is the calculated average of each section. The *m'* factor ranges from 0 for an impenetrable boundary, to 1, for a transparent boundary.

Although TEM data provide important information on the dislocation distribution, the scale of the observations prevents statistical rigor. Therefore, we focus our work on EBSD analyses to investigate the spatial distribution of lattice distortions in proximity to grain boundaries. Geometrically necessary dislocations induce gradients in the elastic and plastic distortion of the crystal (Ashby, 1970). Gradients in the distortion can be estimated from EBSD data as local variations in the lattice orientation (e.g., Wilkinson and Randman, 2010). We used the kernel average misorientation (KAM) to quantify the misorientation over a 3x3 kernel for a maximum misorientation angle of 8º, and then investigate the magnitude of local misorientation as a function of distance to the grain boundary (Figure 4.11). This approach yields a qualitative proxy for the density of geometrically necessary dislocations. The grain boundaries used in the calculations include low- and high-angle grain boundaries. If the grain boundaries were to impose obstacles for the transfer of dislocations, we expect lattice distortion to increase near the grain boundaries (e.g., see Fig. 4d in Wallis et al. (2018)). However, a correlation between the distance to the grain boundary and the local misorientation is not observed. KAM values follow similar distributions for the three considered data

sets from low-, moderate-, and high-strain portions of the sample (Figures 4.11 a, b, and c, respectively).

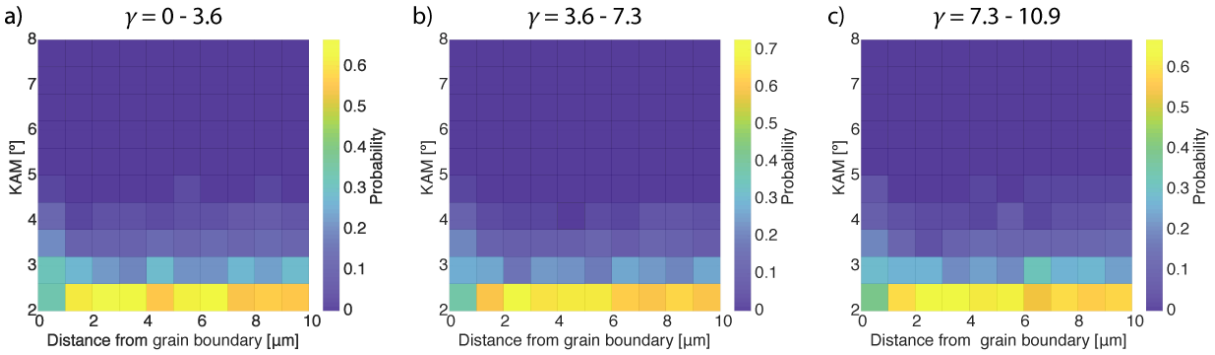

Figure 4.11: Kernel Average Misorientation (KAM) as a function of distance to the nearest grain boundary for strains intervals of a) 0 to 3.6, b) 3.6 to 7.3 and c) 7.3 to 10.9. Probabilities are calculated for each map pixel at the given distance to the grain boundary (i.e., on a column-by-column basis) to account for the higher likelihood for any given pixel to be near a boundary rather than in the center of a grain. Measurements were made in the transverse section (XY plane of Figure 4.1).

Note that the ability of the KAM measurement to detect geometrically necessary dislocations is limited by the angular and spatial resolution of the EBSD data. The minimum detectible dislocation density, ρ, is given by

$$\rho = \frac{\theta}{b\lambda}, \tag{4.8}$$

where θ is the angular resolution of the EBSD measurement, b is the magnitude of the Burgers vector, and λ, is the step size in the EBSD map (Wilkinson and Randman, 2010). The angular resolution of standard-resolution EBSD performed on olivine is on the order of 5×10^{-3} radians (Wallis et al., 2019). Given a Burgers vector of 5 nm and a step size of 1 μm, the minimum dislocation density that would produce misorientations we can detect is ~10^{13} m^{-2} (10 μm^{-2}), which is comparable to the density of dislocations next to the boundary imaged by TEM in Figure A.3.5d. Therefore, if dislocation pileups at boundaries are in abundance, they are limited to densities less than or equal to those in Figure A.3.5d.

4.4. Discussion

The sample analyzed here and others deformed in similar conditions were previously studied by Hansen et al. (2012a, 2012b, 2011). Based on the flow laws obtained from the torsion tests and the microstructural evidence, the authors interpreted the main

deformation mechanism to be dislocation-accommodated grain-boundary sliding. This mechanism was demonstrated to have a measurable grain-size sensitivity (i.e., samples are weaker for smaller grain sizes) and to produce strong CPOs. The total observed weakening of the material during torsion was attributed to both grain-size reduction and geometric softening (i.e., rotation of grains into an easy orientation for dislocation slip) associated with CPO development. As discussed by Hansen et al. (2012a, 2012b, 2011) and illustrated in Figure 4.4, the olivine CPO is consistent with dislocation motion on the [100](010) slip system, with [100] axes parallel to the shear direction and (010) planes parallel to the shear plane.

The most frequent grain-boundary planes at low strains are of the {*hk*0} type. This type of grain-boundary plane increases in abundance as strain increases (Figure 4.6). Specifically, (*hk*0)-type planes dominate the GBPD at the maximum strain reached. This distribution is notably different from the GBPD that results from normal grain growth (Marquardt et al., 2015; Marquardt and Faul, 2018). Marquardt and Faul (2018) found that, for Fo_{90}, the (001) and (0*kl*) planes dominate the average crystal habits during normal grain growth.

We suggest the observed modification of the GBPD during deformation arises from the interaction of dislocations with grain boundaries. Associated with the strong CPO are high values of the average *m*' factor, which indicates most boundaries are between grains with similar orientations of their most favorable slip system. The proportion of boundaries with high values of *m'* initially increases rapidly with increasing strain (Figures 4.9, 4.10) and becomes approximately constant after moderate strains ($\gamma \geq 4$), similar to the CPO strength (Figure 4.4 and Figure 4.8).

However, even though grain orientations are favorable for dislocation transmission, our TEM analysis provides no evidence of dislocations being transmitted across high-angle grain boundaries. Thus, it seems likely that the dislocations interact intimately with the high-angle grain boundaries. Figure A.3.5d illustrates that the dislocation spacing is reduced near the grain boundary on the left side, consistent with a model of dislocations piling up against a grain-boundary that act as a barrier (e.g., Hirth (1972)). However, lattice distortion measured with EBSD suggests dislocation pile-ups near grain boundaries are not widespread, even at low strains (Figure 4.11a), for which there is a greater abundance of grain boundaries with low values of *m*' (Figure 4.9 and Figure 4.10).

A possible explanation for the discrepancy between observations of pileup in TEM and observations of low KAM observed more broadly is that dislocations are constantly absorbed by grain boundaries. It is possible that long-range stresses (i.e., related to the extrinsic dislocations already inside the grain boundary) could prevent the continuous incorporation of dislocations (Dingley and Pond, 1979). However, as pointed out by Shirokoff et al. (1993), these long-range stresses are reduced if, once the dislocations enter the boundary, they become mobile in the grain-boundary plane, a process identified to promote grain-boundary sliding (e.g., Ishida and Brown, 1967; Pond et al., 1978b). As the new grain-boundary dislocations dissociate into partial dislocations with smaller Burgers vectors, the elastic energy of the dislocation is reduced (Dingley and Pond, 1979; Ishida and Brown, 1967; Pond and Smith, 1977). The process of dissociation of grain-boundary dislocations was previously predicted to occur in olivine by atomistic simulations (Adjaoud et al., 2012). It is reasonable to assume that grain-boundary sliding in olivine is intimately coupled to the incorporation of lattice dislocations into the boundary and their dissociation into mobile grain-boundary dislocations.

This process of incorporation and dissociation of dislocations into the boundary is compatible with existing models of disGBS that seek to explain the basic observation that more grain boundaries lead to higher strain rates. Langdon (1994) suggested that sliding on boundaries leads to stress concentrations at grain-boundary ledges or grain-boundary triple junctions, which act as sources for lattice dislocations. A larger number of boundaries provides more dislocation sources, more sliding, and faster strain rates, but the overall rate is dictated by the rate of incorporation of dislocations into distant boundaries after the dislocations traverse the grain. Notably, the incorporation rate is likely limited by the rate of dissociation and climb of dislocations already in the boundary. Indeed, in a set of early models, Gifkins (1976) suggested that the overall strain rate is limited by the dissociation and movement of grain-boundary dislocations. Those grain-boundary dislocations are thought to pileup in the boundary, and their mutual annihilation by climb within the boundary limits the rate of sliding. Pshenichnyuk et al. (1998) later provided a model that incorporates all of these processes in which sliding requires lattice dislocations to enter the boundary, but the rate at which lattice dislocations are incorporated is ultimately limited by the climb and annihilation of grain-boundary dislocations. This model is consistent with the observations of Yoshida et al. (2004), in which zirconia bicrystals exhibit faster rates of sliding if lattice dislocations

are more active. Although we cannot discuss the influence of this process on the overall strain rate in olivine, our data suggest that dislocation incorporation into grain boundaries is a key process.

Our observations have implications for the process of formation of new grain boundaries in olivine during deformation. As a starting point, our data support that, with increasing strain, the glide and climb of lattice dislocations form LAGBs (Read and Shockley, 1950), consistent with the microstructures associated with dynamic recrystallization frequently observed in minerals (e.g., Lloyd et al., 1997; Urai et al., 1986). As illustrated in Figure 4.12 a-c, we suggest that, as new HAGBs are formed from LAGBs, progressive shape change of the crystal associated with the most active slip system will lead to tilting the high-angle boundary around a misorientation axis in the glide plane and normal to the Burgers vector (akin to tilt-wall formation). Therefore, we argue that the character of grain boundaries produced during deformation is intimately linked to interactions with dislocations of the dominant slip system.

In summary, the key observations and interpretations are:

1. The fraction of potentially slip-transparent boundaries, as measured by the *m'* factor, increases with strain.
2. TEM data indicate that low-angle boundaries are not efficient barriers for slip transfer. In contrast, based on the *m*' factor, high-angle boundaries are inferred to be strong barriers for dislocation motion, but we did not observe an abundance of lattice distortion near those boundaries. This observation suggests that dislocations are absorbed by high-angle grain boundaries. The incorporation of dislocations into grain boundaries provides a recovery mechanism for intragranular deformation.
3. High-angle boundaries are dominated by (*hk*0)-type planes, which we suggest results from continued absorption of dislocations on the [100](010) slip system into the LAGB and simultaneous competing grain growth. The formation of new grain-boundary planes in this fashion must be associated with grain rotation, which inherently involves grain-boundary sliding (e.g., Lim and Raj, 1985; Pond et al., 1978b)
4. The mechanical data presented in Hansen et al. (2012a) demonstrate mechanical weakening with decreasing grain size, which they interpreted to reflect increasing rates of deformation in the disGBS regime. Our observations suggest that the rate of grain-boundary sliding and therefore, the overall strain

rate, will depend on the rate at which dislocations are delivered to and assimilated into the boundaries, consistent with existing models of disGBS.

Our extension of existing models allows us to predict the grain-boundary types potentially resulting from different slip system activities (Figure 4.13). For example, the HAGBs in this sample are dominated by (*hk*0)-type planes (Figure 4.6). Based on the indices of these planes and the available slip systems for olivine, we suggest these HAGBs are produced mainly through slip on the [100](010) slip system (Figure 4.13), which is also consistent with the slip system predicted by the Schmid analysis to be most active in this experiment (Figure 4.10). This prediction is similar to the criterion established by Signorelli and Tommasi (2015, see their equation 4) for the formation of new LAGBs. The large population of (*hk*0)-type boundaries (Figure 4.6) is consistent with these grain boundaries forming from LAGBs as a result of continued [100](010) slip (Figure 4.12 d-e). The input of dislocations into the grain boundary continuously induces small rotations of the grain-boundary plane. This change in the grain-boundary plane orientation induces stresses in adjacent grains. If the neighboring grain does not have a slip system oriented favorably for dislocation transfer (Figure 4.12 f), this stress either causes nucleation of new dislocations or induces a rotation on the neighboring grain. In order to rotate, a sliding motion at the interface is required (e.g., Lim and Raj, 1985; Pond et al., 1978b).

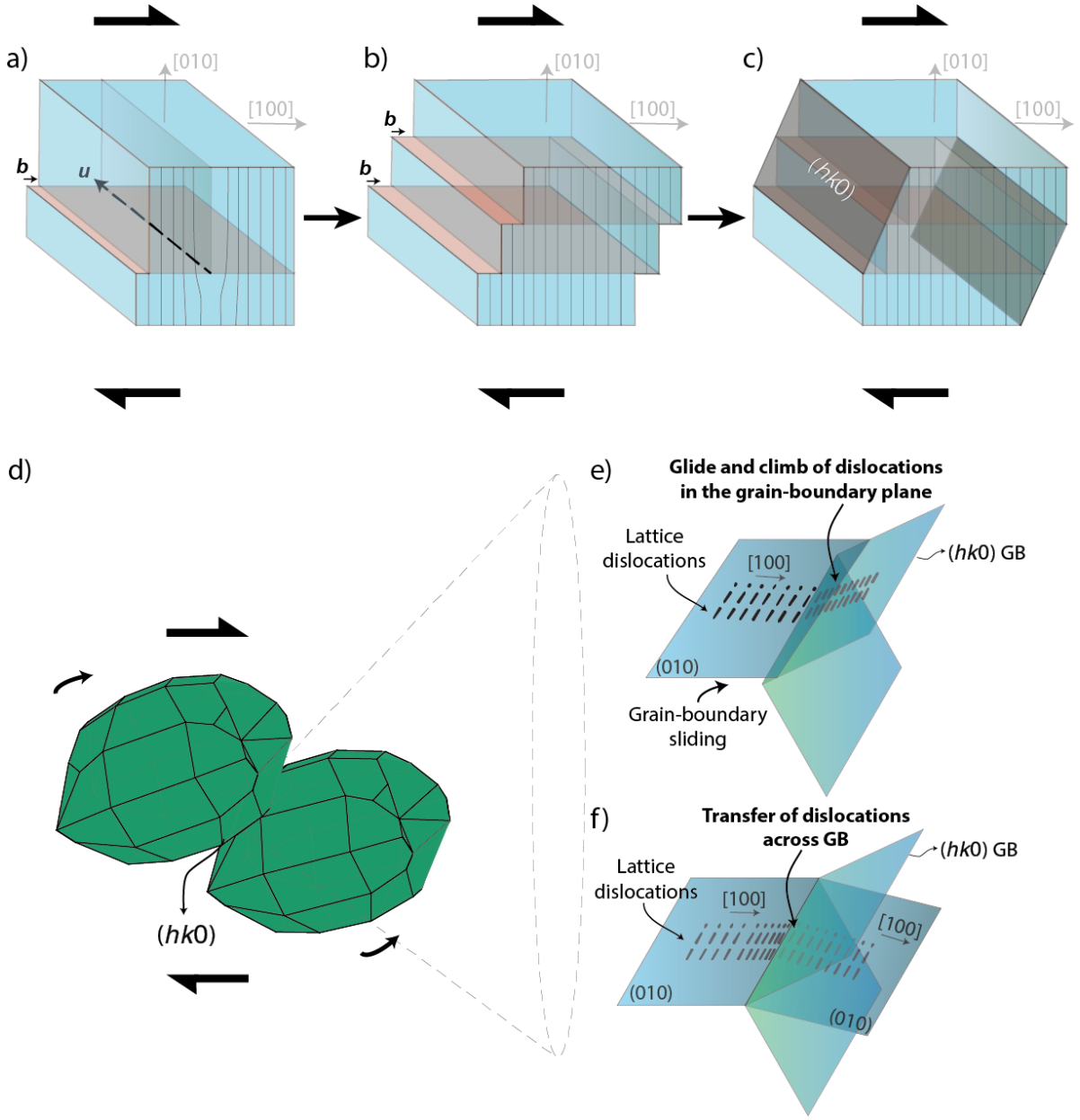

Figure 4.12: Schematic model of the proposed grain-boundary formation mechanism and its influence on grain-boundary sliding. a) A dislocation with line direction ***u*** glides through the crystal on the [100](010) slip system, shearing the crystal by one Burgers vector, ***b***. b) Progressive deformation leads to continued shearing of the crystal. c) As a result of the general shape change of the crystal, the grain boundaries become parallel to approximately (140). The continuous absorption of dislocations into the grain boundaries leads to relative rotation between grains d) and e), which progresses until the neighboring grains are oriented in such a manner that f) dislocations are easily transferred to the neighboring crystal. This transfer occurs when the burgers vectors of the active dislocations in neighboring lattices are close to parallelism.

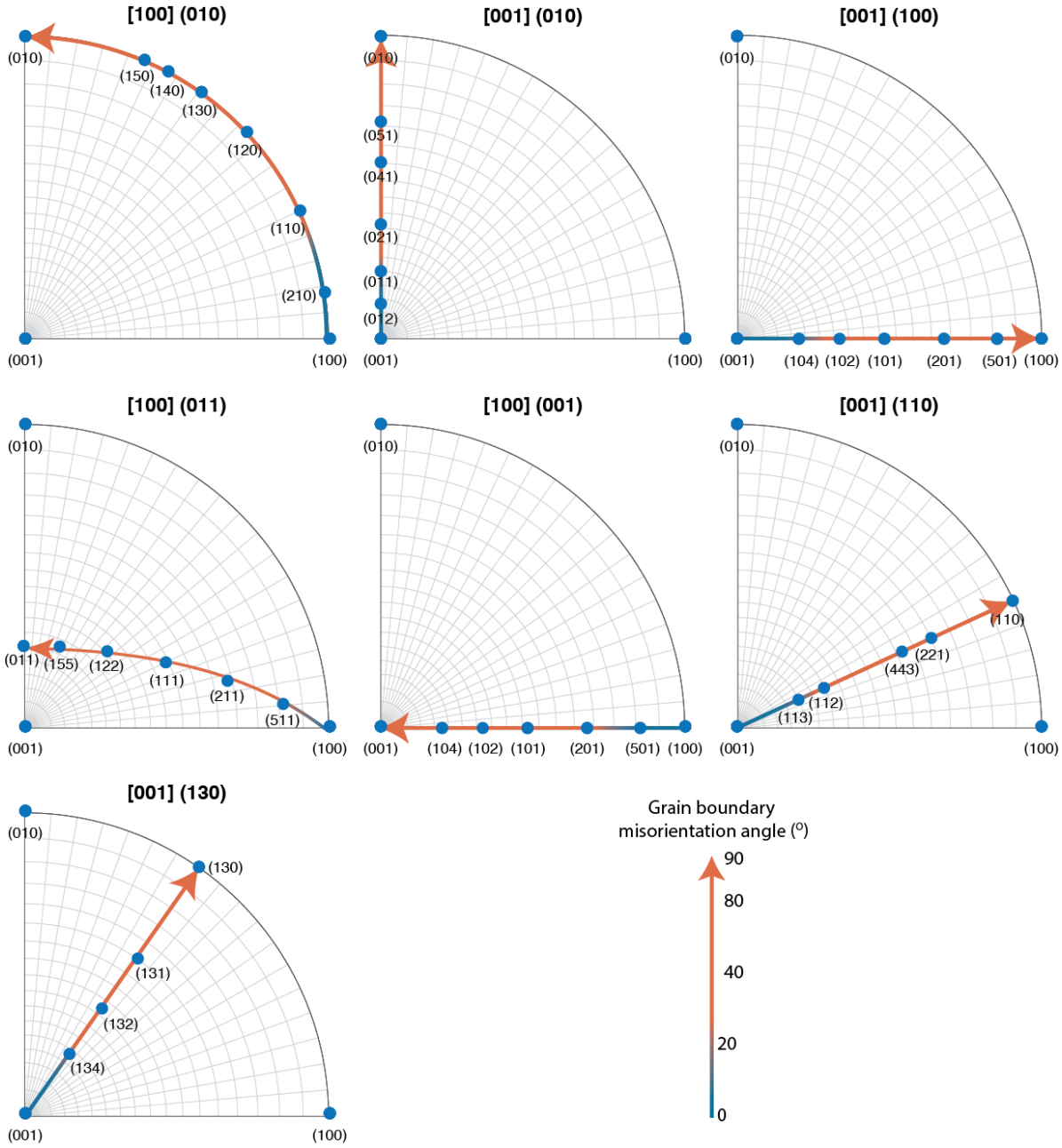

Figure 4.13: Equal-angle stereographic projection illustrating the formation of high-angle grain boundaries due to dislocation creep, assuming that only edge dislocations from the slip systems provided in Table 4.1 are involved and that only one single slip system is active in each case. The poles to the grain boundaries are marked with blue dots. The arrows indicate the evolution of low-angle grain boundaries (blue) to high-angle grain boundaries (red).

Based on the discussion above, a sustained input of dislocations into HAGBs would imply continuous rotation of the boundaries. This rotation of the boundary plane would also be associated with an increase in boundary area, and therefore an increase in surface energy. Note that dynamic recrystallization does involve a reduction in strain energy due to the formation of LAGBs, which have lower energies compared to the same amount of dislocations distributed in the crystal lattice (Read and Shockley,

1950). In contrast, it has been previously suggested that, in static systems, grain-boundary energy reduction is dominated by reduction of single-crystal surface energies, promoting boundaries with low-index planes and low energy and resulting in a GBPD inversely related to the anisotropic grain-boundary energy (e.g., Rohrer, 2011). Correspondingly, Marquardt et al., (2015) found that (010) and (001) planes in olivine are the most abundant planes formed during normal grain growth.

We suggest that both of these processes are operating in our experiment. The increase in boundary area resulting from the incorporation of dislocations (dynamic recrystallization) competes with the process of energy minimization due to grain-boundary area reduction (grain growth), leading to the emergence of a stable, statistically preferred boundary plane in the proximity of (*hk*0).

The predominance of the (*hk*0)-type boundary might also be influenced by the kinematic framework. For example, our analyses of the shape-preferred orientation (Figure 4.5) indicate that the long axes of grains align with the instantaneous stretching axes and their preferred direction does not evolve significantly with strain. This stable shape-preferred orientation is consistent with the balance of processes described above. Furthermore, the combination of a stable shape-preferred orientation and a stable CPO clearly suggest that the dominant grain-boundary plane will be stable. However, kinematic frameworks other than simple shear should result in a different relationship between the grain long axes and the CPO, and therefore a different GBPD, which is a hypothesis to be tested by future work. Interestingly, Miyazaki et al. (2013) did not observe a difference in dominant grain-boundary plane between experiments on forsterite conducted in compression and extension, observing that (010) and (001) were the most prevalent boundaries regardless of the kinematics. These experiments were in the diffusion creep regime, and therefore, we further hypothesize that dislocation-dominated mechanisms couple the GBPD to the kinematics whereas diffusion-dominated mechanisms do not.

The model for grain-boundary evolution proposed here can help predict the predominant type of grain boundary in Earth's upper mantle. Hansen et al. (2011) provided evidence of disGBS as a dominant mechanism for olivine deformation in lithospheric shear zones. Supporting evidence provided by Kohlstedt and Hansen (2015) from calculations based on laboratory data and by Ohuchi et al. (2015) from experiments at conditions of the middle of Earth's upper mantle, suggests that disGBS might be the main mechanism of olivine deformation throughout much of the upper

mantle. Our results support the inference that the evolution of the grain boundary population is a key feature of deformation in this regime. Thus, the microstructural evolution we observe may characterize the microstructural evolution throughout the upper mantle. Specifically, we demonstrate here that certain grain boundaries (i.e., (*hk*0)-type boundaries) form and evolve as a result of deformation and activation of a specific slip system. If our model for the evolution of the GBPD is characteristic of the upper mantle, then the activation of different slip systems will result in different GBPDs. Therefore, the GBPD could also be sensitive to thermochemical conditions. Different effects of varying grain boundary types on a wide range of geophysical properties are to be expected. For example, the existence of certain grain boundaries with higher electrical conductivity was suggested by Pommier et al. (2018) and cited as a key mechanism for generating electrical anisotropy in Earth's interior.

We emphasize that our study only investigates grain-boundary dynamics in a single sample deformed under a single set of conditions, yet we observe a markedly different GBPD than observed in static systems (e.g. Marquardt et al., 2015; Marquardt and Faul, 2018). Further understanding of the specific role of grain boundaries in olivine deformation should investigate the effects of grain size, strain rate, geometry and magnitude of stress, water content, melt fraction, segregated elements at the grain boundaries, interphase boundaries, and the activity of specific grain-boundary dislocations. Bicrystal experiments seem particularly well suited to these future studies since they allow direct correlation of grain-boundary structure to macroscopic properties (e.g., Dingley and Pond, 1979).

4.5. Conclusions

The role and evolution of olivine grain boundaries during plastic deformation was investigated using EBSD analysis of a polycrystalline sample of olivine (Fo_{50}) deformed in the disGBS regime. Our results suggest that grain boundaries act to promote deformation through interaction with dislocations via grain-boundary sliding. In disGBS, grain boundaries evolve as a consequence of dislocation interaction with the grain boundaries. The formation of specific grain-boundary plane distributions can be linked to specific dynamic processes, in our case a combination of normal grain growth and dynamic recrystallization in the presence of a dominant slip system, [100](010). It has been demonstrated that anisotropy in grain-boundary energy affects grain growth

rates (Salama et al., 2020). The formation of low-angle grain boundaries and their evolution into high-angle grain boundaries involves crystal rotation, which geometrically requires grain-boundary sliding. We found evidence of dislocations being transmitted across low-angle grain boundaries but not across high angle grain boundaries. For grains separated by a high misorientation (low *m'* factor), our data suggests that the dislocations are instead absorbed into the grain boundaries, causing the grain-boundary plane orientation to change and neighboring grains to rotate. During simple shear of fine-grained olivine (Fo_{50}) in the disGBS regime, dislocation creep on the [100](010) slip system causes CPO development and controls the formation of (*hk*0)-type grain boundaries, especially those close to (010) and (110) at higher strains. Consequently, we suggest that if different dislocation systems are activated, different types of grain boundaries will be created. Because different grain boundaries have different physical properties (Sutton and Balluffi, 1995), grain-size sensitive geophysical observables, such as electrical conductivity (Pommier et al., 2018; ten Grotenhuis et al., 2004) and seismic attenuation (Jackson et al., 2002) may exhibit variable responses accordingly.

Acknowledgments

We thank C. Bollinger, R. Farla, F. Heidelbach, Z. Michels, N. Miyajima, M. Thielmann, and D. Wallis for discussions. Furthermore, the manuscript has benefitted from detailed and constructive reviews of T. Hiraga and S. Demouchy, which were highly appreciated. This work was supported by the Deutsche Forschungsgemeinschaft (DFG), grant no. INST 91/315-1 FUGG and DFG grant MA 6287/6 to Katharina Marquardt. Data supporting the conclusions will be made available in a repository that supports the FAIR principles.

Chapter 5: Pressure dependence of olivine grain growth at upper mantle conditions

Filippe Ferreira[1], Marcel Thielmann[1], Robert Farla[2], Sanae Koizumi[3], Katharina Marquardt[1,+]

[1] Bayerisches Geoinstitut, Universität Bayreuth, Bayreuth, Germany

[2] Deutsches Elektronen-Synchrotron (DESY), Hamburg, Germany

[3] Earthquake Research Institute, Tokyo, Japan

[+] Now at Faculty of Engineering, Department of Materials. Imperial College of London, London, UK

Corresponding author: Filippe Ferreira (filippe.ferreira@uni-bayreuth.de)

This chapter is under review at the *Journal of Geophysical Research: Solid Earth*

Author Contributions:

F. Ferreira performed the experiments, collected and analysed the data and wrote the first draft of the manuscript. M. Thielmann and K. Marquardt contributed to data analysis and manuscript writing. R. Farla assisted with the multianvil experiments and contributed to manuscript writing. S. Koizumi provided vacuum-sintered olivine aggregates. K. Marquardt designed the study.

Abstract

The grain size of olivine influences several processes in the Earth's upper mantle such as mass and heat flux. However, grain growth, one of the main processes controlling grain size, is still poorly constrained for olivine at upper mantle conditions. Experimental data on grain-growth kinetics of olivine is to date restricted to pressures of up to 1.2 GPa (corresponding to depths ≈ 50 km). To evaluate the effects of pressure on grain growth of olivine, we performed annealing experiments using hot-isostatically-pressed synthetic aggregates of olivine plus 6 and 13 vol.% of pyroxene. The experiments were performed at pressures ranging from 1 to 12 GPa and temperatures from 1323 to 1793 K, using piston cylinder and multianvil apparatus. We determined grain-size distributions for all experimental run products using Electron backscatter diffraction. The best fit to the resulting data requires an activation volume of 4.3×10^{-6} m^3/mol. This value is similar to previously reported activation volumes for silicon grain-boundary diffusion at high pressures. This indicates that grain growth of dry, melt-free olivine in the upper mantle is likely controlled by silicon grain-boundary diffusion. Notably, our data show that the olivine grain-growth rate is reduced as pressure increases. These results suggest that with increasing depths in the Earth's upper mantle, the reduction of grain-growth rates due to increasing pressure may offset the temperature effect. In consequence, this may result in smaller average grain sizes and thus promote a transition from grain-size insensitive dislocation creep to grain-size sensitive diffusion creep at shallower depths than previously expected.

Plain language summary

The grain size of olivine, the major mineral phase in the Earth's upper mantle, influences several processes in this region such as mass and heat flux. However, we lack information on how pressure affects grain growth, one of the main processes controlling grain size. Experimental data on grain-growth of olivine is to date restricted

to pressures of up to 1.2 GPa (corresponding to depths ≈ 50 km). To evaluate the effects of pressure on grain growth of olivine, we performed grain-growth experiments using synthetic aggregates of olivine and pyroxene. The experiments were performed at pressures ranging from 1 to 12 GPa and temperatures from 1323 to 1793 K, using high-pressure apparatus. After the experiments, we determined the grain-size distributions using electron microscopy. Our data demonstrate that the olivine grain-growth rate is reduced as pressure increases. With increasing depths in the Earth's upper mantle, the increase in temperature leads lo increasing grain-growth rates. However, our results suggest that the reduction of the grain-growth rate of olivine due to increasing pressure may offset the temperature effect. In consequence, smaller average grain sizes could be maintained in the middle to deep upper mantle, promoting deformation mechanisms that are dependent on grain size.

5.1. Introduction

Grain size is one of the main factors affecting rock viscosity and therefore plays an important role in different geodynamic processes. Through its influence on rock viscosity, grain size impacts the Earth's heat flux and thus its thermal evolution (Hall and Parmentier, 2003; Rozel, 2012; Solomatov, 2001), the Earth's chemical mixing and the formation of heterogeneities in the Earth's mantle (Solomatov and Reese, 2008), the dynamics of subduction slabs and plumes (Dannberg et al., 2017) and localization of deformation (Mulyukova and Bercovici, 2019; Thielmann, 2018; Thielmann et al., 2015). Grain size also has a strong effect on the interpretation of geophysical observations such as seismic attenuation (Dannberg et al., 2017; Jackson et al., 2002; Tan et al., 1997) and electrical conductivity (Pommier et al., 2018; ten Grotenhuis et al., 2004). The grain size in the Earth's mantle is controlled by a few factors: grain-size reduction via dynamic or static recrystallization, grain growth and phase transitions (Solomatov and Reese, 2008). When considering deeper parts of the upper mantle (depths > 200km), static and dynamic recrystallization become less important as shear stresses decrease and diffusion creep arguably becomes the main deformation mechanism (Karato, 1992). Thus, grain growth is likely the most important factor controlling grain sizes in the deep upper mantle.

Grain growth is a mechanism driven by the need to minimize the high energy of grain boundaries. Grain boundaries have high energy in comparison to crystal lattices. Thus, grains grow to minimize this energy by decreasing their surface area to volume ratio via grain-boundary migration. This process is called normal grain growth (Atkinson, 1988; Burke and Turnbull, 1952; Evans et al., 2001; Humphreys and Hatherly, 2004), and is commonly described by the equation:

$$d^n - d_0^n = kt \tag{5.1}$$

where d and d_0 are the grain sizes at time = t and 0, respectively, n is the grain growth exponent and k is a rate constant given by:

$$k = k_0 \exp\left(-\frac{E^* + PV^*}{RT}\right) \tag{5.2}$$

where k_0 is a material-dependant pre-exponential constant, E^* the activation energy, P the pressure, V^* the activation volume, R the gas constant and T the temperature.

Grain growth is also affected by the presence or absence of a second phase. Particles of secondary phases might lead to modifications in grain growth of the major phase (matrix) by exerting a retarding force on the migrating boundaries (Humphreys and Hatherly, 2004). This effect, known as Zener pinning (here used independent of particle size), is dependent on the properties of the moving boundary, such as energy and mobility, as well as the properties of the second-phase particles, such as its size, shape and distribution (Nes et al., 1985). Another less frequently observed phenomenon related to second-phase particles is abnormal or discontinuous grain growth of the matrix, i.e. the major phase (Hillert, 1965). Abnormal grain growth might also take place due to anisotropic grain-boundary mobility or anisotropic grain-boundary energy (Rollett and Mullins, 1997).

Grain growth of olivine, the main phase in the Earths' upper mantle (Ringwood, 1970), has been investigated by several authors (Table 5.1). Karato (1989) investigated the grain growth of reconstituted San Carlos olivine aggregates at pressures of 0.1 MPa to 1 GPa, at dry and water-saturated conditions. He found that at lower pressures, pores act as pinning particles, inhibiting grain growth. The same effect was found for water, that, when in excess (i.e., in free-water conditions), fills the pores and also act as pinning particles. At lower concentrations, however, water was found to promote grain growth. Nichols and Mackwell (1991) investigated the grain growth of San Carlos

olivine at atmospheric pressure, for varying oxygen fugacity. They found that the grain-growth rate increased for increased oxygen fugacity. Faul and Scott (2006) studied the effect of melt in the grain growth kinetics of sol-gel olivine and they found that an increase in melt content led to a decrease in the grain-growth rate. This suggests that melt also inhibits grain growth of olivine in partially molten aggregates. Ohuchi and Nakamura (2007a, 2007b) analysed the grain growth of sol-gel forsterite in the forsterite-diopside and forsterite-diopside-water systems. They found that abnormal grain growth of forsterite was abundant when the secondary phase content (diopside) was less than 20 vol.%. Hiraga et al. (2010), Tasaka and Hiraga (2013) and Nakakoji and Hiraga (2018) investigated the grain growth of vacuum-sintered forsterite aggregates with different amounts of enstatite content. They found that the increase in the second phase content reduced the rate of forsterite grain growth due to Zenner pinning. Nakakoji and Hiraga (2018) further concluded that grain-boundary diffusion is a common mechanism responsible for grain growth and diffusion creep for olivine-dominated rocks.

All these above-summarized studies on olivine grain growth were conducted at relatively low pressures (up to 1.2 GPa). However, olivine dominates the lithologies of the upper mantle to pressures of 14 GPa (e.g. Ringwood, 1970). Here we aim to investigate grain growth kinetics of olivine in aggregates containg 6% and 13 % of pyroxene (corresponding to dunite and harzburgite, respectively) at temperatures spanning from 1323 K to 1793 K and pressures from 1 GPa to 12 GPa. These parameters cover pressure and temperature conditions found in most of the Earth's upper mantle.

Table 5.1: Summary of experimental conditions for previously reported olivine grain growth experiments and the present study. *P* is pressure in GPa, *T* temperature in K, *t* experimental duration in hours and f_{Px} is the pyroxene fraction.

Starting material	*P* (GPa)	*T* (K)	*t* (h)	fO_2 / Buffer	Reported Water content	Melt content	Porosity (%)	f_{Px}	Study
San Carlos olivine	10^{-4} – 1	1473-1673	0.5-200	10^{-5} Pa, I-W buffer	water free, water saturated	small amount [1]	0 - 4,8% [2]	-	Karato (1989)
San Carlos olivine	10^{-4}	1473-1673	10-200	10 Pa – 10^{-6} Pa	water free	-	<5%	very small amount [3]	Nichols and Mackwell (1991)
Sol-gel olivine	1	1523-1723	2-700	C-CO buffer	water free	2 wt.%, 4 wt.%	-	small amount	Faul and Scott (2006)
Sol-gel olivine	1.2	1473	2-763	Ni-NiO buffer	water free	-	<1%	0.1 - 0.9	Ohuchi and Nakamura (2007a)
Sol-gel olivine	1.2	1473	1.5-763	Ni-NiO buffer	water added	-	<1%	0.1 - 0.9	Ohuchi and Nakamura (2007b)
Vacuum sintered Forsterite	5 x 10^{-12}	1633	0-50	vacuum	water free	-	-	0 - 0.42	Hiraga et al. (2010)
Vacuum sintered Forsterite	10^{-4}	1533 – 1633	0-100	-	water free	-	-	0.01 - 0.97	Tasaka and Hiraga (2013)
Vacuum sintered Forsterite	10^{-4}	1322 - 1669	500	-	water free	-	-	0.2	Nakakoji and Hiraga (2018)
Sol-gel olivine	1 -12	1323-1793	8 - 72	Ni-NiO buffer	water free	-	<0.5%	0.06, 0.13	This study

1 - Glassy phases were found in the samples

2 - Estimated from density measurements

3 - SiO_2 originated from abrasion with agate mortar

5.2. Methods

5.2.1 **Sample preparation**

Here we studied grain growth in olivine and pyroxene aggregates fabricated through a solution-gelation method. The solution-gelation (sol-gel) method is an effective process to create chemically pure and homogeneous solids (Edgar, 1973; Hench and West, 1990). The procedure used here for olivine sol-gel synthesis is similar to the one previously described by Jackson et al. (2002). The precursors used as source of SiO_2, MgO and FeO were respectively tetraethyl orthosilicate (TEOS, $Si(OC_2H_5)_4$, *Sigma-Aldrich*, purity ≥ 99.0%), magnesium nitrate hexahydrate ($Mg(NO_3)_2 \cdot 6H_2O$, *Roth*, purity ≥ 99.999%) and Iron (III) nitrate nonahydrate ($Fe(NO_3)_3 \cdot 9H_2O$, *Sigma-Aldrich*, purity ≥ 98%).

Two different batches were fabricated with different amounts of TEOS, creating SiO_2 in excess to produce 6 vol.% (FSG4 batch) and 13 vol.% of pyroxenes (FSG5 batch). The reactants were dissolved in ethanol and gelation was reached by adding NH_4OH (*Sigma Aldrich*, 25% NH_3). The gel was dried at increasing temperatures up to 773 K in air. The resulting powder was grounded and pelletized. The green body was then sintered in a gas mixing furnace with a controlled oxygen fugacity between the F-MQ and I-W buffers, while increasing temperature from 700 to 1673 K at a rate not higher than 300 K/hour. The sample was sintered at 1673 K for 8 hours and then slowly quenched by turning off the furnace power and waiting until the temperature reached 973 K, when the sample was removed from the furnace. The sintered olivine was reground, and the resulting powder pressed into a $Ni_{80}Fe_{20}$ capsule, filled at the top and bottom with a thin layer of NiO, to buffer the oxygen fugacity to the Ni-NiO buffer. The sample was kept in an oven at 423 K for at least 1 day before the capsule was weld shut. The sample was subsequently hot-pressed in a piston-cylinder apparatus at 0.7 GPa and 1473 K for 2 hours, yielding the starting material for all experiments. For the grain-growth experiments in the piston cylinder, the starting material remained in the piston cylinder and the pressure and temperature were adjusted to the desired

experimental conditions and held for the experimental duration. In preparation for the multianvil experiments, the sample pieces were cored out of the starting material and fired at 1273 K for 1 hour in a gas-mixing furnace. The firing of the samples at the respective temperature and time does not cause noticeable grain growth. These firing and annealing steps ensured that olivine aggregates were kept dry during the experiments, as water might affect olivine grain growth (S. Karato, 1989; Ohuchi and Nakamura, 2007b).

5.2.2 **Grain growth experiments**

The grain growth experiments at 1 GPa were performed in a piston-cylinder apparatus and the experiments at higher pressures in a multianvil press. The assemblies were designed to reduce any deviatoric stress on the sample during compression. The piston-cylinder experiments were conducted using a 19 mm talc/Pyrex assembly (Figure 5.1a). The temperature was monitored during the experiments with an S-type (90% Pt/10% Rh–Pt) thermocouple. The experiments were performed by adjusting pressure to the target pressure, heating the sample to the target temperature at a 100 K/minute rate and maintaining these conditions for the experimental duration. The samples were quenched by reducing the current in the sample heater, to achieve 300 K temperature reduction per minute. This step reduces thermal shock in the sample and subsequent fracturing of grains. The pressure was reduced over 8 hours. The multianvil experiments were performed using second-stage WC anvils of 11 mm truncated edge length, acting on a Cr_2O_3-doped MgO octahedra (Figure 5.1b) with an edge length of 18 mm. The experiments in the multianvil apparatus were performed in analogy to the piston-cylinder experiments, except that longer decompression duration of at least 12 hours were necessary. The temperature in the multianvil experiments was monitored using a D-type (97% W/3% Re–75% W/25% Re) thermocouple. Uncertainties in pressure for the 19 mm piston-cylinder assembly are in the order of 0.02 GPa and thermal gradients are approximately 25 K within the sample at our experimental conditions (Watson et al., 2002). Uncertainties in pressure for the 18/11 multianvil assembly are around 0.5 GPa and thermal gradients in the order of 40 K within the sample at our experimental conditions (Walter et al., 1995). No correction was applied for the pressure effect on the electromotive force (emf) of the thermocouple.

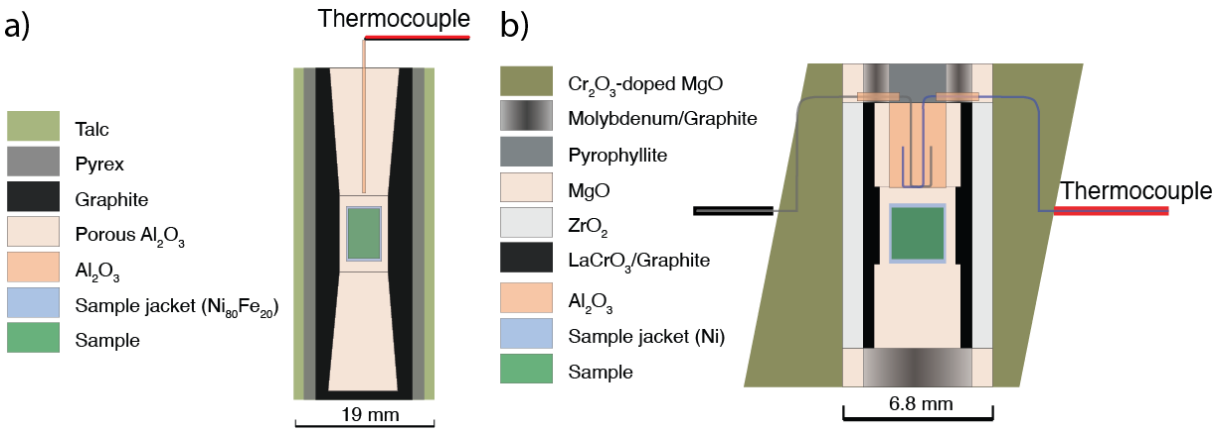

Figure 5.1: Cross-section diagrams of assemblies used in the a) piston cylinder and b) multianvil experiments.

5.2.3 **Analytical techniques and grain-size measurements**

Grain sizes were obtained from Electron Backscattered Diffraction (EBSD) data. EBSD data were collected with an *EDAX DigiView 5* EBSD detector mounted onto an *FEI Scios Dual-Beam* scanning electron microscope. For EBSD data acquisition we used an acceleration voltage of 20 to 30 keV and beam current of 3.2 to 6.4 nA. The EBSD data was acquired with the *EDAX TEAM*™ software. The step size chosen for EBSD measurements for each sample is at least 10 times smaller than the sample's average grain size and ranged from 0.1 to 0.5 µm. Thus, the uncertainty in grain size measurement of olivine for each sample is expected to be smaller than 10% of its average grain size. Pyroxene grains are in average 1.6 times smaller than olivine grains. Therefore, uncertainties in the EBSD measurements of pyroxene grains are higher, especially for smaller grain sizes, where the pyroxene grains are likely smaller than 10 times the step size in our EBSD measurements.

The EBSD data was cleaned using the *EDAX OIM Analysis*™ software. First, electron backscatter patterns were re-indexed using the neighbour pattern averaging (NPAR) method (Wright et al., 2015). Subsequently, one iteration of grain dilation processing was applied, where pixels with low indexing quality, given by the confidence index, are assigned to the orientation of neighbours with a higher indexing quality. Olivine presents a pseudo-symmetry misindexing which correlates to a misorientation of 60° around the [100] axis (e.g., Marquardt et al., 2017). A pseudo-symmetry correction was therefore applied by merging neighbouring grains sharing a boundary with a

misorientation axis of [100] and angle of 60º, keeping the orientation of the largest grain. Lastly, one more step of grain dilation was performed. Examples of the raw data and the effect of the cleaning steps are shown in Figure A.3.6. EBSD data was analysed with *MTEX* (Hielscher and Schaeben, 2008). Grains were defined as bounded regions where the misorientation angle exceeds 20°. This choice is based on the critical misorientation angle for the occurrence of dislocation arrays in olivine, as observed by Heinemann et al. (2005). Grains containing less than 20 indexed pixels were not considered.

Grain size was measured with two different methods: i) the largest dimension between any two vertices in a grain, which is the standard diameter function in MTEX, and ii) by the mean intercept length (MIL) using a rectangular grid. In the MIL method, the average grain size is given by the ratio between the length of a line and the number of grains intercepted by it. This method is usually used to measure grain sizes in micrographs (e.g., S. Karato, 1989). We adapted this method for use with EBSD measurements of a single phase. Unless stated, measurements of grain size, *d*, presented here are obtained using the first method due to faster computation. Although the methods provide different results, the results are proportionally correlated (see Table 5.3), with the first method providing grain sizes on average 1.5 times larger than the second method. However, this highlights the fact that caution should be employed when comparing absolute grain size values between different studies. Moreover, grain sizes obtained from 2D sections are often converted to 3D grain sizes by multiplying by a constant. Nonetheless, the grain sizes from 2D and 3D data are not that simply correlated (Panozzo-Heilbronner and Barrett, 2014) and therefore, we did not use any conversion factor. The grain size populations were fitted to log-normal distributions, which are often used to describe grain-size distributions (e.g., Faul and Scott, 2006; Tasaka and Hiraga, 2013).

Major and minor element chemistry was obtained from an electron microprobe equipped with a wavelength-dispersive spectrometer. The data was collected with an electron-beam voltage and current of 15 keV and 15 nA, respectively. Counting time was 20 seconds per element peak acquisition and 10 seconds for background collection. The water content was measured by unpolarized Fourier-transform infrared spectroscopy (FTIR), under atmospheric conditions. Doubly polished samples of 200 μm thickness were used. The spectra were obtained using an aperture of 100 μm and

a resolution of 2 cm^{-1}. The spectrum baseline was fitted to a spline curve estimated using the *MATLAB*'s function *msbackadj.*

5.3. Results

5.3.1 Starting material: Microstructure, chemistry, and water content

The starting material for the grain-growth experiments was characterized for its chemistry, microstructure, and water content. The chemical composition of the starting material (FSG4 and FSG5 batches) is exhibited in Table 5.2. Olivine and pyroxene have a composition of approximately Fo_{90} and En_{90}, respectively. Pt and Ni impurities are related to the crucible and capsule used during the sintering and hot-pressing, respectively. The microstructure of the starting material shows olivine and pyroxene grains uniformly distributed throughout the sample (Figure 5.2a). The grain size of olivine is generally larger compared to pyroxene. Furthermore, olivine grains surrounded by other olivine grains are usually larger than the olivine grains surrounded by pyroxene grains (Figure 5.2b and Figure 5.2c, respectively). Pyroxene grains regularly show nm-sized twinning (Figure 5.2d), causing the indexing of EBSD patterns of pyroxene to be difficult for the starting material. Note, that such twins, however, were not observed after the grain growth experiments at higher pressures (i.e., P ≥ 1 GPa). These polysynthetic twins are likely related to a transition between orthoenstatite (Pbca) and clinoenstratite ($P2_1/c$) (Ohashi, 1984), probably produced at low temperatures (T < 873 K) during quenching.

The grain-size population shows a narrow log-normal distribution with modes (Mo_{FIT}) at 1.9 µm and 2.2 µm for batches FSG4 and FSG5, respectively (Figure 5.2e). The porosity of the samples was estimated from secondary electron imaging of the starting material. The pores (or inclusions) are mainly found at the grain boundaries and, rarely, in a grain's interior (Figure 5.2d). The pore area, calculated for different samples, averages to less than 0.5%. Because grains might be plucked out during grinding and polishing of the sample, thus leaving holes that appear as porosity, the actual porosity is significantly less. No melt was observed in any of the samples. Cold compression of samples using solid pressure media might induce shear stresses within the sample (e.g., Liebermann and Wang, 2013; Rubie et al., 1993). The accumulated stresses in the sample might lead to modifications in the grain sizes. The effect of grain size

modification because of cold compression was evaluated through an experiment in the multianvil apparatus at 10 GPa without heating. The results of this experiment, Z1993, are compared to its starting material, sample FSG4, in Figure 5.2e. The similar grain-size distribution between FSG4 and the Z1993 samples, indicates that no grain-size reduction during cold compression and decompression occurred. Similarly, neither the starting material nor experimental run products from the piston-cylinder based experiments show signs of intergranular fracturing or grain size reduction (Figure 5.2a-d).

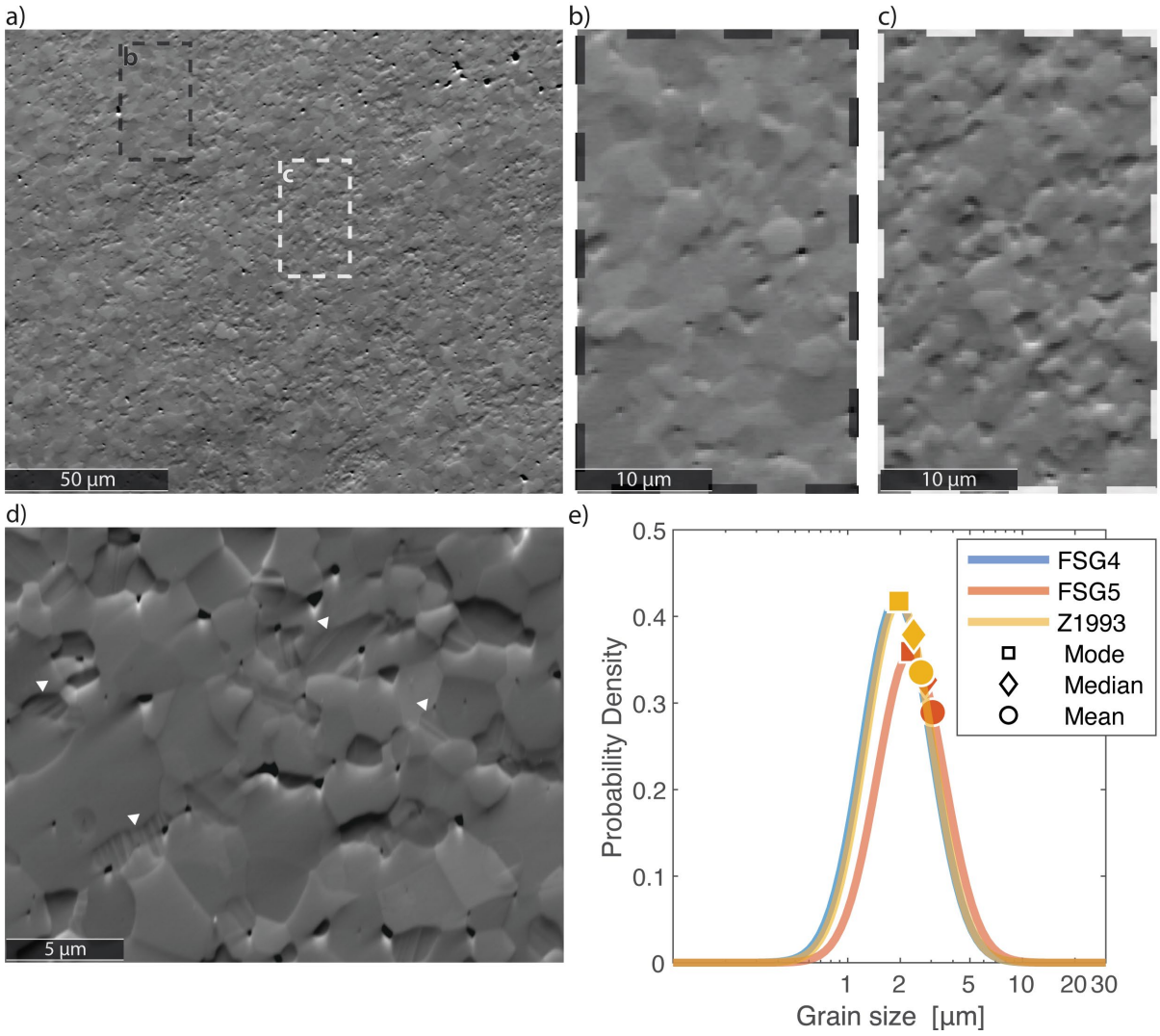

Figure 5.2: Starting material microstructure and grain-size distribution: Forescattered electron images (a-d) shows olivine grains elevated with respect to pyroxene grains. Holes appear dark. a) Olivine grains not in contact with pyroxene (black rectangle, magnified in b)) are on average larger than those surrounded by pyroxene (white rectangle, magnified in c)). d) High magnification image shows that pores/holes are mostly distributed at the grain boundaries. Pyroxene often presents lamellar twinning, as indicated by the white arrowheads. e) Grain-size distribution of starting material of batches FSG4 (6 vol.% Px) and FSG5 (13 vol.% Px) and of sample Z1993 (High pressure experiment without heating).

The water content was measured for a sample of the starting material after hot-pressing in the piston cylinder. The measured water content falls below the detection limit of approximately 50 ppm (Figure 5.3), indicating that the aggregates were dry (see Figure 5 of Faul & Jackson (2007) for an FTIR spectrum comparison of dry and wet olivine aggregates).

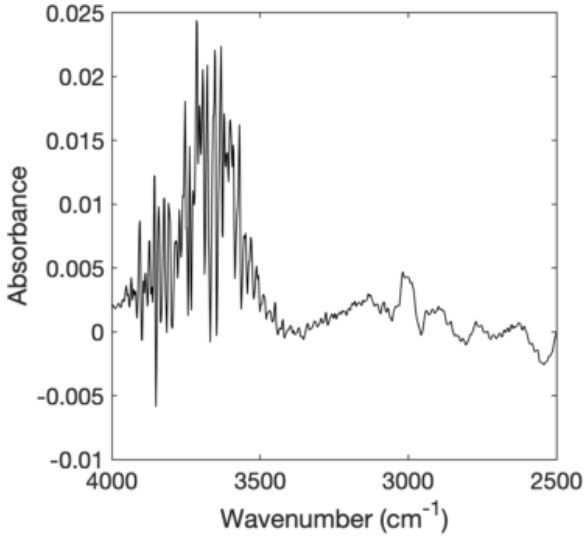

Figure 5.3: Representative FTIR spectrum measured for the starting material after sintering. Note the absence of sharp peaks in the 2950 cm^{-1} 3750 cm^{-1} range and of a broad peak around 3400 cm^{-1}. The noise is due to atmospheric moisture adsorbed to the sample surface.

Table 5.2: Electron Microprobe chemical analyses. Analyses were done over 178 and 339 randomly selected points for samples FSG4 (6 vol.% Px) and FSG5 (13 vol.% Px), respectively.

	FSG4		**FSG5**	
Oxide	**Average (wt.%)**	**Standard Deviation**	**Average (wt. %)**	**Standard Deviation**
MgO	48,67	3,15	47,91	3,47
SiO_2	42,89	3,76	43,85	4,19
FeO	9,21	1,13	9,68	1,00
PtO	0,07	0,12	0,07	0,12
NiO	0,02	0,02	0,01	0,02

5.3.2 **Grain-size evolution**

Experimental conditions were chosen to allow investigation of the effect of time, temperature, and pressure on grain growth of olivine. Figure 5.4 shows the microstructure after the experiments and Figure 5.5 shows the log-normal fit to the

grain-size distributions. Histograms of the grain-size distributions are shown in Figure A.3.7. In the series of experiments for different annealing times (Figure 5.5a-c) we analysed the effect of annealing time on grain growth with experiments performed at 1673 K, pressures of 1 and 7 GPa and experimental durations of 8 to 72 hours. In the temperature series (Figure 5.5d-f) we evaluate the effect of temperature on grain growth with experiments performed at an experimental duration of 24 hours, pressures of 1 and 7 GPa and temperatures of 1323 K to 1793 K. In the pressure series (Figure 5.5g-i) we analysed the effect of pressure on grain growth with experiments performed at an experimental duration of 24 hours, temperature of 1673 K and pressures between 1 and 12 GPa for 6 and 13% Px vol.%. Table 5.3 shows a summary of the obtained experimental data.

The grain-size distribution resulting from the series of experiments at different annealing times at 1 GPa (Figure 5.5a) demonstrates a flattening and spreading compared with the grain-size distribution of the starting material (Figure 5.2e). The average grain size for the 8 hours experiment is very similar to the average grain size of the 72 hours experiment. Similar flattening and spreading of the grain-size distribution occur only after 72 hours for experiments conducted at 7 GPa (Figure 5.5b). The temperature series of experiments at 1GPa (Figure 5.5d), demonstrates grain-size distributions similar to the starting material for the samples annealed at 1323 K and 1473 K. For the experiment at 1673 K, the grain-size distribution is flattened, with its peak shifted towards larger grain sizes. At 7 GPa (Figure 5.5e), a comparable effect is only observed for the experiment done at 1793 K.

Table 5.3: Experimental Data: P is pressure in GPa, T temperature in K, t experimental duration in hours, d average grain size in µm, d_{MIL} the mean intercept length in µm. Mo_{Fit}, μ_{Fit} and σ_{Fit} are the mode, mean and standard deviation of the lognormal fit to the grain-size distribution, respectively. f_{Px} is the pyroxene fraction as measured by EBSD and n is the number of grains analysed for each sample.

Sample	Starting Material	P (GPa)	T (K)	t (h)	d (µm)	d_{MIL} (µm)	Mo_{FIT}	μ_{FIT}	σ_{FIT}	f_{Px} (EBSD)	n
FSG4	Sol-gel Ol (Fo_{90}) + 6%Px	0.7	1473	2	2.57	1.44	1.91	0.85	0.45	0.01	1046
FSG5	Sol-gel Ol (Fo_{90}) + 13%Px	0.7	1473	2	3.06	1.91	2.29	1.02	0.44	0.07	1578
Z1993	FSG4	10	25	1	2.62	1.47	1.96	0.87	0.44	0.02	3850
Z1962	FSG4	5	1673	24	15.39	10.05	9.76	2.59	0.56	0.06	4185
Z1965	FSG4	7	1673	24	9.09	5.75	6.44	2.09	0.47	0.02	22315
Z1968	FSG4	12	1673	24	8.48	5.52	6.07	2.02	0.47	0.01	21069
A1178	FSG5	1	1673	12	6.94	4.84	4.62	1.8	0.52	0.08	1550
A1179	FSG5	1	1673	72	6.1	4.43	3.92	1.66	0.54	0.1	2296
A1182	FSG5	1	1673	8	6.13	4.41	3.88	1.66	0.55	0.1	3335
B1272	FSG5	1	1673	24	6.49	4.61	4.33	1.73	0.51	0.09	4697
B1273	FSG5	1	1473	72	4.01	2.75	2.8	1.26	0.48	0.1	6087
B1274	FSG5	1	1473	24	3.45	2.25	2.55	1.13	0.44	0.08	7146
B1275	FSG5	1	1323	24	3.16	2.01	2.36	1.05	0.44	0.11	8692
B1276	FSG5	1	1473	12	3.71	2.35	2.67	1.19	0.46	0.09	9717
Z2032	FSG5	10	1673	24	3.46	2.16	2.69	1.16	0.41	0.09	14505
Z2033	FSG5	7	1473	24	3.34	2.1	2.6	1.12	0.41	0.08	8450
Z2034	FSG5	7	1473	12	2.85	1.67	2.31	0.98	0.37	0.07	11578
Z2035	FSG5	7	1323	24	3.3	2.09	2.53	1.1	0.42	0.09	9587
Z2047	FSG5	7	1673	12	4.1	2.57	3.11	1.32	0.43	0.12	3808
Z2049	FSG5	7	1793	24	11.42	7.76	7.22	2.28	0.55	0.13	5112
Z2051	FSG5	7	1673	72	5.44	3.89	3.45	1.54	0.55	0.12	5862
Z2060	FSG5	7	1673	24	3.62	2.25	2.8	1.2	0.41	0.08	4484
Z2062	FSG5	7	1673	48	4.83	3.31	3.37	1.45	0.48	0.08	5039

The pressure series of experiments for samples with 6 vol.% of pyroxene (Figure 5.5g), demonstrates similar distributions for experiments performed at 7 and 12 GPa, while, in comparison, the experiment performed at 5 GPa shows more spread in the grain-size distribution, which is also shifted towards larger grain sizes. The experiments

performed with aggregates containing 13 vol.% of pyroxene (Figure 5.5h) present a similar effect. While the experiments done at 7 and 10 GPa exhibit similar grain-size distributions, larger grain sizes resulted at experiments performed at 1 GPa.

Figure 5.6b displays the minimum distance between pyroxene grains (see scheme in Figure 5.6a) normalized by the mean grain size. In our experiments, we observe that this distance increases for increasing pressure. The mean normalized distance between pyroxene grains at 7 GPa and 12 GPa is approximately 25% larger than at 1 GPa (1.23, 1.25 and 0.99, respectively). Figure 5.6c demonstrates the local grain-size distribution of olivine grains (FSG5 sample) as a function of the ratio between the number of pyroxene neighbours and all neighbours. Olivine grains presenting a high neighbour ratio are generally smaller than olivine grains mainly in contact with other olivine grains. This effect is independent of pressure, temperature, and duration of experiments (see Figure 5.4).

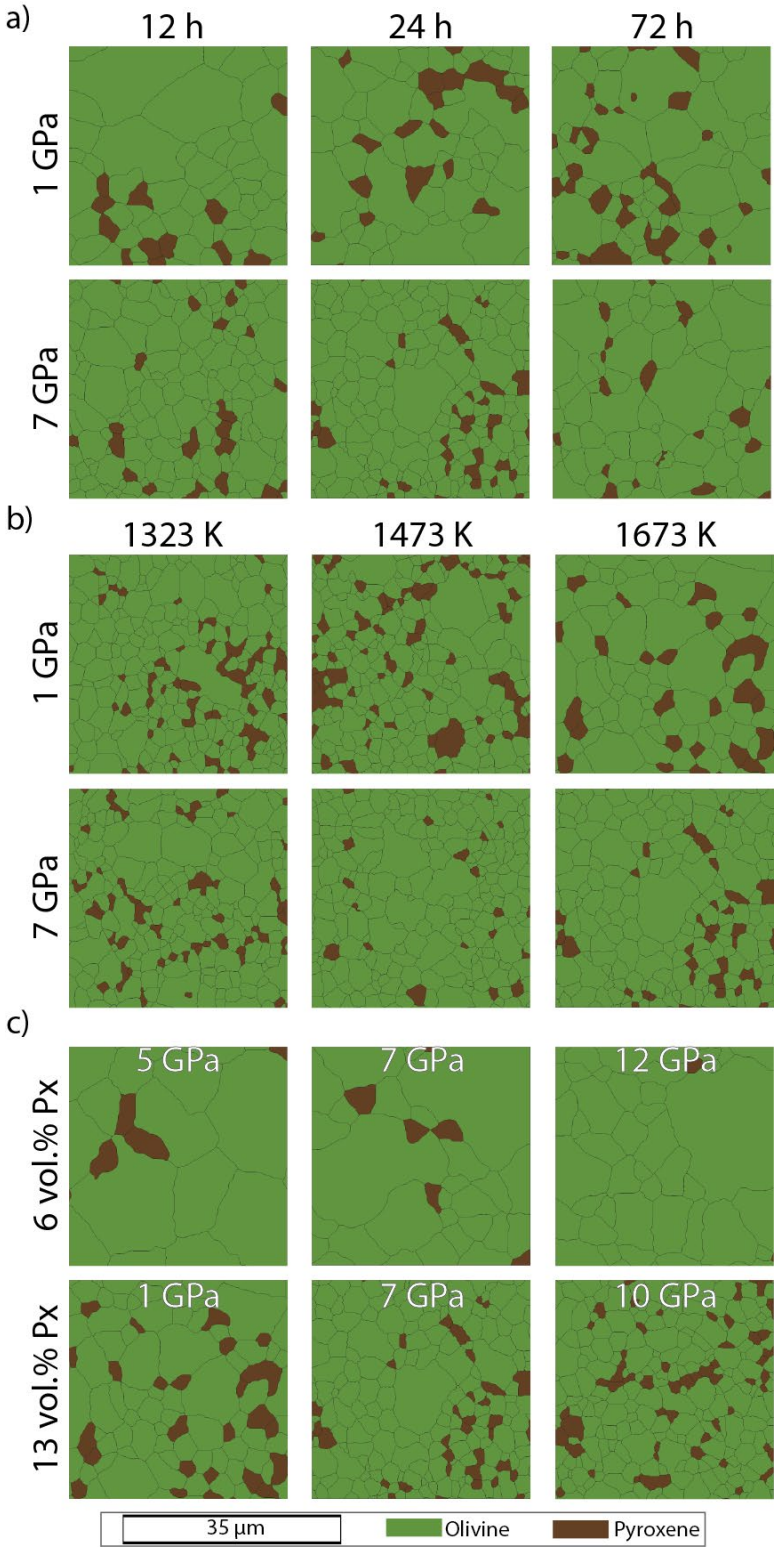

Figure 5.4: Microstructure evolution after grain growth experiments. Phase maps show a small representative subsection of the areas analysed: a) Time series of experiments b) Temperature series and c) Pressure series. Olivine grains are coloured green and pyroxene brown. Plot areas are 35 x 35 µm.

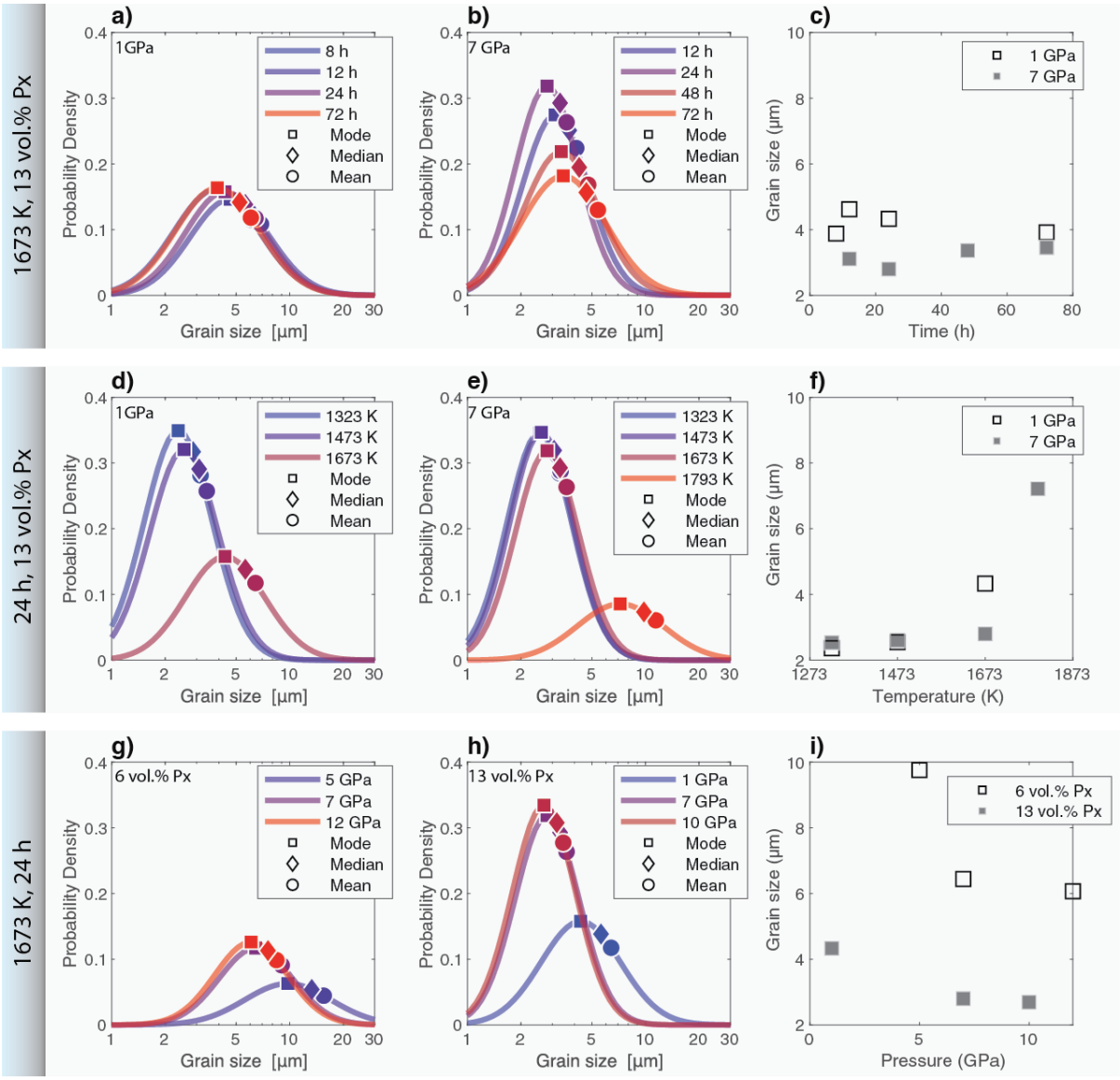

Figure 5.5: Lognormal fit to the grain-size distributions: The upper row (a-c) shows a time series of experiments performed at 1673 K and pressures of a) 1 GPa and b) 7GPa. c) Mode of the of the fit to the grain-size distribution as a function of time. The middle row (d-f) shows the temperature series of experiments performed for 24 hours at pressures of d) 1 GPa and e) 7GPa. f) Mode of the of the fit to the grain-size distribution as a function of temperature. The bottom row (g-i) shows the pressure series of experiments performed at 1673 K for 24 hours for samples containing g) 6 vol.% and h) 13 vol.% of pyroxene. i) Mode of the fit to the grain-size distribution as a function of pressure for samples with a Pyroxene content of 6 vol.% and 13 vol.%.

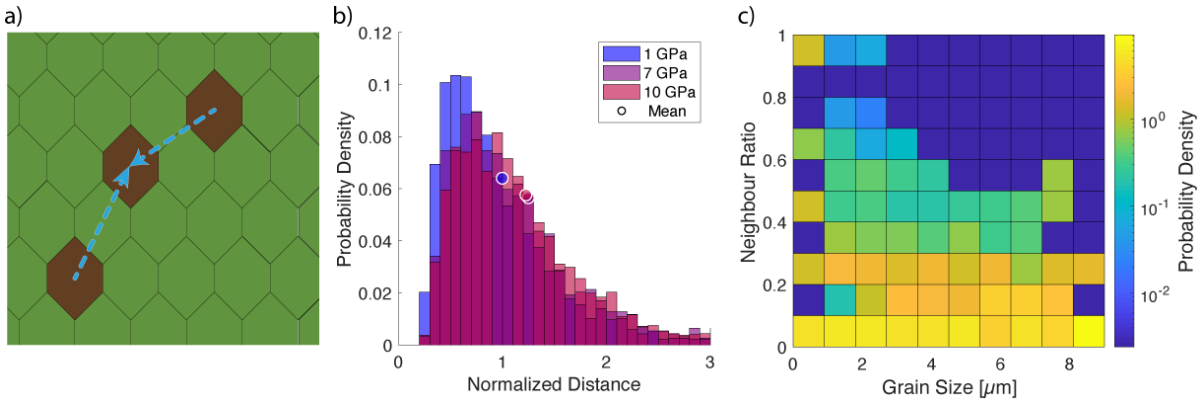

Figure 5.6: Effect of pyroxene on local grain-size distribution: a) Schematic of an aggregate containing olivine (coloured green) and pyroxene (coloured brown). Arrows indicate the distance between the centroid of pyroxene grains to the nearest pyroxene grain. b) Minimum distance between pyroxene grains (as shown by the arrows in figure a) normalized by the average grain size. Experiments performed at 1673 K, 24h, and pressures of 1, 7 and 10 GPa. c) Olivine grain size as a function of ratio between the number of pyroxene grains and all neighbour grains for sample FSG5 (starting material, 13 vol% Px). Each column is a probability density function.

5.4. Discussion

Our results show that pressure has a significant effect on olivine grain growth. Figures 5.4a-b and Figures 5.5a-c demonstrate that grain growth is faster at 1 GPa compared to 7 GPa. For instance, at a temperature of 1673 K and annealing time of 24 hours, grain growth is approximately 4 times slower at 7 GPa than at 1 GPa (Figures 5.4a and 5.5a-c). A comparable effect is observed in the temperature series (Figures 5.4b and 5.5d-f): At low temperatures (T≤ 1473 K) olivine grain growth is slow, irrespective of the applied pressure. At 1673 K, grains grow rapidly at 1GPa (Mo_{FIT} = 4,3 μm), while at 7 GPa the grain-size distribution is similar to its starting material (Mo_{FIT} = 2.8 μm and 2.3 μm, respectively).

It is important to highlight that at pressures smaller than at least 1 GPa, pressure has an opposite effect than the one discussed here. That is, because pressure in this range acts to reduce porosity, the olivine grain-growth rate increases due to fewer pores acting as pinning particles (e.g., S. Karato, 1989). To test this observation, we performed grain-growth experiments with vacuum-sintered forsterite +10 vol.% enstatite (Koizumi et al., 2010) at 1673 K during 24 h, at atmospheric pressure (0.1 MPa), using a tube furnace (HV806-HT) and using a piston-cylinder apparatus at 1 GPa (HV806-HP). The results reported in Table A.4.1 and Figure A.3.8 demonstrate that, after 24 hours, grains grow 3 times faster at 1 GPa than at 0.1 MPa. This

demonstrates that even a very low number of pores act to highly inhibit grain growth. Therefore, studies on grain growth and diffusion creep obtained at environmental or low pressures, even for a starting material with very low porosity, must be interpreted also considering the porosity effect.

Figures 5.4c and 5.5g-i demonstrate that the pressure effect on the grain-growth rate is more pronounced for pressures between 1 and 7 GPa. For experiments containing 6 vol.% of pyroxene (Figure 5.5g), grains grow approximately two times more at 5 GPa than at 7 and 12 GPa. For experiments containing 13 vol.% of pyroxene (Figure 5.5h), grains grow approximately 4 and 5 times more at 1 GPa than at 7 and 10 GPa, respectively.

The results presented in Figure 5.5i indicate that the effect of pressure on slowing down grain growth of olivine increases with increasing pyroxene content. One possible explanation is that the grain-growth rate of pyroxene is also reduced for increasing pressures. With a slower grain-growth rate (for example at pressures higher than 7 GPa), the pyroxene grains are kept far apart from each other (Figure 5.6b). This results in a larger diffusion path, for example of Si, through olivine grain boundaries. This may reduce the coalescence of pyroxene grains (Nakakoji and Hiraga, 2018). In other words, there is a higher ratio between the number of pyroxene grains and their total area, that is, a larger number of small grains. In fact, our results show that, at the same temperature, annealing duration and pyroxene content (1673 K, 24 h and 13 vol.% Px, respectively), the population density of pyroxene grains at 7 and 12 GPa (0.34 μm^{-2}) is more than twice that of at 1 GPa (0.16 μm^{-2}).

The larger amount of neighbouring pyroxene grains is correlated with smaller olivine grain sizes (Figure 5.6c). This result demonstrates that in olivine and pyroxene aggregates, grain growth of the primary phase is strongly influenced by the growth of the secondary phase (see also Tasaka and Hiraga, 2013, section 2.2). Therefore, a slower grain growth of pyroxene at larger pressures also means that olivine grain growth is supressed.

Figure 5.5g and Figure 5.5i demonstrate that the grain-growth rate decreases considerably in a narrow range of pressure, between 5 and 7 GPa. Lithostatic pressures in this range correspond to depths of approximately 200 km. At this depth, a marked seismic discontinuity is observed (Lehmann, 1961, 1959), which has been argued to be related to a change in olivine main deformation mechanism, from

dislocation creep to diffusion creep for increasing depths (Karato, 1992; Karato and Wu, 1993). Our data suggest that smaller grain sizes, resulting from the pressure effect on the grain growth, could be maintained at larger depths. This change in grain size might influence the variation in the dominant deformation mechanism in this region, facilitating grain-size sensitive mechanisms, such as diffusion creep, as depth and pressure increases.

Here we presented experimental evidence that the grain-growth rate of olivine in aggregates containing olivine and pyroxene decreases for increasing pressures. Grain-boundary diffusion was proposed to be the main process controlling grain growth and diffusion creep of olivine (Nakakoji and Hiraga, 2018). A possible explanation for the observed effect of pressure on grain growth may be the rate of grain-boundary diffusion. Si is the slowest diffusing species in both the lattice and at the grain boundaries of olivine (Farver and Yund, 2000) and thus limiting the rate of grain-boundary diffusion. The Si grain-boundary diffusion coefficient was shown to decrease for increasing pressure (Fei et al., 2016). Consequently, we propose that the decrease in the grain-growth rate of olivine can be explained by the decrease in the rates of Si grain-boundary diffusion for increasing pressures. This is further supported by the finding that:

1. An increase in pressure correlates to an increase in the melting temperature of olivine. In other words, at the same nominal temperature, the homologous temperature is reduced at high pressures. For example, the homologous temperatures for forsterite at 1623 K and pressures of 1 GPa, 7 GPa and 12 GPa are 0.72, 0.63 and 0.58, respectively (Davis and England, 1964; Ohtani and Kumazawa, 1981). Lower homologous temperatures would thus explain the reduced grain-boundary diffusion kinetics (e.g., Atkinson, 1985).
2. An increase in pressure correlates with an increase in the energy of formation of vacancies. As grain-boundary diffusion is mediated by the motion of vacancies (e.g., Balluffi, 1982), a lower concentration of vacancies leads to slower grain-boundary diffusion.
3. Grain-boundary energy anisotropy and the presence of specific grain boundaries with low mobility or with high solute segregation rate was found to be a relevant mechanism to modify grain-growth rates in metals and ceramics (e.g., Bäurer et al., 2013; Gottstein and Shvindlerman, 2009; Rheinheimer et

al., 2015). As specific grain boundaries are preferentially developed during grain growth in olivine (Ferreira et al., 2021; Marquardt et al., 2015; Marquardt and Faul, 2018) and may change with pressure, this could also contribute to the decrease in the olivine grain-growth rate reported here.

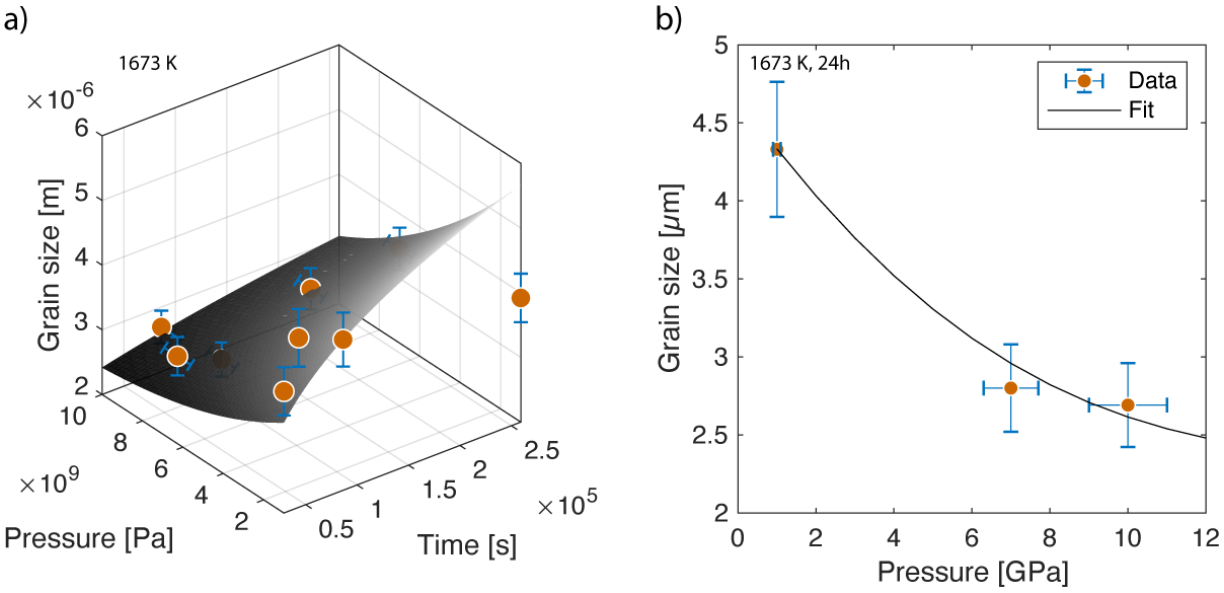

Figure 5.7: Fitting of grain growth data: a) Fitting of data at 1673 K (13 vol.% Px) b) Section of the fitting surface at a time t = 24h. Error bars show uncertainties in pressure and grain size determination.

Non-linear least-squares fitting of our data at 1673 K and 13 vol.% Px to the equations 5.1 and 5.2 (Figure 5.7) give k_0 = 2.11 x 10^{-7} ($m^{3.88}s^{-1}$), n = 3.88, V^* = 4.30 x 10^{-6} (m^3/mol) and E^* = 607 (kJ/mol). These values, however, carry great uncertainty. The 95% confidence intervals for k_0, n, V^*, and E^* are respectively: [-12.86, 12.86] $m^{3.88}s^{-1}$, [-6.168, 13.93], [-2.527 x 10^{-6}, 1.112 x 10^{-5}] m^3/mol and [-8.464 x 10^{11}, 8.464e x 10^{11}] kJ/mol. Comparison of our grain growth equation with previously published olivine grain growth data shows that at 1673 K, 7 GPa and 13 vol.% Px, our results and those from by Tasaka and Hiraga (2013) indicate smaller grain sizes than those found by Karato (2008, p. 241). This difference is likely related to the low amount of pyroxene in the experiments of Karato (2008, p. 241) when compared to our results and those of Tasaka and Hiraga (2013). Our results show similar grain-size evolution as predicted by Tasaka and Hiraga (2013) at 9 vol.% En and P = 0.1 MPa extrapolated to 1673 K (Figure 5.8a-b). Furthermore, the activation volume found in our study is effectively the same as found by Fei et al. (2016) for Si grain-boundary diffusion at high pressures

(4.0 ± 0.7 cm^3/mol). Simple extrapolation of our data to geological time scales (Figure 5.8b) would indicate that olivine grain sizes (based on grain growth only) at 7 GPa and 1673 K are expected to reach 0.4 mm in approximately 1 Ma and 1.4 mm in 100 Ma. Combining these results with existing olivine flow laws (low-T plasticity: Goetze et al. (1978); dislocation creep (dry olivine): Hirth and Kohlstedt (2003), diffusion creep (dry olivine): Hirth and Kohlstedt (2003) revised by Hansen et al. (2011); disGBS (dry olivine): Hansen et al. (2011)), and considering that shear stresses are on the order of 0.1-1 MPa at a depth of ~210 km (P ≈ 7 GPa) (Kohlstedt and Hansen, 2015), olivine is expected to deform in a grain-size sensitive rheology, between the diffusion creep and dislocation-accommodated grain-boundary sliding (disGBS) fields (Figure 5.8c). Therefore, the results reported here would indicate that a change to a Newtonian rheology at deeper parts of the upper mantle (e.g. Karato and Wu, 1993) may be influenced by smaller olivine grain sizes due to a decrease in its growth rate. Nakakoji and Hiraga (2018) proposed that grain-boundary diffusion is a common mechanism for grain growth and diffusion creep of olivine. As strain rates in the Coble creep regime are proportional to the grain-boundary diffusivity, we anticipate that viscosities in the upper mantle are increased for increasing pressures, if the deformation of olivine is accommodated by grain-boundary diffusion.

When extrapolating our data to conditions of the Earth (Figure 5.9), two main uncertainties are the initial grain size, d_0, and the annealing time, t. Grain sizes of approximately 10 μm are the smallest grain sizes observed in xenoliths (e.g., Aupart et al., 2018; Falus et al., 2011). However, these grain sizes are likely a result of dynamic recrystallisation, and the “initial conditions” are not accessible. The first grains of olivine to nucleate, either during downwelling (e.g., Plümper et al., 2017) or upwelling (e.g., Satsukawa et al., 2015), are likely nm- to 100s of μm -sized. However, when the transformation to olivine is complete (e.g. from dehydration of serpentine at downwelling or from transition from wadsleyite at upwelling), the olivine grains grow at a fast rate due to the decrease in free energy (e.g. Koizumi et al., 2010; Tasaka and Hiraga, 2013). Figure 5.9 demonstrates the grain growth of olivine considering an initial grain size of 10 μm. Figure A.3.9 illustrates the effect of different initial grain sizes from 10 μm to 1mm. The residence time at a certain depth or annealing time is also uncertain. Using our grain growth equation, 1 Ma to 10 Ma are necessary to provide mm-sized grains as seen in some xenoliths (e.g., Boullier and Nicolas, 1975). Furthermore, a rough estimation of a slab moving at 5 cm/year with a dip angle of 35º,

would need at least a similar duration, between 5 and 10 Ma, to move from the middle of the upper mantle to the transition zone. We thus base our calculations of the grain size evolution of olivine considering residence times of 1 and 10 Ma (Figure 5.9).

The impact of an activation volume for grain growth on the deep upper-mantle viscosity is illustrated in Figure 5.9. The parameters used for the viscosity estimations are detailed in S.1. Considering the evolution of temperature with depth in the deep upper mantle (Figure 5.9a) and an activation volume of 0 m^3/mol (i.e., no pressure effect on grain growth) the grain-growth rate would increase with depth, due to the increase of temperature with depth (Figure 5.9b). Conversely, considering an activation volume of 4.3×10^{-6} m^3/mol, as found here, grain sizes would only change marginally at depth. Hence, viscosities are not expected to change significantly due to pressure in the 200-400 km depth interval (Figure 5.9c). The expected viscosities when considering an activation volume of 4.3×10^{-6} m^3/mol are approximately one order of magnitude lower than when no activation volume is considered. These results suggest that mantle viscosities may be lower at increasing pressures than previously expected. This interpretation is corroborated by estimations of viscosities in the upper mantle based on postglacial rebound observations (e.g. Paulson et al., 2007).

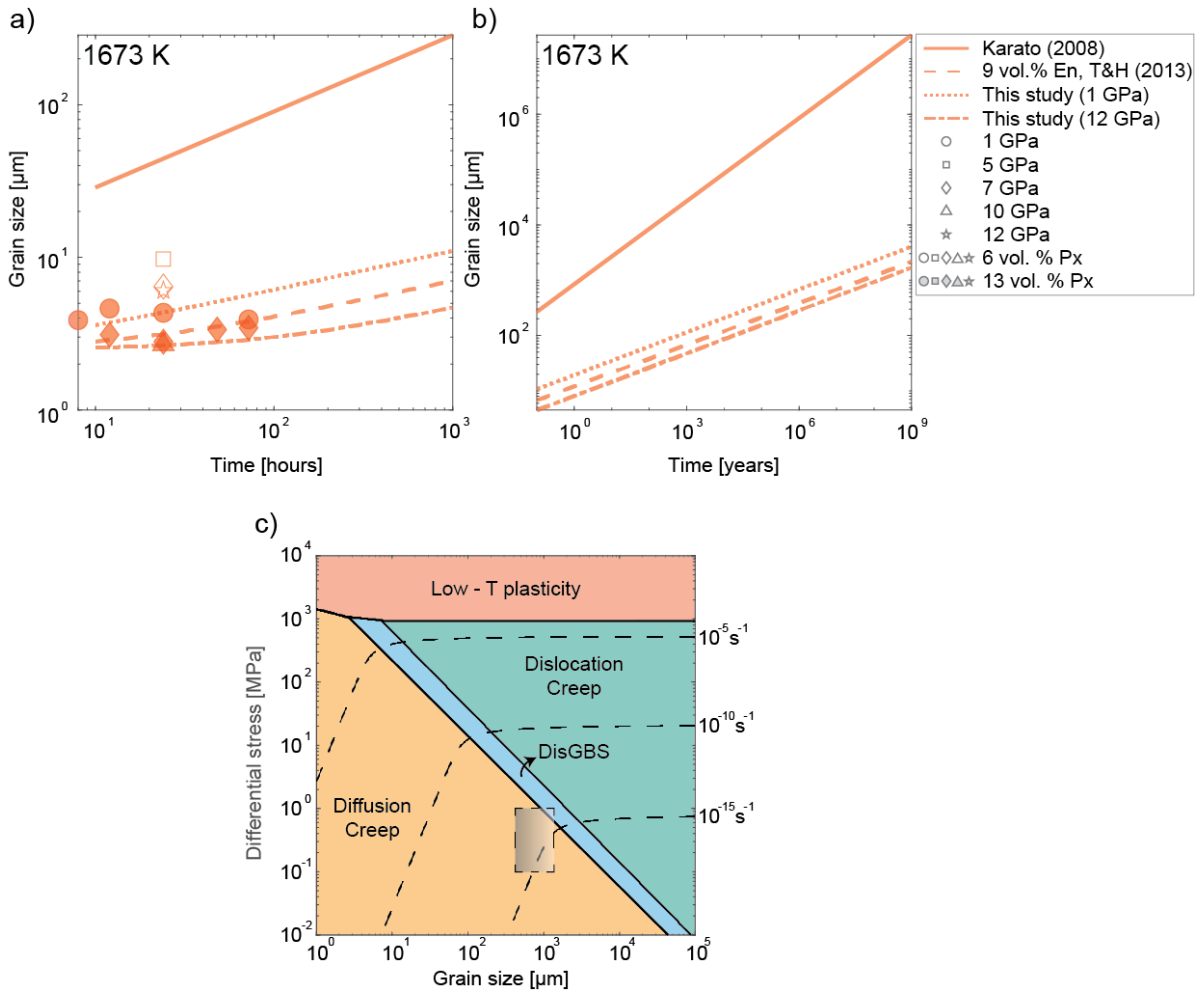

Figure 5.8: Grain growth at upper mantle conditions. a) Comparison of experimental data at 1673 K with grain growth laws of Karato (2008, p. 241) and Tasaka and Hiraga (2013) for 9 vol.% En, normalized to an initial grain size d_0= 2.5 µm. b) Extrapolation of grain growth equations to 1 Ga. c) Deformation mechanism map for olivine at 1673 K and 7 GPa. Dashed rectangle shows the region for predicted olivine grain sizes after an annealing time between 1 Ma and 100 Ma and expected differential stresses at approximately 210 km depth (7 GPa). The flow laws used in the construction of the deformation mechanism map of olivine are from: low-T plasticity: Goetze et al. (1978), dislocation creep: Hirth and Kohlstedt (2003), diffusion creep: Hirth and Kohlstedt (2003) revised by Hansen et al. (2011) and disGBS: Hansen et al. (2011).

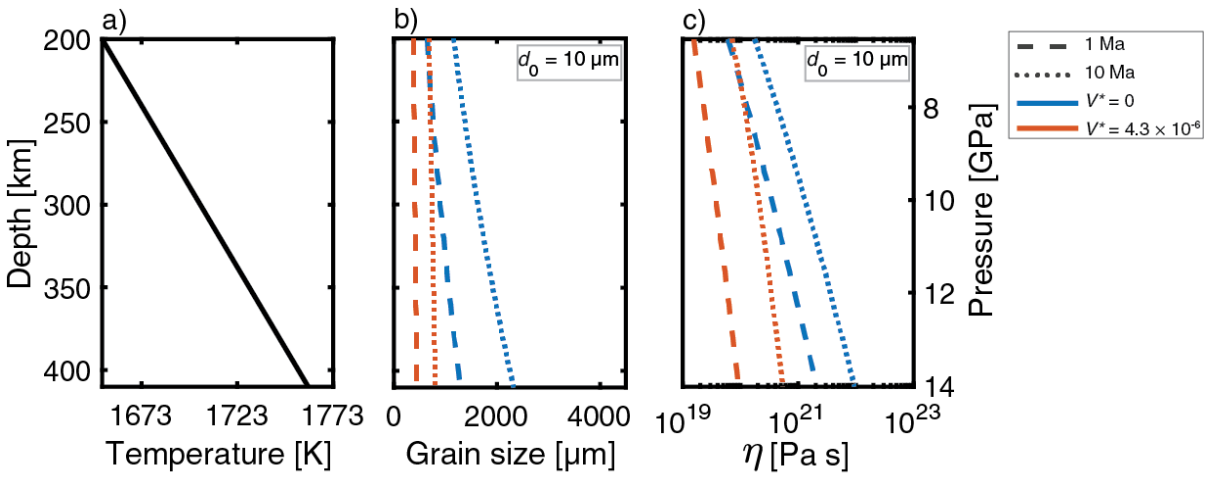

Figure 5.9: Viscosity estimation at deep upper mantle conditions: a) Average temperature profile of the deep upper mantle (Katsura et al., 2004). b) Expected grain sizes at 1 Ma (dashed lines) and 10 Ma (dotted lines) at the conditions of the geotherm shown in figure a, considering an initial grain size d_0= 10 µm, an activation volume of V^* = 0 m^3/mol (blue lines) and V^* = 4.3 x 10^{-6} m^3/mol (orange lines). Resulting viscosity profile of the deep upper mantle considering the grain size evolution shown in b, for a constant shear stress of 1 MPa and strain rates from experimental flow laws of diffusion creep (Hansen et al., 2011; Hirth and Kohlstedt, 2003), disGBS (Hansen et al., 2011), and dislocation creep (Hirth and Kohlstedt, 2003).

5.5. Conclusions

We investigated grain growth of olivine in dry, melt-free aggregates of olivine plus 6 and 13 vol.% of pyroxene (dunite and harzburgite, respectively), at pressure and temperature conditions of the Earth's upper mantle. Olivine is the main phase in the upper mantle and its grain size plays a major role in controlling viscosity in this region. Here we show that the olivine grain-growth rate decreases as pressure increases. We propose that this effect is a result of slower grain-boundary diffusion at high pressures (Fei et al., 2016). The implications for this finding are two-fold: i) changes in grain size due to slower grain growth might influence a transition to a Newtonian rheology in deeper parts of the upper mantle, and ii) because grain-boundary diffusion is proposed to be also the main mechanism for diffusion creep in olivine (Tasaka and Hiraga, 2013), an increase in viscosity in the deep upper mantle as a function of pressure is expected, if diffusion creep is the dominant deformation mechanism in this region. We show that for increasing depths in the upper mantle, the increase in the grain-growth rate of olivine due to an increase in temperature is counteracted by the inhibition of grain growth due to an increase in pressure. Estimation of a viscosity profile as a function of

depth based on the grain-size evolution of olivine predicted here and existing flow laws, indicates that viscosity in the deep upper mantle is lower than previously expected.

Acknowledgments

We thank H. Keppler for help with the synthesis of sol-gel olivine. This work was supported by the Deutsche Forschungsgemeinschaft (DFG), grant no. INST 91/315-1 FUGG. KM and FF acknowledge financial support through DFG grant MA 6287/6. MT was supported by the Visitor’s program of the Bavarian Geoinstitute. SK acknowledges the support of the Earthquake Research Institute's cooperative research program to Takehiko Hiraga and by the JSPS through Grant-in-Aid for Scientific Research no. 18K03799 to SK. The data that supports our research will be deposited in a repository compliant with FAIR principles.

Chapter 6: Towards the investigation of the grain-boundary effects in the plastic deformation of olivine at high pressures

Filippe Ferreira[1], Robert Farla[2], Marcel Thielmann[1], Katharina Marquardt[3]

[1] Bayerisches Geoinstitut, Universität Bayreuth, Bayreuth, Germany

[2] Deutsches Elektronen-Synchrotron (DESY), Hamburg, Germany

[3] Faculty of Engineering, Department of Materials. Imperial College of London, London, UK

Corresponding author: Filippe Ferreira (filippe.ferreira@uni-bayreuth.de)

This chapter is being prepared for submission

Author Contributions:

F. Ferreira performed the experiments, collected and analysed the data and wrote the manuscript. R. Farla performed the experiments and commented on the manuscript. M. Thielmann and K. Marquardt assisted with data analysis and contributed to manuscript writing. K. Marquardt designed the study.

Abstract

The microphysical processes that result in ductile deformation of Earth's deep upper mantle (depths>200 km) are still not fully understood. Information on the natural deformation of olivine under these conditions is limited and experimental data is scarce. Based on laboratory data and interpretation of geophysical observations, diffusion creep has been credited to explain the reduced seismic anisotropy in this region. However, different studies have challenged this idea. Here, we investigate the effect of grain boundaries on the strength of olivine-dominated aggregates at deep upper mantle conditions (7-10 GPa,1400 ºC). We present a new set of deformation anvils and assembly used to investigate the simultaneous deformation of coarse and fine-grained olivine. Under these conditions, fine grained olivine deforms 7-9 times faster than coarse-grained olivine. Examination of crystallographic preferred orientations and microstructures indicate that deformation was accommodated by dislocation creep. These results suggest that grain boundaries promote deformation through grain-boundary sliding and that disGBS might also be the main process for ductile deformation in the deep upper mantle.

6.1. Introduction

Olivine is the main mineral phase in the Earth's upper mantle. Therefore, the deformation of olivine has a major control on the rheology of the upper mantle. As outcrops of naturally-deformed samples from depths larger than 200 km are extremely rare, insights into the deformation mechanisms of olivine at the deep upper mantle comes in great part from experimental work. However, experimental deformation at deep upper mantle conditions, that is, at confining pressures higher than 6 GPa and temperatures higher than 1300 ºC, is technically complex. The first studies to reach such conditions used modified assemblies in a multi-anvil apparatus (e.g., Bussod et al., 1994; Cordier and Rubie, 2001; Durham and Rubie, 1996; Karato and Rubie, 1997). The incorporation of synchrotron-radiation techniques later on allowed for the real-time monitoring of stress and strain evolution during the experiments (e.g., Couvy

et al., 2004; Li et al., 2004, 2003). These studies provide important information on the pressure-sensitivity of the activity of slip systems of olivine at high pressure. However, these early high-pressure deformation experiments consisted of stress-relaxation experiments rather than constant strain rate or constant stress experiments. Therefore, obtaining rheological parameters from the resulting mechanical data carried large uncertainties. The development of specific high-pressure apparatuses for deformation experiments, such as the rotational Drickamer apparatus (RDA; Yamazaki and Karato, 2001) and the deformation-DIA (D-DIA; Wang et al., 2003), allowed for quantitative measurements on the strength of olivine and larger strains to be reached. These experimental innovations permitted improved investigation on the microphysical process responsible for large-scale geodynamical process such as flow at deep upper mantle and transition zone conditions (Kawazoe et al., 2016, 2009), the onset of plate tectonics (Amiguet et al., 2012), the origin of deep-focus earthquakes (Schubnel et al., 2013) and the water circulation in the Earth's mantle (Précigout et al., 2017).

Here we present new developments in the study of the olivine deformation at deep upper mantle conditions using a cubic multianvil apparatus (Manthilake et al., 2012). This apparatus provides more precise controls on strain rate than the RDA and D-DIA apparatuses, while its open geometry provides better clearance for in-situ measurements such as X-ray and neutron diffraction (e.g., Sano-Furukawa et al., 2014). This apparatus was previously used for olivine deformation at pressures up to 5 GPa at 1200 ºC (Bollinger et al., 2019). We present modifications in the second-stage anvils and deformation assembly that allow for the extension of the pressure and temperature range to 7 GPa and 1400 ºC, using a right-cylindrical sample of 1.5 mm diameter. We present examples of microstructures and textures of coarse and fine-grained olivine that developed during high-pressure and temperature deformation experiments. Finally we discuss the results while attempting to increase the usage range of this assembly to confining pressures up to 10 GPa.

6.2. Methods

6.2.1 Sample preparation

We fabricated coarsely-grained olivine aggregates from reconstituted San Carlos olivine and fine-grained olivine aggregates were synthesized through the solution-gelation (sol-gel) method. Coarsely-grained aggregates were prepared from San Carlos olivine crystals that were optically inspected for homogeneity and ground in an agate mortar. The resulting powder was hot-pressed in a piston cylinder at 0.7 GPa and 1200 ºC for 12 hours. Hot-pressing allows for densification (i.e. reduction of porosity) and grain growth. The grain size after hot-press sintering was approximately 30 µm. Aggregates of sol-gel olivine were hot-pressed at 0.7 GPa and 1200 ºC for 2 hours, yielding grain sizes of approximately 2 µm. The SiO_2 activity was buffered during sintering through the presence of pyroxene grains amounting to 1% and 5%, for the coarse and fine-grained aggregates, respectively. The oxygen fugacity during hot-press was buffered by the Ni-NiO reaction between the $Ni_{80}Fe_{20}$ capsule and NiO powder placed at the top and bottom of the sample.

6.2.2 Deformation experiments

The experiments were conducted using the *MAVO-6* presses (*Max Voggenreiter GmbH*) at the Deutsches Elektronen-Synchrotron in Hamburg, Germany and at the Bayerisches Geoinstitut, in Bayreuth, Germany. The press consists of 6 hydraulic rams arranged in a cubic design (MA 6-6; Figure 6.1). The advancement of each ram towards the sample is controlled independently through the adjustment of oil pressures. The rams act on second stage-anvils made of tungsten carbide doped with 5% of cobalt (*hawedia Ha-5%*). The pyramidal second-stage anvils used in our study have a squared truncation edge of 5 mm. They act on a truncated cubic assembly, with 8 mm in the long edge and 5 mm in the short edge (Figure 6.1b). The relation between press load and hydrostatic pressure at room temperature was measured by monitoring the change in electrical resistance due to phase transitions of Bi, ZnTe and ZnS. The pressure points were fitted to an exponential equation of the form:

$$P = a \exp\left(\frac{-F}{b}\right) + c \quad (5.1)$$

where P is the sample pressure in GPa and F the press load in MN. The data points were best-fitted using a non-linear-least-squares regression with a = -17.28, b = 2.216 and c = 17.16 (Figure 6.2). Extrapolation of these results to high temperature include uncertainties in the pressure estimation on the order of $\pm$ 0.5 GPa (cf., Manthilake et al., 2012).

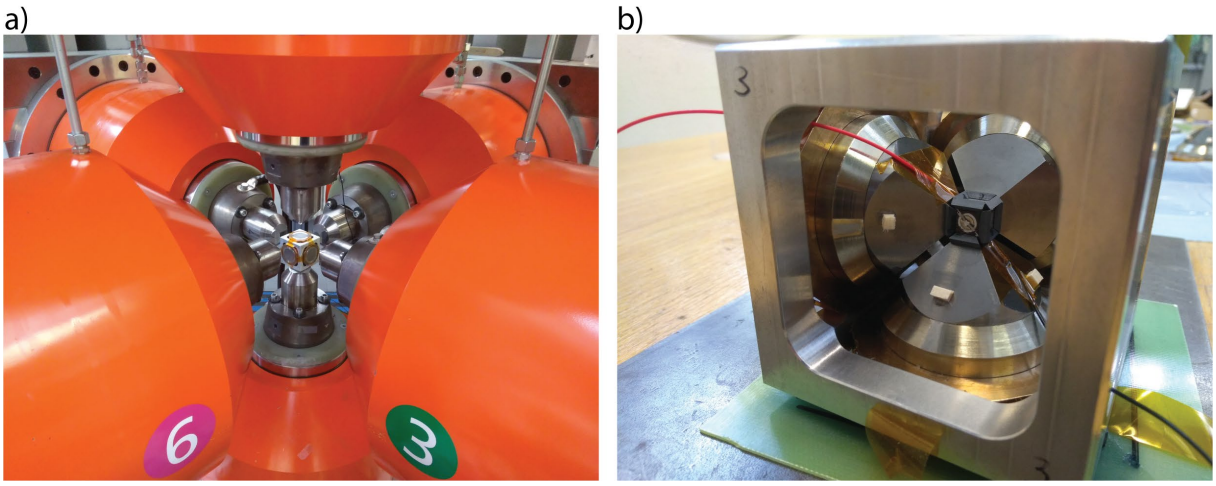

Figure 6.1: Deformation experiments in the MAVO press: a) Six rams are computer-controlled to provide hydrostatic pressure and differential stresses. b)The rams exert load on a cubic assembly with a 5 mm truncated-edge length.

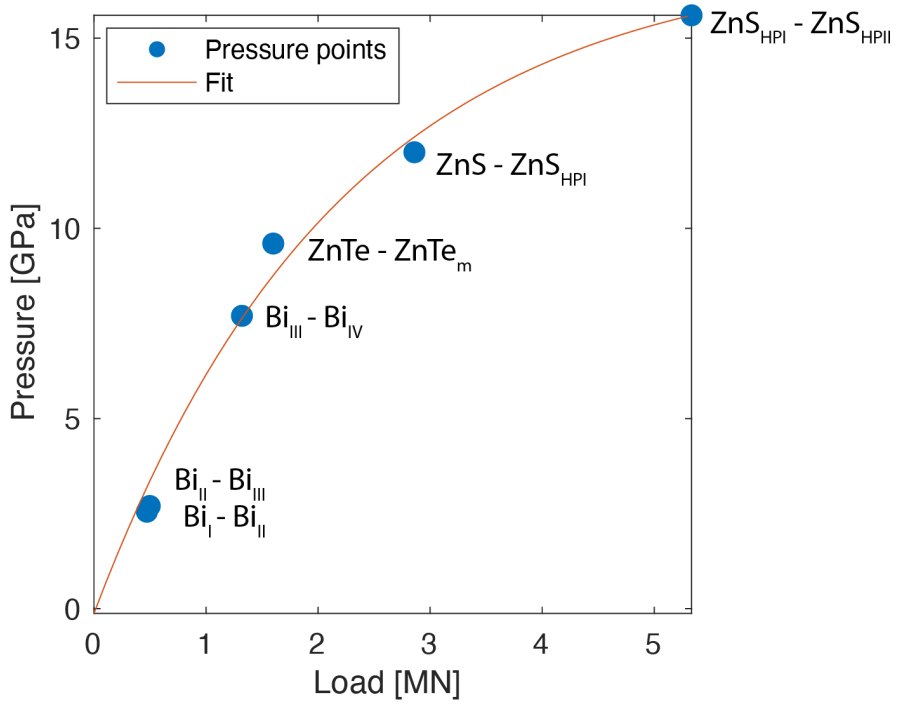

Figure 6.2: Pressure calibration for the 8/5 assembly at room temperature. Data points from Farla, R. (personal communication).

Schematic drawings of the assembly parts, secondary-stage anvil, and gasket used in this study are shown in Figures A.3.10-12, respectively. The pyrophyllite pressure media and gaskets were pre-fired at 500 ºC for 12 hours. The MgO parts were pre-fired at 1000 ºC for 12 hours. The experiments were carried out by first hydrostatically compressing the samples to the experimental confining pressure. The confining pressure is kept constant by the control of oil pressure to a master ram (middle bottom ram in Figure 6.1a), and adjusting the pressure of the other rams to keep the cubic geometry (i.e., equal distance between the rams). The sample is then heated to the experimental temperature and annealed for 30 minutes, which allows for the recovery of the microstructure before the deformation experiment. The deformation experiment in pure-shear geometry is done by advancing the rams parallel to the assembly compression axis (lower right and upper left rams in Figure 6.1a) and retracting the rams normal to it in the horizontal plane (lower left and upper right rams in Figure 6.1a), while the remaining rams (middle bottom and top rams in Figure 6.1a) maintain their relative position. The position of the rams is monitored by linear-displacement encoders with a precision of 0.1 μm.

The experimental conditions of the deformation experiments are summarized in Table 6.1. The deformation experiments were conducted at confining pressures of 7-10 GPa, temperatures of 1100-1400 ºC and constant displacement rate of the rams to achieve a nominal constant strain rate of 10^{-4}-10^{-5} s^{-1}. We performed simultaneous tests with coarse-grained and fine-grained olivine inside a capsule, separated by a Ni-foil of 10 μm thickness. The strain experienced by each sample was calculated individually by measuring the samples before deformation with a calliper (uncertainty: 5 μm) and after deformation using SEM images (uncertainty smaller than 0.5 μm). The average strain-rates were then calculated by the ratio between the strain and the duration of the deformation experiment. The oxygen fugacity was buffered by the Ni-NiO reaction between the Ni-capsule and NiO powder added to the top and bottom of the capsule.

Table 6.1: Experimental conditions

Experiment	Pressure (GPa)	Temperature (ºC)	Bulk strain	Bulk strain rate (s^{-1})
HH221	7	1400	0.1	1.00E-05
HH222	7	1400	0.3	1.00E-04
HH224	10	1400	0.2	1.00E-05
HH225	10	1400	0.3	1.00E-05
HH226	10	1400	0.3	1.00E-04
M716	10	1100	0.3	1.00E-05

6.2.3 **EBSD analyses**

Electron Backscattered diffraction data was collected at a step size of 0.5 µm for the fine-grained olivine and at 1 µm for coarse-grained olivine. Operation conditions of the Scanning Electron Microscope (*FEI SCIOS Dual Beam*) was 20 kV and 3.2 nA for acceleration voltage and beam current, respectively.

The EBSD data was treated using the *EDAX OIM Analysis*™ software. EBSD data was re-indexed using the neighbour pattern averaging routine (Wright et al., 2015). Afterwards, a grain-dilation routine was applied, which assigns the crystal orientation of low-quality measurements within a grain to the mean orientation of its neighbours. Grains were assigned to areas containing more than 20 indexed pixels and bounded by a misorientation angle equal or higher than 20º. A pseudo-symmetry correction was applied to olivine, where grains separated by boundaries with a misorientation of 60° around the [100] axis are merged together (e.g., Marquardt et al., 2017). Finally, another iteration of grain dilation was applied. After the aforementioned cleaning steps, at least 95% of the mapped areas were assigned with crystal orientations. The remaining not-indexed areas are mainly a result of decompression cracks. The EBSD data was subsequently analysed with *MTEX* (Hielscher and Schaeben, 2008).

6.3. Results

6.3.1 Deformation experiments at 7 GPa

Two deformation experiments were performed at 7 GPa and 1400 ºC. The HH221 experiment was carried out at a bulk strain rate of 10^{-5} s^{-1} to a total bulk strain of 0.1 (10% compression). The HH222 experiment was carried out at a bulk strain rate of 10^{-4} s^{-1} to a bulk strain of 0.3 (30% compression). The post-mortem average strain and strain rates calculated for the coarse (San Carlos olivine) and fine-grained (sol-gel olivine) are presented in Table 6.2 and SEM images are shown in Figure 6.3. The strain rate of the fine-grained olivine was substantially higher in both experiments. The fine-grained olivine deformed approximately 7 and 9 times faster than the coarse-grained olivine for experiments HH221 and HH222, respectively.

Table 6.2: Experimental results at 7 GPa

Experiment	Strain Coarse-grained	Strain rate (s^{-1}) Coarse-grained	Strain Fine-grained	Strain rate (s^{-1}) Fine-grained
HH221	0.01	1.43E-06	0.08	8.45E-06
HH222	0.08	2.62E-05	0.31	1.02E-04

The olivine crystal preferred orientations (CPO) of samples HH221 and HH222 are presented in Figures 6.4a and 6.4b, respectively. The pole figures for the fine-grained olivine samples for both experiments show an uniform distribution. The pole figures for the coarse-grained olivine in both samples show similar distributions, with strong clustering of (010) planes parallel to σ_1. The poles to the (100) planes show a girdle distribution in the horizontal plane, while the poles to the (001) planes present a rather uniform distribution. Intragranular misorientations developed after deformation are illustrated in Figure 6.5 for fine-grained olivine and in Figure 6.6 for coarse-grained olivine. The presence of sharp misorientation edges within the grains can be observed for the coarse and fine-grained samples. These features are also present in grains smaller than ~ 10 μm, as indicated in the insets in Figure 6.5. Figure 6.6 also shows the presence of a narrow band where a noticeable decrease in grain size occurs.

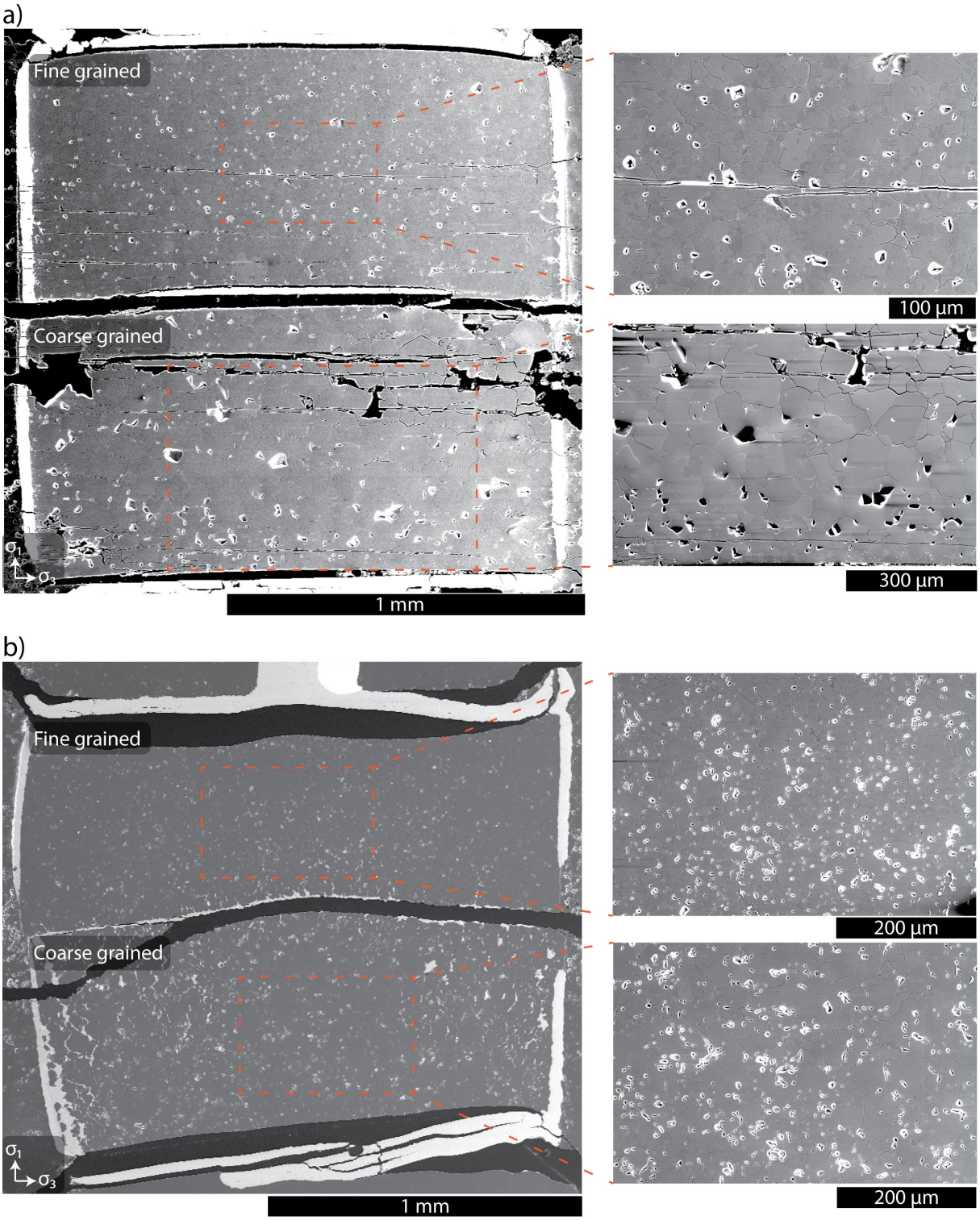

Figure 6.3: Secondary electron images of recovered samples after deformation at a confining pressure of 7 GPa: a) Experiment HH221. b) Experiment HH222. The direction of maximal compression, σ_1, is vertical and the direction of minimal compression, σ_3, horizontal.

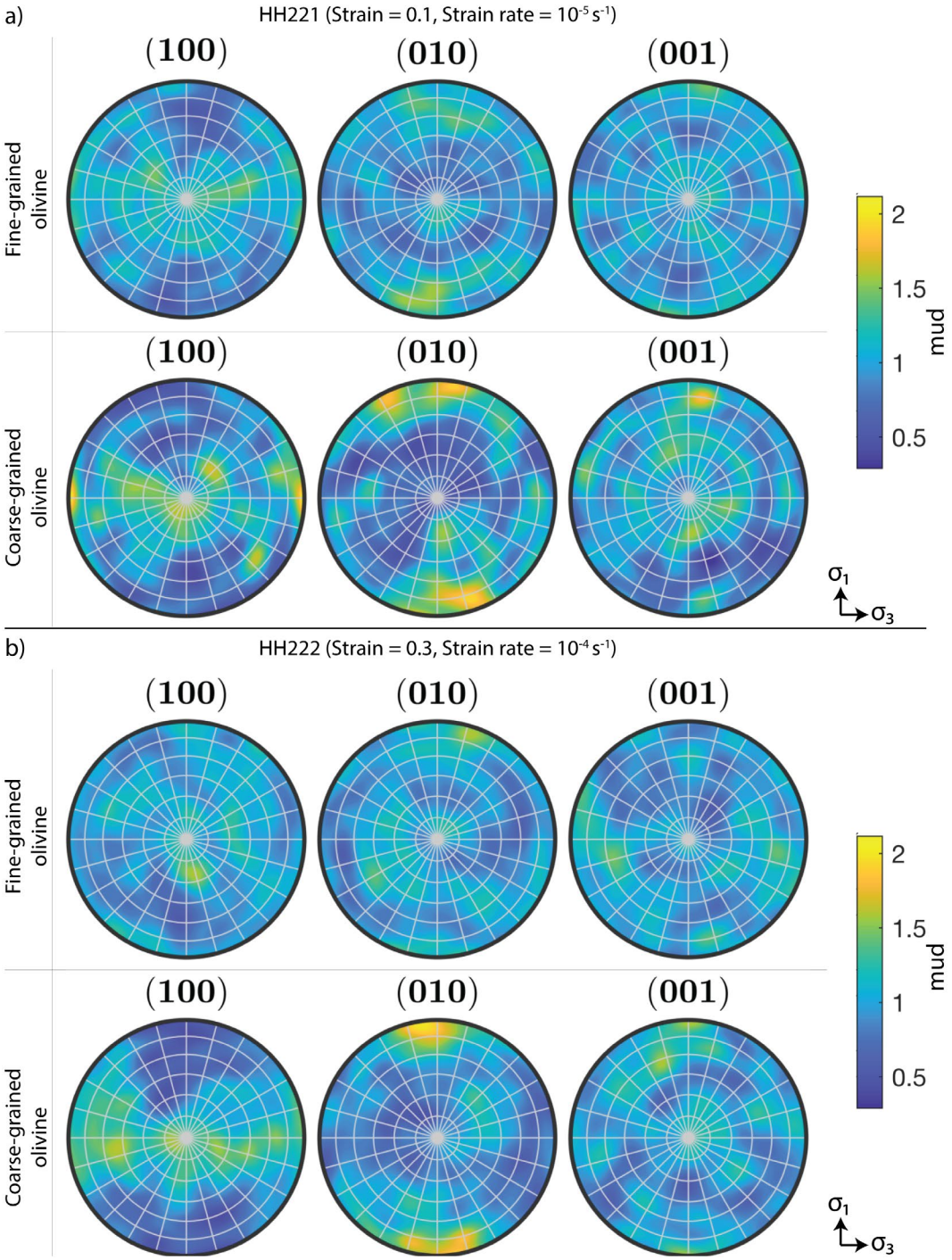

Figure 6.4: Olivine pole figures of experiments a) HH221 and b) HH222. One point per grain (mean orientation). Lower-hemisphere projection.

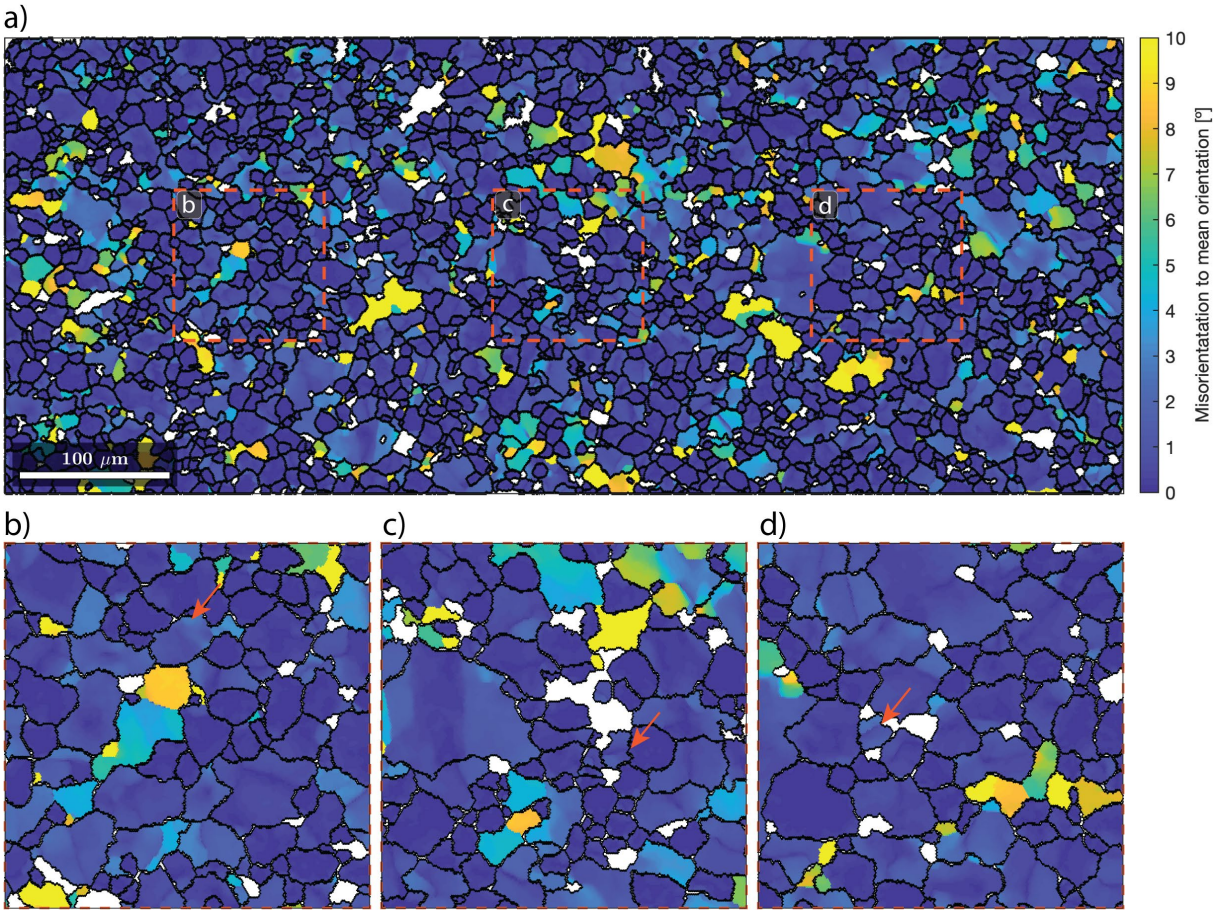

Figure 6.5: Intergranular misorientation of fine-grained olivine in experiment HH222. EBSD data are colour-coded by the angular misorientation to the mean orientation of the grains, from 0º (dark blue) to 10º (light yellow). Arrows in b-d) indicate sharp misorientation bands in very small grains (<10 µm). Insets dimensions are 100 µm x 100 µm.

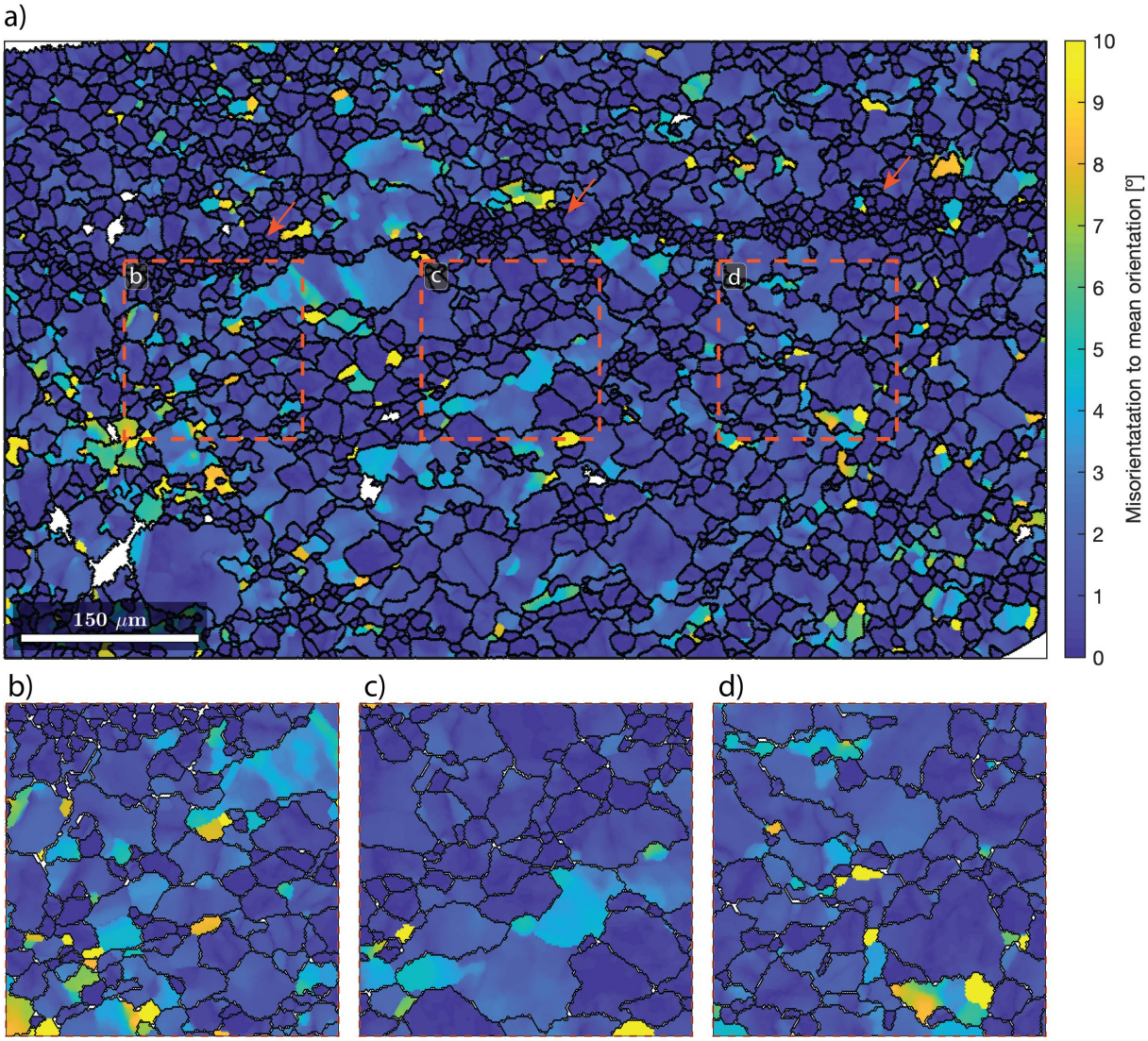

Figure 6.6: Intergranular misorientation of coarse-grained olivine in experiment HH222. EBSD data are colour-coded by the angular misorientation to the mean orientation of the grains, from 0º (dark blue) to 10º (light yellow). Arrows in a) indicate a narrow horizontal band where extensive grain size reduction occurred. Insets b, c and d shown in a) are magnified in b), c) and d), respectively. Insets dimensions are 150 μm x 150 μm.

6.3.2 **Deformation experiments at 10 GPa**

Four experiments were carried out at a confining pressure of 10 GPa. Despite the similar assembly configuration and procedure, all experiments at 10 GPa presented features of brittle faulting. For example, fault planes at approximately 30-45º from the maximum compression direction developed during experiments HH225 (Figure 6.7a) and HH226 (Figure 6.7b). Inter-and transgranular microfractures can also be observed in similar directions (insets in Figure 6.7). The widespread microfracturing introduced a large amount of distortion to the crystals, which impeded the indexing of crystal orientations using the EBSD technique. Figure 6.7 also shows that substantial

shortening of the samples occurred along the compression direction. This can be seen in Figure 6.7b where the fine-grained sample of experiment HH226, for example, presents a shortening strain of approximately 0.2. Furthermore, grain sizes of the fine-grained olivine (insets in Figure 6.7) shows average grain sizes of approximately 20 µm, considerably larger than the average grain size of the starting material (~2.5 µm).

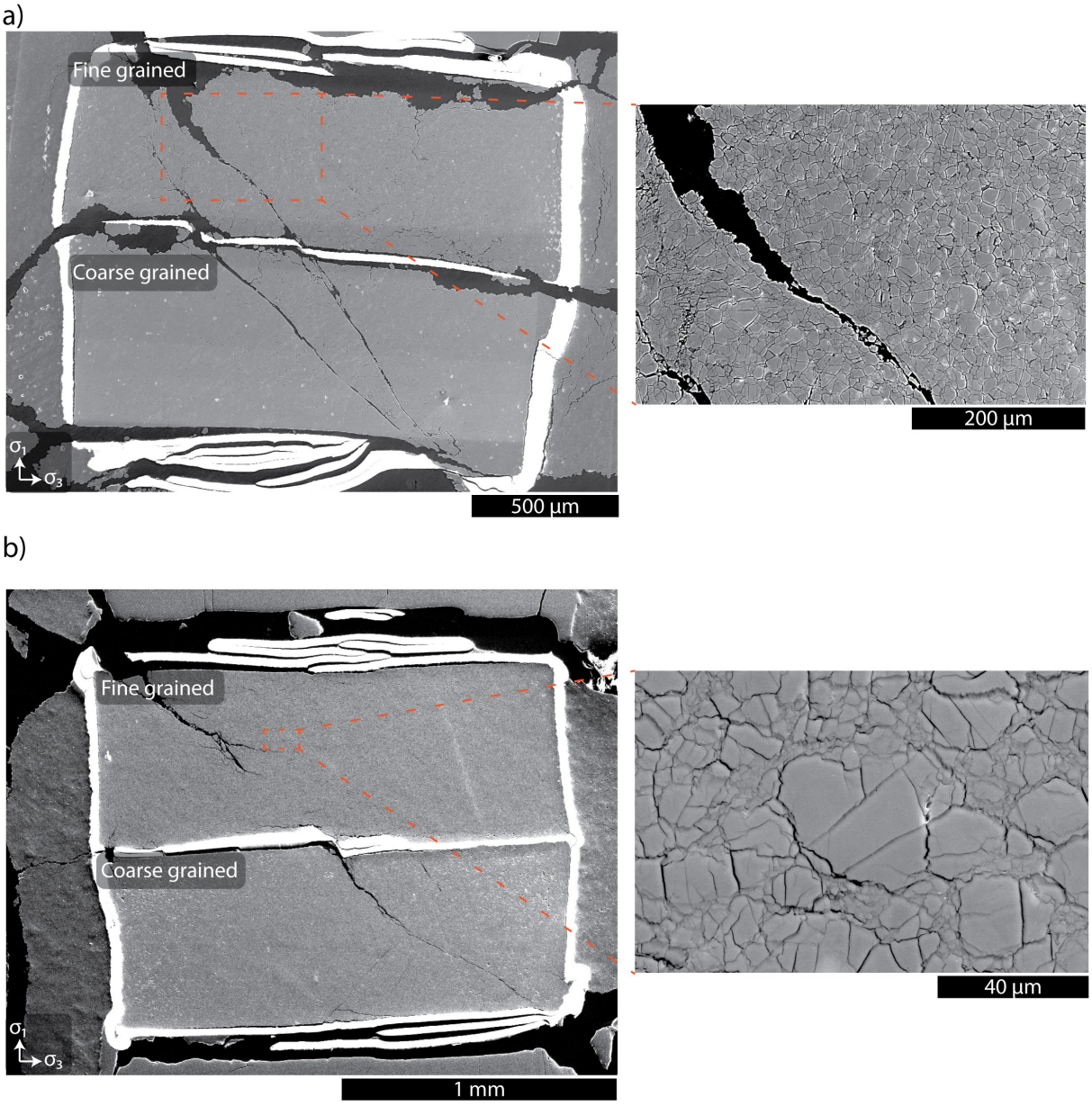

Figure 6.7: Secondary electron images of recovered samples after deformation at a confining pressure of 10 GPa: a) Experiment HH225. b) Experiment HH226. The direction of maximal compression, σ_1, is vertical and the direction of minimal compression, σ_3, horizontal.

6.4. Discussion

Experiments performed using a new high-pressure deformation assembly (8/5) in a multianvil cubic press (MA 6-6) were successfully performed at a confining pressure of 7 GPa at 1400 ºC. In these experiments, deformation of fine-grained olivine occurs at a faster rate (almost one order of magnitude) than coarse-grained olivine (Figure 6.3). These results are opposite to those observed for low-temperature deformation of olivine (e.g., Hansen et al., 2019; Kumamoto et al., 2017). At low temperature, the recovery of the microstructure is limited. Hence, the dislocations present within the grains inhibit further incorporation of dislocations, leading to strain hardening. Because in fine-grained aggregates more obstacles for the movement of dislocations are present (i.e., grain boundaries), this hardening effect is maximized for decreasing grain size (Hall, 1951; Petch, 1953). At higher temperatures, however, dislocations are allowed to climb obstacles such as grain boundaries (Goetze and Kohlstedt, 1973; Weertman, 1957). Furthermore, dislocations can be incorporated in grain boundaries leading to grain-boundary sliding (e.g., Langdon, 1994), as discussed in Chapter 4. This results in strain softening for an increasing amount of grain boundaries, that is, for decreasing average grain size. This is a possible reason why fine-grained olivine is weaker than coarse-grained olivine in experiments HH221 and HH222. Another possibility is that diffusion creep was operative. For example, deformation appears to be localized in shear bands (Figure 6.6a), where substantial grain size reduction occurs. These grains appear free of internal distortion and thus, a grain-size sensitive mechanism, such as diffusion creep, might be dominant. However, it is shown here the abundance of low-angle grain boundaries and lattice distortion, even for the fine-grained aggregates (Figure 6.5). These are strong evidences that deformation was accommodated by dislocation creep (e.g., Wallis et al., 2016).

The experiments performed at a confining pressure of 10 GPa present brittle deformation features. For example, shear fractures are observed crossing the whole assembly (Figure 6.7). Microfracturing is also observed across grains and along grain boundaries. At such high confining pressures, brittle processes are expected to be suppressed (Byerlee, 1968; Lockner and Beeler, 2002). Nonetheless, their occurrence in nature might be a source of deep-focus earthquakes (Frohlich, 1989). The substantial grain growth of olivine and the shortening of the samples along the

compression axis (Figure 6.7), suggest, however, that high-temperature deformation was maintained during most of the duration of the experiments. If failure occurred during deformation, possible causes include faulting due to localized heating (e.g., Hobbs et al., 1986; Ogawa, 1987; Ohuchi et al., 2017; Thielmann, 2018; Zhan, 2020) or due to stress-promoted phase transitions (e.g., Burnley et al., 1991; Schubnel et al., 2013; Wang et al., 2017). However, because the fractures do not show evidence of healing, it is probable that failure occurred at the end of the experiments or during decompression. If failure occurred at the end of the experiment, one possible reason is that the fast quenching led to fast contraction and fracturing of grains. This rapid volume change might create widespread fractures that would coalesce at the plane of maximum resolved shear stress (i.e. ~ 30 to 45º from the maximal compression direction) and allow failure to occur. In this case, a possible solution would be a slower quenching rate of the experiment, although this could lead to recovery of the microstructure and obliteration of deformation structures. If failure occurred during decompression, a possible reason could be the sudden release of stored elastic energy by the anvils and/or assembly. Such events might lead to breakage of the anvils (i.e., blow out), although they might also remain unnoticed. In-situ monitoring of acoustic emissions (e.g., Ohuchi et al., 2017; Wang et al., 2017) could provide valuable information of time and source of such failure events, leading to a better understanding of the mechanisms involved in this process. Acoustic-emission measurements could also potentially reveal whether the brittle events occurred due to brittle failure or as a result of thermal runaway.

6.5. Conclusions

A new assembly was developed that allows deformation of relatively large samples (1.5 mm right cylinder) at pressure and temperature conditions of the deep upper mantle (e.g. 7 GPa and 1400 ºC). It is shown that fine-grained olivine deforms considerably faster than coarse-grained olivine at these conditions, even during deformation accommodated by dislocation creep. Similar experiments using this assembly at a confining pressure of 10 GPa resulted in deformation in the brittle regime, while plastic deformation was expected. Nonetheless, the results presented here suggests that high-temperature deformation was achieved during most of the duration of the experiments. The reason for brittle deformation is unclear but possible

causes include failure due to localized heating, phase transitions, thermal contraction, and release of elastic energy from the anvils or assembly parts.

Chapter 7: A *MATLAB*®/*MTEX* toolbox for grain boundary plane and character distribution

Filippe Ferreira[1], Gregory Rohrer[2], Marcel Thielmann[1], Katharina Marquardt[1+]

[1] Bayerisches Geoinstitut, Universität Bayreuth, Bayreuth, Germany

[2] Department of Materials Science and Engineering, Carnegie Mellon University, Pittsburgh, PA 15213, USA

[+]Now at Faculty of Engineering, Department of Materials. Imperial College of London, London, UK

Corresponding author: Filippe Ferreira (filippe.ferreira@uni-bayreuth.de)

This chapter is being prepared for submission

Author Contributions:

F. Ferreira wrote the *MATLAB*® toolbox, analysed the data and wrote the manuscript. G. Rohrer wrote the original programs on which the toolbox is based, provided test data and assisted with code writing. M. Thielmann and K. Marquardt assisted with code writing and the manuscript writing.

Abstract

Grain boundaries impact the function and performance of polycrystalline materials. The characterization of the grain boundary structure is an important step to better understand the effects of grain boundaries on bulk properties of materials. The grain boundary plane and character distribution (GBPD and GBCD, respectively) are largely-used techniques to characterise the macroscopic structure of grain boundaries. Here we provide a *MATLAB*® toolbox to extract grain boundary information from electron backscatter diffraction (EBSD) data and display the grain boundary plane and character distribution. The tools provided here extend the use of the GBPD/GBCD techniques to data of multiple EBSD vendors and allows better access and handling of the data to be exported and plotted. Furthermore, it provides integration with *MTEX*, which is broadly used for microstructure and texture analyses of EBSD data.

7.1. Background

Many properties of polycrystalline materials are directly correlated with the composition and structure of grain boundaries (Sutton and Balluffi, 1995). Grain boundaries play an important role in moderating several bulk mechanical properties such as deformation, fracture, corrosion, segregation and diffusion (Watanabe, 2011). Therefore, the characterization of grain boundary distributions is of crucial importance for correlations between microstructure and properties. The grain boundary plane and character distribution (GBPD and GBCD) calculated from 2D EBSD data are cost-effective and fast techniques to obtain a macroscopic description of grain boundaries. Computer programs created by Rohrer and collaborators (Saylor et al., 2002; Saylor and Rohrer, 2002) made possible to obtain the GBPD/GBCD from EBSD data. Nonetheless, tools for importing, visualizing, treating and exporting EBSD-related data in proprietary software packages are still limited. With the increasing number of users migrating to open software, an alternative is proposed here to perform these tasks and execute the GBPD/GBCD programs using the *MTEX* toolbox for *MATLAB*® (Hielscher and Schaeben, 2008). *MTEX* allows EBSD data from several vendors or any generic

spatial/crystal orientation data to be imported and analysed. Furthermore, it provides a growing number of tools for crystal orientation and symmetry operations. Here we aim at presenting a way to easily combine *MTEX* routines and the GBPD/GBCD programs. We will also compare the segments output from *MTEX* and *EDAX OIM*™ and discuss the minor variations between them. We will show that the scripts presented here provides similar results and allows for time optimization and increased range of use of the GBPD/GBCD technique.

Here we provide a toolbox to import the EBSD data, export grain and grain boundaries properties to the GBPD/GBCD programs, execute the programs and visualize the grain boundary plane and character distribution. Additionally, auxiliary scripts are added and being developed to include functionality of *MTEX* to work with its native grain boundary class.

7.2. Methods

We present here an example from EBSD data obtained from polycrystalline olivine synthesized via sol-gel method. Olivine is a nesosilicate with a $(Mg,Fe)_2SiO_4$ composition. Olivine is the most common mineral in the Earth's upper mantle and commonly found in mantle xenoliths. EBSD data was obtained using a step size of 0.5 µm, using a hexagonal grid. The EBSD data and reconstructed grain boundary-segments were exported from the *EDAX OIM*™ v8 software. Grain boundaries were defined for a misorientation threshold of 20 degrees and for grains composed of at least 10 pixels. EBSD measurements with confidence index smaller than 0.1 were deleted.

The computer scripts were written in the *MATLAB*® environment. They can be run on *Linux*, *MacOS* or *Windows* platforms. The flowchart of the code execution is shown in Figure 6.1. The following sections will describe the main functions as well as the expected input and output data.

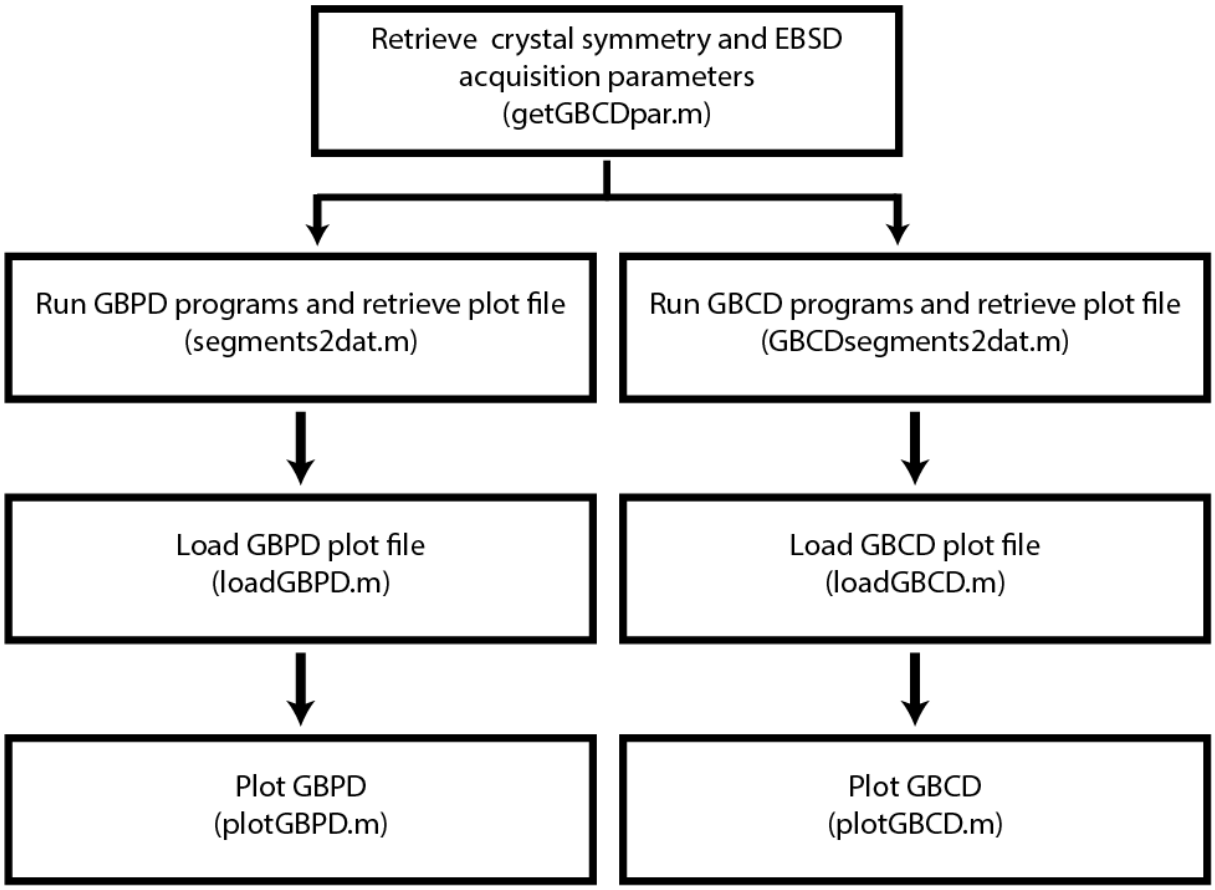

Figure 7.1: Flowchart of data import and code execution.

7.2.1 **Extract GBPD/GBCD parameters (*getGBCDpar* function)**

The *getGBCDpar* function extracts parameters necessary for the calculation of the GBPD and GBCD. They include: the *crystal symmetry* and the EBSD acquisition *step size*, which can be extracted from the EBSD data, the *rotation* framework, dependent on the EBSD vendor, the *unit* of Euler angles, in radians or degrees, the *resolution*, as the number of bins per 90º, the activation of *segment size* analyses, and a small length *cutoff*, as the length of segments in case the segment analyses is activated. These parameters are then written in the input files for the calculation of the GBPD and GBCD.

The call for the function is of the form:

GBCD_par = getGBCDpar(ebsd, cs);

where the arguments *ebsd* is a *MTEX* variable (class *EBSD*) and *cs* is the crystal symmetry (class *crystalSymmetry*) for the phase to be analysed. The output *GBCD_par* is an array with double variables of size 1x8.

7.2.2 GBPD/GBCD segments to plot file (*segments2dat* and *GBCDsegments2dat* functions)

The *segments2dat* (*GBCDsegments2dat*) function runs the GBPD (GBCD) programs. The GBPD (GBCD) program output is shown in the *MATLAB*® command window, without the need to open a command-line interface. After the programs are run, a text file with a .dat extension is created containing three columns: the polar coordinates(θ, ϕ) of each bin and their respective multiples of uniform distribution (MUD) values. The call for the function for GBPD and GBCD, respectively, is of the form:

datFname = segments2dat (GBCDfolder, segFname, GBCD_par);

and

datFname = GBCDsegments2dat (ax, ang, GBCDfolder, segFname, GBCD_par);

where the argument *GBCDfolder* is a string with the path to the folder containing the GBPD/GBCD programs, *segFname* is a string with the path to the segments file, *phaseName* is a string with the EBSD phase to be analyzed, *ax* the misorientation axes as a *MTEX* variable (class *Miller*) and *ang* the misorientation angles in degrees as a double array. The output *datFname* is a string variable containing the path to the exported .dat file. For the *GBCDsegments2dat* function, multiple misorientation axes/angles combinations can be provided as a input and the *datFname* will contain a cell array with the same amount of paths.

7.2.3 Import GBPD/GBCD plot files (*loadGBPD* and *loadGBCD* functions)

The *loadGBPD* (*loadGBCD*) function loads the .dat file created with the GBPD (GBCD) containing the coordinates and the MUD values. The call for the function for GBPD and GBCD, respectively, is of the form:

gbpd=loadGBPD(datFname);

and

gbcd = loadGBCD(datFname);

where the argument *datFname* is a string with the path to the .dat file created in the previous step. The output *gbpd* (*gbcd*) is a structure variable containing the polar coordinates (θ, ϕ) and the MUD values. For the *GBCDsegments2dat* function, the *datFname* variable may contain several paths as a cell array of strings.

7.2.4 **Plot GBPD/GBCD (*plotGBPD* and *plotGBCD* functions)**

The *plotGBPD* (*plotGBCD*) function plots the GBPD (GBCD) in a stereographic projection. The data can be visualized as a scatter or interpolated plot. The scatter plot is obtained using the flag *'scatter'*. An interpolation using an inverse distance weighing is performed using the flag *'smooth'*.

The call for the function is of the form:

plotGBPD(gbpd,cs);

and

plotGBCD(gbcd,cs, ax, ang)

where the argument *gbpd* is a structure containing the polar coordinates (θ, ϕ) coordinates and the MUD values obtained in the previous step and *cs* is the crystal symmetry (class *crystalSymmetry*) for the phase to be analyzed, *ax* the misorientation axes as a *MTEX* variable (class *Miller*) and *ang* the misorientation angle in degrees as a double array.

7.3. Results and discussion

Here we show an application example of the tools provided for the analyses of the GBPD and GBCD. The process of obtaining grain-boundary segments from EBSD data differs between *EDAX OIM*™ and *MTEX*. The *OIM*™ system method create segments by connecting triple junctions following the calculated grain boundaries (Figure 7.2a), within a given user defined pixel tolerance (Wright and Larsen, 2002). Because of the nature of this method, one important limitation is that inclusions in grains are omitted because they do not encompass triple junctions. Furthermore, the geometry of grain boundaries might be also oversimplified (Figure 7.2a).

MTEX uses a Voronoi tessellation to reconstruct polygons from EBSD measurements (Bachmann et al., 2011). This method provides better accuracy to describe the geometry of the grain boundaries and allows for grain inclusions to be analysed. Grain boundaries are defined in *MTEX* when at least one of the two criteria are met: Measurement points separate different phases or their misorientation angle exceeds a defined threshold.

Because EBSD data is assigned to pixels of square or hexagonal shape, a staircase effect would be present when assigning grain boundaries. To address this issue, grain boundaries must be smoothed (Figure 7.2). As discussed above, *EDAX OIM Analysis*™ reconstructs boundaries by connecting neighbouring triple points (Figure 7.2a). *MTEX* assigns Voronoi cells comprising similar data (orientation and phase). The smoothing is done by the *MTEX* function *smooth* (class *grain2D*). The default *'rate'* smoothing method averages the spatial orientation of grain boundaries, except triple points. The number of iterations is given by a smooth factor parameter. Figure 7.2 exemplifies the effect of increasing smoothing iterations. Figure 7.2b shows the grain boundary traces calculated without smoothing. The reconstructed grain boundaries outline the hexagonal shaped pixels (EBSD measurement points). This staircase effect becomes less evident as the grain boundaries are smoothed out, especially after 5 iterations (Figure 7.2c-f).

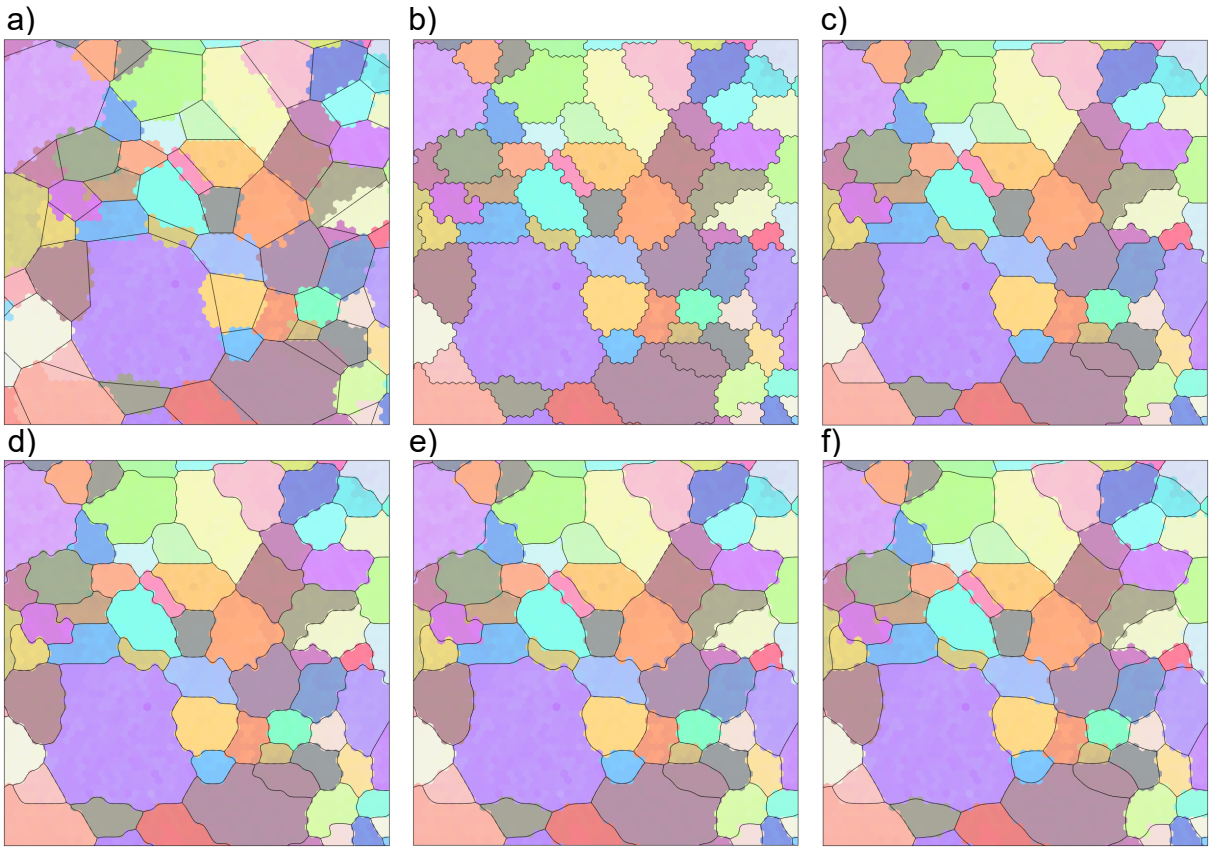

Figure 7.2: Comparison of segments (black lines) exported from a) *EDAX OIM*™ and *MTEX* for b) no smoothing and increasing number of smoothing iterations of c) 1, d) 2, e) 5 and f) 10 iterations.

7.4. Conclusions

We provide here a toolbox written in *MATLAB*® to extract grain boundary information from EBSD data, execute the grain boundary plane and character distribution programs and plot the results. *MTEX* provide functions to access and classify grain boundaries according to their misorientation axis and angle, phase and orientation of neighbouring grains, or any other user-defined criteria. This allows for better control on the exported grain-boundary segments and improved understanding of grain-boundary types and populations. Furthermore, any generic EBSD data can be used, independent of acquisition system.

Conclusions

In this work, the effect of grain boundaries in the deformation and grain growth of olivine at upper mantle conditions was investigated. The main findings are summarized below:

- The results presented in Chapter 4 suggest that grain boundaries act to promote deformation in the dislocation-accommodated grain-boundary sliding regime through the interaction with dislocations. The distribution of grain-boundary types evolves as a function of strain. The creation of grain boundaries starts by the formation of dislocation arrays (low-angle grain boundaries) that evolve into high-angle grain boundaries by crystal rotation via grain-boundary sliding.
- I show evidence suggesting transfer of dislocations across low-angle grain boundaries. For grains separated by a high misorientation angle (> 20º), the data suggest that the dislocations are instead absorbed into the grain boundaries, also causing grain rotation. This process would change the grain boundary plane and involve grain-boundary sliding.
- In simple shear deformation of olivine, the [100](010) is one of the main active slip systems. I show here that dislocation creep in these conditions leads to the formation of (hk0) grain boundaries in polycrystalline olivine. The activity of slip systems in olivine changes with stress, water content, pressure and temperature. Thus, if different dislocation systems are activated, different grain boundaries are created. Because different grain boundaries have different physical properties (Sutton and Balluffi, 1995), grain-size sensitive geophysical observables, such as electrical conductivity (Pommier et al., 2018; ten Grotenhuis et al., 2004) and seismic attenuation (Jackson et al., 2002) may exhibit variable responses accordingly.
- Our understanding of the role of grain boundaries in deformation and in the interpretation of geophysical observables would greatly benefit from in-situ experiments using bicrystals. For example, nanoindentation experiments (e.g., Britton et al., 2009) could provide information on the different factors involved in the assimilation and transmission of dislocations. Measurements of electrical conductivity in bicrystals (e.g., Kim et al., 2019; Osburn and Vest, 1971) would

provide valuable information on the effect of (specific) grain boundaries on the electrical conductivity of the Earth's mantle.

- In Chapter 5, I showed that the olivine grain-growth rate decreases at high pressures. I propose that this effect is a result of slower grain-boundary diffusion at high pressures. The implications for this finding are two-fold: i) changes in grain size due to slower grain growth might influence a transition to diffusion creep in deeper parts of the upper mantle, and ii) because grain-boundary diffusion is proposed to be also the main mechanism for diffusion creep in olivine (Tasaka and Hiraga, 2013), an increase in viscosity in the deep upper mantle as a function of pressure is expected if diffusion creep is the dominant mechanism, as previously suggested (e.g., Karato, 1992). Experimental studies focused on diffusion creep of olivine at high pressures are thus necessary to understand the effect of pressure on the rheology of the upper mantle.
- The grain-size evolution of olivine in the deep upper mantle (depths larger than 200 km) was estimated based on the grain-growth data presented here. I estimate a viscosity profile as a function of depth using the grain-size evolution predicted here and existing flow laws. The results indicate that viscosity is approximately constant in this region.
- The inference of mantle viscosity as a function of depth from surface measurements, such as post-glacial rebound, is less reliable as depth increases (e.g., Milne et al., 1998). Thus, experimental data exploring the factors controlling viscosity at large depths, such as reported here, are timely and crucial to advance our understanding on the dynamics of the Earth's mantle.
- In Chapter 6, I presented a new assembly (8/5) designed for pure shear deformation experiments at conditions of the deep upper mantle (e.g. 7 GPa, 1400 ºC). During experimental deformation at these conditions, olivine deformation is accommodated by dislocation creep, with fine-grained olivine significantly weaker than coarse-grained olivine. Measurements of the strength of olivine at these conditions (e.g., using synchrotron radiation) are necessary for quantitative estimations of the effect of grain boundaries on the rheology of the upper mantle.
- Attempts to extend the range of confining pressure of the 8/5 assembly to 10 GPa resulted in deformation in the brittle regime, while plastic deformation was expected. Possible explanations include failure due to localized heating, phase

transitions, thermal contraction, and release of elastic energy from the anvils or assembly parts. The in-situ monitoring of acoustic emissions could provide information on the processes involved and their implications for the understanding of deep-focus earthquakes.

- I introduced in Chapter 7 a toolbox developed to analyse the results of grain boundary-plane and character distribution calculations from 2-D EBSD data. The scripts are presented in the Appendix A.2. This toolbox simplifies and automate tasks and expand the use of these techniques for a great number of users. The toolbox is open source, which allows for continuous improvement and increasing number of functions.

References

Adjaoud, O., Marquardt, K., Jahn, S., 2012. Atomic structures and energies of grain boundaries in Mg2SiO4 forsterite from atomistic modeling. Phys Chem Minerals 39, 749–760. https://doi.org/10.1007/s00269-012-0529-5

Amiguet, E., Reynard, B., Caracas, R., Van de Moortèle, B., Hilairet, N., Wang, Y., 2012. Creep of phyllosilicates at the onset of plate tectonics. Earth and Planetary Science Letters 345–348, 142–150. https://doi.org/10.1016/j.epsl.2012.06.033

Anderson, O.L., 1980. The temperature profile of the upper mantle. Journal of Geophysical Research 85, 7003. https://doi.org/10.1029/JB085iB12p07003

Ashby, M.F., 1970. The deformation of plastically non-homogeneous materials. The Philosophical Magazine: A Journal of Theoretical Experimental and Applied Physics 21, 399–424. https://doi.org/10.1080/14786437008238426

Atkinson, A., 1985. Grain boundary diffusion - structural effects and mechanisms. J. Phys. Colloques 46, C4-379-C4-391. https://doi.org/10.1051/jphyscol:1985441

Atkinson, H.V., 1988. Overview no. 65: Theories of normal grain growth in pure single phase systems. Acta Metallurgica 36, 469–491. https://doi.org/10.1016/0001-6160(88)90079-X

Aupart, C., Dunkel, K.G., Angheluta, L., Austrheim, H., Ildefonse, B., Malthe-Sørenssen, A., Jamtveit, B., 2018. Olivine Grain Size Distributions in Faults and Shear Zones: Evidence for Nonsteady State Deformation. Journal of Geophysical Research: Solid Earth 123, 7421–7443. https://doi.org/10.1029/2018JB015836

Ave'lallemant, H.G., Carter, N.L., 1970. Syntectonic Recrystallization of Olivine and Modes of Flow in the Upper Mantle. GSA Bulletin 81, 2203–2220. https://doi.org/10.1130/0016-7606(1970)81[2203:SROOAM]2.0.CO;2

Bachhav, M., Dong, Y., Skemer, P., Marquis, E.A., 2015. Atomic Scale Investigation of Orthopyroxene and Olivine Grain Boundaries by Atom Probe Tomography. Microscopy and Microanalysis 21, 1315–1316. https://doi.org/10.1017/S1431927615007369

Bachmann, F., Hielscher, R., Schaeben, H., 2011. Grain detection from 2d and 3d EBSD data—Specification of the MTEX algorithm. Ultramicroscopy 111, 1720–1733. https://doi.org/10.1016/j.ultramic.2011.08.002

Bai, Kohlstedt, 1992. Substantial hydrogen solubility in olivine and implications for water storage in the mantle. Nature 357, 672–674. https://doi.org/10.1038/357672a0

Bai, Q., Mackwell, S.J., Kohlstedt, D.L., 1991. High-temperature creep of olivine single crystals 1. Mechanical results for buffered samples. Journal of Geophysical Research 96, 2441. https://doi.org/10.1029/90JB01723

Balluffi, R.W., 1982. Grain boundary diffusion mechanisms in metals. MTB 13, 527–553. https://doi.org/10.1007/BF02650011

Bäurer, M., Syha, M., Weygand, D., 2013. Combined experimental and numerical study on the effective grain growth dynamics in highly anisotropic systems: Application to barium titanate. Acta Materialia 61, 5664–5673. https://doi.org/10.1016/j.actamat.2013.06.007

Bayerschen, E., McBride, A.T., Reddy, B.D., Böhlke, T., 2016. Review on slip transmission criteria in experiments and crystal plasticity models. Journal of Materials Science 51, 2243–2258. https://doi.org/10.1007/s10853-015-9553-4

Bell, D.R., Rossman, G.R., Maldener, J., Endisch, D., Rauch, F., 2003. Hydroxide in olivine: A quantitative determination of the absolute amount and calibration of the IR spectrum: HYDROXIDE IN OLIVINE. J. Geophys. Res. 108. https://doi.org/10.1029/2001JB000679

Bercovici, D., 2003. The generation of plate tectonics from mantle convection. Earth and Planetary Science Letters 205, 107–121. https://doi.org/10.1016/S0012-821X(02)01009-9

Bercovici, D., Ricard, Y., 2012. Mechanisms for the generation of plate tectonics by two-phase grain-damage and pinning. Physics of the Earth and Planetary Interiors 202–203, 27–55. https://doi.org/10.1016/j.pepi.2012.05.003

Berry, A.J., Hermann, J., O'Neill, H.S., Foran, G.J., 2005. Fingerprinting the water site in mantle olivine. Geology 33, 869–872.

Bieler, T.R., Eisenlohr, P., Zhang, C., Phukan, H.J., Crimp, M.A., 2014. Grain boundaries and interfaces in slip transfer. Current Opinion in Solid State and Materials Science, Slip Localization and Transfer in Deformation and Fatigue of Polycrystals 18, 212–226. https://doi.org/10.1016/j.cossms.2014.05.003

Birle, J.D., Gibbs, G.V., Moore, P.B., Smith, J.V., 1968. Crystal structures of natural olivines. American Mineralogist 53, 807–824.

Bolfan-Casanova, N., 2005. Water in the Earth's mantle. Mineralogical Magazine 69, 229–257. https://doi.org/10.1180/0026461056930248

Bollinger, C., Marquardt, K., Ferreira, F., 2019. Intragranular plasticity vs. grain boundary sliding (GBS) in forsterite: Microstructural evidence at high pressures (3.5–5.0 GPa). American Mineralogist 104, 220–231. https://doi.org/10.2138/am-2019-6629

Boullier, A.M., Nicolas, A., 1975. Classification of textures and fabrics of peridotite xenoliths from South African kimberlites. Physics and Chemistry of the Earth 9, 467IN7469-468475.

Boyd, F.R., England, J.L., 1960. Apparatus for phase-equilibrium measurements at pressures up to 50 kilobars and temperatures up to 1750°C. J. Geophys. Res. 65, 741–748. https://doi.org/10.1029/JZ065i002p00741

Brinker, C.J., Scherer, G.W., 2013. Sol-gel science: the physics and chemistry of sol-gel processing. Academic press.

Britton, T.B., Randman, D., Wilkinson, A.J., 2009. Nanoindentation study of slip transfer phenomenon at grain boundaries. Journal of Materials Research 24, 607–615. https://doi.org/10.1557/jmr.2009.0088

Burgers, J.M., 1940. Geometrical considerations concerning the structural irregularities to be assumed in a crystal. Proc. Phys. Soc. 52, 23. https://doi.org/10.1088/0959-5309/52/1/304

Bürgmann, R., Dresen, G., 2008. Rheology of the Lower Crust and Upper Mantle: Evidence from Rock Mechanics, Geodesy, and Field Observations. Annual Review of Earth and Planetary Sciences 36, 531–567. https://doi.org/10.1146/annurev.earth.36.031207.124326

Burke, J.E., Turnbull, D., 1952. Recrystallization and grain growth. Progress in Metal Physics 3, 220–292. https://doi.org/10.1016/0502-8205(52)90009-9

Burnley, P.C., Green, H.W., Prior, D.J., 1991. Faulting associated with the olivine to spinel transformation in Mg2GeO4 and its implications for deep-focus earthquakes. Journal of Geophysical Research: Solid Earth 96, 425–443. https://doi.org/10.1029/90JB01937

Bussod, G.Y., Katsura, T., Rubie, D.C., 1994. The Large Volume Multi-anvil Press as a High P-T Deformation Apparatus, in: Liebermann, R.C., Sondergeld, C.H. (Eds.), Experimental Techniques in Mineral and Rock Physics: The Schreiber Volume, Pageoph Topical Volumes. Birkhäuser, Basel, pp. 579–599. https://doi.org/10.1007/978-3-0348-5108-4_19

Byerlee, J.D., 1968. Brittle-ductile transition in rocks. J. Geophys. Res. 73, 4741–4750. https://doi.org/10.1029/JB073i014p04741

Callahan, P.G., De Graef, M., 2013. Dynamical Electron Backscatter Diffraction Patterns. Part I: Pattern Simulations. Microsc Microanal 19, 1255–1265. https://doi.org/10.1017/S1431927613001840

Cantwell, P.R., Tang, M., Dillon, S.J., Luo, J., Rohrer, G.S., Harmer, M.P., 2014. Grain boundary complexions. Acta Materialia 62, 1–48. https://doi.org/10.1016/j.actamat.2013.07.037

Carter, C.B., Sass, S.L., 1981. Electron Diffraction and Microscopy Techniques for Studying Grain-Boundary Structure. Journal of the American Ceramic Society 64, 335–345. https://doi.org/10.1111/j.1151-2916.1981.tb10299.x

Castaing, R., 1951. Application of electron probes to local chemical and crystallographic analysis. Ph. D. Thesis (University of Paris).

Christensen, N.I., Crosson, R.S., 1968. Seismic anisotropy in the upper mantle. Tectonophysics 6, 93–107. https://doi.org/10.1016/0040-1951(68)90013-9

Christensen, U.R., 1987. Some geodynamical effects of anisotropic viscosity. Geophys J Int 91, 711–736. https://doi.org/10.1111/j.1365-246X.1987.tb01666.x

Coble, R.L., 1963. A Model for Boundary Diffusion Controlled Creep in Polycrystalline Materials. Journal of Applied Physics 34, 1679–1682. https://doi.org/10.1063/1.1702656

Condie, K.C., 1997. Plate tectonics and crustal evolution, 4th ed. ed. Butterworth Heinemann, Oxford ; Boston.

Cordier, P., 2002. Dislocations and Slip Systems of Mantle Minerals. Reviews in Mineralogy and Geochemistry 51, 137–179. https://doi.org/10.2138/gsrmg.51.1.137

Cordier, P., Demouchy, S., Beausir, B., Taupin, V., Barou, F., Fressengeas, C., 2014. Disclinations provide the missing mechanism for deforming olivine-rich rocks in the mantle. Nature 507, 51–56. https://doi.org/10.1038/nature13043

Cordier, P., Rubie, D.C., 2001. Plastic deformation of minerals under extreme pressure using a multi-anvil apparatus. Materials Science and Engineering: A, Dislocations 2000: An International Conference on the Fundamentals of Plastic Deformation 309–310, 38–43. https://doi.org/10.1016/S0921-5093(00)01795-0

Couvy, H., Frost, D.J., Heidelbach, F., Nyilas, K., Ungár, T., Mackwell, S., Cordier, P., 2004. Shear deformation experiments of forsterite at 11 GPa - 1400°C in the multianvil apparatus. European Journal of Mineralogy 16, 877–889. https://doi.org/10.1127/0935-1221/2004/0016-0877

Dannberg, J., Eilon, Z., Faul, U., Gassmöller, R., Moulik, P., Myhill, R., 2017. The importance of grain size to mantle dynamics and seismological observations. Geochemistry, Geophysics, Geosystems 18, 3034–3061. https://doi.org/10.1002/2017GC006944

Davies, P., Randle, V., 2001. Grain boundary engineering and the role of the interfacial plane. Materials Science and Technology 17, 615–626. https://doi.org/10.1179/026708301101510384

Davis, B.T.C., England, J.L., 1964. The melting of forsterite up to 50 kilobars. J. Geophys. Res. 69, 1113–1116. https://doi.org/10.1029/JZ069i006p01113

De Hoog, J.C.M., Gall, L., Cornell, D.H., 2010. Trace-element geochemistry of mantle olivine and application to mantle petrogenesis and geothermobarometry. Chemical Geology 270, 196–215. https://doi.org/10.1016/j.chemgeo.2009.11.017

de Koning, M., Kurtz, R.J., Bulatov, V.V., Henager, C.H., Hoagland, R.G., Cai, W., Nomura, M., 2003. Modeling of dislocation–grain boundary interactions in FCC metals. Journal of Nuclear Materials, Proceedings of the Second IEA Fusion

Materials Agreement Workshop on Modeling and Experimental Validation 323, 281–289. https://doi.org/10.1016/j.jnucmat.2003.08.008

Demouchy, S., 2010. Diffusion of hydrogen in olivine grain boundaries and implications for the survival of water-rich zones in the Earth's mantle. Earth and Planetary Science Letters 295, 305–313. https://doi.org/10.1016/j.epsl.2010.04.019

Demouchy, S., Bolfan-Casanova, N., 2016. Distribution and transport of hydrogen in the lithospheric mantle: A review. Lithos 240–243, 402–425. https://doi.org/10.1016/j.lithos.2015.11.012

Dillon, S., Harmer, M., 2007. Multiple grain boundary transitions in ceramics: A case study of alumina. Acta Materialia 55, 5247–5254. https://doi.org/10.1016/j.actamat.2007.04.051

Dingley, D., Pond, R., 1979. On the interaction of crystal dislocations with grain boundaries. Acta Metallurgica 27, 667–682.

Durham, W.B., Goetze, C., Blake, B., 1977. Plastic flow of oriented single crystals of olivine: 2. Observations and interpretations of the dislocation structures. J. Geophys. Res. 82, 5755–5770. https://doi.org/10.1029/JB082i036p05755

Durham, W.B., Rubie, D.C., 1996. Can the multianvil apparatus really be used for high-pressure deformation experiments? (No. UCRL-JC-123733; CONF-960193-1). Lawrence Livermore National Lab., CA (United States).

Dziewonski, A.M., Anderson, D.L., 1981. Preliminary reference earth model. Physics of the earth and planetary interiors 25, 297–356.

Edgar, A.D., 1973. Experimental petrology: basic principles and techniques. Oxford University Press.

Edmond, J.M., Paterson, M.S., 1971. Strength of solid pressure media and implications for high pressure apparatus. Contr. Mineral. and Petrol. 30, 141–160. https://doi.org/10.1007/BF00372255

Evans, B., Renner, J., Hirth, G., 2001. A few remarks on the kinetics of static grain growth in rocks. Int J Earth Sci 90, 88–103. https://doi.org/10.1007/s005310000150

Falus, G., Tommasi, A., Soustelle, V., 2011. The effect of dynamic recrystallization on olivine crystal preferred orientations in mantle xenoliths deformed under varied

stress conditions. Journal of Structural Geology 33, 1528–1540. https://doi.org/10.1016/j.jsg.2011.09.010

Farver, J.R., Yund, R.A., 2000. Silicon diffusion in forsterite aggregates: Implications for diffusion accommodated creep. Geophys. Res. Lett. 27, 2337–2340. https://doi.org/10.1029/2000GL008492

Faul, U.H., Cline II, C.J., Berry, A., Jackson, I., Garapić, G., 2018. Constraints on oxygen fugacity within metal capsules. Phys Chem Minerals 45, 497–509. https://doi.org/10.1007/s00269-017-0937-7

Faul, U.H., Jackson, I., 2007. Diffusion creep of dry, melt-free olivine. Journal of Geophysical Research: Solid Earth 112. https://doi.org/10.1029/2006JB004586

Faul, U.H., Scott, D., 2006. Grain growth in partially molten olivine aggregates. Contributions to Mineralogy and Petrology 151, 101–111. https://doi.org/10.1007/s00410-005-0048-1

Fegley Jr, B., 2012. Practical chemical thermodynamics for geoscientists. Academic Press.

Fei, H., Koizumi, S., Sakamoto, N., Hashiguchi, M., Yurimoto, H., Marquardt, K., Miyajima, N., Yamazaki, D., Katsura, T., 2016. New constraints on upper mantle creep mechanism inferred from silicon grain-boundary diffusion rates. Earth and Planetary Science Letters 433, 350–359. https://doi.org/10.1016/j.epsl.2015.11.014

Fei, H., Wiedenbeck, M., Yamazaki, D., Katsura, T., 2014. No effect of water on oxygen self-diffusion rate in forsterite. J. Geophys. Res. Solid Earth 119, 2014JB011141. https://doi.org/10.1002/2014JB011141

Fei, H., Wiedenbeck, M., Yamazaki, D., Katsura, T., 2013. Small effect of water on upper-mantle rheology based on silicon self-diffusion coefficients. Nature 498, 213–215. https://doi.org/10.1038/nature12193

Ferreira, F., Hansen, L.N., Marquardt, K., 2021. The Effect of Grain Boundaries on Plastic Deformation of Olivine. Journal of Geophysical Research: Solid Earth 126, e2020JB020273. https://doi.org/10.1029/2020JB020273

Freed, A.M., 2004. Earthquake triggering by static, dynamic, and postseismic stress transfer. Annu. Rev. Earth Planet. Sci. 33, 335–367. https://doi.org/10.1146/annurev.earth.33.092203.122505

Frohlich, C., 1989. The Nature of Deep-Focus Earthquakes. Annual Review of Earth and Planetary Sciences 17, 227–254. https://doi.org/10.1146/annurev.ea.17.050189.001303

Frost, D.J., Dolejš, D., 2007. Experimental determination of the effect of H2O on the 410-km seismic discontinuity. Earth and Planetary Science Letters 256, 182–195. https://doi.org/10.1016/j.epsl.2007.01.023

Frost, D.J., Poe, B.T., Trønnes, R.G., Liebske, C., Duba, A., Rubie, D.C., 2004. A new large-volume multianvil system. Physics of the Earth and Planetary Interiors 143–144, 507–514. https://doi.org/10.1016/j.pepi.2004.03.003

Gardés, E., Wunder, B., Marquardt, K., Heinrich, W., 2012. The effect of water on intergranular mass transport: new insights from diffusion-controlled reaction rims in the MgO–SiO2 system. Contributions to Mineralogy and Petrology 164, 1–16. https://doi.org/10.1007/s00410-012-0721-0

Gifkins, R.C., 1976. Grain-boundary sliding and its accommodation during creep and superplasticity. Metallurgical Transactions A 7, 1225–1232. https://doi.org/10.1007/BF02656607

Gleiter, H., 1985. The significance of the structure of internal interfaces for the properties of materials. Le Journal de Physique Colloques 46, C4-393-C4-404. https://doi.org/10.1051/jphyscol:1985442

Goetze, C., Kohlstedt, D.L., 1973. Laboratory study of dislocation climb and diffusion in olivine. J. Geophys. Res. 78, 5961–5971. https://doi.org/10.1029/JB078i026p05961

Goetze, C., Poirier, J.P., Kelly, A., Cook, A.H., Greenwood, G.W., 1978. The mechanisms of creep in olivine. Philosophical Transactions of the Royal Society of London. Series A, Mathematical and Physical Sciences 288, 99–119. https://doi.org/10.1098/rsta.1978.0008

Goldstein, J., Newbury, D.E., Michael, J.R., Ritchie, N.W.M., Scott, J.H.J., Joy, D.C., 2018. Scanning electron microscopy and X-ray microanalysis, Fourth edition. ed. Springer, New York, NY, U.S.A.

Gottstein, G., Shvindlerman, L.S., 2009. Grain boundary migration in metals: thermodynamics, kinetics, applications. CRC press.

Gurmani, S.F., Jahn, S., Brasse, H., Schilling, F.R., 2011. Atomic scale view on partially molten rocks: Molecular dynamics simulations of melt-wetted olivine grain boundaries. Journal of Geophysical Research: Solid Earth 116.

Hall, C.E., Parmentier, E.M., 2003. Influence of grain size evolution on convective instability: CONVECTIVE INSTABILITY. Geochem. Geophys. Geosyst. 4. https://doi.org/10.1029/2002GC000308

Hall, E.O., 1951. The deformation and ageing of mild steel: III discussion of results. Proceedings of the Physical Society. Section B 64, 747.

Hansen, L.N., Kumamoto, K.M., Thom, C.A., Wallis, D., Durham, W.B., Goldsby, D.L., Breithaupt, T., Meyers, C.D., Kohlstedt, D.L., 2019. Low-Temperature Plasticity in Olivine: Grain Size, Strain Hardening, and the Strength of the Lithosphere. Journal of Geophysical Research: Solid Earth 124, 5427–5449. https://doi.org/10.1029/2018JB016736

Hansen, L.N., Zhao, Y.-H., Zimmerman, M.E., Kohlstedt, D.L., 2014. Protracted fabric evolution in olivine: Implications for the relationship among strain, crystallographic fabric, and seismic anisotropy. Earth and Planetary Science Letters 387, 157–168. https://doi.org/10.1016/j.epsl.2013.11.009

Hansen, L.N., Zimmerman, M.E., Dillman, A.M., Kohlstedt, D.L., 2012a. Strain localization in olivine aggregates at high temperature: A laboratory comparison of constant-strain-rate and constant-stress boundary conditions. Earth and Planetary Science Letters 333–334, 134–145. https://doi.org/10.1016/j.epsl.2012.04.016

Hansen, L.N., Zimmerman, M.E., Kohlstedt, D.L., 2012b. The influence of microstructure on deformation of olivine in the grain-boundary sliding regime. Journal of Geophysical Research: Solid Earth 117, n/a-n/a. https://doi.org/10.1029/2012JB009305

Hansen, L.N., Zimmerman, M.E., Kohlstedt, D.L., 2011. Grain boundary sliding in San Carlos olivine: Flow law parameters and crystallographic-preferred orientation. Journal of Geophysical Research 116. https://doi.org/10.1029/2011JB008220

Hayden, L.A., Watson, E.B., 2008. Grain boundary mobility of carbon in Earth's mantle: A possible carbon flux from the core. Proc Natl Acad Sci U S A 105, 8537–8541. https://doi.org/10.1073/pnas.0710806105

Head, A.K., 1953. X. The Interaction of Dislocations and Boundaries. The London, Edinburgh, and Dublin Philosophical Magazine and Journal of Science 44, 92–94. https://doi.org/10.1080/14786440108520278

Heinemann, S., Wirth, R., Gottschalk, M., Dresen, G., 2005. Synthetic [100] tilt grain boundaries in forsterite: 9.9 to 21.5°. Phys Chem Minerals 32, 229–240. https://doi.org/10.1007/s00269-005-0448-9

Hench, L.L., West, J.K., 1990. The sol-gel process. Chem. Rev. 90, 33–72. https://doi.org/10.1021/cr00099a003

Herring, C., 1950. Diffusional Viscosity of a Polycrystalline Solid. Journal of Applied Physics 21, 437–445. https://doi.org/10.1063/1.1699681

Hess, H., 1964. Seismic anisotropy of the uppermost mantle under oceans.

Hielscher, R., Schaeben, H., 2008. A novel pole figure inversion method: specification of the MTEX algorithm. Journal of Applied Crystallography 41, 1024–1037.

Hillert, M., 1965. On the theory of normal and abnormal grain growth. Acta Metallurgica 13, 227–238. https://doi.org/10.1016/0001-6160(65)90200-2

Hiraga, T., Anderson, I., Zimmerman, M., Mei, S., Kohlstedt, D., 2002. Structure and chemistry of grain boundaries in deformed, olivine + basalt and partially molten lherzolite aggregates: evidence of melt-free grain boundaries. Contributions to Mineralogy and Petrology 144, 163–175. https://doi.org/10.1007/s00410-002-0394-1

Hiraga, T., Anderson, I.M., Kohlstedt, D.L., 2004. Grain boundaries as reservoirs of incompatible elements in the Earth's mantle. Nature 427, 699–703.

Hiraga, T., Anderson, I.M., Kohlstedt, D.L., 2003. Chemistry of grain boundaries in mantle rocks. American Mineralogist 88, 1015–1019.

Hiraga, T., Tachibana, C., Ohashi, N., Sano, S., 2010. Grain growth systematics for forsterite ± enstatite aggregates: Effect of lithology on grain size in the upper mantle. Earth and Planetary Science Letters 291, 10–20. https://doi.org/10.1016/j.epsl.2009.12.026

Hirth, G., Kohlstedt, D., 2003. Rheology of the upper mantle and the mantle wedge: A view from the experimentalists, in: Eiler, J. (Ed.), Geophysical Monograph Series. American Geophysical Union, Washington, D. C., pp. 83–105.

Hirth, G., Kohlstedt, D.L., 1996. Water in the oceanic upper mantle: implications for rheology, melt extraction and the evolution of the lithosphere. Earth and Planetary Science Letters 144, 93–108.

Hirth, G., Kohlstedt, D.L., 1995. Experimental constraints on the dynamics of the partially molten upper mantle: 2. Deformation in the dislocation creep regime. Journal of Geophysical Research: Solid Earth 100, 15441–15449.

Hirth, J.P., 1972. The influence of grain boundaries on mechanical properties. MT 3, 3047–3067. https://doi.org/10.1007/BF02661312

Hobbs, B.E., Ord, A., Teyssier, C., 1986. Earthquakes in the ductile regime? PAGEOPH 124, 309–336. https://doi.org/10.1007/BF00875730

Holm, E.A., Foiles, S.M., 2010. How Grain Growth Stops: A Mechanism for Grain-Growth Stagnation in Pure Materials. Science 328, 1138–1141. https://doi.org/10.1126/science.1187833

Humphreys, F.J., Hatherly, M., 2004. Recrystallization and related annealing phenomena. Elsevier, Amsterdam; Boston.

Hunter, A., Leu, B., Beyerlein, I.J., 2018. A review of slip transfer: applications of mesoscale techniques. J Mater Sci 53, 5584–5603. https://doi.org/10.1007/s10853-017-1844-5

Ishida, Y., Brown, M.H., 1967. Dislocations in grain boundaries and grain boundary sliding. Acta Metallurgica 15, 857–860. https://doi.org/10.1016/0001-6160(67)90367-7

Ismaïl, W.B., Mainprice, D., 1998. An olivine fabric database: an overview of upper mantle fabrics and seismic anisotropy. Tectonophysics 296, 145–157. https://doi.org/10.1016/S0040-1951(98)00141-3

Ito, E., 2007. 2.08 - Theory and Practice – Multianvil Cells and High-Pressure Experimental Methods, in: Schubert, G. (Ed.), Treatise on Geophysics. Elsevier, Amsterdam, pp. 197–230. https://doi.org/10.1016/B978-044452748-6.00036-5

Jackson, I., Faul, U.H., Fitz Gerald, J.D., Tan, B.H., 2004. Shear wave attenuation and dispersion in melt-bearing olivine polycrystals: 1. Specimen fabrication and mechanical testing. Journal of Geophysical Research: Solid Earth 109. https://doi.org/10.1029/2003JB002406

Jackson, I., Fitz Gerald, J.D., Faul, U.H., Tan, B.H., 2002. Grain-size-sensitive seismic wave attenuation in polycrystalline olivine: Seismic wave attenuation in olivine. Journal of Geophysical Research: Solid Earth 107, ECV 5-1-ECV 5-16. https://doi.org/10.1029/2001JB001225

Jaupart, C., Labrosse, S., Mareschal, J.-C., 2007. 7.06 - Temperatures, Heat and Energy in the Mantle of the Earth, in: Schubert, G. (Ed.), Treatise on Geophysics. Elsevier, Amsterdam, pp. 253–303. https://doi.org/10.1016/B978-044452748-6.00114-0

Jung, H., 2001. Water-Induced Fabric Transitions in Olivine. Science 293, 1460–1463. https://doi.org/10.1126/science.1062235

Jung, H., Karato, S.-I., 2001. Effects of water on dynamically recrystallized grain-size of olivine. Journal of Structural Geology 23, 1337–1344. https://doi.org/10.1016/S0191-8141(01)00005-0

Jung, H., Katayama, I., Jiang, Z., Hiraga, T., Karato, S.-I., 2006. Effect of water and stress on the lattice-preferred orientation of olivine. Tectonophysics 421, 1–22.

Kacher, J., Eftink, B.P., Cui, B., Robertson, I.M., 2014. Dislocation interactions with grain boundaries. Current Opinion in Solid State and Materials Science, Slip Localization and Transfer in Deformation and Fatigue of Polycrystals 18, 227–243. https://doi.org/10.1016/j.cossms.2014.05.004

Kacher, J.P., Liu, G.S., Robertson, I.M., 2011. Visualization of grain boundary/dislocation interactions using tomographic reconstructions. Scripta Materialia 64, 677–680. https://doi.org/10.1016/j.scriptamat.2010.12.020

Kaminsky, W., 2005. WinXMorph: a computer program to draw crystal morphology, growth sectors and cross sections with export files in VRML V2.0 utf8-virtual reality format. J Appl Cryst 38, 566–567. https://doi.org/10.1107/S0021889805012148

Karato, S., 2012. Deformation of Earth Materials: An Introduction to the Rheology of Solid Earth. Cambridge University Press.

Karato, S., 2008. Deformation of Earth Materials: An Introduction to the Rheology of Solid Earth. Cambridge University Press, Cambridge. https://doi.org/10.1017/CBO9780511804892

Karato, S., 1992. On the Lehmann discontinuity. Geophysical Research Letters 19, 2255–2258.

Karato, Shun-ichiro, 1989. Plasticity-crystal structure systematics in dense oxides and its implications for the creep strength of the Earth's deep interior: a preliminary result. Physics of the Earth and Planetary Interiors 55, 234–240. https://doi.org/10.1016/0031-9201(89)90071-X

Karato, S., 1989. Grain growth kinetics in olivine aggregates. Tectonophysics 168, 255–273. https://doi.org/10.1016/0040-1951(89)90221-7

Karato, S. -i., Wu, P., 1993. Rheology of the Upper Mantle: A Synthesis. Science 260, 771–778. https://doi.org/10.1126/science.260.5109.771

Karato, S., Jung, H., 1998. Water, partial melting and the origin of the seismic low velocity and high attenuation zone in the upper mantle. Earth and Planetary Science Letters 157, 193–207.

Karato, S., Jung, H., Katayama, I., Skemer, P., 2008. Geodynamic Significance of Seismic Anisotropy of the Upper Mantle: New Insights from Laboratory Studies. Annual Review of Earth and Planetary Sciences 36, 59–95. https://doi.org/10.1146/annurev.earth.36.031207.124120

Karato, S., Rubie, D.C., 1997. Toward an experimental study of deep mantle rheology: A new multianvil sample assembly for deformation studies under high pressures and temperatures. J. Geophys. Res. 102, 20111–20122. https://doi.org/10.1029/97JB01732

Karato, S.-I., 2003. Mapping water content in the upper mantle. Inside the subduction factory 135–152.

Karato, S.-I., Paterson, M.S., FitzGerald, J.D., 1986. Rheology of synthetic olivine aggregates: Influence of grain size and water. J. Geophys. Res. 91, 8151–8176. https://doi.org/10.1029/JB091iB08p08151

Katsura, T., Yamada, H., Nishikawa, O., Song, M., Kubo, A., Shinmei, T., Yokoshi, S., Aizawa, Y., Yoshino, T., Walter, M.J., Ito, E., Funakoshi, K., 2004. Olivine-wadsleyite transition in the system (Mg,Fe)2SiO4. Journal of Geophysical Research: Solid Earth 109. https://doi.org/10.1029/2003JB002438

Kawazoe, T., Karato, S., Otsuka, K., Jing, Z., Mookherjee, M., 2009. Shear deformation of dry polycrystalline olivine under deep upper mantle conditions using a

rotational Drickamer apparatus (RDA). Physics of the Earth and Planetary Interiors, Advances in High Pressure Mineral Physics: from Deep Mantle to the Core 174, 128–137. https://doi.org/10.1016/j.pepi.2008.06.027

Kawazoe, T., Nishihara, Y., Ohuchi, T., Miyajima, N., Maruyama, G., Higo, Y., Funakoshi, K., Irifune, T., 2016. Creep strength of ringwoodite measured at pressure–temperature conditions of the lower part of the mantle transition zone using a deformation–DIA apparatus. Earth and Planetary Science Letters 454, 10–19. https://doi.org/10.1016/j.epsl.2016.08.011

Kelly, M.N., Glowinski, K., Nuhfer, N.T., Rohrer, G.S., 2016. The five parameter grain boundary character distribution of α-Ti determined from three-dimensional orientation data. Acta Materialia 111, 22–30. https://doi.org/10.1016/j.actamat.2016.03.029

Khorashadizadeh, A., Raabe, D., Zaefferer, S., Rohrer, G.S., Rollett, A.D., Winning, M., 2011. Five-Parameter Grain Boundary Analysis by 3D EBSD of an Ultra Fine Grained CuZr Alloy Processed by Equal Channel Angular Pressing. Advanced Engineering Materials 13, 237–244. https://doi.org/10.1002/adem.201000259

Kim, Y.-W., Tochigi, E., Tatami, J., Kim, Y.-H., Jang, S.H., Javvaji, S., Jung, J., Kim, K.J., Ikuhara, Y., 2019. Carrier Depletion near the Grain Boundary of a SiC Bicrystal. Scientific Reports 9, 18014. https://doi.org/10.1038/s41598-019-54525-z

Klinger, M., Jäger, A., 2015. Crystallographic Tool Box (CrysTBox): automated tools for transmission electron microscopists and crystallographers. J Appl Crystallogr 48, 2012–2018. https://doi.org/10.1107/S1600576715017252

Kohlstedt, D.L., Goetze, C., Durham, W.B., Sande, J.V., 1976. New Technique for Decorating Dislocations in Olivine. Science 191, 1045–1046. https://doi.org/10.1126/science.191.4231.1045

Kohlstedt, D.L., Hansen, L.N., 2015. Constitutive Equations, Rheological Behavior, and Viscosity of Rocks, in: Treatise on Geophysics. Elsevier, pp. 441–472. https://doi.org/10.1016/B978-0-444-53802-4.00042-7

Kohlstedt, D.L., Keppler, H., Rubie, D.C., 1996. Solubility of water in the α, β and γ phases of (Mg,Fe)2SiO4. Contrib Mineral Petrol 123, 345–357. https://doi.org/10.1007/s004100050161

Kohlstedt, D.L., Li, Y., Mackwell, S.J., 2012. O Water in Olivine, Where Art Thou?, in: AGU Fall Meeting Abstracts.

Kohlstedt, D.L., Weathers, M.S., 1980. Deformation-induced microstructures, paleopiezometers, and differential stresses in deeply eroded fault zones. J. Geophys. Res. 85, 6269–6285. https://doi.org/10.1029/JB085iB11p06269

Koizumi, S., Hiraga, T., Tachibana, C., Tasaka, M., Miyazaki, T., Kobayashi, T., Takamasa, A., Ohashi, N., Sano, S., 2010. Synthesis of highly dense and fine-grained aggregates of mantle composites by vacuum sintering of nano-sized mineral powders. Physics and Chemistry of Minerals 37, 505–518. https://doi.org/10.1007/s00269-009-0350-y

Kondo, S., Mitsuma, T., Shibata, N., Ikuhara, Y., 2016. Direct observation of individual dislocation interaction processes with grain boundaries. Sci Adv 2. https://doi.org/10.1126/sciadv.1501926

Kumamoto, K.M., Thom, C.A., Wallis, D., Hansen, L.N., Armstrong, D.E.J., Warren, J.M., Goldsby, D.L., Wilkinson, A.J., 2017. Size effects resolve discrepancies in 40 years of work on low-temperature plasticity in olivine. Science Advances 3, e1701338. https://doi.org/10.1126/sciadv.1701338

Langdon, T.G., 2006. Grain boundary sliding revisited: Developments in sliding over four decades. J Mater Sci 41, 597–609. https://doi.org/10.1007/s10853-006-6476-0

Langdon, T.G., 1994. A unified approach to grain boundary sliding in creep and superplasticity. Acta Metallurgica et Materialia 42, 2437–2443. https://doi.org/10.1016/0956-7151(94)90322-0

Langdon, T.G., 1970. Grain boundary sliding as a deformation mechanism during creep. The Philosophical Magazine: A Journal of Theoretical Experimental and Applied Physics 22, 689–700. https://doi.org/10.1080/14786437008220939

Larsen, R.J., Adams, B.L., 2004. New stereology for the recovery of grain-boundary plane distributions in the crystal frame. Metall and Mat Trans A 35, 1991–1998. https://doi.org/10.1007/s11661-004-0148-y

Laumonier, M., Farla, R., Frost, D.J., Katsura, T., Marquardt, K., Bouvier, A.-S., Baumgartner, L.P., 2017. Experimental determination of melt interconnectivity

and electrical conductivity in the upper mantle. Earth and Planetary Science Letters 463, 286–297. https://doi.org/10.1016/j.epsl.2017.01.037

Lee, T.C., Robertson, I.M., Birnbaum, H.K., 1990. TEM in situ deformation study of the interaction of lattice dislocations with grain boundaries in metals. Philosophical Magazine A 62, 131–153. https://doi.org/10.1080/01418619008244340

Lee, T.C., Robertson, I.M., Birnbaum, H.K., 1989. Prediction of slip transfer mechanisms across grain boundaries. Scripta Metallurgica 23, 799–803. https://doi.org/10.1016/0036-9748(89)90534-6

Lehmann, I., 1961. S and the structure of the upper mantle. Geophyical Journal of the Royal Astronomical Society 124–138.

Lehmann, I., 1959. Velocities of longitudinal waves in the upper part of the earth's mantle. Annales de Geophysique 15, 93.

Lejcek, P., 2010. Grain Boundary Segregation in Metals, Springer Series in Materials Science. Springer Berlin Heidelberg, Berlin, Heidelberg.

Li, L., Raterron, P., Weidner, D., Chen, J., 2003. Olivine flow mechanisms at 8 GPa. Physics of the Earth and Planetary Interiors 138, 113–129. https://doi.org/10.1016/S0031-9201(03)00065-7

Li, L., Weidner, D., Raterron, P., Chen, J., Vaughan, M., 2004. Stress measurements of deforming olivine at high pressure. Physics of the Earth and Planetary Interiors, New Developments in High-Pressure Mineral Physics and Applications to the Earth's Interior 143–144, 357–367. https://doi.org/10.1016/j.pepi.2003.09.022

Liebermann, R.C., 2011. Multi-anvil, high pressure apparatus: a half-century of development and progress. High Pressure Research 31, 493–532. https://doi.org/10.1080/08957959.2011.618698

Liebermann, R.C., Wang, Y., 2013. Characterization of Sample Environment in a Uniaxial Split-Sphere Apparatus, in: Syono, Y., Manghnani, M.H. (Eds.), Geophysical Monograph Series. American Geophysical Union, Washington, D. C., pp. 19–31. https://doi.org/10.1029/GM067p0019

Lim, L.C., Raj, R., 1985. Interaction between lattice and grain boundary dislocations and their role in mechanical properties of interfaces. Le Journal de Physique Colloques 46, C4-581-C4-595.

Liu, F., Kirchheim, R., 2004. Nano-scale grain growth inhibited by reducing grain boundary energy through solute segregation. Journal of Crystal Growth 264, 385–391. https://doi.org/10.1016/j.jcrysgro.2003.12.021

Lloyd, G.E., Farmer, A.B., Mainprice, D., 1997. Misorientation analysis and the formation and orientation of subgrain and grain boundaries. Tectonophysics 279, 55–78. https://doi.org/10.1016/S0040-1951(97)00115-7

Lockner, D.A., Beeler, N.M., 2002. 32 - Rock Failure and Earthquakes, in: Lee, W.H.K., Kanamori, H., Jennings, P.C., Kisslinger, C. (Eds.), International Geophysics, International Handbook of Earthquake and Engineering Seismology, Part A. Academic Press, pp. 505–537. https://doi.org/10.1016/S0074-6142(02)80235-2

Luster, J., Morris, M.A., 1995. Compatibility of deformation in two-phase Ti-Al alloys: Dependence on microstructure and orientation relationships. MMTA 26, 1745–1756. https://doi.org/10.1007/BF02670762

Mackwell, S.J., Kohlstedt, D.L., 1990. Diffusion of hydrogen in olivine: Implications for water in the mantle. J. Geophys. Res. 95, 5079–5088. https://doi.org/10.1029/JB095iB04p05079

Mackwell, S.J., Kohlstedt, D.L., Paterson, M.S., 1985. The role of water in the deformation of olivine single crystals. J. Geophys. Res. 90, 11319–11333. https://doi.org/10.1029/JB090iB13p11319

Mainprice, D., Tommasi, A., Couvy, H., Cordier, P., Frost, D.J., 2005. Pressure sensitivity of olivine slip systems and seismic anisotropy of Earth’s upper mantle. Nature 433, 731–733. https://doi.org/10.1038/nature03266

Manthilake, M.A.G.M., Walte, N., Frost, D.J., 2012. A new multi-anvil press employing six independently acting 8 MN hydraulic rams. High Pressure Research 32, 195–207. https://doi.org/10.1080/08957959.2012.680450

Marquardt, K., Faul, U.H., 2018. The structure and composition of olivine grain boundaries: 40 years of studies, status and current developments. Phys Chem Minerals 45, 139–172. https://doi.org/10.1007/s00269-017-0935-9

Marquardt, K., Graef, M.D., Singh, S., Marquardt, H., Rosenthal, A., Koizuimi, S., 2017. Quantitative electron backscatter diffraction (EBSD) data analyses using the dictionary indexing (DI) approach: Overcoming indexing difficulties on

geological materials. American Mineralogist 102, 1843–1855. https://doi.org/10.2138/am-2017-6062

Marquardt, K., Rohrer, G.S., Morales, L., Rybacki, E., Marquardt, H., Lin, B., 2015. The most frequent interfaces in olivine aggregates: the GBCD and its importance for grain boundary related processes. Contributions to Mineralogy and Petrology 170. https://doi.org/10.1007/s00410-015-1193-9

Maruyama, G., Hiraga, T., 2017. Grain- to multiple-grain-scale deformation processes during diffusion creep of forsterite + diopside aggregate: 2. Grain boundary sliding-induced grain rotation and its role in crystallographic preferred orientation in rocks. Journal of Geophysical Research: Solid Earth 122, 5916–5934. https://doi.org/10.1002/2017JB014255

McDade, P., Wood, B.J., Westrenen, W.V., Brooker, R., Gudmundsson, G., Soulard, H., Najorka, J., Blundy, J., 2002. Pressure corrections for a selection of piston-cylinder cell assemblies. Mineralogical Magazine 66, 1021–1028. https://doi.org/10.1180/0026461026660074

McLaren, A.C., 2005. Transmission Electron Microscopy of Minerals and Rocks, Cambridge Topics in Mineral Physics and Chemistry. CUP.

McLean, D., 1971. Grain boundary dislocations: Their effect on vacancies and sliding. The Philosophical Magazine: A Journal of Theoretical Experimental and Applied Physics 23, 467–472. https://doi.org/10.1080/14786437108216396

Mei, S, Kohlstedt, D., 2000. Influence of water on plastic deformation of olivine aggregates: 1. Diffusion creep regime. Journal of Geophysical Research: Solid Earth 105, 21457–21469.

Mei, S., Kohlstedt, D.L., 2000. Influence of water on plastic deformation of olivine aggregates: 2. Dislocation creep regime. J. Geophys. Res. 105, 21471–21481. https://doi.org/10.1029/2000JB900180

Milne, G.A., Mitrovica, J.X., Forte, A.M., 1998. The sensitivity of glacial isostatic adjustment predictions to a low-viscosity layer at the base of the upper mantle. Earth and Planetary Science Letters 154, 265–278. https://doi.org/10.1016/S0012-821X(97)00191-X

Misener, D.J., 1973. Cation diffusion in olivine to 1400°C and 35 KB. University of British Columbia. https://doi.org/10.14288/1.0302660

Miyazaki, T., Sueyoshi, K., Hiraga, T., 2013. Olivine crystals align during diffusion creep of Earth's upper mantle. Nature 502, 321–326. https://doi.org/10.1038/nature12570

Mulyukova, E., Bercovici, D., 2019. The Generation of Plate Tectonics From Grains to Global Scales: A Brief Review. Tectonics 38, 4058–4076. https://doi.org/10.1029/2018TC005447

Mussi, A., Cordier, P., Demouchy, S., Vanmansart, C., 2014. Characterization of the glide planes of the [001] screw dislocations in olivine using electron tomography. Phys Chem Minerals 41, 537–545. https://doi.org/10.1007/s00269-014-0665-1

Mussi, A., Nafi, M., Demouchy, S., Cordier, P., 2015. On the deformation mechanism of olivine single crystals at lithospheric temperatures: an electron tomography study. ejm 27, 707–715. https://doi.org/10.1127/ejm/2015/0027-2481

Nabarro, F., 1948. Report of a conference on the strength of solids Physical Society.

Nakakoji, T., Hiraga, T., 2018. Diffusion Creep and Grain Growth in Forsterite +20 vol% Enstatite Aggregates: 2. Their Common Diffusional Mechanism and Its Consequence for Weak-Temperature-Dependent Viscosity. Journal of Geophysical Research: Solid Earth 123, 9513–9527. https://doi.org/10.1029/2018JB015819

Nes, E., Ryum, N., Hunderi, O., 1985. On the Zener drag. Acta Metallurgica 33, 11–22. https://doi.org/10.1016/0001-6160(85)90214-7

Nicholls, I., Ringwood, A., 1973. Effect of water on olivine stability in tholeiites and the production of silica-saturated magmas in the island-arc environment. The Journal of Geology 285–300.

Nichols, S.J., Mackwell, S.J., 1991. Grain growth in porous olivine aggregates. Phys Chem Minerals 18, 269–278. https://doi.org/10.1007/BF00202580

Nisbet, E.G., Sleep, N.H., 2001. The habitat and nature of early life. Nature 409, 1083–1091. https://doi.org/10.1038/35059210

Nitsan, U., 1974. Stability field of olivine with respect to oxidation and reduction. Journal of Geophysical Research 79, 706–711.

Noels, L., Cdang, 2020. Fracture Mechanics online class [WWW Document]. URL http://www.ltas-cm3.ulg.ac.be/FractureMechanics/print.php?p=overview_P3 (accessed 8.3.21).

Ogawa, M., 1987. Shear instability in a viscoelastic material as the cause of deep focus earthquakes. Journal of Geophysical Research: Solid Earth 92, 13801–13810. https://doi.org/10.1029/JB092iB13p13801

Oh, S.H., Legros, M., Kiener, D., Dehm, G., 2009. In situ observation of dislocation nucleation and escape in a submicrometre aluminium single crystal. Nat Mater 8, 95–100. https://doi.org/10.1038/nmat2370

Ohashi, Y., 1984. Polysynthetically-twinned structures of enstatite and wollastonite. Phys Chem Minerals 10, 217–229. https://doi.org/10.1007/BF00309314

Ohtani, E., 2005. Water in the mantle. Elements 1, 25–30.

Ohtani, E., Kumazawa, M., 1981. Melting of forsterite Mg2SiO4 up to 15 GPa. Physics of the Earth and Planetary Interiors 27, 32–38. https://doi.org/10.1016/0031-9201(81)90084-4

Ohuchi, T., Kawazoe, T., Higo, Y., Funakoshi, K., Suzuki, A., Kikegawa, T., Irifune, T., 2015. Dislocation-accommodated grain boundary sliding as the major deformation mechanism of olivine in the Earth's upper mantle. Science Advances 1, e1500360. https://doi.org/10.1126/sciadv.1500360

Ohuchi, T., Lei, X., Ohfuji, H., Higo, Y., Tange, Y., Sakai, T., Fujino, K., Irifune, T., 2017. Intermediate-depth earthquakes linked to localized heating in dunite and harzburgite. Nature Geoscience 10, 771–776. https://doi.org/10.1038/ngeo3011

Ohuchi, T., Nakamura, M., 2007a. Grain growth in the forsterite–diopside system. Physics of the Earth and Planetary Interiors 160, 1–21. https://doi.org/10.1016/j.pepi.2006.08.003

Ohuchi, T., Nakamura, M., 2007b. Grain growth in the system forsterite–diopside–water. Physics of the Earth and Planetary Interiors 161, 281–304. https://doi.org/10.1016/j.pepi.2007.02.009

Osburn, C.M., Vest, R.W., 1971. Electrical properties of NiO grain boundaries. Journal of Physics and Chemistry of Solids 32, 1355–1363. https://doi.org/10.1016/S0022-3697(71)80193-2

Panozzo-Heilbronner, R., Barrett, S., 2014. Image Analysis in Earth Sciences: Microstructures and Textures of Earth Materials. Springer.

Paterson, M., 1982. The determination of hydroxyl by infrared absorption in quartz, silicate glasses and similar materials. Bulletin de Minéralogie 105, 20–29. https://doi.org/10.3406/bulmi.1982.7582

Paterson, M.S., 1970. A high-pressure, high-temperature apparatus for rock deformation. International Journal of Rock Mechanics and Mining Sciences & Geomechanics Abstracts 7, 517–526. https://doi.org/10.1016/0148-9062(70)90004-5

Paterson, M.S., Olgaard, D.L., 2000. Rock deformation tests to large shear strains in torsion. Journal of Structural Geology 22, 1341–1358. https://doi.org/10.1016/S0191-8141(00)00042-0

Paulson, A., Zhong, S., Wahr, J., 2007. Limitations on the inversion for mantle viscosity from postglacial rebound. Geophysical Journal International 168, 1195–1209. https://doi.org/10.1111/j.1365-246X.2006.03222.x

Petch, N.J., 1953. The cleavage strengh of polycrystals. J. of the Iron and Steel Inst. 174, 25–28.

Plümper, O., John, T., Podladchikov, Y.Y., Vrijmoed, J.C., Scambelluri, M., 2017. Fluid escape from subduction zones controlled by channel-forming reactive porosity. Nature Geosci 10, 150–156. https://doi.org/10.1038/ngeo2865

Pommier, A., Kohlstedt, D.L., Hansen, L.N., Mackwell, S., Tasaka, M., Heidelbach, F., Leinenweber, K., 2018. Transport properties of olivine grain boundaries from electrical conductivity experiments. Contributions to Mineralogy and Petrology 173. https://doi.org/10.1007/s00410-018-1468-z

Pond, R.C., Smith, D.A., 1977. On the absorption of dislocations by grain boundaries. Philosophical Magazine 36, 353–366. https://doi.org/10.1080/14786437708244939

Pond, R.C., Smith, D.A., Southerden, P.W.J., 1978a. On the role of grain boundary dislocations in high temperature creep. Philosophical Magazine A 37, 27–40. https://doi.org/10.1080/01418617808239160

Pond, R.C., Smith, D.A., Southerden, P.W.J., 1978b. On the role of grain boundary dislocations in high temperature creep. Philosophical Magazine A 37, 27–40. https://doi.org/10.1080/01418617808239160

Précigout, J., Prigent, C., Palasse, L., Pochon, A., 2017. Water pumping in mantle shear zones. Nature Communications 8, 15736. https://doi.org/10.1038/ncomms15736

Priester, L., 2013. Grain Boundaries - From Theory to Engineering. Springer.

Prior, D.J., Boyle, A.P., Brenker, F., Cheadle, M.C., Day, A., Lopez, G., Peruzzi, L., Potts, G., Reddy, S., Spiess, R., Timms, N.E., Trimby, P., Wheeler, J., Zetterstrom, L., 1999. The application of electron backscatter diffraction and orientation contrast imaging in the SEM to textural problems in rocks. American Mineralogist 84, 1741–1759. https://doi.org/10.2138/am-1999-11-1204

Pshenichnyuk, A.I., Astanin, V.V., Kaibyshev, O.A., 1998. The model of grain-boundary sliding stimulated by intragranular slip. Philosophical Magazine A 77, 1093–1106. https://doi.org/10.1080/01418619808221231

Raj, R., Ashby, M.F., 1971. On grain boundary sliding and diffusional creep. MT 2, 1113–1127. https://doi.org/10.1007/BF02664244

Randle, V., 2006. ‘Special’ boundaries and grain boundary plane engineering. Scripta Materialia 54, 1011–1015. https://doi.org/10.1016/j.scriptamat.2005.11.050

Randle, V., 1996. The role of the coincidence site lattice in grain boundary engineering, Book / The Institute of Materials. Institute of Materials, London.

Randle, V., 1993. The measurement of grain boundary geometry. Institute of Physics Pub., Bristol; Philadelphia.

Randle, V., Dingley, D., 1989. Measurement of Boundary Plane Inclination in a Scanning Electron-Microscope. Scripta Metallurgica 23, 1565–1569. https://doi.org/10.1016/0036-9748(89)90129-4

Randle, V., Ralph, B., 1988. Grain boundary structure and mechanical properties. Revue de physique appliquée 23, 501–512.

Raterron, P., Bollinger, C., Merkel, S., 2019. Olivine intergranular plasticity at mantle pressures and temperatures. Comptes Rendus Geoscience, High-Pressure

Mineral Physics Seminar(HPMPS-9, Saint-Malo, France, 24–28 September 2017) 351, 80–85. https://doi.org/10.1016/j.crte.2018.10.001

Raterron, P., Chen, J., Li, L., Weidner, D., Cordier, P., 2007. Pressure-induced slip-system transition in forsterite: Single-crystal rheological properties at mantle pressure and temperature. American Mineralogist 92, 1436–1445. https://doi.org/10.2138/am.2007.2474

Raven, P.H., Axelrod, D.I., 1972. Plate Tectonics and Australasian Paleobiogeography. Science 176, 1379–1386.

Read, W.T., Shockley, W., 1950. Dislocation Models of Crystal Grain Boundaries. Physical Review 78, 275–289. https://doi.org/10.1103/PhysRev.78.275

Rheinheimer, W., Bäurer, M., Chien, H., Rohrer, G.S., Handwerker, C.A., Blendell, J.E., Hoffmann, M.J., 2015. The equilibrium crystal shape of strontium titanate and its relationship to the grain boundary plane distribution. Acta Materialia 82, 32–40. https://doi.org/10.1016/j.actamat.2014.08.065

Rhines, F.N., 1970. Geometry of grain boundaries. Metall and Materi Trans 1, 1105–1120. https://doi.org/10.1007/BF02900223

Ribe, N.M., 1989. Seismic anisotropy and mantle flow. Journal of Geophysical Research: Solid Earth 94, 4213–4223.

Ricoult, D.L., Kohlstedt, D.L., 1983. Structural width of low-angle grain boundaries in olivine. Physics and Chemistry of Minerals 9, 133–138. https://doi.org/10.1007/BF00308370

Ringwood, A.E., 1975. Composition and petrology of the earth's mantle [by] AE Ringwood.

Ringwood, A.E., 1970. Phase transformations and the constitution of the mantle. Physics of the Earth and Planetary Interiors 3, 109–155. https://doi.org/10.1016/0031-9201(70)90047-6

Rohrer, G.S., 2011. Grain boundary energy anisotropy: a review. Journal of Materials Science 46, 5881–5895. https://doi.org/10.1007/s10853-011-5677-3

Rohrer, G.S., Saylor, D.M., Dasher, B.E., Adams, B.L., Rollett, A.D., Wynblatt, P., 2004. The distribution of internal interfaces in polycrystals. Zeitschrift für Metallkunde 95, 197–214.

Rollett, A.D., Brahme, A.P., Roberts, C.G., 2007a. An Overview of Accomplishments and Challenges in Recrystallization and Grain Growth. MSF 558–559, 33–42. https://doi.org/10.4028/www.scientific.net/MSF.558-559.33

Rollett, A.D., Lee, S.-B., Campman, R., Rohrer, G.S., 2007b. Three-Dimensional Characterization of Microstructure by Electron Back-Scatter Diffraction. Annual Review of Materials Research 37, 627–658. https://doi.org/10.1146/annurev.matsci.37.052506.084401

Rollett, A.D., Mullins, W.W., 1997. On the growth of abnormal grains. Scripta Materialia 36, 975–980. https://doi.org/10.1016/S1359-6462(96)00501-5

Roşca, D., Graef, M.D., 2013. Area-preserving projections from hexagonal and triangular domains to the sphere and applications to electron back-scatter diffraction pattern simulations. Modelling Simul. Mater. Sci. Eng. 21, 055021. https://doi.org/10.1088/0965-0393/21/5/055021

Rozel, A., 2012. Impact of grain size on the convection of terrestrial planets: CONVECTION AND GRAIN SIZE. Geochem. Geophys. Geosyst. 13, n/a-n/a. https://doi.org/10.1029/2012GC004282

Rubie, D.C., Karato, S., Yan, H., O'Neill, H.St.C., 1993. Low differential stress and controlled chemical environment in multianvil high-pressure experiments. Phys Chem Minerals 20, 315–322. https://doi.org/10.1007/BF00215102

Salama, H., Kundin, J., Shchyglo, O., Mohles, V., Marquardt, K., Steinbach, I., 2020. Role of inclination dependence of grain boundary energy on the microstructure evolution during grain growth. Acta Materialia 188, 641–651. https://doi.org/10.1016/j.actamat.2020.02.043

Sangid, M.D., Ezaz, T., Sehitoglu, H., Robertson, I.M., 2011. Energy of slip transmission and nucleation at grain boundaries. Acta Materialia 59, 283–296. https://doi.org/10.1016/j.actamat.2010.09.032

Sano-Furukawa, A., Hattori, T., Arima, H., Yamada, A., Tabata, S., Kondo, M., Nakamura, A., Kagi, H., Yagi, T., 2014. Six-axis multi-anvil press for high-pressure, high-temperature neutron diffraction experiments. Review of Scientific Instruments 85, 113905. https://doi.org/10.1063/1.4901095

Satsukawa, T., Griffin, W.L., Piazolo, S., O'Reilly, S.Y., 2015. Messengers from the deep: Fossil wadsleyite-chromite microstructures from the Mantle Transition Zone. Scientific Reports 5, 16484. https://doi.org/10.1038/srep16484

Saylor, D.M., Fridy, J., El-Dasher, B.S., Jung, K.-Y., Rollett, A.D., 2004. Statistically representative three-dimensional microstructures based on orthogonal observation sections. Metall and Mat Trans A 35, 1969–1979. https://doi.org/10.1007/s11661-004-0146-0

Saylor, D.M., Morawiec, A., Rohrer, G.S., 2002. Distribution and Energies of Grain Boundaries in Magnesia as a Function of Five Degrees of Freedom. Journal of the American Ceramic Society 85, 3081–3083. https://doi.org/10.1111/j.1151-2916.2002.tb00583.x

Saylor, D.M., Rohrer, G.S., 2002. Determining crystal habits from observations of planar sections. Journal of the American Ceramic Society 85, 2799–2804.

Schubnel, A., Brunet, F., Hilairet, N., Gasc, J., Wang, Y., Green, H.W., 2013. Deep-Focus Earthquake Analogs Recorded at High Pressure and Temperature in the Laboratory. Science 341, 1377–1380. https://doi.org/10.1126/science.1240206

Shen, Z., Wagoner, R.H., Clark, W.A.T., 1988. Dislocation and grain boundary interactions in metals. Acta Metallurgica 36, 3231–3242. https://doi.org/10.1016/0001-6160(88)90058-2

Shirokoff, J., Robertson, I.M., Birnbaum, H.K., 1993. The Slip Transfer Process Through Grain Boundaries in HCP Ti. MRS Online Proceedings Library Archive 319. https://doi.org/10.1557/PROC-319-263

Signorelli, J., Tommasi, A., 2015. Modeling the effect of subgrain rotation recrystallization on the evolution of olivine crystal preferred orientations in simple shear. Earth and Planetary Science Letters 430, 356–366. https://doi.org/10.1016/j.epsl.2015.08.018

Singh, S., Graef, M.D., 2016. Orientation sampling for dictionary-based diffraction pattern indexing methods. Modelling Simul. Mater. Sci. Eng. 24, 085013. https://doi.org/10.1088/0965-0393/24/8/085013

Solomatov, V.S., 2001. Grain size-dependent viscosity convection and the thermal evolution of the Earth. Earth and Planetary Science Letters 191, 203–212. https://doi.org/10.1016/S0012-821X(01)00426-5

Solomatov, V.S., Reese, C.C., 2008. Grain size variations in the Earth's mantle and the evolution of primordial chemical heterogeneities. J. Geophys. Res. 113, B07408. https://doi.org/10.1029/2007JB005319

Soustelle, V., Manthilake, G., 2017. Deformation of olivine-orthopyroxene aggregates at high pressure and temperature: Implications for the seismic properties of the asthenosphere. Tectonophysics 694, 385–399. https://doi.org/10.1016/j.tecto.2016.11.020

Spearot, D.E., Sangid, M.D., 2014. Insights on slip transmission at grain boundaries from atomistic simulations. Current Opinion in Solid State and Materials Science 18, 188–195.

Stevens, R.N., 1971. Grain-boundary sliding and diffusion creep in polycrystalline solids. Philosophical Magazine 23, 265–283. https://doi.org/10.1080/14786437108216383

Stuart, B., 2004. Infrared spectroscopy: fundamentals and applications, Analytical techniques in the sciences. J. Wiley, Chichester, West Sussex, England ; Hoboken, NJ.

Sutton, A.P., Balluffi, R.W., 1995. Interfaces in crystalline materials.

Tackley, P.J., 2000. Self-consistent generation of tectonic plates in time-dependent, three-dimensional mantle convection simulations. Geochemistry, Geophysics, Geosystems 1, n/a-n/a. https://doi.org/10.1029/2000GC000036

Takeuchi, S., Argon, A.S., 1976. Steady-state creep of alloys due to viscous motion of dislocations. Acta Metallurgica 24, 883–889. https://doi.org/10.1016/0001-6160(76)90036-5

Tan, B.H., Jackson, I., Fitz Gerald, J.D., 1997. Shear wave dispersion and attenuation in fine-grained synthetic olivine aggregates: Preliminary results. Geophys. Res. Lett. 24, 1055–1058. https://doi.org/10.1029/97GL00860

Tan, B.H., Jackson, I., Gerald, J.D.F., 2001. High-temperature viscoelasticity of fine-grained polycrystalline olivine. Phys Chem Min 28, 641–664. https://doi.org/10.1007/s002690100189

Tasaka, M., Hiraga, T., 2013. Influence of mineral fraction on the rheological properties of forsterite + enstatite during grain-size-sensitive creep: 1. Grain size and grain

growth laws. Journal of Geophysical Research: Solid Earth 118, 3970–3990. https://doi.org/10.1002/jgrb.50285

ten Grotenhuis, S.M., Drury, M.R., Peach, C.J., Spiers, C.J., 2004. Electrical properties of fine-grained olivine: Evidence for grain boundary transport. Journal of Geophysical Research: Solid Earth 109. https://doi.org/10.1029/2003JB002799

Thielmann, M., 2018. Grain size assisted thermal runaway as a nucleation mechanism for continental mantle earthquakes: Impact of complex rheologies. Tectonophysics 746, 611–623. https://doi.org/10.1016/j.tecto.2017.08.038

Thielmann, M., Rozel, A., Kaus, B.J.P., Ricard, Y., 2015. Intermediate-depth earthquake generation and shear zone formation caused by grain size reduction and shear heating. Geology 43, 791–794. https://doi.org/10.1130/G36864.1

Tielke, J.A., Hansen, L.N., Tasaka, M., Meyers, C., Zimmerman, M.E., Kohlstedt, D.L., 2016. Observations of grain size sensitive power law creep of olivine aggregates over a large range of lattice-preferred orientation strength: GSS power law creep of olivine. Journal of Geophysical Research: Solid Earth 121, 506–516. https://doi.org/10.1002/2015JB012302

Tommasi, A., Mainprice, D., Canova, G., Chastel, Y., 2000. Viscoplastic self-consistent and equilibrium-based modeling of olivine lattice preferred orientations: Implications for the upper mantle seismic anisotropy. Journal of Geophysical Research: Solid Earth 105, 7893–7908. https://doi.org/10.1029/1999JB900411

Turner, F.J., 1942. Preferred orientation of olivine crystals in peridotites, with special reference to New Zealand examples. Trans. Roy. Soc. NZ 72, 280–300.

Twiss, R.J., 1977. Theory and applicability of a recrystallized grain size paleopiezometer. PAGEOPH 115, 227–244. https://doi.org/10.1007/BF01637105

Uberuaga, B.P., Vernon, L.J., Martinez, E., Voter, A.F., 2015. The relationship between grain boundary structure, defect mobility and grain boundary sink efficiency. Scientific Reports 5, 9095. https://doi.org/10.1038/srep09095

Urai, J.L., Means, W.D., Lister, G.S., 1986. Dynamic recrystallization of minerals, in: Hobbs, B.E., Heard, H.C. (Eds.), Geophysical Monograph Series. American Geophysical Union, Washington, D. C., pp. 161–199. https://doi.org/10.1029/GM036p0161

USGS, 1999. Inside the Earth [This Dynamic Earth, USGS] [WWW Document]. URL https://pubs.usgs.gov/gip/dynamic/inside.html (accessed 7.1.20).

Van der Wal, D., Chopra, P., Drury, M., Gerald, J.F., 1993. Relationships between dynamically recrystallized grain size and deformation conditions in experimentally deformed olivine rocks. Geophysical Research Letters 20, 1479–1482. https://doi.org/10.1029/93GL01382

Vernon, R.H., 2004. A practical guide to rock microstructure. Cambridge University Press, Cambridge, UK ; New York.

Wallis, D., Hansen, L.N., Ben Britton, T., Wilkinson, A.J., 2016. Geometrically necessary dislocation densities in olivine obtained using high-angular resolution electron backscatter diffraction. Ultramicroscopy 168, 34–45. https://doi.org/10.1016/j.ultramic.2016.06.002

Wallis, D., Hansen, L.N., Britton, T.B., Wilkinson, A.J., 2019. High-Angular Resolution Electron Backscatter Diffraction as a New Tool for Mapping Lattice Distortion in Geological Minerals. Journal of Geophysical Research: Solid Earth 124, 6337–6358. https://doi.org/10.1029/2019JB017867

Wallis, D., Lloyd, G.E., Hansen, L.N., 2018. The role of strain hardening in the transition from dislocation-mediated to frictional deformation of marbles within the Karakoram Fault Zone, NW India. Journal of Structural Geology 107, 25–37. https://doi.org/10.1016/j.jsg.2017.11.008

Walte, N.P., Solferino, G.F.D., Golabek, G.J., Silva Souza, D., Bouvier, A., 2020. Two-stage formation of pallasites and the evolution of their parent bodies revealed by deformation experiments. Earth and Planetary Science Letters 546, 116419. https://doi.org/10.1016/j.epsl.2020.116419

Walter, M.J., Thibault, Y., Wei, K., Luth, R.W., 1995. Characterizing experimental pressure and temperature conditions in multi-anvil apparatus. Can. J. Phys. 73, 273–286. https://doi.org/10.1139/p95-039

Wang, D., Mookherjee, M., Xu, Y., Karato, S., 2006. The effect of water on the electrical conductivity of olivine. Nature 443, 977–980. https://doi.org/10.1038/nature05256

Wang, Q., 2016. Homologous temperature of olivine: Implications for creep of the upper mantle and fabric transitions in olivine. Sci. China Earth Sci. 59, 1138–1156. https://doi.org/10.1007/s11430-016-5310-z

Wang, Y., Durham, W.B., Getting, I.C., Weidner, D.J., 2003. The deformation-DIA: A new apparatus for high temperature triaxial deformation to pressures up to 15 GPa. Review of Scientific Instruments 74, 3002–3011. https://doi.org/10.1063/1.1570948

Wang, Y., Zhu, L., Shi, F., Schubnel, A., Hilairet, N., Yu, T., Rivers, M., Gasc, J., Addad, A., Deldicque, D., Li, Z., Brunet, F., 2017. A laboratory nanoseismological study on deep-focus earthquake micromechanics. Science Advances 3, e1601896. https://doi.org/10.1126/sciadv.1601896

Watanabe, T., 2011. Grain boundary engineering: historical perspective and future prospects. Journal of Materials Science 46, 4095–4115. https://doi.org/10.1007/s10853-011-5393-z

Watanabe, T., 1988. Grain boundary design for desirable mechanical properties. Le Journal de Physique Colloques 49, C5-507-C5-519. https://doi.org/10.1051/jphyscol:1988562

Watanabe, T., 1984. An approach to grain boundary design for strong and ductile polycrystals. Res Mechanica 11, 47–84.

Watson, E., Wark, D., Price, J., Van Orman, J., 2002. Mapping the thermal structure of solid-media pressure assemblies. Contrib Mineral Petrol 142, 640–652. https://doi.org/10.1007/s00410-001-0327-4

Weertman, J., 1957. Steady-State Creep through Dislocation Climb. Journal of Applied Physics 28, 362–364. https://doi.org/10.1063/1.1722747

Wenk, H.R., 1985. Preferred Orientation in Deformed Metal and Rocks: An Introduction to Modern Texture Analysis. Academic Press, Inc., Orlando, FL.

Wignall, P.B., Sun, Y., Bond, D.P.G., Izon, G., Newton, R.J., Védrine, S., Widdowson, M., Ali, J.R., Lai, X., Jiang, H., Cope, H., Bottrell, S.H., 2009. Volcanism, Mass Extinction, and Carbon Isotope Fluctuations in the Middle Permian of China. Science 324, 1179–1182. https://doi.org/10.1126/science.1171956

Wilkinson, A.J., Randman, D., 2010. Determination of elastic strain fields and geometrically necessary dislocation distributions near nanoindents using

electron back scatter diffraction. Philosophical Magazine 90, 1159–1177. https://doi.org/10.1080/14786430903304145

Williams, D.B., Carter, C.B., 2009. Transmission electron microscopy: a textbook for materials science, 2. ed. ed. Springer, New York.

Withers, A.C., 2013. On the use of unpolarized infrared spectroscopy for quantitative analysis of absorbing species in birefringent crystals. American Mineralogist 98, 689–697. https://doi.org/10.2138/am.2013.4316

Wright, S.I., Adams, B.L., 1992. Automatic analysis of electron backscatter diffraction patterns. MTA 23, 759–767. https://doi.org/10.1007/BF02675553

Wright, S.I., Larsen, R.J., 2002. Extracting twins from orientation imaging microscopy scan data. Journal of Microscopy 205, 245–252. https://doi.org/10.1046/j.1365-2818.2002.00992.x

Wright, S.I., Nowell, M.M., Lindeman, S.P., Camus, P.P., De Graef, M., Jackson, M.A., 2015. Introduction and comparison of new EBSD post-processing methodologies. Ultramicroscopy 159, 81–94. https://doi.org/10.1016/j.ultramic.2015.08.001

Yabe, K., Sueyoshi, K., Hiraga, T., 2020. Grain-Boundary Diffusion Creep of Olivine: 1. Experiments at 1 atm. Journal of Geophysical Research: Solid Earth 125, e2020JB019415. https://doi.org/10.1029/2020JB019415

Yagi, T., Ida, Y., Sato, Y., Akimoto, S.-I., 1975. Effect of hydrostatic pressure on the lattice parameters of Fe2SiO4 olivine up to 70 kbar. Physics of the Earth and Planetary Interiors 10, 348–354. https://doi.org/10.1016/0031-9201(75)90062-X

Yamazaki, D., Karato, S., 2001. Some mineral physics constraints on the rheology and geothermal structure of Earth's lower mantle. American Mineralogist 86, 385–391. https://doi.org/10.2138/am-2001-0401

Yoshida, H., Yokoyama, K., Shibata, N., Ikuhara, Y., Sakuma, T., 2004. High-temperature grain boundary sliding behavior and grain boundary energy in cubic zirconia bicrystals. Acta Materialia 52, 2349–2357. https://doi.org/10.1016/j.actamat.2004.01.026

Zeng, X.H., Eisenlohr, P., Blum, W., 2008. Modelling the transition from strengthening to softening due to grain boundaries. Materials Science and Engineering: A,

14th International Conference on the Strength of Materials 483, 95–98. https://doi.org/10.1016/j.msea.2006.09.130

Zhan, Z., 2020. Mechanisms and Implications of Deep Earthquakes. Annual Review of Earth and Planetary Sciences 48, 147–174. https://doi.org/10.1146/annurev-earth-053018-060314

Zhao, Y.-H., Zimmerman, M.E., Kohlstedt, D.L., 2009. Effect of iron content on the creep behavior of olivine: 1. Anhydrous conditions. Earth and Planetary Science Letters 287, 229–240. https://doi.org/10.1016/j.epsl.2009.08.006

Zheng, Z., Waheed, S., Balint, D.S., Dunne, F.P.E., 2018. Slip transfer across phase boundaries in dual phase titanium alloys and the effect on strain rate sensitivity. International Journal of Plasticity 104, 23–38. https://doi.org/10.1016/j.ijplas.2018.01.011

Zuiderveld, K., 1994. Contrast Limited Adaptive Histogram Equalization. Graphics Gems 474–485.

A: Appendix

A.1. Calculation of viscosity profiles

Viscosity, η, as shown in the viscosity profiles in Figure 9, is given by the ratio between the shear stress, σ, and strain rate, $\dot{\varepsilon}$, that is:

$$\eta = \frac{\sigma}{\dot{\varepsilon}} \tag{A.1.1}$$

Our calculations assume σ =1 MPa (Kohlstedt and Hansen, 2015), and the strain rate is given by the sum of the strain rates of dislocation creep ($\dot{\varepsilon}_{dis}$), dislocation-accommodated grain-boundary sliding ($\dot{\varepsilon}_{disGBS}$) and diffusion creep ($\dot{\varepsilon}_{dif}$):

$$\dot{\varepsilon} = \dot{\varepsilon}_{dis} + \dot{\varepsilon}_{GBS} + \dot{\varepsilon}_{dif} \tag{A.1.2}$$

The strain rate for dislocation creep is given by (dry olivine, Hirth and Kohlstedt, 2003):

$$\dot{\varepsilon}_{dis} = (1.1 \times 10^5) \exp\left(\frac{-(5.3\times10^5)+P\,(14\times10^{-6})}{RT}\right) \tag{A.1.3}$$

for dislocation-accommodated grain-boundary sliding by (dry olivine; Hirth and Kohlstedt, 2003; modified by Hansen et al., 2011):

$$\dot{\varepsilon}_{GBS} = (10^{4.8})\ \frac{1}{d^{0.73}} \exp\left(\frac{-(4.45\times10^5-(300\times10^6\times18\times10^{-6}))+P\,(18\times10^{-6})}{RT}\right) \tag{A.1.4}$$

and for diffusion creep by (dry olivine; Hirth and Kohlstedt, 2003):

$$\dot{\varepsilon}_{dif} = (10^{7.6})\ \frac{1}{d^3} \exp\left(\frac{-(3.7\times10^5)+P\,(6\times10^{-6})}{RT}\right) \tag{A.1.5}$$

where P is pressure in GPa R is the gas constant in J·K^{-1}·mol^{-1}, T is the temperature in K, and d is grain size in µm. The grain-size evolution as a function of pressure, P (Pa), temperature, T (K), and time, t (s), is given by Eq. 1 and Eq. 2, using the parameters obtained in this study, that is:

$$d = \left({d_0}^{3.88} + \left((2.11 \times 10^{-7}) \exp\left(\frac{-(608 \times 10^3) + P(4.3 \times 10^{-6})}{RT} \right) \right) t \right)^{1/3.88} \quad \text{(A.1.6)}$$

Pressure and temperature as a function of depth were obtained from Dziewonski and Anderson (1981) and Katsura et al. (2004), respectively. Our calculations were performed using an initial grain size, d_0, of 10×10^{-6} m.

A.2. Computer Scripts

This section presents the scripts included in the toolbox described in Chapter 7. The scripts are also available at the following repository: https://doi.org/10.5281/zenodo.5344419. The scripts were written by Filippe Ferreira (Universität Bayreuth, Germany), supervised by Dr. Katharina Marquardt (Imperial College London, United Kingdom) and Dr. Marcel Thielmann (Universität Bayreuth, Germany). The scripts are licensed under the MIT license available at: https://opensource.org/licenses/MIT.

A.2.1. Function getGBCDpar

```
function GBCD_par=getGBCDpar(ebsd, cs)
%Function actions:
    %Reads EBSD file and outputs:
    % msym, rot, rad, resolution, seg, stepSize, cutOff
    % to input.txt files. Edit this file for the desired parameters.
%Input:
    % ebsd = root folder with gbpd/gbcd programs
    % segments_fname = file name of segments
    % GBCD_par = gbpd/gbcd/parameters (obtained from getGBCDpar.m)
%Output:
    %datFname: Path to the GBPD .dat file located in the graph_pd folder to be ploted


%% Check symmetry
```

```
switch cs.lattice
    case 'cubic'
        msym=3;
    case 'hexagonal'
        msym=2;
    case 'tetragonal'
        msym=1;
    case 'trigonal'
        msym=4;
    case 'orthorhombic'
        msym=5;
    otherwise
        error('Crystal symmetry not available')
end

% Rotation %** Change accordingly
%  rot=0;% HKL system
rot=1; % TSL system

% Euler angles in rad or deg
% rad=0% degree
rad=1; % rad

% Resolution (bins per 90 degrees) -maximum:18.      %** Change accordingly
resolution=[9, 9];

% Segment analysys %** Change accordingly
```

```
% Recomended to leave at zero when using Mtex exported data
% (in mtex every segment has the same size)
seg= 0;

%Check step size
ucell=ebsd.unitCell;
area_shape=polyarea(ucell(:,1),ucell(:,2));

switch size(ucell,1)
    case 4 % square grid
        stepSize=sqrt(area_shape);
    case 6 % hexagonal grid
        stepSize=sqrt(area_shape/sind(60));
    case 16 % ? grid
        stepSize=sqrt((area_shape)/pi);% check this
    otherwise
         stepSize= input('Enter EBSD step size and press enter:  ');
end

% small length cutoff %** Change accordingly
% Recomended to leave at zero when using Mtex exported data
cutOff= 0.0;

%Join all parameters in array
GBCD_par=[msym, rot, rad, resolution, seg, stepSize, cutOff];
%
```

fprintf('\n -getGBCDpar: The following parameters will be used in the GBPD/CD calculations: \nSymmetry | Rotation | Radians | Resolution | Segment analysys | Step size | Small length Cut off \n %11.0f | %12.0f | %11.0f | %10.0f x %.0f| %25.0f | %10.2f | %28.2f \n ', GBCD_par);

A.2.2. Function segments2dat

```
function datFname = segments2dat(GBCDfolder,segments_fname,GBCD_par)
%Function actions:
    %1- Copy boundary segments file to GBPD folder
    %2- Change  input.txt file
    %3- run GBPD program
%Input:
    % GBCDfolder = root folder with gbpd/gbcd programs
    % segments_fname = file name of segments
    % GBCD_par = gbpd/gbcd/parameters (obtained from getGBCDpar.m)
%Output:
    %datFname: Path to the GBPD .dat file located in the graph_pd folder to be ploted
%% Set file names, folder paths
    oldFolder=pwd;
    cd (GBCDfolder)
    [~,sample_name,ext] = fileparts(segments_fname) ;
    % output file name should be:
     datFname = fullfile(GBCDfolder, 'graph_pd',['gbpd_', sample_name, '_2d_gmt.dat']);
```

```
%% Replace location of boundary segments file in 'calc GBPD' input file
    calcGbpdFolder = fullfile(GBCDfolder,'calc_gbpd');
    inputFname=fullfile(calcGbpdFolder,'input.txt');

    % replace second line of input file with the name of segment file
    clear A; A = regexp(fileread(inputFname), '\n', 'split');% read all data to A, line by line
    A{2} = sprintf([sample_name,ext]);% replace content of 2nd line

    % Replace parameters in 'calc GBPD' input file
    %GBCD_par=[msym, rot, rad, resolution, seg, stepSize, cutOff];
    A{4} = sprintf( '%d\t%d\t%d', GBCD_par(1:3)); % replace symmetry, rotation, radian
    A{6} = sprintf( '%d\t%d', GBCD_par(4:5)); % replace resolution
    A{8} = sprintf( '%d', GBCD_par(6)); % replace segment analysis
    A{10} = sprintf( '%.2f', GBCD_par(7)); % replace step size
    A{12} = sprintf( '%.2f', GBCD_par(8)); % replace small length cutoff

    fid = fopen(inputFname, 'w'); % Open 'input.txt'
    fprintf(fid, '%s\n', A{:}); %
    fclose(fid);

    %copy file
    copyfile(segments_fname,fullfile(calcGbpdFolder,[sample_name,ext]) , 'f');

%% Replace parameters in  'plot GBPD' input file
    inputFname=fullfile(GBCDfolder,'graph_pd','input.txt');

    clear A; A = regexp(fileread(inputFname), '\n', 'split');% read all data to A, line by line
```

```
% replace file name
A{1} = sprintf(['gbpd_',sample_name,ext]);% replace content of 1st line

%GBCD_par=[msym, rot, rad, resolution, seg, stepSize, cutOff];
A{3} = sprintf( '%d ', GBCD_par(1));% replace symmetry
A{5} = sprintf( '%d\t%d', GBCD_par(4:5));% replace resolution

fid = fopen(inputFname, 'w');% open input.txt
fprintf(fid, '%s\n', A{:}); % write A
fclose(fid); % close

%% Run GBPD script

% Set Fortran path For MATLAB (if not already):
try
    if contains(computer , 'MAC' ) % MAC
        if ~contains(getenv('PATH'), ':/usr/local/bin')
            setenv('PATH', [getenv('PATH') ':/usr/local/bin']); %set path for mac
        end
        system(['chmod +x ',fullfile(GBCDfolder, 'gbpd.sh')]);% make shell file executable (Mac/Linux)
        system(['. ',fullfile(GBCDfolder, 'gbpd.sh')]);% Run and Show output
        fprintf('\n -segments2dat: GBPD wrote to file: %s \n ', datFname)

    elseif contains(computer , 'LNX' ) % Linux
```

```
            system(['chmod +x ',fullfile(GBCDfolder, 'gbpd.sh')]);% make shell file executable (Mac/Linux)
            system(['. ',fullfile(GBCDfolder, 'gbpd.sh')]);% Run and Show output
            fprintf('\n -segments2dat: GBPD wrote to file: %s \n ', datFname)


        elseif contains(computer , 'WIN' )
            system(['chmod +x ',fullfile(GBCDfolder, 'gbpd_WIN.sh')]);% make shell file executable (Mac/Linux)
            system(['sh ',fullfile(GBCDfolder, 'gbpd_WIN.sh')]);% Run and Show output
            fprintf('\n -segments2dat: GBPD wrote to file: %s \n ', datFname)

        end

     catch
            error('It was not possible to execute the shell Files. ')
    end
   % [x,y]=system([GBCDfolder, '/gbpd.sh']) % work with output
    % [~, ~]=system([GBCDfolder, '/gbpd.sh']);% omit output
    %add GMT folder to path
    %setenv('PATH', [getenv('PATH') ':/opt/local/bin']); %set GMT path for mac
    %system('./Draw_stereograms 1 gbpd_SrTiO3_all_EDAX_2d_gmt 2d rainbow 0.76 1.37 0.06 stereo CUB')

    cd (oldFolder)
end
```

A.2.3. Function GBCDsegments2dat

```
function datFname = GBCDsegments2dat(ax,ang,GBCDfolder,segments_fname, GBCD_par)
%Function actions:
   %1- Copy boundary segments file to GBCD folder
   %2- Change  input.txt file
   %3- run GBCD program
%Input:
   % ax= Axis of misorientation (MTEX class Miller)
   % ang= Angles of misorientation in degrees (double array)
   % GBCDfolder = root folder with gbpd/gbcd programs
   % segments_fname = path to segments file
   % GBCD_par = gbpd/gbcd/parameters (obtained from getGBCDpar.m)
%Output:
   %datFname: Path to the GBCD .dat file located in the gbcd_graph_fd folder to be ploted
%% Set file names, folder paths
oldFolder=pwd;
cd (GBCDfolder)

if length(ax)~=length(ang)
      error ('Different axis/ angle size. They must be the same size.')
end
[~,sample_name,ext] = fileparts(segments_fname) ;

% output file names should be:
```

```
for i=1:length(ang)
 datFname{i}          =          fullfile(GBCDfolder,'gbcd_graph_fd',['gbcd_',sample_name,
'_gmt_',num2str(i),'.dat']);
end

%% Replace location of boundary segments file in 'calc GBCD' input file
inputFname = fullfile(GBCDfolder,'calc_gbcd_stereo_fd','input.txt');

% replace second line of 'gbcd calc' input file with the name of segment file
clear A; A = regexp(fileread(inputFname), '\n', 'split');% read all data to A, line by line
A{2} = sprintf([sample_name,ext]);% replace content of 2nd line
fid = fopen(inputFname, 'w');% open input.txt

% Replace parameters in 'calc GBCD' input file
%GBCD_par=[msym, rot, rad, resolution, seg, stepSize, cutOff];
A{4} = sprintf( '%d\t%d\t%d', GBCD_par(1:3)); % replace symmetry, rotation, radian
A{6} = sprintf( '%d\t%d', GBCD_par(4:5)); % replace resolution
A{8} = sprintf( '%d', GBCD_par(6)); % replace segment analysis
A{10} = sprintf( '%4.1f', GBCD_par(7)); % replace step size
A{12} = sprintf( '%4.2f', GBCD_par(8)); % replace small length cutoff

fprintf(fid, '%s\n', A{:});
fclose(fid);

%copy file
copyfile(segments_fname,fullfile(GBCDfolder,'calc_gbcd_stereo_fd',
[sample_name,ext]), 'f');
```

```
%% Replace file path, axis and angle in  'plot GBCD' input file
inputFname = fullfile(GBCDfolder,'gbcd_graph_fd','input.txt');

% replace 12+(1:length(ang)) lines of 'gbcd plot' input file with the ax(x,y,z)/ang(deg)
clear A; A = regexp(fileread(inputFname), '\n', 'split');% read all data to A, line by line
% replace file name
   A{1} = sprintf(['gbcd_',sample_name,ext]);% replace content of 1st line

A(13:end) = [];% clear existing ax/angle
A(~cellfun('isempty',A)); % clear empty lines

for i=1:length(ang)
   A{12+i} = sprintf( '%4.2f \t %4.2f \t %4.2f \t %4.1f', ax(i).x, ax(i).y, ax(i).z, ang(i)');%
replace content of 13th to (12+max(i)) lines
end
% Replace parameters in 'plot GBCD' input file
%GBCD_par=[msym, rot, rad, resolution, seg, stepSize, cutOff];
A{3} = sprintf( '%d ', GBCD_par(1));% replace symmetry
A{9} = sprintf( '%d\t%d', GBCD_par(4:5));% replace resolution
A{11} = sprintf( '%d ', length(ax));% replace number of plots

fid = fopen(inputFname, 'w');% open input.txt
fprintf(fid, '%s\n', A{:}); % write A
fclose(fid); % close

  %% Run GBCD script
```

```
    % Set Fortran path For MATLAB (if not already):
try
    if contains(computer , 'MAC' ) % MAC
        if ~contains(getenv('PATH'), ':/usr/local/bin')
            setenv('PATH', [getenv('PATH') ':/usr/local/bin']); %set path for mac
        end
        system(['chmod +x ',fullfile(GBCDfolder, 'gbcd.sh')]);% make shell file executable (Mac/Linux)
        system(['. ',fullfile(GBCDfolder, 'gbcd.sh')]);% Run and Show output
        fprintf('\n-GBCDsegments2dat: GBCD wrote to file(s): \n ')
        disp(datFname);
        fprintf('\n')

    elseif contains(computer , 'LNX' ) % Linux
            system(['chmod +x ',fullfile(GBCDfolder, 'gbcd.sh')]);% make shell file executable (Mac/Linux)
            system(['. ',fullfile(GBCDfolder, 'gbcd.sh')]);% Run and Show output
            fprintf('\n-GBCDsegments2dat: GBCD wrote to file(s): \n ')
            disp(datFname);
            fprintf('\n')

    elseif contains(computer , 'WIN' )
        system(['chmod +x ',fullfile(GBCDfolder, 'gbcd_WIN.sh')]);% make shell file executable (Mac/Linux)
        system(['sh ',fullfile(GBCDfolder, 'gbcd_WIN.sh')]);% Run and Show output
        fprintf('\n-GBCDsegments2dat: GBCD wrote to file(s): \n ')
        disp(datFname);
```

```
        fprintf('\n')
    end

 catch
        error('It was not possible to execute the shell Files. ')
end
%add GMT folder to path
%     setenv('PATH', [getenv('PATH') ':/opt/local/bin']); %set path for mac

cd (oldFolder)
end
```

A.2.4. Function loadGBPD

```
function GBPD = loadGBPD(datFname, varargin)
%Function actions:
    % Load rho, theta and mud from gbpd .dat file
%Input:
    % datFname = GBPD structure containing rho, theta and m.u.d.
%Output:
    % GBPD = Structure with coordinates and multiple of uniform distribution (m.u.d.)
values
%% Create gbpd structure
GBPD=dlmread(datFname);
GBPD(1,:)=[];GBPD(:,4)=[];
```

```
GBPD=array2table(GBPD);
% Rename Columns
GBPD.Properties.VariableNames{1}='theta';
GBPD.Properties.VariableNames{2}='rho';
GBPD.Properties.VariableNames{3}='mud';
% Round values
GBPD.theta=round(GBPD.theta);
% Round values and convert rho to Matlab reference frame
GBPD.rho=round(GBPD.rho-90);


%% Area fraction calculation example
% cs=crystalSymmetry('mmm', [4.762 10.225 5.994]);
%       m=Miller(vector3d('polar',GBPD.rho,GBPD.theta),cs);%       transform       polar
coordinates to miller idx
% mr=round(m); %round miller index
%
% mt=table(m.hkl);% create table from hkl  indexes...
% mt.Properties.VariableNames{1}='hkl'; %rename column
%  mrt=table(mr.hkl);
%  mrt.Properties.VariableNames{1}='hkl_Round';
%
% areafraction=(GBPD.mud/81)*100;
% dists=(areafraction.^-1)/max((areafraction.^-1)); %distance normalized from 0 to 1
%
% GBPD=[GBPD table(areafraction) table(dists) mt mrt];
%%
fprintf('\n -loadGBPD: GBPD imported with the following properties: \n')
```

```
disp(GBPD.Properties.VariableNames)
end
```

A.2.5. Function loadGBCD

```
function GBCD = loadGBCD(datFnames)
%Function actions:
    % Load rho, theta and mud from gbcd .dat file
%Input:
    % datFnames = Cell with GBCD file names containing rho, theta and m.u.d.
%Output:
    % GBCD = Cell containing structures (gbcd) with coordinates and multiple of uniform distribution (m.u.d.) values

%% Read GBCD from all files
for i=1:length(datFnames)
    datFname=datFnames{i};
    gbcd=dlmread(datFname);
    gbcd(1,:)=[];gbcd(:,4)=[];
    gbcd=array2table(gbcd);
    % Rename Columns
    gbcd.Properties.VariableNames{1}='theta';%rename column
    gbcd.Properties.VariableNames{2}='rho';
    gbcd.Properties.VariableNames{3}='mud';
    % Round values
```

```
    gbcd.theta=round(gbcd.theta);
    % Round values and onvert rho to Matlab reference frame
    gbcd.rho=round(gbcd.rho-90); %

    %% Area fraction calculation example
%     cs=crystalSymmetry('mmm', [4.762 10.225 5.994]);
%     m=Miller(vector3d('polar',gbcd.rho,gbcd.theta),cs);% transform polar coordinates
to miller idx
%     mr=round(m); %round miller index
%
%     mt=table(m.hkl);% create table from hkl  indexes...
%     mt.Properties.VariableNames{1}='hkl'; %rename column
%      mrt=table(mr.hkl);
%      mrt.Properties.VariableNames{1}='hkl_Round';
%
%     areafraction=(gbcd.mud/81)*100;
%      dists=(areafraction.^-1)/max((areafraction.^-1)); %distance normalized from 0 to
1
%
%     gbcd=[gbcd table(areafraction) table(dists) mt mrt];

    GBCD{i}=gbcd;
end
    fprintf('\n -loadGBCD: GBCD of %.0f files imported. \n ', length(GBCD))

end
```

A.2.6. Function plotGBPD

```
function  plotGBPD(gbpd,cs,varargin)
%Function actions:
    % Plot GBPD in a stereographic projection
%Input:
    % gbpd = GBPD structure containing rho, theta and m.u.d.
%Output:
    % Stereographic projection plot of the GBPD
%Flags:
    % 'scatter' : Plot scatter plot of the GBPD
    % 'fundamentalRegion' : Plot in the fundamental Region of the crystal symmetry

%% Plot gbpd
fprintf(1,'\n -plotGBPD: Plotting GBPD...')

vec=vector3d('polar', deg2rad(gbpd.rho), deg2rad(gbpd.theta));

% Scatter plot
if ~isempty(varargin) && any(contains(varargin, 'scatter'))
      if contains(varargin, 'fundamentalRegion')
        m=Miller(vec,cs);
        figure;plot(m,gbpd.mud,'fundamentalRegion')

    else
         figure;plot(vec,gbpd.mud,'upper')
      end
```

```
% Interpolation plot
else
    if ~isempty(varargin) && any(contains(varargin, 'fundamentalRegion'))
        m=Miller(vec,cs);
        figure;plot(m,gbpd.mud,'fundamentalRegion','smooth')
    else
        grid_res=round(mode(diff(gbpd.theta))); % Grid resolution: angle interval between values (in deg)
        % grid_res=9;
        equiGrid=plotS2Grid('resolution',grid_res*degree);

        idwVec = interp(vec,gbpd.mud,equiGrid,'inverseDistance');
        pcolor(equiGrid,idwVec,'projection','edist','upper','smooth'); %
    end

end
% Plot Miller index above it
% h = [cs.aAxis,cs.bAxis,cs.cAxis];
% hold on
% plot(h,'markerFaceColor',[ 0.5765 0.2314 0.2549],'markerSize',5, 'labeled','all', 'fontSize',12,'Color',[ 0.5765 0.2314 0.2549],'upper')
% hold off
%
% set(gca,'fontSize',18)
%
% mtexColorMap(parula)
```

```
% hold on
%     plotMirrorPlanes(cs,'upper')
% hold off

%% Plot max/min

% [~,id_max_mud]=max(gbpd.mud);
% [~,id_min_mud]=min(gbpd.mud);
%
% % m_max=round(Miller(vec(id_max_mud),cs));
% % m_min=round(Miller(vec(id_min_mud),cs));
% m_max=Miller(vec(id_max_mud),cs);
% m_min=Miller(vec(id_min_mud),cs);
%
%%Low id Miller idx
% maxIdx=4;
% equiGrid=plotS2Grid('resolution', 2*degree,'fundmentalRegion');
% m=Miller(equiGrid,cs);
% m=round(m); m=unique(m);
% m=m(m.h<=maxIdx & m.k<=maxIdx & m.l<=maxIdx);
% m=symmetrise(m,cs,'upper');m=m(:);
%
% [~,id_max]=min(angle(m_max,m));
% m_max=m(id_max);
% [~,id_min]=min(angle(m_min,m));
% m_min=m(id_min);
```

```
% % f=newMtexFigure;plot(m, 'labeled','all', 'fontSize',8,'upper','figSize','huge','markerSize',3,'grid','grid_res',pi/2)
%
% %plot Miller IDX
% hold on
% plot(m_max,'markerFaceColor',[0 0 0],'markerSize',8, 'labeled','all', 'fontSize',16,'Color',[0 0 0],'upper','parent',gca)
% hold off
%
% hold on
% plot(m_min,'markerFaceColor',[1 1 1],'markerSize',8, 'labeled','all', 'fontSize',16,'Color',[1 1 1],'upper','parent',gca)
% hold off

% Correct colorbar position
% set(gca,'fontSize',18)
%
% mtexColorMap(parula)
% vbar=mtexColorbar('fontSize', 18);
% ylabel(vbar,'m.u.d.','Interpreter','tex','fontSize',18);
% vbarPos = get(vbar,'Position');
% x_offset=round(vbarPos(1)*0.05);
% set(vbar,'Position',[vbarPos(1)+x_offset vbarPos(2) vbarPos(3) vbarPos(4)])
fprintf(1,' Done! \n ')
end
```

A.2.7. Function plotGBCD

```
function  plotGBCD(gbcds, cs, axs, angs,varargin)
%Function actions:
    % Plot GBCD in a stereographic projection
%Input:
    % gbcds = GBCD structure(s) containing rho, theta and m.u.d.
    % ax= Axis of misorientation (MTEX class Miller)
    % ang= Angles of misorientation in degrees (double array)
%Output:
    % Stereographic projection plot of the GBCD
%Flags:
    % 'scatter' : Plot scatter plot of the GBCD
    % 'smooth' : Interpolated plot
    % 'fundamentalRegion' : Plot in the fundamental Region of the crystal symmetry

%% Plot gbcd
fprintf(1,'\n -plotGBCD: Plotting GBCD...')

mtexFig=newMtexFigure;



for i=1:length(gbcds)
    gbcd=gbcds{i};
    ax=round(Miller(axs(i),'uvw'));
    ang=angs(i);
```

```
    if i~=1
        mtexFig.nextAxis;
    else
        mtexFig.gca;
    end

    vec=vector3d('polar', deg2rad(gbcd.rho),deg2rad(gbcd.theta));

% Scatter plot
    if contains(varargin, 'scatter')
        if contains(varargin, 'fundamentalRegion')
            m=Miller(vec,cs);
            plot(m,gbcd.mud,'fundamentalRegion','parent', mtexFig.gca)
        else
            plot(vec,gbcd.mud,'upper','parent', mtexFig.gca)
        end
% Interpolation plot
    else
        if contains(varargin, 'fundamentalRegion')
            m=Miller(vec,cs);
            plot(m,gbcd.mud,'fundamentalRegion','smooth','parent', mtexFig.gca)
        else
            grid_res=round(mode(diff(gbcd.theta))); % Grid resolution: angle interval between values
            equiGrid=plotS2Grid('resolution',grid_res*degree);

            idwVec = interp(vec,gbcd.mud,equiGrid,'inverseDistance');
```

```
        pcolor(equiGrid,idwVec,'projection','edist','upper','smooth','parent',
mtexFig.gca); %
      end


   end
   % Set title
   strTitle= sprintf('[%.0f %.0f %.0f] %.0f%c',
round(ax.u),round(ax.v),round(ax.w),ang,char(176));
   mtexTitle(strTitle,'interpreter','tex','parent', mtexFig.gca)%
end
fprintf(1,' Done! \n ')
end
```

A.3. Supplemental Figures

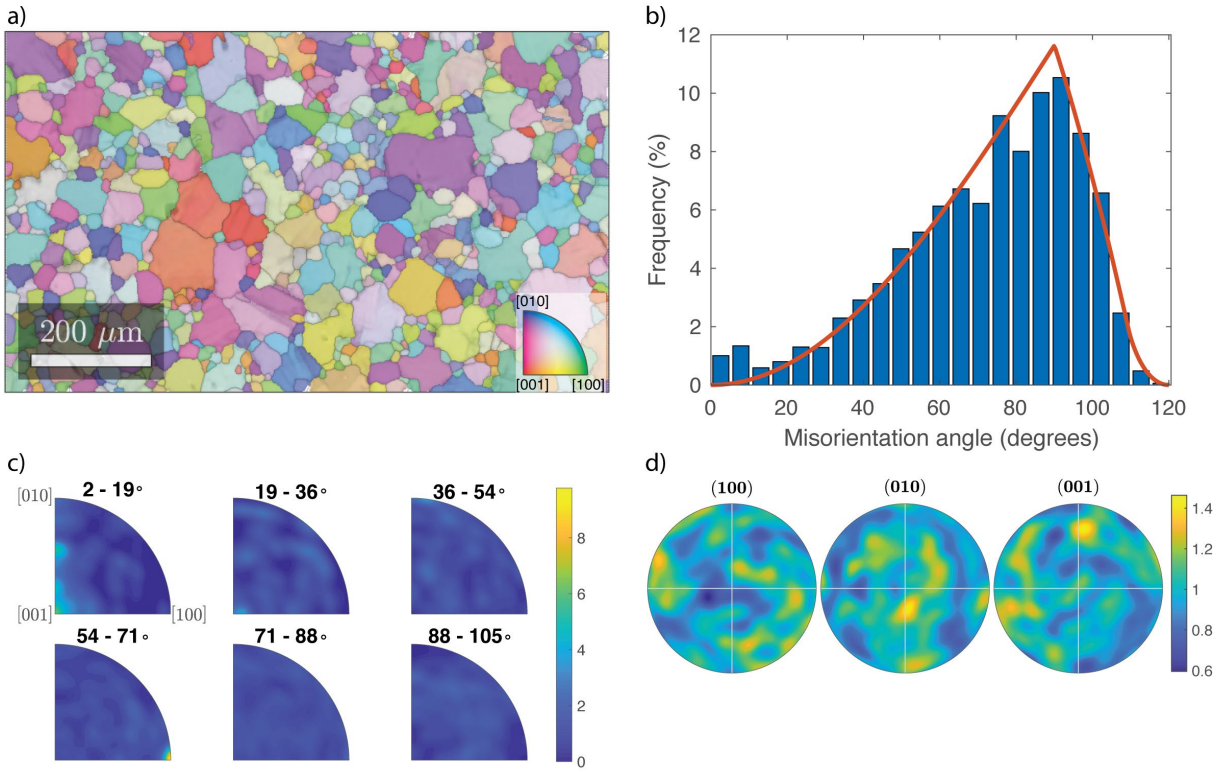

Figure A.3.1: Microstructures, misorientation and crystal preferred orientation of the starting material: a) Inverse pole figure map in the direction normal to the plane of the page. b) Misorientation angle and c) misorientation axis distribution in crystal coordinates. Uniform misorientation angle distribution is shown as a red line for reference. d) Pole figures of (100), (010) and (001) planes.

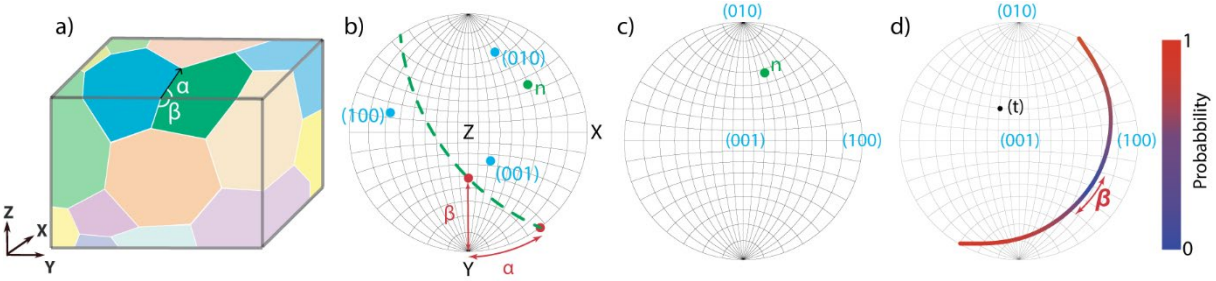

Figure A.3.2: Estimation of the orientation of grain boundaries. a) 3-D microstructure displaying the two spherical angles (α and β that define the grain-boundary plane. b) The grain-boundary plane is defined in a stereographic projection by a great circle (dashed green

line). c) The grain-boundary normal (*n*) and the principal crystal directions (poles to the a, b, and c planes) are plotted in the crystal reference frame. The Miller index of the respective boundary plane can be extracted using this construction. d) For EBSD data from 2-D sections, for example the XY plane presented in a), β is unknown but must be in the range of 0 to π, and the grain-boundary normal should contain the pole to the grain-boundary trace (t). Poles of grain-boundary planes perpendicular to the XY surface (red) are sampled with a higher probability than those parallel to that surface (blue).

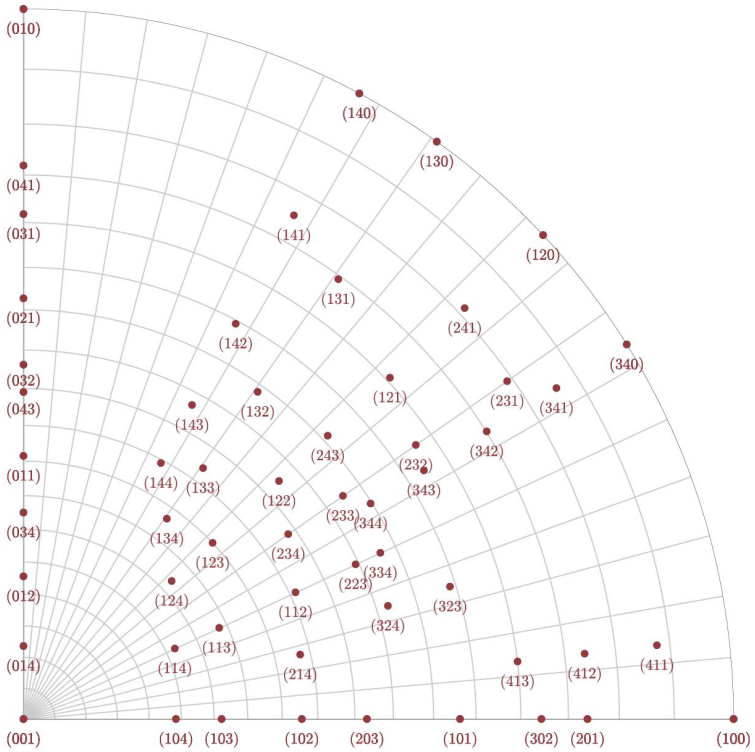

Figure A.3.3: Equal-angle stereographic projection of olivine crystallographic planes. Miller indices up to 4 are shown.

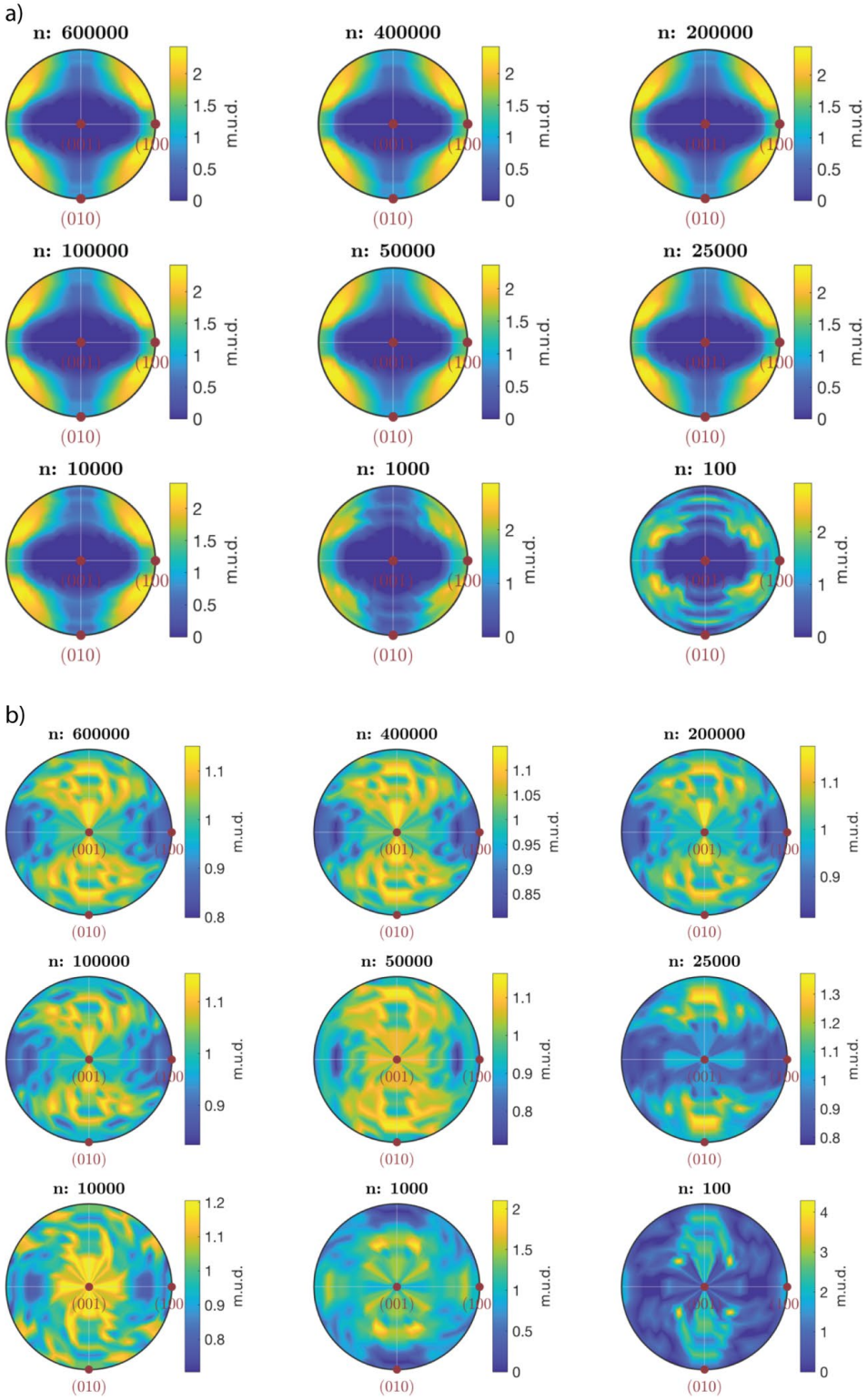

Figure A.3.4: Grain boundary plane distribution as a function of number of segments: a) GBPD of textured sample shows no significant modifications from a minimum of 10 000 segments. b) GBPD of untextured sample (sample PT0535) shows no significant modifications from a minimum of 100 000 segments, one order of magnitude higher than textured samples. The number of uniformly sampled segments (n) is given above each plot. Note that a) refers to only one section (XZ) of PT0499, which is a textured sample, therefore the data differs from overall GBPD data depicted in Figure 3.8.

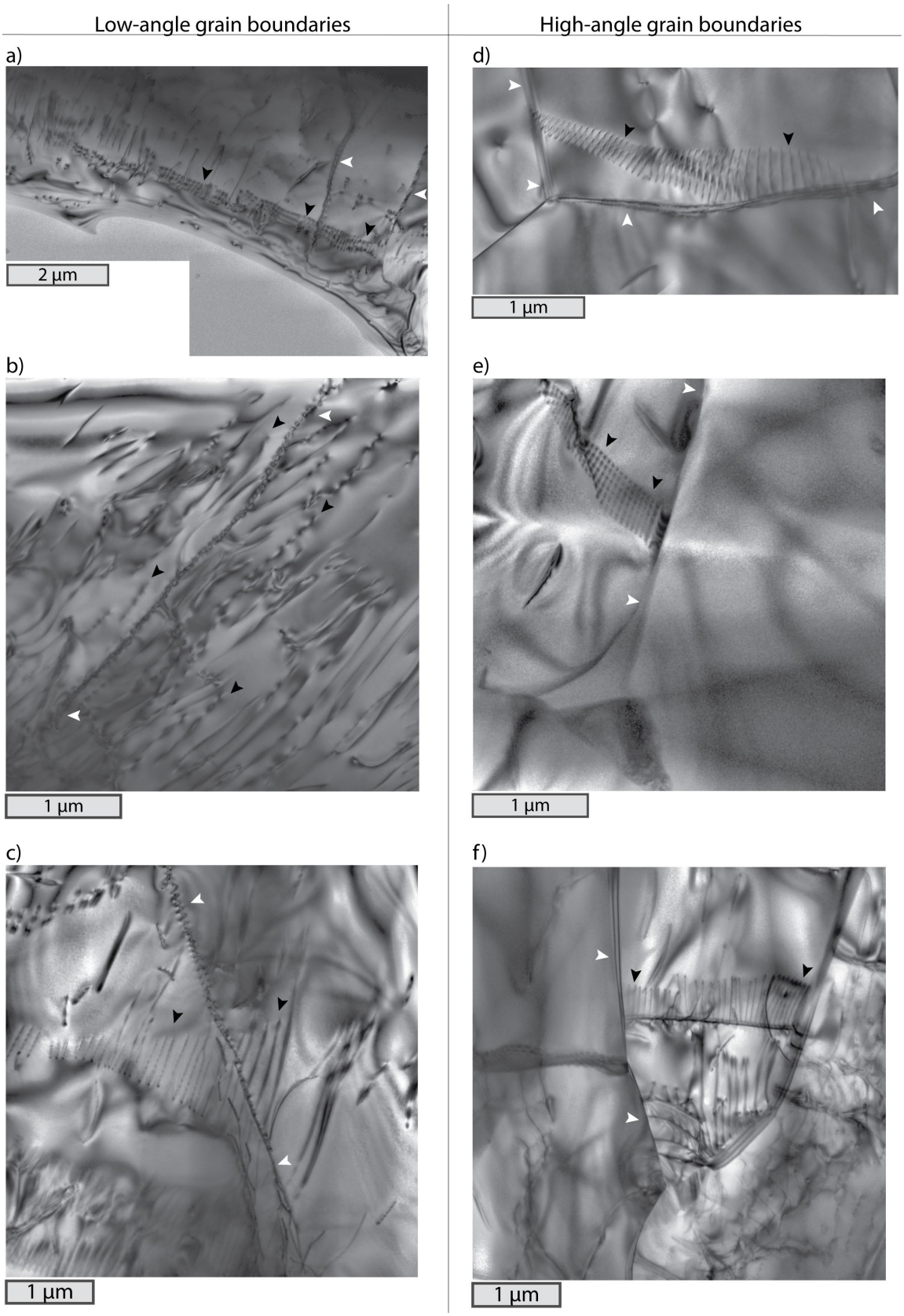

Figure A.3.5: TEM bright field images illustrating the interaction between dislocations and grain boundaries. a-c) Slip bands (black arrows) transmitted across low-angle grain boundaries (white arrows). d-f) Slip band (black arrows) blocked by high-angle grain boundaries (white arrows). Contrast-limited adaptive histogram equalization was applied to all TEM images. TEM images are form sections XZ' and XZ" (see Figure 2). The diffraction vector (*g*) was not measured.

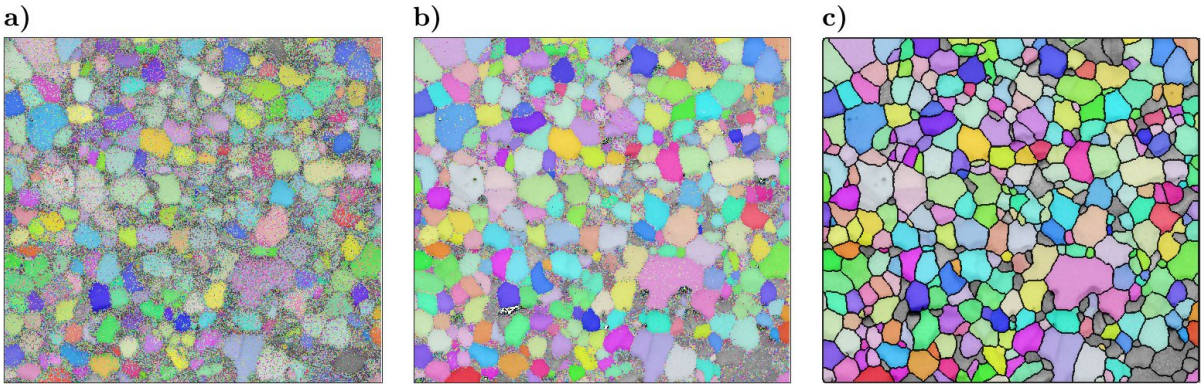

Figure A.3.6: Cleaning of EBSD data exemplified with the sample FSG5 - starting material. EBSD data is shown by inverse pole figure maps of olivine overlaying grayscale image quality maps: a) EBSD data as acquired, b) after NPAR re-indexing and c) after grain-dilation and pseudo-symmetry correction. Resulting grain boundaries are also shown in this figure. Images are 35 x 35 µm wide. Grey areas are poorly indexed or pyroxene grains.

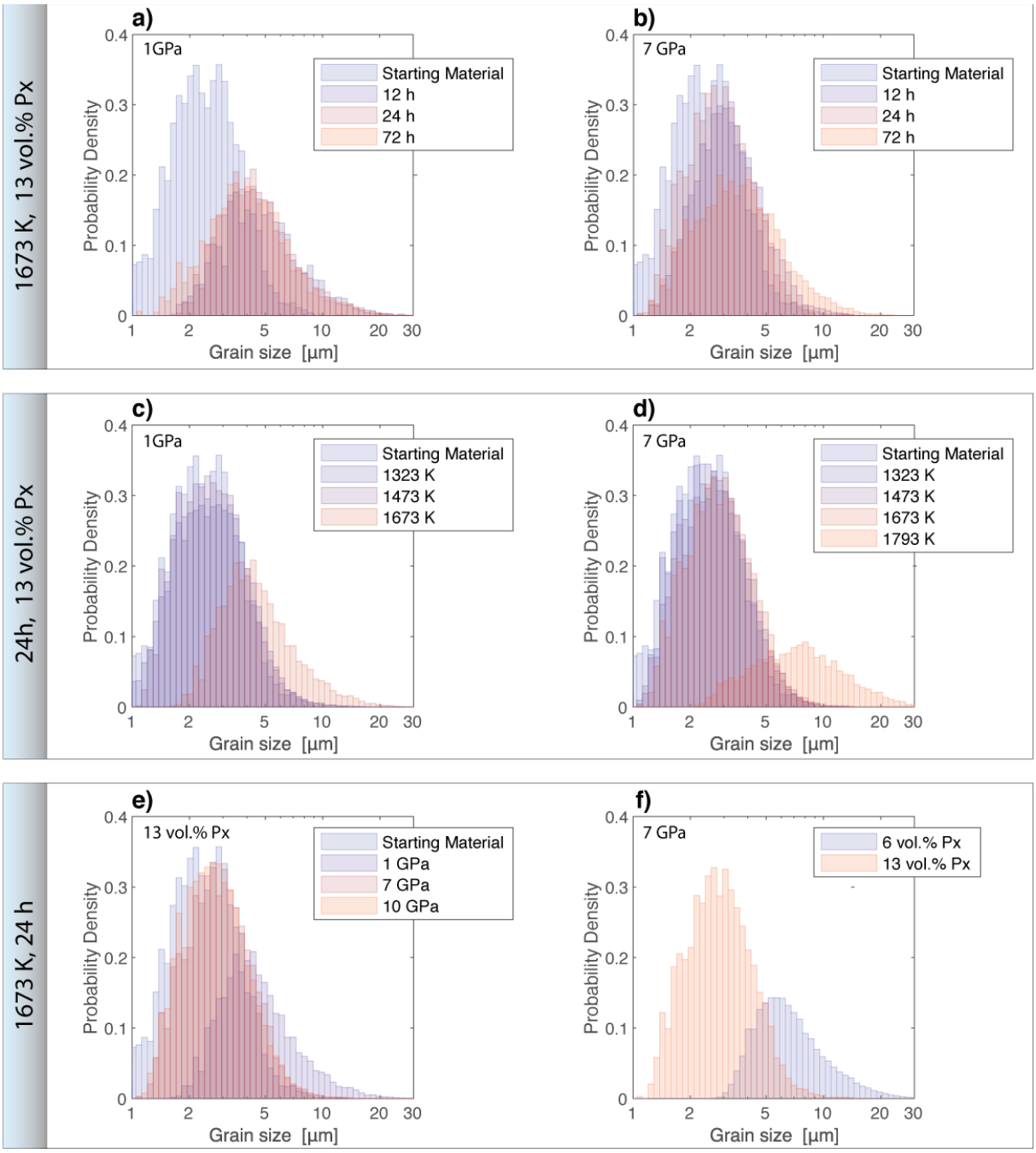

Figure A.3.7: Grain size distributions: The first row shows the series of experiments for different annealing time, performed at 1673 K and pressures of a)1 GPa and b) 7GPa. The second row shows the temperature series of experiments performed for 24 hours at pressures of c)1 GPa and d) 7GPa. The third row shows the pressure and pyroxene content series of experiments performed at 1673 K for 24 hours. e) Grain size distribution for experiments performed at pressures of 1 GPa, 7 GPa and 10 GPa. f) Grain size distribution for experiments performed at 7 GPa for different pyroxene contents: 6 vol.% and 13 vol.%.

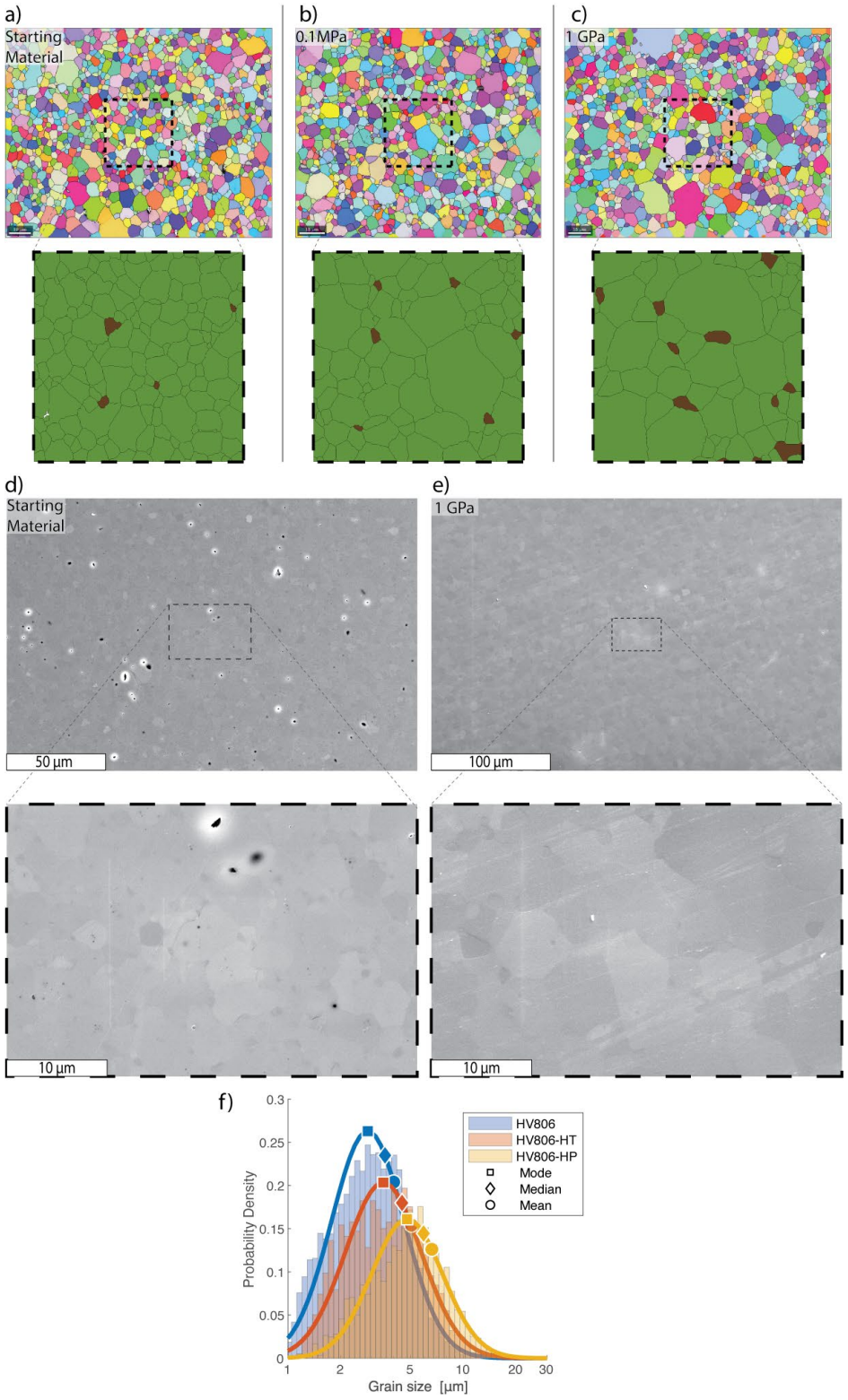

Figure A.3.8. Microstructure of samples a)HV806 (vacuum sintered Fo+10 vol.% En, starting material), b)HV806-HT (1673 K, 24 h, 0.1 MPa) and c)HV806-HP (1673 K, 24 h, 1 GPa). Images show inverse pole figure maps of olivine with insets showing phase maps: olivine is green and pyroxene is brown. Secondary electron image of samples d) HV806 and e) HV806-HP. Insets show magnified regions. Insets are 50 µm x 50µm. Note pores and holes in the starting material (d) and its virtually absence after high pressure experiments(e).f) Grain size distribution (bars) and its respective log-normal distribution (curves) of samples HV806, HV806-HT and HV806-HP.The mode, median and mean of each distribution is shown by squares, diamonds and circles respectively.

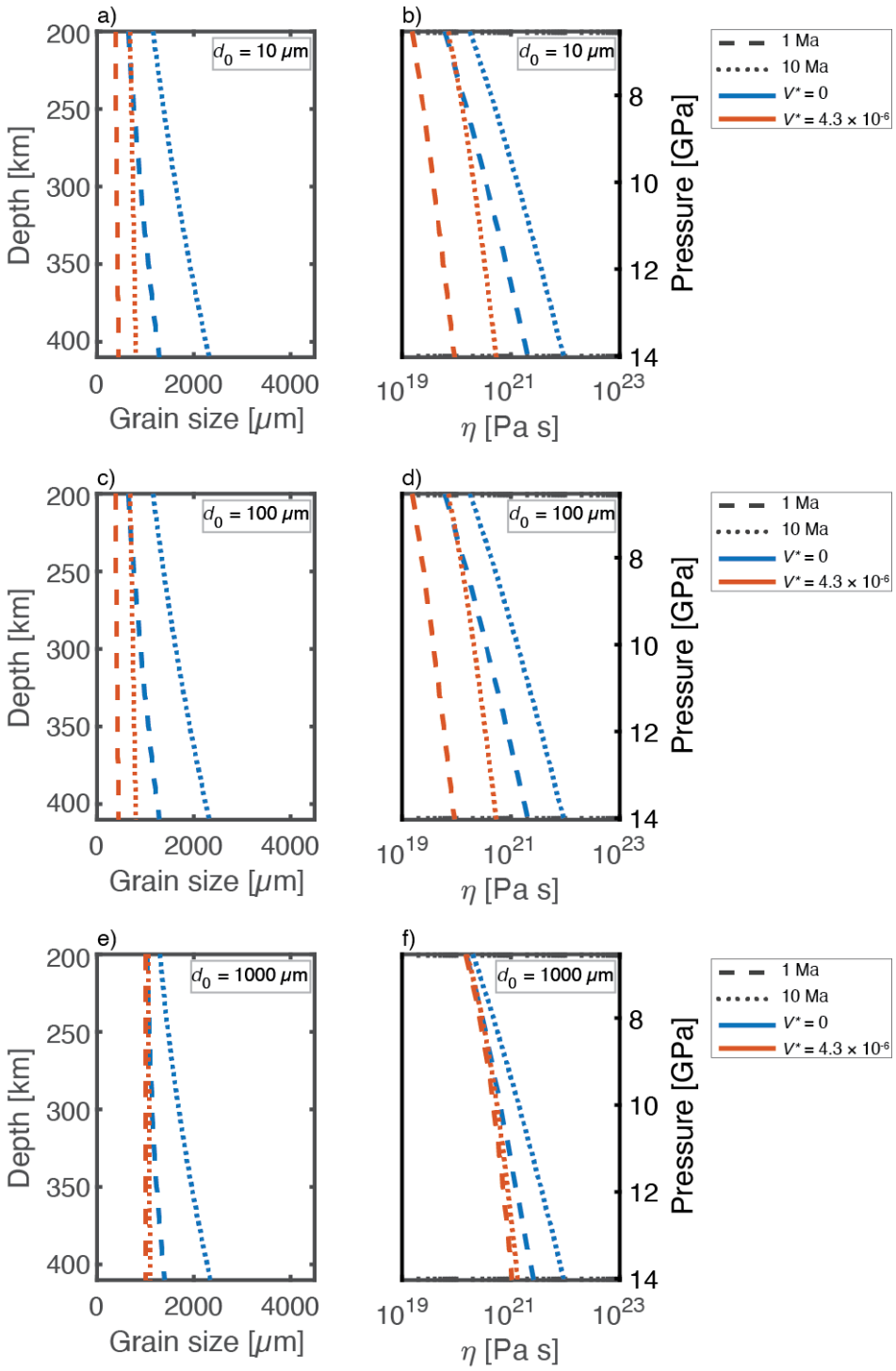

Figure A.3.9. The effect of different initial grain sizes on the viscosity estimation at deep upper mantle conditions: Figures on the left column demonstrate the expected grain sizes at 1 Ma (dashed lines) and 10 Ma (dotted lines) at the conditions of the geotherm shown in figure 9a, considering an activation volume of $V^* = 0$ m^3/mol (blue lines) and $V^* = 4.3 \times 10^{-6}$ m^3/mol (orange lines). Figures on the right column show the resulting viscosity profile of the deep upper mantle at 1 Ma and 10 Ma, for constant shear stress of 1 MPa and strain rates from experimental flow laws of disGBS, diffusion creep (Hansen et al., 2011; Hirth and Kohlstedt, 2003) and dislocation creep (Hirth and Kohlstedt, 2003). Figures in the upper(a, b), middle(c, d) and bottom row were calculated considering initial grain sizes of 10 μm, 100 μm and 1000 μm (1 mm), respectively.

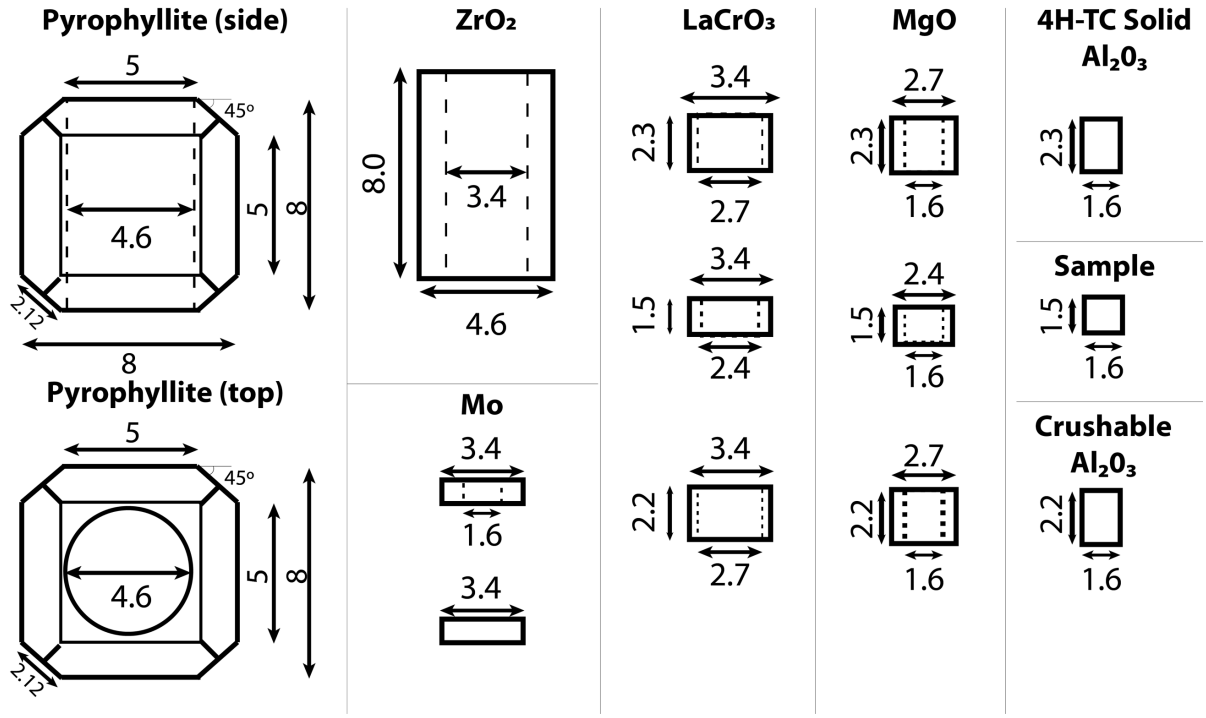

Figure A.3.10: Dimensions of parts in a 8/5 deformation assembly. Dimensions are in mm.

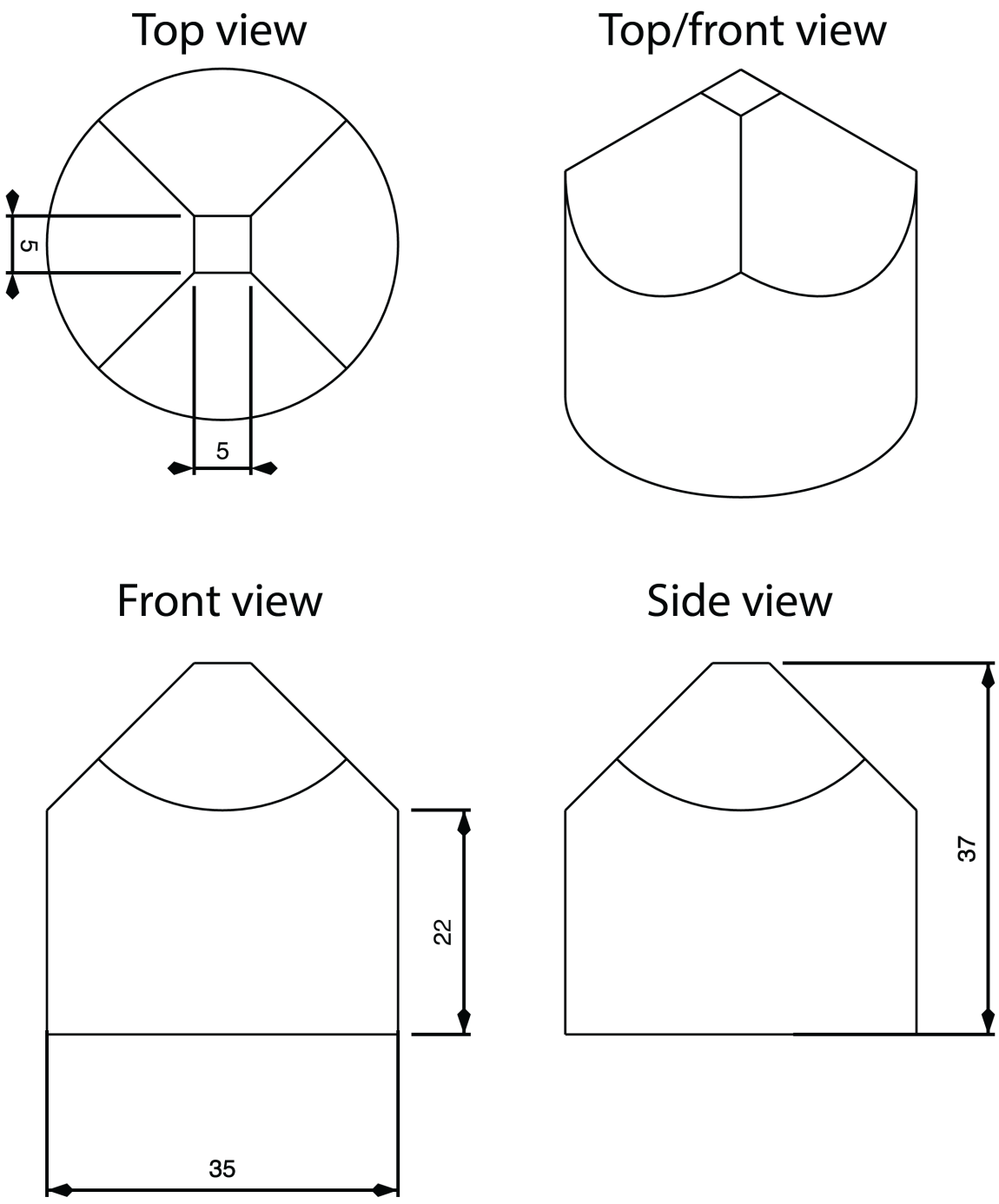

Figure A.3.11: Dimensions of second-stage anvil with a 5 mm truncated edge length. Dimensions are in mm.

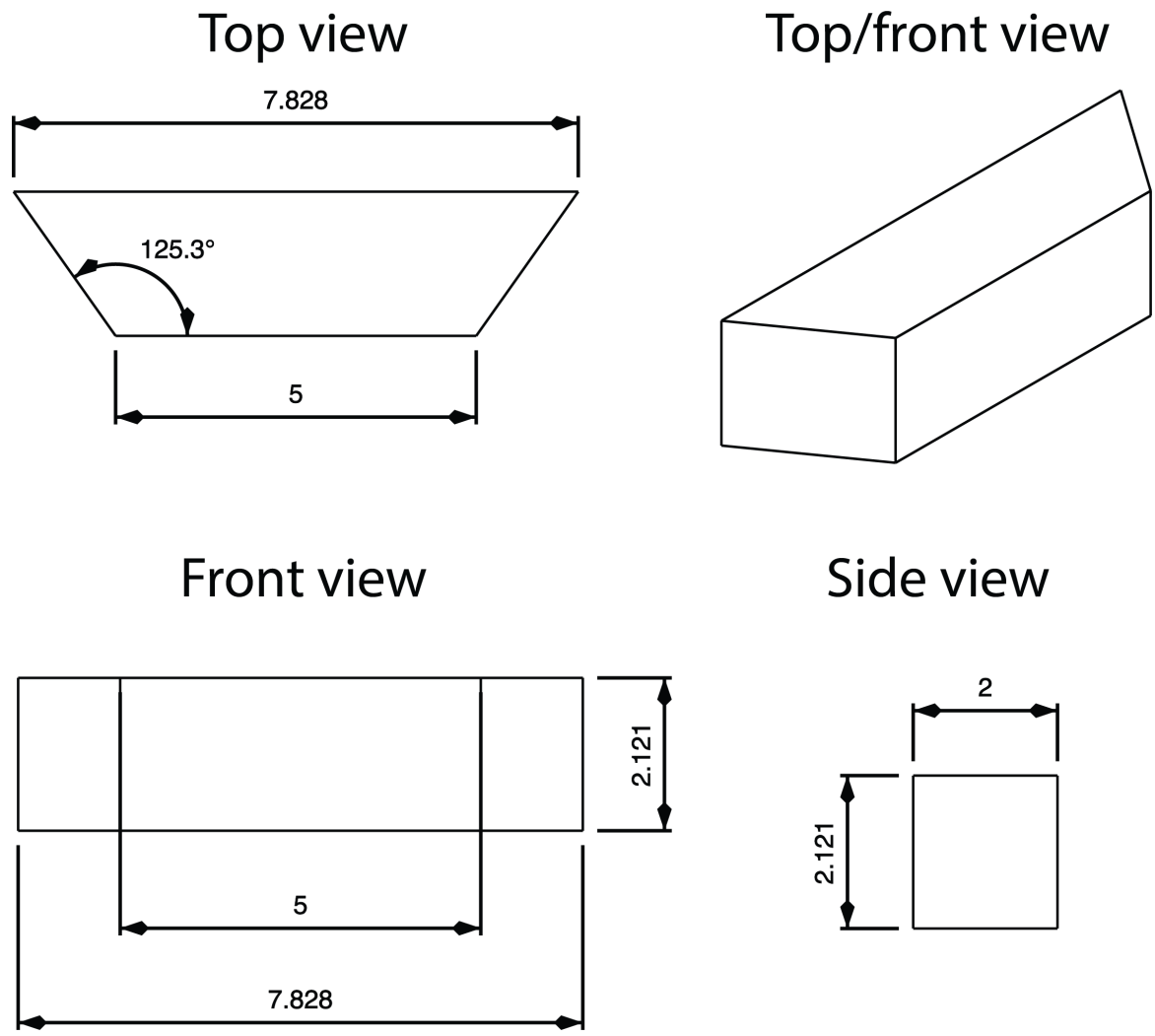

Figure A.3.12: Dimensions of gasket used together with the 8/5 assembly. Dimensions are in mm.

A.4. Supplemental Tables

Table A.4.1: Experimental data of samples HV806, the vacuum-sintered starting material, HV806-HP, the grain growth experiment at 1 GPa and HV806-HT , the grain growth experiment at 1 atm. *P* is pressure in GPa, *T* temperature in ºC, *t* experimental duration in hours, *d* average grain size in µm, d_{MIL} the mean intercept length in µm. Mo_{Fit}, μ_{Fit} and σ_{Fit} are the mode, mean and standard deviation of the lognormal fit to the grain-size distribution, respectively. f_{Px} is the pyroxene fraction as measured by EBSD and *n* is the number of grains analysed for each sample.

Sample	Starting Material	*P* (GPa)	*T* (K)	*t* (h)	*d* (µm)	d_{MIL} (µm)	Mo_{FIT}	μ_{FIT}	σ_{FIT}	f_{Px} (EBSD)	*n*
HV806	Vacuum sintered Fo + 10% Px	10^{-11}	1523	3	4	2,6	2,85	1,27	0,48	0,01	5424
HV806-HP	HV806	1	1673	24	6,59	4,14	4,77	1,78	0,47	0,02	3013
HV806-HT	HV806	10^{-4}	1673	24	5,04	3,38	3,49	1,5	0,5	0,02	2415

(Eidesstattliche) Versicherungen und Erklärungen

(§ 9 Satz 2 Nr. 3 PromO BayNAT)

Hiermit versichere ich eidesstattlich, dass ich die Arbeit selbstständig verfasst und keine anderen als die von mir angegebenen Quellen und Hilfsmittel benutzt habe (vgl. Art. 64 Abs. 1 Satz 6 BayHSchG).

(§ 9 Satz 2 Nr. 3 PromO BayNAT)

Hiermit erkläre ich, dass ich die Dissertation nicht bereits zur Erlangung eines akademischen Grades eingereicht habe und dass ich nicht bereits diese oder eine gleichartige Doktorprüfung endgültig nicht bestanden habe.

(§ 9 Satz 2 Nr. 4 PromO BayNAT)

Hiermit erkläre ich, dass ich Hilfe von gewerblichen Promotionsberatern bzw. -vermittlern oder ähnlichen Dienstleistern weder bisher in Anspruch genommen habe noch künftig in Anspruch nehmen werde.

(§ 9 Satz 2 Nr. 7 PromO BayNAT)

Hiermit erkläre ich mein Einverständnis, dass die elektronische Fassung meiner Dissertation unter Wahrung meiner Urheberrechte und des Datenschutzes einer gesonderten Überprüfung unterzogen werden kann.

(§ 9 Satz 2 Nr. 8 PromO BayNAT)

Hiermit erkläre ich mein Einverständnis, dass bei Verdacht wissenschaftlichen Fehlverhaltens Ermittlungen durch universitätsinterne Organe der wissenschaftlichen Selbstkontrolle stattfinden können.

…….
Ort, Datum, Unterschrift